DEVELOPMENT OF SURFACE SENSITIVITY IN SCANNING X-RAY MICROSCOPY AND NEXAFS SPECTROSCOPY OF ORGANOSULPHUR COMPOUNDS

A Thesis Submitted to the

College of Graduate Studies and Research

In Partial Fulfillment of the Requirements

For the Degree of Doctor of Philosophy

In the Department of Chemistry

University of Saskatchewan

Saskatoon, Saskatchewan

By

Shirin Behyan

PERMISSION TO USE

In presenting this thesis in partial fulfillment of the requirements for a postgraduate degree from the University of Saskatchewan, I agree that the libraries of this University may make it freely available for inspection. I further agree that permission for copying of this thesis in any manner, in whole or in part, for scholarly purposes may be granted by Dr. S.G. Urquhart who supervised my thesis work or, in his absence, by the department Head of the Department of Chemistry or the Dean of the College of Graduate Studies and Research in which my thesis work was done. It is understood that any copy or publication or use of this thesis or parts thereof for financial gain shall not be allowed without my written permission. It is also understood that due recognition shall be given to me and to the University of Saskatchewan in any use which may be made of any material in my thesis.

Request for permission to copy or to make other use of material in this thesis in whole or in part should be addressed to:

The Head
Department of Chemistry
University of Saskatchewan
Saskatoon, Saskatchewan
Canada S7N 5C9

ABSTRACT

In this thesis, two objectives related to Near Edge X-ray Absorption Fine Structure (NEXAFS) spectroscopy have been studied. The first objective was to develop surface sensitivity in Scanning Transmission X-ray Microscopy (STXM) at the Canadian Light Source (CLS) and the Advanced Light Source (ALS). The second objective was to study sulphur 1s NEXAFS spectra of organosulphur compounds relevant to petroleum by experimental and computational methods.

Towards the first objective, Total Electron Yield (TEY) detection has been implemented in a STXM microscope, by conventional sample current and single electron counting detection modes. This provides improved surface-sensitive detection, simultaneous with existing bulk-sensitive transmission detection in the STXM microscopes. Both approaches provide improved surface sensitive imaging and spectroscopy, although channeltron-based detection is superior. TEY-STXM provides surface sensitive imaging of ultrathin films such as phase-separated Langmuir-Blodgett monolayer films, phase separated polymer thin films, as well as differentiation of surface and bulk oxides of patterned metal thin films. The challenge for TEY-STXM measurements is the poor vacuum environment in the STXM chamber at the CLS, which greatly impacts the function of the channeltron as well as the rate of the photodeposition. Although the effect of photodeposition can be minimal in bulk spectroscopy of organic samples, it is a challenge in spectroscopy of organic thin films, where the photodeposits can dominate the weak signal originating from the surface. Chapter 4 of this thesis discusses the details of this study along with the challenges encountered in the development of this new TEY-STXM technique.

The second goal of my research was the detailed study of sulphur 1s NEXAFS spectra of organosulphur compounds by experimental and computational methods to obtain a complete database of sulphur 1s NEXAFS spectra. The speciation and quantification of sulphur compounds is of great interest in different areas such as fossil fuel studies, biology, geology, and archaeology. Sulphur 1s NEXAFS spectroscopy can be used for speciation and quantification of these compounds. For this purpose a firm understanding of NEXAFS spectra of sulphur compounds is required. Therefore, the

sulphur 1s NEXAFS spectra of different sulphur functionalities have been studied including thiols, thioethers, disulphides, sulfoxides, sulfones, and thiophenic compounds in gas and condensed phases. These highly resolved spectra have been further analyzed with the aid of *ab initio* calculations. The highly resolved experimental spectra showed fine features predicted by calculations. The combination of experiment and calculation has been used to improve assignment of spectroscopic features relevant for the speciation and quantification of sulphur compounds.

ACKNOWLEDGMENTS

I would like to thank my supervisor, Professor Stephen G. Urquhart, for all of his kind help and support as well as his great teaching and guidance through my PhD program.

I would like to thank the members of my advisory committee: Professor Steve Reid, Professor Andrew Grosvenor, and Professor Derek Peak and my external examiner Professor John J. Neville for their valuable advice and discussions.

I am also grateful to the members of the Physics Machine Shop and of the Chemistry-Electronic Shop of the University of Saskatchewan, and the beamline scientists Dr. Tolek Tyliszczak from the Advanced Light Source (ALS) and Dr. Jian Wag and Dr. Chithra Karunkaran from the Canadian Light Source (CLS).

I am also thankful to Dr. Brian Haines and Dr. Jian Wang at the CLS and Dr. Tolek Tyliszczak at the ALS for their help during TEY-STXM experiments.

Finally, I am really grateful to my family: my mother Batoul Hamedian Esfahani and my father Yadolah Behyan, my sisters Mina, Mitra, and Zinat, and my brother Mahamoudreza who helped and supported me during these years and without them I could have never achieved my goals.

TABLE OF CONTENTS

LIST OF TABLES

LIST OF FIGURES

Chapter 1

Chapter 2

Chapter 8

LIST OF ABBREVATIONS

AEY: Auger Electron Yield
ALS: Advanced Light Source
BE: Binding Energy
BM: Bending Magnet
CLS: Canadian Light Source
CVD: Chemical Vapour Deposition
EPU: Elliptically Polarized Undulator
eV: electron volt
EXAFS: Extended X-ray Absorption Fine Structure
GSCF: Gaussian Self Consistent Field
GTO: Gaussian Type Orbital
HF: Hartree-Fock
HOMO: Highest Occupied Molecular Orbital
ID: Insertion Device
IP: Ionization Potential
IR: Infrared
IUPAC: International Union of Pure and Applied Chemistry
IVO: Improved Virtual Orbital
LCAO: Linear Combination of Atomic Orbital
MO: Molecular Orbital
NEXAFS: Near Edge X-ray Absorption Fine Structure
OD: Optical Density
OSA: Order Sorting Aperture
PEY: Partial Electron Yield
PMT: Photomultiplier Tube
SCF: Self-Consistent Field
SGM: Spherical Grating Monochromator
SM: Spectromicroscopy
STO: Slater Type Orbital
STXM: Scanning Transmission X-ray Microscopy
TEM: Transition Electron Microscope
TEY: Total Electron Yield
TEY-STXM: Total Electron Yield-Scanning Transmission X-ray Microscopy
UV: Ultraviolet
XAS: X-ray Absorption Spectroscopy
Z: atomic number
ZP: Zone Plate
Δ(SCF): Δ(Self Consistent Field)

CHAPTER 1 INTRODUCTION

Near Edge X-ray Absorption Fine Structure (NEXAFS) spectroscopy is a powerful technique in providing information on chemical composition and molecular orientation studies in different fields such as chemistry, materials, and the life sciences.[1.1-5] The theory of X-ray absorption spectroscopy is reviewed in §**1.1**, and then a detailed description of NEXAFS spectroscopy is provided in §**1.2**. Because of the chemical sensitivity of NEXAFS spectroscopy, this technique has been used in quantitative and qualitative analysis in a diversity of fields such as biology,[1.4, 1.6, 1.7] fossil fuels,[1.8-10] and archaeology.[1.10, 1.11] The applications of this technique as a qualitative and quantitative tool are described in §**1.3**. The chemical sensitivity of NEXAFS spectroscopy and its application in highly resolved chemical imaging were the motives to use this technique to explore my two research objectives.

The first objective of this research study was to develop a surface sensitive detection mode in Scanning Transmission X-ray Microscopy (STXM) at the Canadian Light Source (CLS) and the Advanced Light Source (ALS). STXM combines the high spatial resolution imaging of X-ray microscopy, based on a Fresnel zone plate-focusing element, with the chemical sensitivity of NEXAFS spectroscopy. However, STXM microscopes operate with transmission detection that is sensitive to the bulk chemistry of the sample. For improved surface analysis with STXM, the goal was to add surface sensitive detection mode to STXM microscopes by implementing total electron yield detection of NEXAFS signal (e.g., TEY-STXM). Secondly, the function of this new technique was to be examined with model samples. The motives for these studies are described in §**1.4**.

The second objective of my research was to study the sulphur 1s NEXAFS spectra of different sulphur functionalities relevant to petroleum through experimental and computational studies. The purpose of this study was to obtain a fully defined database of interpreted sulphur 1s NEXAFS spectra for sulphur compounds that are used in sulphur speciation and quantification of fossil fuels, and to examine how these studies can improve sulphur speciation. The motives for this study are described in full detail in §**1.5**. In §**1.6**, a summary of the project objectives along with an outline of the studies

performed toward the goals of this project is provided. The references for this chapter are provided in §**1.7**.

1.1 X-ray Absorption Spectroscopy

X-ray radiation is one form of electromagnetic radiation similar to visible light, but with more energetic photons.[1.12] X-rays are absorbed when a beam passes through a sample. The attenuation of the radiation intensity follows an exponential decay with sample thickness. The intensity of transmitted beam at a certain energy is related to the intensity of the beam before the sample, and the X-ray absorption cross-section (**§1.2**, **Equation 1.2**) following Lambert-Beer's law:

$$I = I_0 e^{-\mu x} \tag{1.1}$$

where I is the intensity of the transmitted beam, I_0 is the intensity of the incident beam, μ is the linear absorption coefficient, and x is the sample thickness. Generally, the absorption coefficient is inversely dependent on photon energy (i.e. photons with higher energies are more penetrating except at the absorption edges).[1.13] This process is shown schematically in **Figure 1.1**.

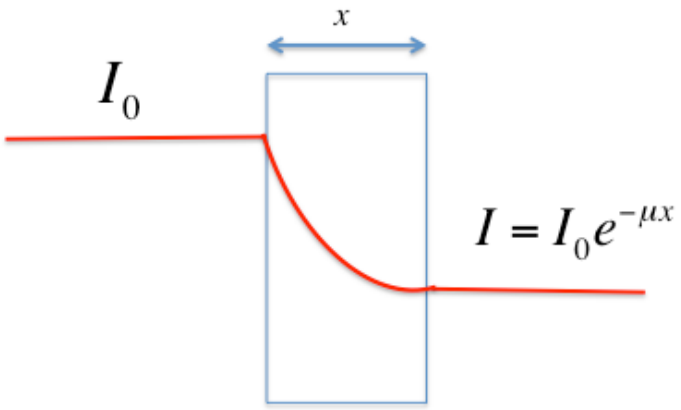

Figure 1.1 Schematic diagram of the transmission of light through a uniform sample.

There are different mechanisms that contribute to the attenuation of X-ray radiation; of these, absorption is the most important. In this mechanism, when the X-ray photon energy matches the energy of excitation or ionization of a bound core electron, the X-ray photon can be absorbed. At this energy the material has strong X-ray absorption referred to as atomic absorption edge. After this edge the absorption probability decreases monotonically. The atomic absorption edge depends on the electron

binding energy (BE) which is the minimum energy required to ionize an electron. As the BE is related to atomic number (Z), each element absorbs X-rays at specific energies, resulting in different edges for each element. For example sulphur 1s (corresponding to the excitation of a 1s electron of a sulphur atom) occurs at 2472.0 eV, Cr $2p_{3/2}$ and Cr $2p_{1/2}$ edges occur at 574.1 eV and 583.8 eV respectively. **Figure 1.2** shows an example of an X-ray absorption spectrum, which shows the absorption coefficient of an element versus photon energy in 1s and 2s and 2p edges.

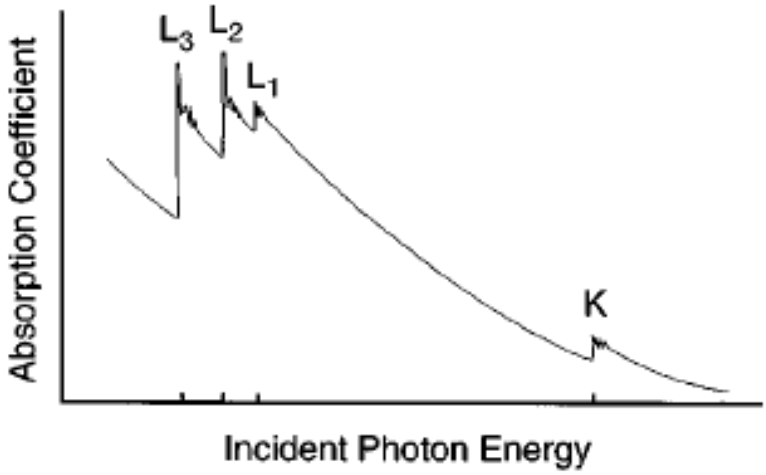

Figure 1.2 Schematic view of X-ray absorption coefficient as a function of incident photon energy. Four X-ray edges are shown: K (1s), L_1 (2s), L_2 ($2p_{3/2}$), and L_3 ($2p_{1/2}$). Note that the overall decrease in absorption as a function of energy is punctuated by four sharp, step-function-like increase at each edge.[1.14] [Reprinted with permission from Reviews of Modern Physics, 72 (3), Rehr, J. J.; Albers, R. C., Theoretical approaches to x-ray absorption fine structure, 621-654, Copyright 2000 by the American Physical Society.]

The energy spacing of the 1s, 2s and 2p edges of different elements are typically hundreds of electron volts, which makes it possible to study each element separately in any specific energy regime. This is referred to as element specificity.[1.13]

1.2 Near Edge X-ray Absorption Fine Structure (NEXAFS) Spectroscopy

NEXAFS spectroscopy refers to the area just below and up to 50 eV after the absorption edge in X-ray absorption spectrum. NEXAFS probes the absorption of X-ray radiation for the excitation of core electrons into unoccupied molecular orbitals, Rydberg orbitals or the continuum.[1.15] The region after 50 eV is referred to as Extended X-ray Absorption Fine Structure (EXAFS) spectroscopy.[1.13] EXAFS spectroscopy is usually

used for studying inorganic samples in order to determine the number, distance, and type of the ligand groups attached to the absorbing atom.[1.16]

A schematic diagram of a 1s NEXAFS spectrum for a diatomic molecule and its effective potential is represented in **Figure 1.3**.

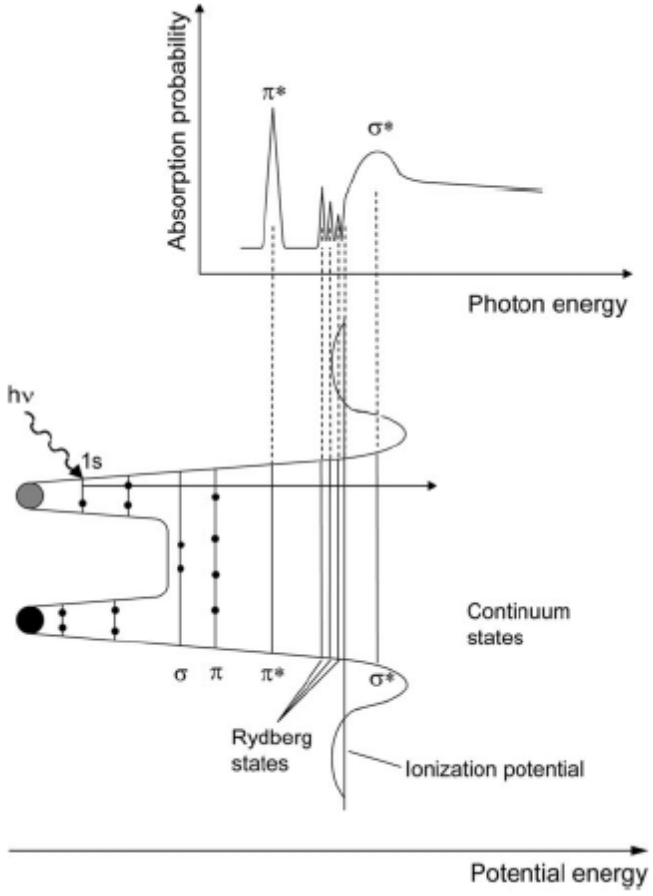

Figure 1.3 Schematic potential (bottom) and corresponding NEXAFS 1s spectrum (top) of a diatomic molecule. The NEXAFS spectrum includes Rydberg and unfilled molecular orbitals, which is reflected in the absorption spectrum.[1.15] [Reprinted from Chemical Society Reviews, *35* (12), Hähner, G., Near edge X-ray absorption fine structure spectroscopy as a tool to probe electronic and structural properties of thin organic films and liquids, 1244-1255, Copyright 2006, Reproduced with permission of The Royal Society of Chemistry, http://dx.doi.org/10.1039/b509853j.]

By scanning the X-ray energy around the ionization threshold, a resonant transition occurs when the energy of X-ray photons matches exactly the energy difference between the initial orbital and the final orbital. These transitions are superimposed on the step-like shape corresponding to the onset of the ionization potential (see **Figure 1.2**). In

this example, unoccupied molecular orbitals are called σ*- or π*-, based on their symmetry.

The lowest unoccupied molecular orbitals in a molecule with π-bonded diatomic subunits are π* orbitals. Because of electron-hole Coulombic interaction, these unoccupied orbitals are pulled below the ionization potential, whereas σ* orbitals lay at higher energies usually above the ionization potential for neutral molecules. Rydberg orbitals are atomic like orbitals and give rise to sharp but weak resonances below the ionization potential. In condensed phase or strongly chemisorbed molecules, these Rydberg resonances are quenched as a result of the large size of the orbitals that extend beyond the molecule. In molecules with carbon-hydrogen bonds, mixing of Rydberg orbitals with hydrogen-derived antibonding orbitals of the same symmetry results in an increase in the intensity of the corresponding resonances.[1.15]

Before proceeding to the application of NEXAFS spectroscopy, a review of the fundamental aspects for the calculation of X-ray absorption spectra is provided. The X-ray absorption probability is usually described by either the X-ray absorption cross-section or the optical oscillator strength. The X-ray absorption cross section is defined as the number of electrons excited per unit time divided by the number of incident photons per unit time per unit area.[1.3] By considering Fermi's golden rule and the dipole approximation the X-ray absorption cross section is described as:

$$\sigma_x = \frac{4\pi^2 h}{m^2}\frac{e^2}{\hbar c}\frac{1}{\hbar\omega}\left|\langle f|\varepsilon.p|i\rangle\right|^2 \rho_f(E) \tag{1.2}$$

where σ_x is the X-ray absorption cross section (cm^2), usually expressed in barn ($1cm^2 = 10^{24}$ barn), $\hbar = {}^{h}/_{2\pi}$, h is the Planck constant, c is the speed of light, e is the electron charge, m is the mass of the electron, $\hbar\omega$ is the photon energy, ε is the electric field vector of X-ray photons, p is the electron momentum, f is the wavefunction of the final orbital, i is the wavefunction of the initial orbital, and $\rho_f(E)$ is the energy density of final state.[1.3] For the convenience in discussion of transitions to bound orbitals and intensities of resonances, instead of absorption cross-section, *optical oscillator strength f* is used. This dimensionless quantity is related to the X-ray absorption cross-section by:

$$\sigma_x(E) = C\frac{df}{dE} \tag{1.3}$$

where $C = 2\pi^2 e^2 \hbar / mc = 1.1 \times 10^2$ Mb eV (1Mb = 1 megabarn). f is the energy integral of the cross section and is a measure of the intensity of a resonance, which often is quoted as "f number"

$$f = \frac{2}{m\hbar\omega}\left|\langle f|\varepsilon.p|i\rangle\right|^2 \tag{1.4}$$

Optical oscillator strength can be converted to cross-section by using equation (1.4):

$$\sigma_x(E) = \frac{2\pi^2 e^2 \hbar}{mc} f\rho_f(E) \tag{1.5}$$

By using polarized X-ray radiation, NEXAFS spectroscopy can be used to reveal orientation information. In this technique, the NEXAFS spectra are measured at two or more angles of polarized X-ray incidence, and as a result the orientation of a particular transition can be obtained. In a molecule, bonds and consequently the molecular orbitals and the transition dipole moment for transition to the molecular orbitals are highly directional. By recalling **Equation (1.2)**, in the case of a linearly polarized light, the angular dependence of the matrix element can be written in a single form as:

$$\left|\langle f|\varepsilon.p|i\rangle\right|^2 = \left|\varepsilon\langle f|p|i\rangle\right|^2 \tag{1.6}$$

For a 1s initial orbital and a directional final orbital O (where transition dipole moment is equal to the directional final orbital O), the transition intensity becomes:

$$I = \left|\varepsilon\langle f|p|i_{1s}\rangle\right|^2 \propto \left|\varepsilon \cdot O\right|^2 \propto \cos^2\delta \tag{1.7}$$

where δ is the angle between the electric field vector, and the direction of the final orbital O (transition dipole moment).[1.15] This effect is schematically shown in **Figure 1.4** where a π-bonded diatomic molecule is absorbed to the surface with its molecular axis perpendicular to the surface. For example the maximum orbital amplitude of σ*-orbitals are along the bond axis whereas the π*-orbitals are normal to the bond direction.

In this geometry the σ and π bonds are normal and parallel to the surface, respectively. When this molecule is irradiated by X-ray radiation in normal incident

angle, the transition intensity is maximized for a π* transition (left panel), as the electric vector is parallel to the direction of the final orbital, opposite to this occurs for the σ* transition where the X-rays are at a grazing angle (right panel).

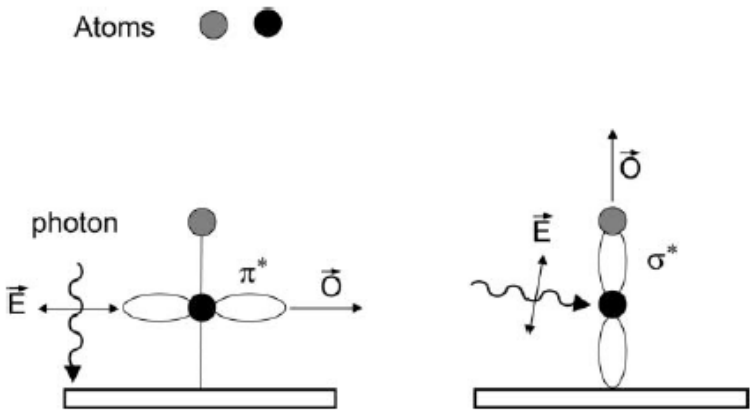

Figure 1.4 Schematic representation of the origin of the angular dependence of NEXAFS resonances for a π-bonded diatomic molecule adsorbed with its molecular axis normal to the surface. As a result of the different projection between the electric field vector, E, and the direction of the final molecular orbital, O, the π*-resonance is maximized at normal incidence (left), while the σ*-resonance is maximized at grazing incidence (right).[1.15] [Reprinted from Chemical Society Reviews, *35* (12), Hähner, G., Near edge X-ray absorption fine structure spectroscopy as a tool to probe electronic and structural properties of thin organic films and liquids, 1244-1255, Copyright 2006, Reproduced by permission of The Royal Society of Chemistry, http://dx.doi.org/10.1039/b509853j.]

1.3 Application of NEXAFS Spectroscopy in Qualitative and Quantitative Analysis

The chemical sensitivity of NEXAFS spectroscopy arises from two factors: the characteristic electron binding energy, and the effect of bonding in different functional groups. For example, the carbon 1s NEXAFS spectrum of poly(styrene-*r*-acrylonitrile) (*r* indicates random) is presented in **Figure 1.5**. There are two low energy transitions observed in the NEXAFS spectrum highlighted by blue and red colour respectively. The first transition is a carbon 1s → π*(C=C) transition at 285 eV, while the second is a carbon 1s → π*(C≡N) transition at 287 eV. The symbol "π*(C=C)" is used to represent the delocalized π* unoccupied molecular orbital of phenyl ring. The difference in the energy position of the π* transitions in these two functional groups is due to different

energy positions of the core (1s) and unoccupied molecular orbitals, as denoted on the y-axis. The carbon 1s binding energy for different C atoms is shown relative to the vacuum level, and the position of the unoccupied molecular orbitals based on term values (TV) (TV= the ionization potential - transition energy) is shown at the top of the figure. The carbon 1s binding energy in (C≡N) functional group is higher than (C=C) in phenyl ring as the carbon atom is attached to nitrogen atom that is more electronegative than the carbon atom in the phenyl ring, therefore the electron density on the carbon atom is depleted resulting in higher electron binding energy.

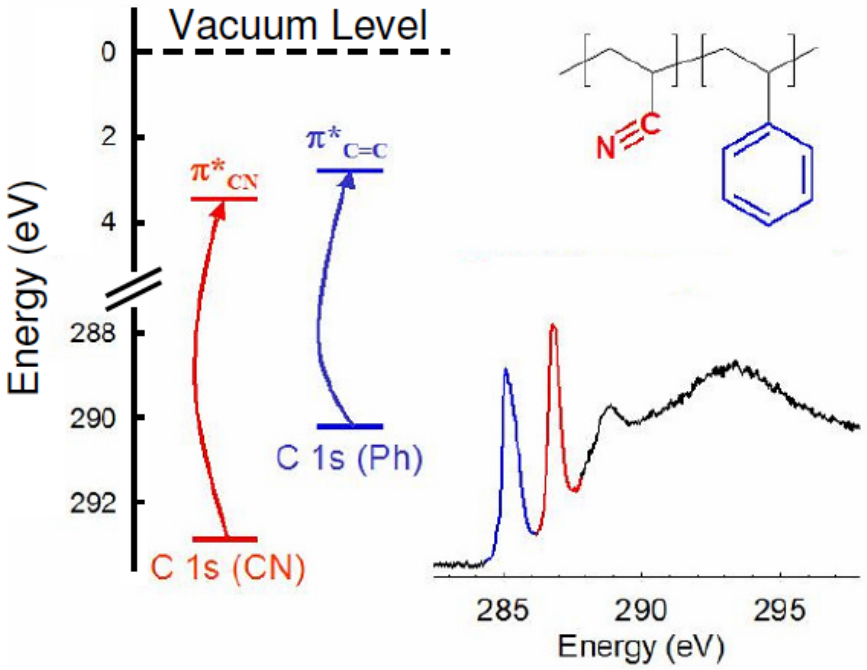

Figure 1.5 Electronic schematic for the NEXAFS photoabsorption spectrum of poly(styrene-*r*-acrylonitrile).[1.17] [Figure courtesy of Dr. Stephen G. Urquhart, 2002]

These energy differences in both core electron binding energy and the excited orbital energies result in different transition energies. In qualitative analysis NEXAFS spectra are used as "fingerprint" of a chemical type. Usually three different approaches are used for this fingerprinting including "building blocks", "functional group fingerprinting" and "molecular modeling" approaches. These approaches use the spectra of building blocks (diatomic or functional group fragments, etc.) in order to reconstruct the NEXAFS spectrum of interest.[1.17] The diatomic building block method relies on

valence-bond theory, where the chemical properties of the molecule are described based on the additivity of diatomic bond properties.[1.17] For example the carbon 1s spectrum of acetonitrile (CH_3CN) can be considered as the sum of diatomic components (i.e. carbon 1s → σ*(C-N), σ*(C-C), and σ*(C-H)). This approach however does not include bond/bond interactions as a result of hyperconjugation and electronic delocalization. The σ* molecular orbital is not localized to specific diatomic bonds, so the addition of individual diatomic bonds is not a good description of core → σ* transitions. For organic molecules and polymers, larger building blocks such as functional groups (i.e. phenyl, ketones, esters, etc.) or model molecules are included in the interpretation of NEXAFS spectra. This way the effects of chemical and electronic properties are considered in the interpretation of NEXAFS spectra.[1.17]

The chemical sensitivity of NEXAFS spectroscopy has had extensive applications in characterization of polymers, biological samples, and organic molecules.[1.4, 1.17-20] For example, **Figure 1.6** shows the NEXAFS spectra of a series of polymers with carbonyl functionality including polycarbonate, polyurethane, and polyurea; each functionality has its own characteristic NEXAFS spectrum. The transitions at 285-286 eV in these spectra have carbon 1s (C-H) → π*(C=C) character as a result of (C=C) bonds of the phenyl groups. The transitions at 286-287 eV are from carbon 1s (C-R) → π*(C=C) transitions.[1.2] In this example substituted "R" shifts the BE of carbon atom in C-R. The carbon atom is more electronegative than the hydrogen, therefore in (C-R), the electron density of the carbon atom is more depleted than the carbon atom in (C-H) that consequently results in the higher ionization potential of carbon in (C-R) and therefore higher energy transition of carbon 1s (C-R) → π*(C=C) transition. The higher energy transitions associated with broad features are from carbon 1s → σ* transitions. The carbon 1s → π*(C=O) transitions are marked with a "+" symbol in **Figure (1.6)**, and the carbon 1s (C-R) → π*(C=C) transitions with a "*". The energy shift of these transitions is due to the inductive effect of the neighbouring atoms on the carbon 1s binding energy.[1.21]

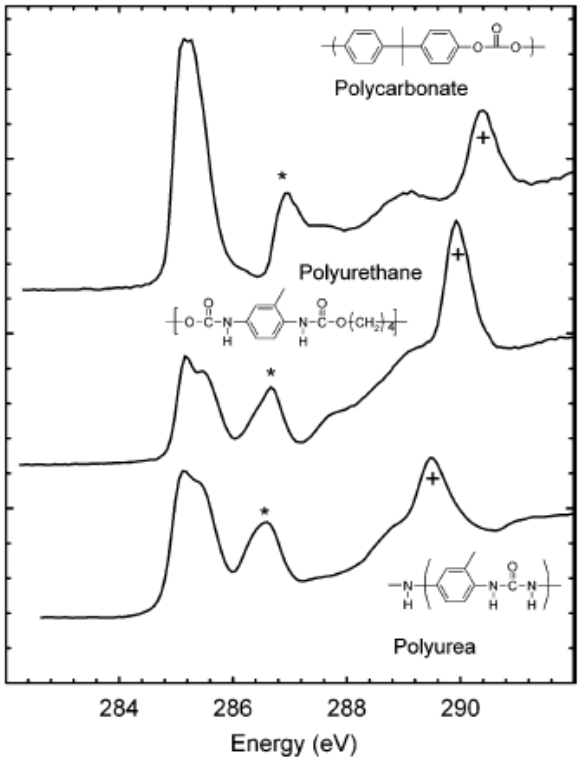

Figure 1.6 Carbon 1s near-edge X-ray absorption fine structure (NEXAFS) of polycarbonate, polyurethane, and polyurea. An asterisk identifies the carbon 1s (C-R) → π*C=C transitions, and "+" identifies the carbon 1s (C=O) → π* C=O transitions.[1.2] [Reprinted with permission from The Journal of Physical Chemistry B, 108 (47), Cooney, R. R.; Urquhart, S. G., Chemical trends in the near-edge X-ray absorption fine structure of monosubstituted and para-bisubstituted benzenes, 18185-18191, Copyright 2004 American Chemical Society.]

When facing an unknown sample, usually the number of chemical components, their chemical identities, and the quantity of each chemical component is of interest. For this purpose there are several techniques that are used to answer these questions. Among them NEXAFS spectroscopy can be used as a qualitative and quantitative tool. The chemical sensitivity of NEXAFS spectroscopy as discussed above, is used as a tool for analyzing the chemical forms of unknown samples that can be referred to as speciation within this thesis. In complex mixtures, the NEXAFS spectra are also sensitive to the chemical environment of the absorbing atom such as oxidation state, phase, pH, and solvents.[1.22] This spectroscopy can be used without any sample pre-treatment, while other methods usually require many pre-treatment procedures for sample preparation such as

dissolving, extraction, and drying which may change the chemical forms of the sample under study.

1.4 Development of Surface Sensitive Scanning X-ray Microscopy

Scanning Transmission X-ray Microscopy (STXM) is a valuable technique for studying the microscopic structure of polymer,[1.17] biological,[1.23] bioinorganic and magnetic materials and dyanamics[1.24, 1.25] and for molecular environmental sciences studies.[1.26, 1.27] The chemical, orientation and magnetic sensitivity[1.3, 1.28-32] of absorption-contrast STXM microscopy comes from the sensitivity of NEXAFS spectroscopy. This can be accessed through spatially resolved spectra, images at specific X-ray energies, or image-sequences[1.33] in STXM microscopes. With a typical lateral spatial resolution of 30-50 nm, STXM provides higher spatial resolution than longer-wavelength spectromicroscopy techniques such as Raman Microscopy, and induces less radiation damage compared to electron based microscopy such as Transmission Electron Microscopy – Electron Energy Loss Spectroscopy (TEM-EELS) when obtaining similar spectroscopic information.[1.34]

As STXM microscopes operate with transmission detection, this microscopy is sensitive to bulk chemistry. It is difficult to explore the chemistry of surfaces and interfaces with STXM microscopy. For example, interfaces have been observed at glancing angle imaging of curved surfaces[1.35] where the interface signal is enhanced by projection and where the interface width is wide enough to be seen by STXM microscopy. Covelli *et al*. found that X-ray induced photodeposition was a significant barrier to the sensitivity of STXM microscopy to thin organic adsorbates on clay surfaces.[1.36, 1.37]

Improved methods for spatially resolved NEXAFS based surface chemical analysis would be of great interest for surface studies of catalysts and nanostructured surfaces. For improved surface analysis with STXM, the first objective of this research study was to add surface sensitivity to STXM microscopes by implementing total electron yield detection of NEXAFS signal (e.g., TEY-STXM). Throughout this study we have used traditional sample current and single electron counting measurement methods. **Chapter 4** presents a full description of the instrumental and experimental procedures

used in this investigation along with the results of this new surface sensitive X-ray microscope method. TEY-STXM demonstrated promising first results on thin film metal samples,[1.38] phase separated Langmuir-Blodgett self-assembled monolayers, and phase segregated polymers.

1.5 Sulphur 1s NEXAFS Spectroscopy of Sulphur Compounds Relevant to Petroleum

Sulphur is a ubiquitous element with important functionalities in environmental and biological processes.[1.5, 1.22, 1.39, 1.40] Sulphur compounds are some of the constituents of crude oils and their form and amount significantly affects the quality of the refined products. The anthropogenic combustion and emission of sulphur compounds produces environmental pollutants such as H_2S, SO_2, and SO_3 gases.[1.41, 1.42] Improving desulphurization and hydrogenation processes in petroleum industries requires a knowledge of crude oil composition at the molecular level.[1.42] Similarly, the application of coal beneficiation technologies is dependent on knowledge of the chemistry of sulphur in the coal. Previously, there have not been any efficient spectroscopic techniques for sulphur measurements, therefore sulphur was called a "silent element".[1.22] To determine sulphur forms in petroleum asphaltanes and coals a few methods combined with C-NMR are normally used; however these methods cannot determine both forms and the amounts of organically bound sulphur in native coals and petroleum materials.[1.43] For example nuclear magnetic resonance (NMR) spectroscopy is a relatively inefficient method, as the spectroscopically active isotope, ^{33}S, has a very low natural abundance (0.78%) and its quadrupole spin (I=3/2) leads to weak and broad signals.[1.22] Instead sulphur NEXAFS spectroscopy, at the sulphur 2p (162 eV) and the sulphur 1s (2472 eV) core edges have been used in speciation and quantification of sulphur compounds in the study of fossil fuels,[1.9, 1.10, 1.43-47] magmatic systems,[1.48] waterlogged wood from historical shipwrecks,[1.11] soils,[1.49] coal samples,[1.50] studies of the surface adsorption by thiol and thiolate species,[1.51-55] and the sulphur chemistry of polymers[1.56, 1.57] and photographic materials.[1.58] Analysis of sulphur 1s NEXAFS spectra has been also used for speciation of sulphur compounds in many biological systems,[1.4-6, 1.59] such as study of biological transformation in cancerous cells.[1.60]

However the requirement of sulphur speciation and quantification is to have a well defined and interpreted database of sulphur NEXAFS spectra. Therefore, in sequence with the development of sulphur 1s NEXAFS spectroscopy capabilities at the STXM at the CLS and the potential for studies of sulphur in asphaltene, and coal species, we have studied sulphur 1s NEXAFS spectra of different sulphur functionalities relevant to petroleum within the framework of this project through experimental and computational methods. The purpose of this research was to acquire a well-interpreted database of sulphur 1s NEXAFS spectra of sulphur compounds used in speciation and quantification of sulphur compounds in fossil fuel studies. The studied sulphur functionalities in this research are thiols, thioethers, disulphides, thiophenic compounds, sulfoxides, and sulfones.

Throughout this study, sulphur 1s NEXAFS spectra of pure sulphur compounds were acquired at the CLS, and were compared to simulated spectra generated with high quality *ab initio* calculations (see **Chapter 3** for details of computational methods). The NEXAFS spectra of these compounds were obtained in gas, solid, and liquid phases based on their physical properties (i.e. vapour pressure, boiling point, etc.). The gas phase spectra are preferred as they are free from charging effects present in total electron yield, saturation effects present in florescence yield, and solid-state broadening problems present in condensed phases. Gas phase spectra are preferred for comparison to the computationally simulated spectra, but condensed phase spectra are more realistic models for speciation and quantification of sulphur compounds.

This study study was started with simple thiol and thioether compounds, as provided in detail in **Chapter 5** of this thesis. The spectral transitions in gas phase spectra were assigned by the aid of *ab initio* calculations. The efficiency of the *ab initio* calculations was tested for these compounds and satisfactory results were obtained which allowed us to expand our study to other sulphur functionalities.

Chapter 6 examines the chemical sensitivity of sulphur 1s NEXAFS spectra in disulphides by changing the ligand groups attached to sulphur atom. The effects of ligand group symmetry, the number of carbon atoms in ligands as well as the effect of changing the nature of the ligand (aliphatic versus unsaturated ligands) on the shape of the

NEXAFS spectra were studied. The spectra of disulphides were also compared to the sulphur 1s NEXAFS of thiols.

Chapter 7 explores the sulphur 1s NEXAFS spectra of sulfoxides and sulfones. The experimental spectra were assigned by the aid of *ab initio* calculations. In this study different sulfoxides and sulfones with different ligands were studied, and it was observed that the nature of the ligand groups could change the shape of the NEXAFS spectra even in the same sulphur group. This effect is very important in sulphur speciation, as usually one representative from each group of sulphur functionalities is chosen for this purpose. This study showed that beside the oxidation state and functionality of the sulphur atom, the nature of the ligand groups plays an important role in the shape of the NEXAFS spectra as well.

Finally **Chapter 8** studies the sulphur 1s NEXAFS spectra of thiophenic and aromatic thioether compounds in gas and liquid/solid phases. The degree of Rydberg-valence mixing was explored for this class of molecules by the aid of high quality *ab initio* calculations. The effect of symmetry, compound phase, and the ratio of different conformers on the NEXAFS spectra were examined as well.

1.6 Summary

NEXAFS spectroscopy has been proved to be an efficient technique in speciation and quantification of different samples in many different fields. The chemical sensitivity of this technique along with the high special resolution of X-ray microscopy were the motives to use both STXM and NEXAFS spectroscopy in this research study.

For improving the surface sensitivity of X-ray microscopy, total electron yield detection is used as a complementary detection mode to the bulk sensitive detection mode of STXM. This enables simultaneous bulk and surface measurements of thin samples such as thin film metal samples, phase separated Langmuir-Blodgett self-assembled monolayers, and phase segregated polymers. The experimental procedures and the challenges for this new developed technique are described in detail in **Chapter 4**.

Sulphur 1s NEXAFS spectroscopy has been proved to be a powerful technique in sulphur speciation and quantification. For this purpose a complete well-defined database of sulphur model standards is required. Therefore, we studied sulphur 1s NEXAFS

spectra of different sulphur functionalities both experimentally and theoretically. The study started with simple thiols and thioethers (**Chapter 5**), and expanded to disulphides and their comparison to sulphides (**Chapter 6**), sulfones and sulfoxides (**Chapter 7**), and thiophenic and aromatic thioethers (**Chapter 8**).

1.7 References

1.1. Fu, J.; Urquhart, S. G., *Journal of Physical Chemistry A,* **2005,** *109* (51), 11724-11732.
1.2. Cooney, R. R.; Urquhart, S. G., *Journal of Physical Chemistry B,* **2004,** *108* (47), 18185-18191.
1.3. Stöhr, J., *NEXAFS Spectroscopy*, Springer-Verlag, Berlin, **1992**.
1.4. Pickering, I. J.; George, G. N.; Yu, E. Y.; Brune, D. C.; Tuschak, C.; Overmann, J.; Beatty, J. T.; Prince, R. C., *Biochemistry,* **2001,** *40* (27), 8138-8145.
1.5. Pickering, I. J.; Prince, R. C.; Divers, T.; George, G. N., *FEBS Letters,* **1998,** *441* (1), 11-14.
1.6. Prange, A.; Dahl, C.; Truper, H. G.; Behnke, M.; Hahn, J.; Modrow, H.; Hormes, J., *European Physical Journal D,* **2002,** *20* (3), 589-596.
1.7. Pickering, T. J.; Prince, R. C.; Divers, T.; George, G. N., *FEBS Letters,* **1998,** *441* (1), 11-14.
1.8. Matsushima, T.; Okuda, T.; Eguchi, T.; Ono, M.; Harasawa, A.; Wakita, T.; Kataoka, A.; Hamada, M.; Kamoshida, A.; Hasegawa, Y.; Kinoshita, T., *Review of Scientific Instruments,* **2004,** *75* (6), 2149-2153.
1.9. Wiltfong, R.; Mitra-Kirtley, S.; Mullins, O. C.; Andrews, B.; Fujisawa, G.; Larsen, J. W., *Energy & Fuels,* **2005,** *19* (5), 1971-1976.
1.10. Sarret, G.; Connan, J.; Kasrai, M.; Bancroft, G. M.; Charrié-Duhaut, A.; Lemoine, S.; Adam, P.; Albrecht, P.; Eybert-Bérard, L., *Geochimica et Cosmochimica Acta,* **1999,** *63* (22), 3767-3779.
1.11. Fors, Y.; Jalilehvand, F.; Sandstrom, M., *Analytical Sciences,* **2011,** *27* (8), 785-792.
1.12. Seward, F. D.; Charles, P. A., *Exploring the X-ray Universe*, 2nd ed.; Cambridge, **2010**.
1.13. Jiang, D. T., *X-Ray Absorption Fine Structure Spectroscopy*. In *Synchrotron Radiation: Earth, Environmental and Material Sciences Applications*, Henderson, G. S., Baker, D. R., Ed. Short Courses Series, **2002**, Vol. 30, 65-98.
1.14. Rehr, J. J.; Albers, R. C., *Reviews of Modern Physics,* **2000,** *72* (3), 621-654.
1.15. Hähner, G., *Chemical Society Reviews,* **2006,** *35* (12), 1244-1255.
1.16. Lee, P. A.; Citrin, P. H.; Eisenberger, P.; Kincaid, B. M., *Reviews of Modern Physics,* **1981,** *53* (4), 769-806.
1.17. Ade, H.; Urquhart, S. G., *X-ray Spectromicroscopy of Polymers*. In *Chemical Applications of Synchrotron Radiation*, Sham, T. K., Ed. World Scientific, **2002**.
1.18. Urquhart, S. G.; Turci, C. C.; Tyliszczak, T.; Brook, M. A.; Hitchcock, A. P., *Organometallics,* **1997,** *16* (10), 2080-2088.

1.19. Ade, H.; Smith, A. P.; Zhang, H.; Zhuang, G. R.; Kirz, J.; Rightor, E.; Hitchcock, A., *Journal of Electron Spectroscopy and Related Phenomena,* **1997,** *84* (1-3), 53-71.
1.20. Urquhart, S. G.; Smith, A. P.; Ade, H. W.; Hitchcock, A. P.; Rightor, E. G.; Lidy, W., *Journal of Physical Chemistry B,* **1999,** *103* (22), 4603-4610.
1.21. Urquhart, S. G.; Ade, H., *Journal of Physical Chemistry B,* **2002,** *106* (34), 8531-8538.
1.22. Jalilehvand, F., *Chemical Society Reviews,* **2006,** *35* (12), 1256-1268.
1.23. Kirz, J.; Jacobsen, C.; Howells, M., *Quarterly Review of Biophyisics,* **1995,** *33*, 33.
1.24. Van Waeyenberge, B.; Puzic, A.; Stoll, H.; Chou, K. W.; Tyliszczak, T.; Hertel, R.; Fähnle, M.; Brückl, H.; Rott, K.; Reiss, G.; Neudecker, I.; Weiss, D.; Back, C. H.; Schütz, G., *Nature,* **2006,** *444*, 461-464.
1.25. Acremann, Y.; Strachan, J. P.; Chembrolu, V.; Andrews, S. D.; Tyliszczak, T.; Katine, J. A.; Carey, M. J.; Clemens, B. M.; Siegmann, H. C.; Stohr, J., *Physical Review Letters,* **2006,** *96* (21).
1.26. Dynes, J. J.; Tyliszczak, T.; Araki, T.; Lawrence, J. R.; Swerhone, G. D. W.; Leppard, G. G.; Hitchcock, A. P., *Environmental Science and Technology,* **2006,** *40*, 1556-1565.
1.27. Brown, G. E., Jr.; Benzerara, K.; Yoon, T. H.; Ha, J.; Cordova, C. D.; Spormann, A. M.; Tyliszczak, T.; Tanwar, K. S.; Trainor, T. P.; P.J. Eng; Kendelwicz, T.; Yamamoto, S.; Bluhm, H.; Ketteler, G.; Salmeron, M.; Nilsson, A., *Geochimica et Cosmochimica Acta,* **2006,** *70*, A69.
1.28. Urquhart, S. G.; Ade, H., *Journal of Physical Chemistry B,* **2002,** *106*, 8531-8538.
1.29. Cooney, R.; Urquhart, S., *Journal of Physical Chemistry B,* **2004,** *108*, 18185-18191.
1.30. Hitchcock, A. P.; Mancici, D. C., *Journal of Electron Spectroscopy and Related Phenomena,* **1994,** *67* (1), 1.
1.31. Stöhr, J.; Outka, D. A., *Physical Review B,* **1987,** *36* (15), 7891-7905.
1.32. Urquhart, S. G.; Lanke, U. D.; Fu, J., *International Journal of Nanotechnology,* **2008,** *5*, 1138.
1.33. Jacobsen, C.; Wirick, S.; Flynn, G.; Zimba, C., *Journal of Microscopy,* **2000,** *197* (2), 173-184.
1.34. Rightor, E. G.; Hitchcock, A. P.; Ade, H.; Leapman, R. D.; Urquhart, S. G.; Smith, A. P.; Mitchell, G.; Fischer, D.; Shin, H. J.; Warwick, T., *Journal of Physical Chemistry B,* **1997,** *101*, 1950-1960.
1.35. Obst, M.; Dynes, J. J.; Lawrence, J. R.; Swerhone, G. D. W.; Benzerara, K.; Karunakaran, C.; Kaznatcheev, K.; Tyliszczak, T.; Hitchcock, A. P., *Geochimica et Cosmochimica Acta,* **2009,** *73* (14), 4180-4198.
1.36. Covelli, D. *X-ray Microscopy of Hydrocarbon-Clay Interactions*, M.Sc. thesis, University of Saskatchewan, Saskatoon, **2007**.
1.37. Covelli, D.; Hernandez-Cruz, D.; Haines, B. M.; Munoz, V.; Omotoso, O.; Mikula, R.; Urquhart, S., *Journal of Electron Spectroscopy and Related Phenomena,* **2009,** *173* (1), 1-6.
1.38. Haines, B.; Behyan, S.; Christensen, S. L.; Obst, M.; Bertwistle, D.; Karunakaran, C.; Tyliszczak, T.; Urquhart, S. G., *Canadian Light Source, Activity Report No. 2008*, **2008**, p 154.

1.39. Pickering, I. J.; Prince, R. C.; Divers, T.; george, G. N., *FEBS Letters,* **1988,** *441*, 11-14.
1.40. Pickering, I. J.; George, G. N.; Yu, E. Y.; Brune, D. C.; Tuschak, C.; Overmnn, J.; Beatty, T.; Prince, R. C., *Biochemistry,* **2001,** *40*, 8138-8145.
1.41. Mori, R. A.; Paris, E.; Giuli, G.; Eeckhout, S. G.; Kavcic, M.; Zitnik, M.; Bucar, K.; Pettersson, L. G. M.; Glatzel, P., *Inorganic Chemistry,* **2010,** *49* (14), 6468-6473.
1.42. Mijovilovich, A.; Pettersson, L. G. M.; Mangold, S.; Janousch, M.; Susini, J.; Salome, M.; de Groot, F. M. F.; Weckhuysen, B. M., *Journal of Physical Chemistry A,* **2009,** *113* (12), 2750-2756.
1.43. George, G. N.; Gorbaty, M. L., *Journal of the American Chemical Society,* **1989,** *111* (9), 3182-3186.
1.44. Matsumoto, S.; Tanaka, Y.; Ishii, H.; Tanabe, T.; Kitajima, Y.; Kawai, J., *Spectrochimica Acta Part B: Atomic Spectroscopy,* **2006,** *61* (8), 991-994.
1.45. George, G. N.; Gorbaty, M. L.; Kelemen, S. R.; Sansone, M., *Energy & Fuels,* **1991,** *5* (1), 93-97.
1.46. Almkvist, G.; Boye, K.; Persson, I., *Journal of Synchrotron Radiation,* **2010,** *17*, 683-688.
1.47. Braun, A.; Janousch, M.; Sfeir, J.; Kiviaho, J.; Noponen, M.; Huggins, F. E.; Smith, M. J.; Steinberger-Wilckens, R.; Holtappels, P.; Graule, T., *Journal of Power Sources,* **2008,** *183* (2), 564-570.
1.48. Jugo, P. J.; Wilke, M.; Botcharnikov, R. E., *Geochimica et Cosmochimica Acta,* **2010,** *74* (20), 5926-5938.
1.49. Prietzel, J.; Botzaki, A.; Tyufekchieva, N.; Brettholle, M.; Thieme, J.; Klysubun, W., *Environmental Science & Technology,* **2011,** *45* (7), 2878-2886.
1.50. Bolin, T. B., *Energy & Fuels,* **2010,** *24*, 5479-5482.
1.51. Allegretti, F.; Bussolotti, F.; Woodruff, D. P.; Dhanak, V. R.; Beccari, M.; Di Castro, V.; Betti, M. G.; Mariani, C., *Surface Science,* **2008,** *602* (14), 2453-2462.
1.52. Sardar, S. A.; Syed, J. A.; Yagi, S.; Tanaka, K., *Thin Solid Films,* **2004,** *450* (2), 265-271.
1.53. Syed, J. A.; Sardar, S. A.; Yagi, S.; Tanaka, K., *Surface Science,* **2004,** *566*, 597-602.
1.54. Syed, J. A.; Sardar, S. A.; Yagi, S.; Tanaka, K., *Journal of Vacuum Science & Technology A,* **2004,** *22* (3), 683-688.
1.55. Syed, J. A.; Sardar, S. A.; Yagi, S.; Tanaka, K., *Thin Solid Films,* **2006,** *515* (4), 2130-2136.
1.56. Modrow, H.; Calderon, G.; Daly, W. H.; de Souza, G. G. B.; Tittsworth, R. C.; Moelders, N.; Schilling, P. J., *Journal of Synchrotron Radiation,* **1999,** *6*, 588-590.
1.57. Winter, I.; Hormes, J.; Hiller, M., *Nuclear Instruments & Methods in Physics Research Section B-Beam Interactions with Materials and Atoms,* **1995,** *97* (1-4), 287-291.
1.58. Smith, T. A.; Dewitt, J. G.; Hedman, B.; Hodgson, K. O., *Journal of the American Chemical Society,* **1994,** *116* (9), 3836-3847.
1.59. Frank, P.; Hedman, B.; Hodgson, K. O., *Inorganic Chemistry,* **1999,** *38* (2), 260-270.
1.60. Ito, A.; Inoue, T.; Takehara, K.; Shimizu, N.; Kitajima, Y.; Shinohara, K., *Journal of X-ray Science and Technology,* **2011,** *19* (2), 249-260.

CHAPTER 2 INSTRUMENTATION AND MEASURENTS

X-ray radiation was first observed by W. C. Röntgen who then was awarded the Physics Nobel prize for his discovery.[2.1] X-rays can be generated in different ways including: bombardment of a metal target by a high energy electron beam resulting in ejection of core electrons and consequent relaxation of the core hole by upper level electrons that cause the emission of X-ray photons; secondary beam of X-ray florescence generated by a primary beam of X-rays; decay processes in radioactive sources; synchrotron radiation sources;[2.2] and Free-Electron Lasers (FEL).[2.3, 2.4] Synchrotron radiation and FELs are highly polarized with high brilliance and cover a wide range of electromagnetic radiation wavelengths that makes them to be unique compared to other sources of X-ray radiation. For NEXAFS spectroscopy, a tunable and collimated source of radiation is required with high photon flux; these requirements are fulfilled by synchrotron radiation.[2.1, 2.4] Therefore, an overview of generation of synchrotron radiation is described in §**2.1** followed by descriptions of different sources such as bending magnets in §**2.1.1**, and insertion devices in §**2.1.2**. For acquiring NEXAFS spectra there are different detection modes that are described in detail in §**2.2**. Different beamlines used in this thesis are described in § **2.3**. The references for this chapter are provided in §**2.4**.

2.1 Synchrotron Radiation

An electron orbiting in a circular path with energies less than its rest mass ($m_e c^2$ = 0.51 MeV) acts as a weak dipole and radiates in all directions. This is schematically illustrated in **Figure 2.1** (left panel**,** $\beta = v/c << 1$, v is electron velocity, and c is the speed of light). However, when the electron energy reaches to relativistic energies, the electron emits radiation in the forward direction into a cone with an opening angle of $\psi \approx 2\gamma^{-1}$:[2.3]

$$\psi \approx 2\gamma^{-1} = 2mc^2 / E \qquad (2.1)$$

where E is the electron energy, and m is the electron mass. Therefore, by increasing the electron energy, the emitted radiation cone angle gets smaller. This effect increases the intensity and power of the radiation emitted in forward direction (**Figure 2.1**, right panel).[2.5]

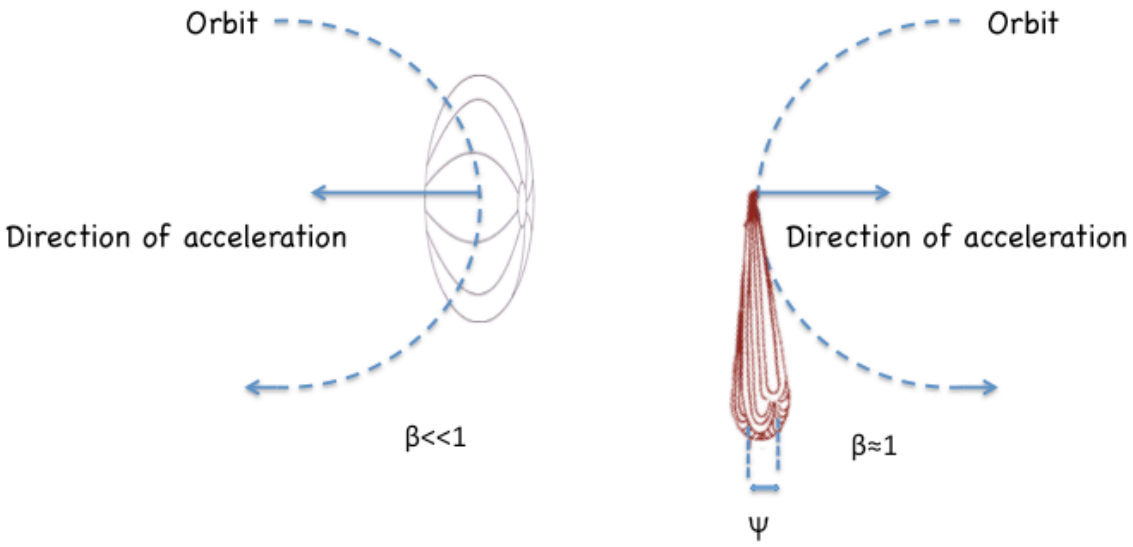

Figure 2.1 Radiation emission patterns for the charged particles moving in a circular orbit. The emitted radiation is in all directions for slow particles (left) ($\beta = v/c << 1$), but is in a narrow cone when $\beta \approx 1$ (right).[2.5] [This figure is adapted from Figure 3 from this reference: Mobilio, S.; Balerna, A. Introduction to the Main Properties of Synchrotron Radiation. In Synchrotron Radiation: Fundamentals, Methodologies and Application, Conference Proceedings-Italian Physical Society: 2003; 1-24.]

This phenomenon is exploited in the generation of synchrotron light, where by forcing the relativistic charged particles to move in a circular path, electromagnetic radiation is generated in a narrow cone tangent to the orbit in the forward direction.[2.6] Energies of these photons range from far infrared to hard X-ray regions. This

phenomenon was first observed in the United States at General Electric.[2.6] Before the1980s, most synchrotron related research was performed in a "parasitic mode" where the radiation was the by-product of high-energy physics experiments.[2.4] These synchrotron sources are referred to as *first-generation* synchrotron radiation sources.[2.3] The new synchrotron facilities within the 1980s were specifically built for producing synchrotron radiation using bending magnets that are called *second-generation* synchrotron sources. In the 1990s, the most advanced synchrotron sources were built to fulfill two criteria: low electron-beam emittance (the product of source size and divergence of the beam)[2.7] and many straight sections for insertion devices (wigglers and undulators). These sources produce a beam with small beam cross section, and a high degree of collimation and are called *third-generation* synchrotron sources. The *fourth-generation* synchrotron sources are under development by having higher brightness (see **Equation (2.3)**) than current sources and femtosecond pulses of coherent radiation such as Energy Recover Linac (ERL) and Free-Electron Laser (FEL) sources.[2.3, 2.4, 2.6] These sources are out of the scope of this thesis and are not described further.

The main components of a synchrotron radiation source are the vacuum system, the injection and accelerator system, beam focusing elements including quadrupole and sextupole magnets, the radiofrequency (RF) system, bending magnets, and insertion devices. An example of a synchrotron radiation source is schematically presented in **Figure 2.2**. Usually a vacuum of less than 10^{-9} torr is required in the storage ring. The electrons are generated in an electron gun, by applying a high voltage electric field within a heated metallic cathode that generates pulses of electrons. These electrons are directed to the Linear accelerator (Linac), where they are entered into the first radiofrequency (RF) cavity. In the RF cavity, the electrons are accelerated and at the same time are grouped into bunches (buckets). The energy of electrons under the microwave RF fields reaches to about 20 MeV per meter of accelerating structure. The electron beam size decreases by focusing elements along the Linac. The pre-accelerated electrons in the Linac are then directed to a circular accelerator (a booster synchrotron) where they are accelerated to the desired energy before entering the storage ring in one turn, and in a synchronized way (where the name synchrotron originates). The booster itself includes bending magnets, focus-defocusing magnets and RF cavities along the circle.[2.8]

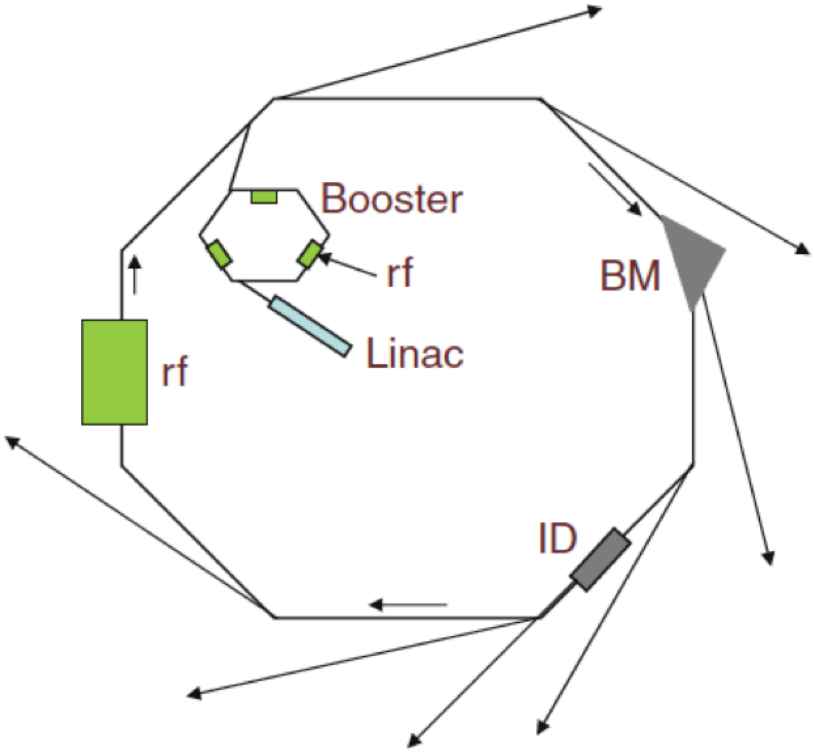

Figure 2.2 Schematic view of a synchrotron radiation source. The injection-accelerating system (Linac+Booster synchrotron) is inside the storage ring that is actually a polygon with the bending magnets at the vertices. Bending magnets, BM, induce the deflection of the electron trajectory and as a consequence it produces synchrotron radiation, which is emitted tangentially. Insertion devices, ID, can be allocated in the straight sectors to produce specific synchrotron light. The radiofrequency (rf) cavity of the storage ring and those of the booster synchrotron are also indicated.[2.8] [Springer, Applications of Synchrotron Light to Scattering and Diffraction in Materials and Life Sciences Lecture Notes in Physics, Vol. 776, 2009, pages 1-22, Bases of Synchrotron Radiation, Light Sources, and Features of X-ray Scattering Beamlines, García-Gutiérrez, M. C.; Rueda, D. R., Figure (1.3), Copyright 2009; with kind permission from Springer Science and Business Media.]

The lifetime of stored electron beam depends on the number of electrons in each bucket as well as the number of filled buckets. The emittance (the product of source size and divergence of the beam)[2.7] of the electron beam depends on quadrupoles and sextupoles in the storage ring. The synchrotron radiation is generated as the electrons are accelerated through the bending magnets (BM) and insertion devices (ID) in the storage ring. The energy lost by the electrons via the emission of synchrotron radiation is

replenished by the radio frequency cavity in the storage ring that gets its power from klystrons.[2.8]

Before describing different sources, there are two terms that can be used to express the properties of radiated beam from different sources, namely flux and brightness.

The flux is defined as the number of photons per second with 0.1% bandwidth (BW) collected in unit angular spread θ in the electron orbit and integrated over the entire vertical opening angle ψ (see **Figure 2.3** for the definition of θ, and ψ):

$$Flux = dF / d\theta \text{ (photons/s/0.1\%BW/mrad)} \tag{2.2}$$

The brightness is defined as photon flux per unit area of the source ($dxdz$) which corresponds to the electron beam size in units of mm^2, and per unit solid angle of the source ($d\theta d\psi$) which shows how much the photon beam diverges as it propagates.[2.1]

$$Brightness = d^4F / d\theta d\psi dxdz \text{ (photons/s/0.1\%BW/mrad}^2\text{mm}^2\text{)} \tag{2.3}$$

In third generation synchrotron sources, low emittance results in high brightness beam.

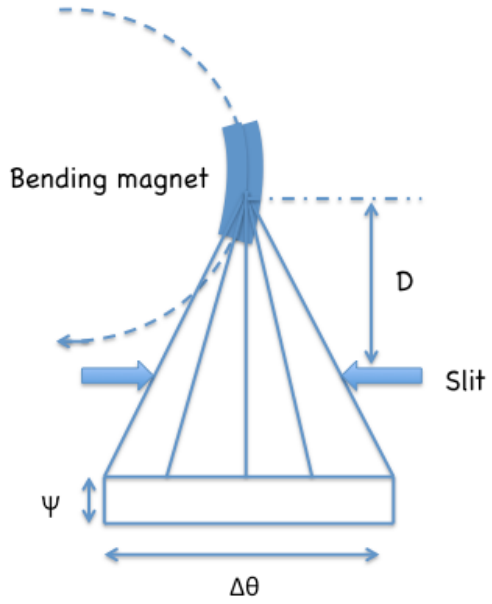

Figure 2.3 Synchrotron radiation produced by a bending magnet. The direction of the magnetic field is perpendicular to the electron orbit plane, ψ is the natural opening angle in the vertical plane and $\Delta\theta$ is horizontal angular distribution, which is much bigger than ψ.[2.5] [This figure is adapted from Figure 4 from this reference: Mobilio, S.; Balerna, A. Introduction to the Main Properties of Synchrotron Radiation. In Synchrotron Radiation: Fundamentals, Methodologies and Application, Conference Proceedings-Italian Physical Society: 2003; 1-24.]

2.1.1 Bending Magnets

Bending magnets are a series of two arc magnets around the storage ring and are interrupted by straight sectors. These straight sectors have quadrupole magnets for focusing the electrons, and a sextupole magnet for correcting the chromatic aberrations as a result of energy spread of electrons.[2.8] The bending magnets are unavoidable in a storage ring as they force the electrons to move in a closed path around the ring and therefore are an unavoidable source of radiation.

When the electrons pass through an arc of the bending magnet, a horizontal fan of white radiation is irradiated in the forward direction with a vertical opening angle of $\psi \approx 2\gamma^{-1}$ (see **Figure 2.3**), while the length of the arc determines the horizontal fan of radiation.[2.3] In general, the horizontal fan of the beam along with the delivered flux for an experiment depends on the acceptance of various geometrical and optical components.

The radiation from a bending magnet is characterized by a critical energy (ε_c), defined as the energy that divides the power spectrum into two equal parts above and below ε_c:[2.3]

$$\varepsilon_c = 2.2E^3 / R = 0.686BE^2 \tag{2.4}$$

where E is the electron energy in GeV, R is the radius of curvature of the electron trajectory through the bending magnet in meters (m), and B is the magnetic filed in Tesla (T). An exact expression for the flux at photon energy (ε) is given by:

$$dF / d\theta(\varepsilon) = 2.46 \times 10^{13} IEG(\varepsilon / \varepsilon_c) \quad \text{(photons/s/mrad/0.1\%BW)} \tag{2.5}$$

where the normalized function $G(\varepsilon / \varepsilon_c)$ governs the spectral shape, I(A) is the stored current, and E is the electron energy in GeV. The total power P (KW) of a bending magnet can be estimated by integrating the flux density over the entire length of the arc L(m):[2.3]

$$P = 1.263B^2E^2IL \tag{2.6}$$

2.1.2 Insertion Device Sources

Insertion devices are wiggler and undulator magnetic arrays that exert periodic magnetic fields on the electron beam. An example of these magnets is illustrated in **Figure 2.4.** These devices can be removed or introduced in the storage ring without any

interruption on the normal operation of storage ring and the name insertion device originates from this fact. These devices are responsible for high brightness of third-generation sources as well as tuning the polarization of radiation.

2.1.2.1 Wigglers. A wiggler is a series of bending magnets that while the electrons pass through it, they experience transverse oscillations with an angular spread much larger than γ^{-1} (see **Figure 2.4**). The superposition of incoherent radiation from each bend causes enhancement of total flux and brightness and is proportional to the number of poles. The horizontal fan of radiation from a wiggler is given by $K\gamma^{-1}$ and K is:

$$K = 0.934\lambda_0 B \tag{2.7}$$

where K is defined as the magnetic period of the wiggler with a peak field of B (T), and λ_0 (cm) is the magnetic period of the wiggler.[2.3] The spectral properties from these devices are similar to bending magnets. The critical energy of wiggler devices is larger than that of bending magnets because of larger magnetic fields in these devices. The total power irradiated by a wiggler is proportional to the number of magnetic periods, N, in the device and is given by the expression used for bending magnets (**Equation 2.6**) with L(m) defined as :

$$L = N\lambda_0 \tag{2.8}$$

The normal incident power received by an optical element at D meters distant from the wiggler is obtained as follows:[2.3]

$$W_{xy} = 10.84E^4 BIN / D^2 \tag{2.9}$$

where W_{xy} is the power received in unit area of the receiver in (W/mm^2), E is the electron energy in (GeV), I is the ring current in (A), and B is the magnetic strength in teslas (T).

2.1.2.2 Undulators. Undulators are another type of insertion device with unique properties that make them a preferred source of X-ray radiation. **Figure 2.4** represents the layout of an undulator magnet. These devices usually operate with K < 2 (see **Equation 2.7**). The magnetic period is typically a few centimeters. The variation in the undulator gap provides the tunability of the X-ray emission energy as the electron beam experiences different magnetic field strength.

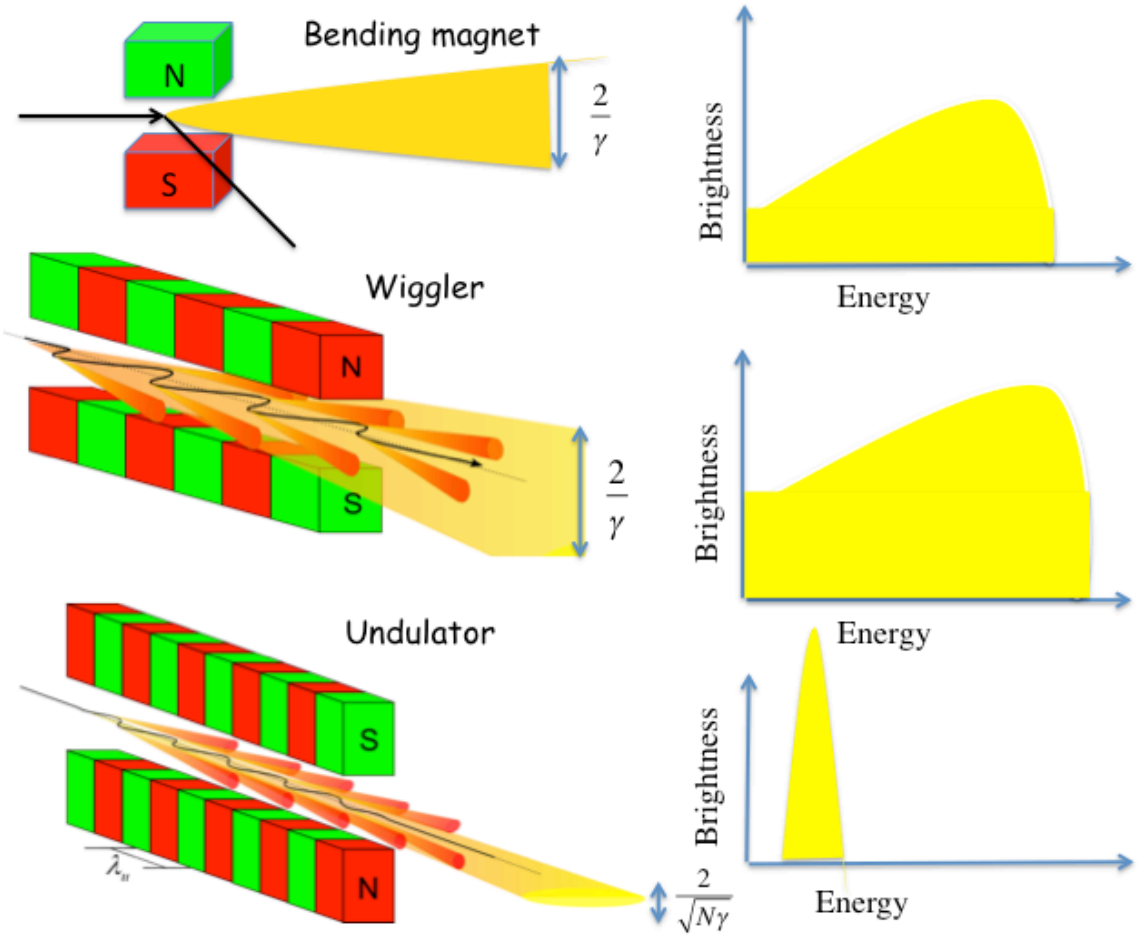

Figure 2.4 (Left) schematic view of bending magnet, wiggler, and undulator; (right) the brightness profile produced by each device.[2.9] [This figure is adapted from Figure 2.2 from this reference: Otero, E. Soft X-ray Spectroscopy of Organic and Organometalic Molecules and Polymers, PhD thesis, University of Saskatchewan, 2008.]

Similar to wigglers, electrons are periodically deflected through the undulator magnets resulting in emission of radiation. Another unique property of an undulator source is its ability to produce pseudo-monochromatic energy bands called harmonics. This is achieved as a result of interference in radiation from a large number of source points from each magnetic pole in the device.

The flux of radiation in the central cone of an undulator harmonic (n) is given by

$$F_n = 1.4310^{14} NI(A)(1+K^2/2) f_n(K)/n \text{ (photons/s/0.1\%BW)} \quad (2.10)$$

where $f_n(K)$ is a tabulated value and equals to zero for even n. The transverse oscillations in these devices have a small angular excursion compared to wigglers. The radiation concentrates in a cone with minimum possible opening angles that is presented in **Figure**

2.4. These properties cause the undulators to have the highest brightness compared to bending magnets and wigglers.

2.2 Measuring NEXAFS Spectra

Several processes can occur during the generation of the NEXAFS spectrum as represented in **Figure 2.5**. The incident photon beam can excite an electron from a core orbital into an unoccupied electronic orbital and the succeeding relaxation of the excited molecule results in the ejection of either an Auger electron or a florescent photon. The cross-section of each process depends on the atomic number (Z) of the absorbing atom. For low-Z molecules (i.e. containing atoms such as carbon, nitrogen or oxygen) Auger electron yield is higher than fluorescence yield.[2.4]

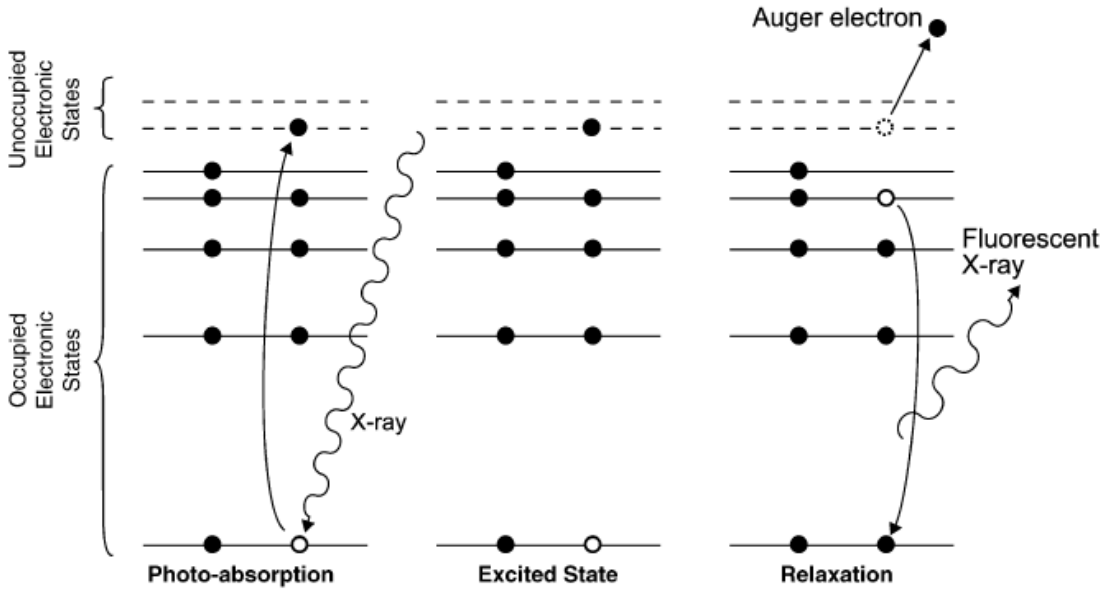

Figure 2.5 Schematic of the photo-absorption and relaxation process occurring in a NEXAFS experiment. An incident photon, whose energy corresponds to a NEXAFS resonance, excites an electron from a core level into an unoccupied, anti-bonding level. This excited state is unstable and the atom relaxes to eject either a fluorescent photon or an Auger electron.[2.10] [Reprinted from Journal of Electron Spectroscopy and Related Phenomena, 151 (2), Watts, B.; Thomsen, L.; Dastoor, P. C., Methods in carbon K-edge NEXAFS: Experiment and analysis, 105-120, Copyright 2006, with permission from Elsevier.]

Each of these processes can be detected and therefore there are several ways for obtaining a NEXAFS spectrum.[2.10] The NEXAFS process can be detected through either the absence of the absorbed photons in the transmitted X-rays (transmission detection) or

through the particles ejected during the relaxation process that follows (fluorescence detection or electron detection). Electron detection can be broken down into Total Electron Yield (TEY), Partial Electron Yield (PEY) and Auger Electron Yield (AEY) detection schemes based on the measured energy regime of the electrons. Different detection modes are presented schematically in **Figure 2.6** and are described in detail in the following sections.

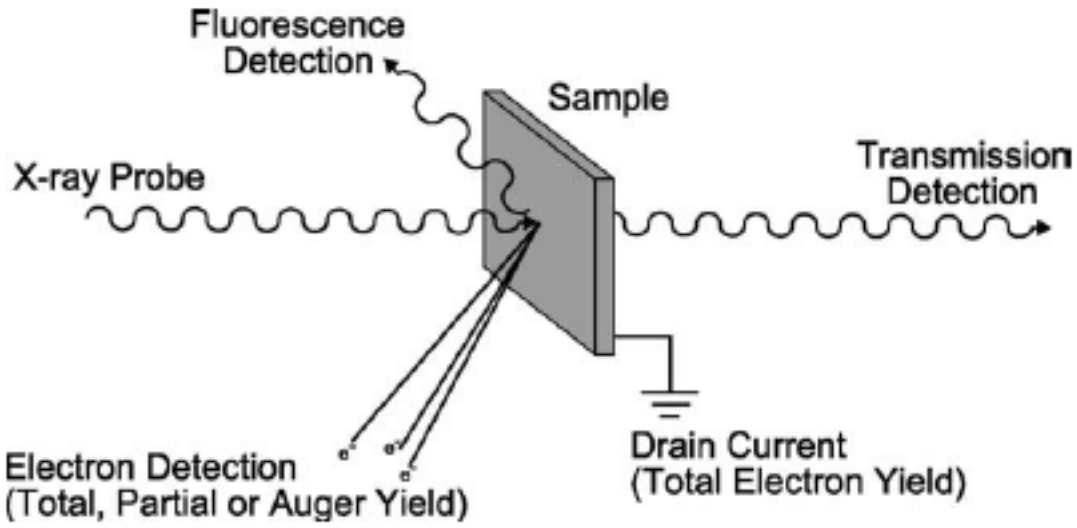

Figure 2.6 Schematic of the possible measurement techniques for NEXAFS spectroscopy. The NEXAFS signal can be detected through the transmitted X-rays (transmission detection) or through the particles ejected during the relaxation process that follow core excitation (fluorescence detection or electron detection). Energy discrimination allows the electron detection technique to be broken down into total (TEY), partial (PEY) and Auger (AEY) electron yield detection schemes.[2.10] [Reprinted from Journal of Electron Spectroscopy and Related Phenomena, 151 (2), Watts, B.; Thomsen, L.; Dastoor, P. C., Methods in carbon K-edge NEXAFS: Experiment and analysis, 105-120, Copyright 2006**,** with permission from Elsevier.]

2.2.1 Transmission Detection Mode

In transmission detection mode the sample is placed between an X-ray source and a detector, and the intensity of transmitted photons (I) is measured and compared to the intensity of incident photons (I_0). The requirements of this method are having a thin layer of sample for penetration of the photons through the sample as well as two detectors for measuring the (I_0) and (I) such as ion chamber detectors. An ion chamber detector is a

tube including two parallel metal plates with an electric field between the electrodes and a filling gas such as N_2, Ar or He. When this chamber is irradiated with X-rays the filling gas is ionized resulting in ejection of electrons and consequent production of ion-electron pairs that are collected by the electrodes. The generated current is proportional to the intensity of the X-ray passing through the chamber. The detection efficiency of the ion chamber can be adjusted by changing the volume of chamber, the gas pressure, and the filling gas mixture.[2.11] A schematic diagram of a typical ion chamber is presented in **Figure 2.7**.

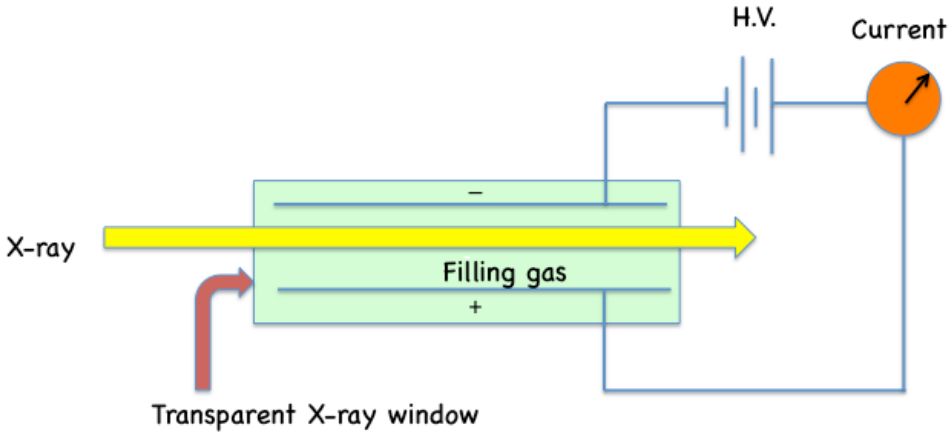

Figure 2.7 Schematic diagram of an ion chamber.

In transmission mode, the detection of the signal in the absence of the sample (I_0) and with the sample (I), recorded as a function of X-ray energy provides I_0 and I spectra. The X-ray transmission spectrum is acquired by calculating the optical density (OD) as follows:

$$OD = -\ln(\frac{I}{I_0}) \tag{2.11}$$

The optical density for all the elements within a sample of thickness t (cm) is:

$$OD = \mu(E) \times \rho \times t \tag{2.12}$$

where at specific energy (E), μ is the mass absorption coefficient ($cm^2.g^{-1}$) and ρ is the sample density ($g.cm^{-3}$) that all, are element specific. The mass absorption coefficient itself is related to atomic absorption cross section σ_x by:

$$\mu = \frac{N_A}{MW}\sum_i n_i \sigma_{xi} \tag{2.13}$$

where N_A is the Avogadro's number, σ_{xi} is the absorption cross section for the n_i atoms of each element (i), and MW is the molecular weight

$$MW = \sum_i n_i A_i \tag{2.14}$$

where A_i is the atomic weight.[2.12]

The transmission method of detection provides the most accurate data for quantitative analysis because of its simplicity and well-defined data reduction, but is only suitable for thin samples of uniform thickness.

2.2.2 Fluorescence Detection Mode

Fluorescence yield detection mode is based on the secondary florescence process that occurs as a result of core hole relaxation. The schematic diagram of fluorescence detection is shown in **Figure 2.8**.

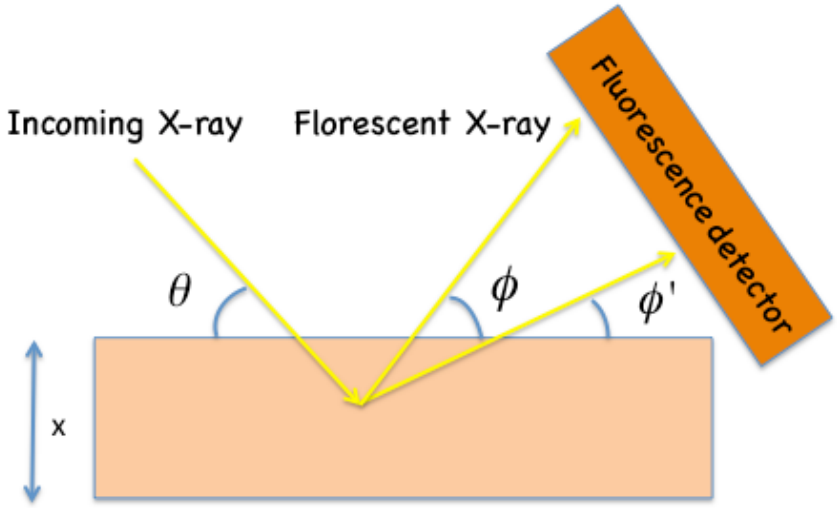

Figure 2.8 Schematic diagram for X-ray fluorescence detection mode. [This figure is adapted from Figure 4.11 from this reference: Jiang, D. T. In Synchrotron Radiation: Earth, Environmental and Material Sciences Applications; Henderson, G. S., Baker, D. R., Ed. Short Courses Series, 2002; Vol. 30, page 74].

However, this mode of detection is not appropriate for thick samples because of the "self-absorption", which is the loss of fluorescence intensity while the fluorescent signal passes through the sample.

For tracking the NEXAFS spectra by fluorescence detection mode, different detectors are available such as ion chambers (non-energy dispersive) and solid-state (energy dispersive) detectors. The advantages of ion chambers over solid-state detectors are their high detection efficiency including high count rate and large solid angle coverage, and their simplicity. The disadvantage of these detectors (non-energy dispersive) is a high background signal in dilute samples that limits the detection sensitivity of these detectors. Instead in samples with complex composition and a low concentration of the element of interest, energy discriminative detectors are usually used. These detectors are based on semiconductors such as silicon (Si). The Si detector includes three layers of P-type Si, Si(Li), and N-type Si respectively, with a bias applied across these layers. When this detector is irradiated by X-rays, electron hole pairs are created in the middle part (Si(Li)) of the detector and will be collected by the electrodes. The number of these electron hole pairs is proportional to the photon energy.[2.11] The Si detector used in this research is a Vortex 4-element detector. The external and internal view of this detector is shown in **Figure 2.9**.

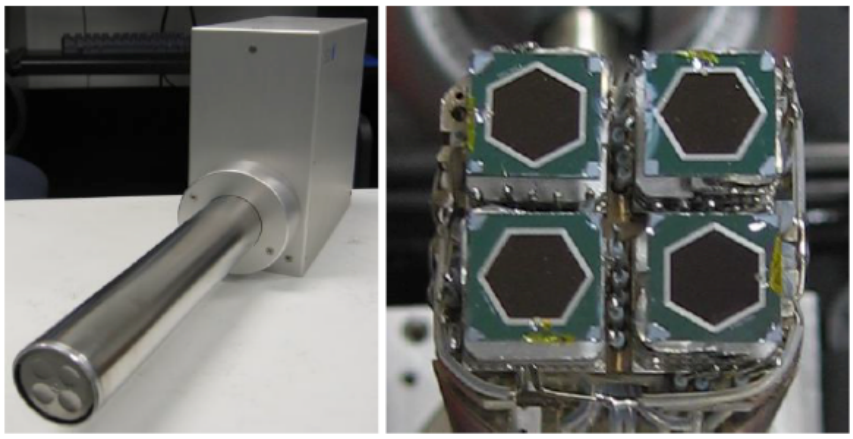

Figure 2.9 Vortex –ME4 4-element spectrometer (a) external view; (b) internal view.

2.2.3 Electron Yield Detection Mode

As mentioned in §**2.2**, ejection of electrons after the relaxation of the core hole can be tracked to measure the NEXAFS spectra. These ejected electrons undergo multiple scattering while approaching the surface of the sample, such as electron-electron and electron-plasmon inelastic scattering, and electron-phonon quasi-elastic scattering.[2.13] Due to these scatterings, electrons generated deep inside the material lose more energy

than the electrons generated at the surface. Total electron yield (TEY) is a very simple technique: all of the electrons that have enough energy to overcome the work function of ejecting from the surface can be measured by the sample drain current or with a channeltron. Although the total count rate is very large in TEY mode, the signal to background ratio is small, because of the electrons emerging from the substrate that contribute to the background signal. In partial electron yield (PEY), low kinetic energy electrons coming from the substrate are repelled by a mesh (placed in front of the sample surface) that is biased with low negative potential, and the more energetic electrons created at the very top layers of the surface are detected by a channeltron; PEY has higher surface sensitivity than TEY mode.[2.13] In Auger electron yield (AEY), the primary electrons (Auger) are measured with an energy analyzer detector that is centered on the energy of an Auger peak. This technique can have the highest surface sensitivity.[2.1] Generally the surface sensitivity increases from transmission to FY to TEY to PEY to AEY.[2.4] In this thesis TEY detection mode has been used to measure the NEXAFS spectra in surface studies provided in **Chapter 4**, and sulphur 1s NEXAFS spectra represented in **Chapters 6, 7**, and **8**.

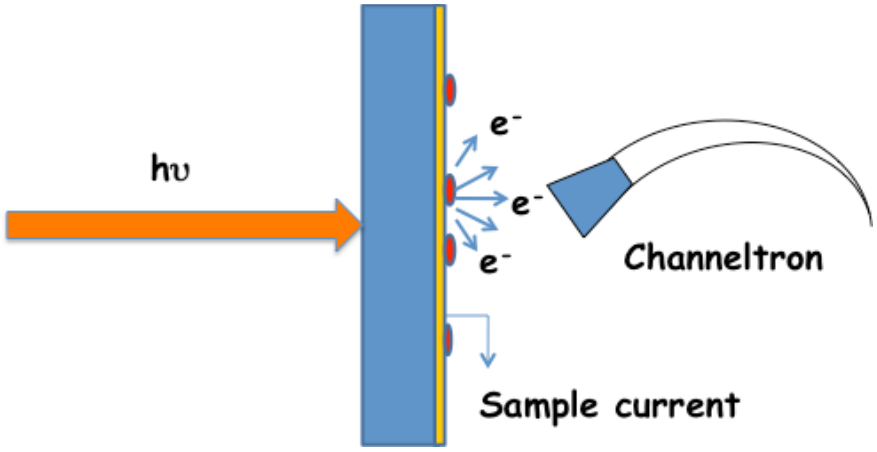

Figure 2.10 Schematic view of a Total Electron Yield detection using a channeltron and sample current measurements.

Figure 2.10 presents the schematic view of a TEY mode by using a channeltron and sample current measurements using a picoammeter. A channeltron is a cylindrical tube with an electron emissive interior surface. A positive high voltage is applied to the tail of the tube. When an electron hits the interior side of the tube an avalanche of

electrons is created and accelerated towards the positively charged tail of the tube. The resulting current is amplified and measured to obtain the NEXAFS spectrum.

For data analysis in TEY detection mode, the incident photon flux I_0 is used for normalizing the sample current; this ratio is proportional to absorption cross section:

$$TEY=I/I_0 \quad (2.15)$$

The details of data analysis are described in each chapter. In **Chapter 4**, the different channeltrons used for electron counting measurements in the surface STXM studies are described. Detailed studies of these detectors are further described in **Chapter 4**.

2.2.4 Total Ionization Yield Detection Mode

Total ionization yield (TIY) detection is used to acquire NEXAFS spectra of gas phase samples.[2.14] Gas phase spectra are free from solid-state broadening, charging in total electron yield (TEY) detection of solids, and self-absorption present in fluorescence yield detection. In this method, the current produced by the ionization of the filling gas (the result of X-ray absorption) is measured and this current is directly proportional to the absorption cross-section. The gas cells used for measuring the gas phase sulphur 1s NEXAFS spectra of sulphur compounds as well as the schematic diagram of its wiring are presented in **Figure 2.11** top and bottom panels respectively. The difference between TIY mode of detection and the ion chambers is in the nature of the filling gas.

In TIY, the filling gas inside the chamber is in fact the sample of interest instead of an inert gas used in ion chambers. In our measurements two gas cells were used and the TIY spectra from these two cells were measured and compared simultaneously to ensure the absence of saturation effects. A 25 μm thick Be window is used to separate the chambers from the beamline vacuum.

Ion-electron pairs created by the ionization of the gas further ionize other molecules in the detector, resulting in a gas amplification of ion signal. A 45 V bias is applied to the electrodes and the ion current is measured with a Keithly picoammeter. The ion current signal (I), and the signal from the upstream (I_0) ion chamber are used to measure the NEXAFS spectra as follows:

$$TIY \propto \frac{I}{I_0} \tag{2.16}$$

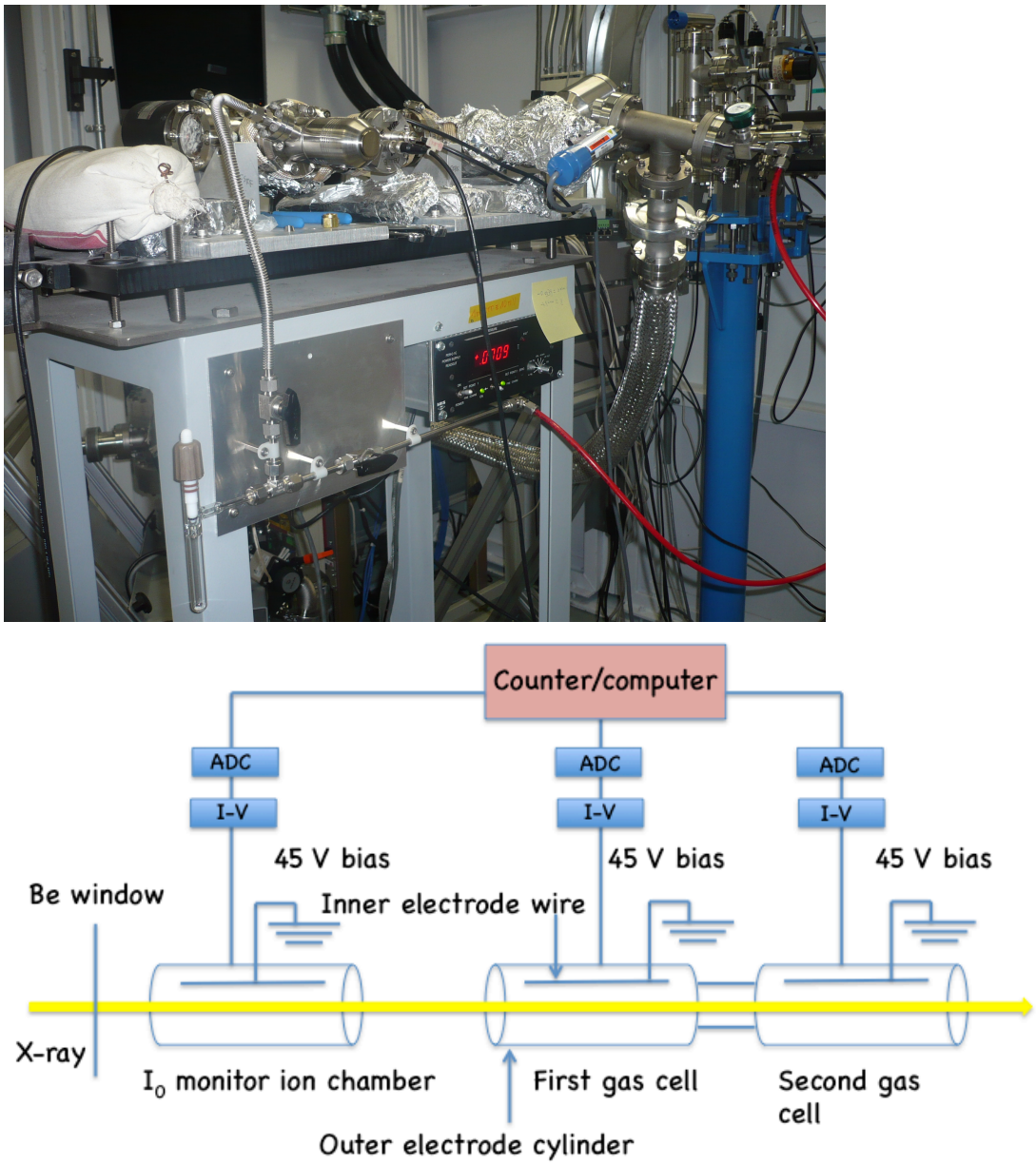

Figure 2.11 Top panel: the ion chambers used at the CLS for TIY detection of the sulphur 1s NEXAFS spectra of sulphur compounds, bottom panel: schematic diagram of the ion chambers and the wiring. [The bottom figure is adapted from the figure 2.1.1. by Urquhart, S. G., Delocalization and Functional Group Fingerprinting in the Core Excitation Spectroscopy of Molecules and Polymers, PhD thesis, McMaster University, 1997.]

The disadvantage of this method is saturation of the signal when the sample pressure is too high. The absence of saturation effect was checked by comparing the NEXAFS spectra from two gas cells in our studies.

2.3 Beamlines Used for NEXAFS Spectroscopy

NEXAFS spectra presented in this thesis were acquired in three different beamlines including Soft X-ray Microcharacterization Beamline (SXRMB) and the Soft X-ray Microscopy beamline (SM) 10ID1 at the Canadian Light Source (CLS) located at the University of Saskatchewan, Saskatoon, Saskatchewan, Canada, and beamline 11.0.2 at the Advanced Light Source (ALS) located in Lawrence Berkley National Laboratory, University of California, US. The details of each beamline are reviewed below.

2.3.1 Spectromicroscopy Beamlines

All the NEXAFS spectra acquired in **Chapter 4** of this thesis were recorded using Scanning Transmission X-ray Microscope (STXM) on beamline 10ID1 at the Canadian Light Source (CLS)[2.15] and on beamline 11.0.2 at the Advanced Light Source (ALS).[2.16] The characteristics of each beamline used for spectromicrocopy studies are provided below followed by a detailed description of the STXM.

The STXM at beamline 11.0.2 at the ALS was designed for molecular environmental science studies. In this beamline the X-rays are produced by an Elliptically Polarized Undulator (EPU) consisting of four quadrants of periodic magnets. Two of these magnets are placed above the electron trajectory and the other two underneath. The schematic diagram of this beamline is represented in **Figure 2.12.**

The light produced by the EPU is then focused by a cylindrical mirror and conducted to the pre-mirror of a monochromator covering the energy range of 75 eV to 2150 eV. The resulting monochromatic light illuminates a toroidal mirror that directs the beam to the exit slits and finally to the STXM chamber labeled 1 in **Figure 2.12**.

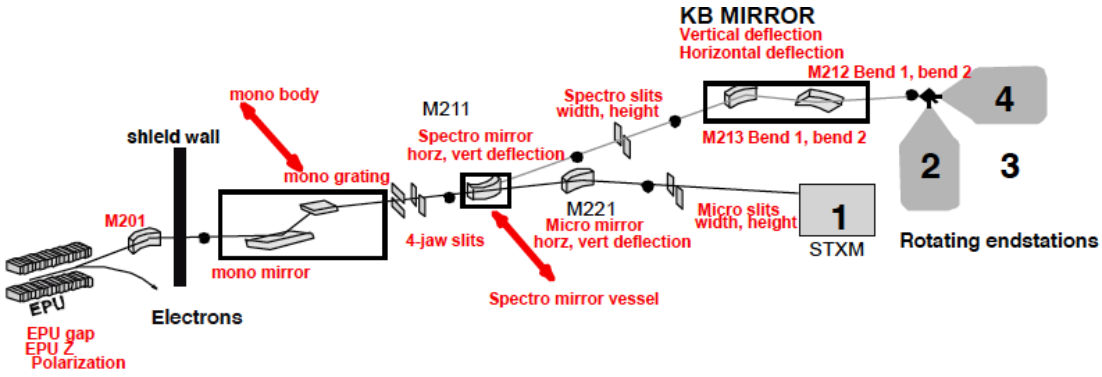

Figure 2.12 Layout of beamline 11.0.2 located at the Advanced Light Source, Berkeley California.[2.16] [Reprinted from Journal of Electron Spectroscopy and Related Phenomena, 150 (2-3), Bluhm, H.; Andersson, K.; Araki, T.; Benzerara, K.; Brown, G. E.; Dynes, J. J.; Ghosal, S.; Gilles, M. K.; Hansen, H. C.; Hemminger, J. C.; Hitchcock, A. P.; Ketteler, G.; Kilcoyne, A. L. D.; Kneedler, E.; Lawrence, J. R.; Leppard, G. G.; Majzlan, J.; Mun, B. S.; Myneni, S. C. B.; Nilsson, A.; Ogasawara, H.; Ogletree, D. F.; Pecher, K.; Salmeron, M.; Shuh, D. K.; Tonner, B.; Tyliszczak, T.; Warwick, T.; Yoon, T. H., Soft X-ray microscopy and spectroscopy at the molecular environmental science beamline at the Advanced Light Source, 86-104, Copyright 2006**,** with permission from Elsevier.]

The schematic view of spectromicroscopy beamline (SM) 10ID1 at the CLS is illustrated in **Figure 2.13**.[2.15] In this beamline the light is also produced by an EPU and the light is directed to a cylindrical mirror, and then onto a plane grating monochromator. The monochromatic light produced is then reflected from a toroidal mirror towards the exit slit and finally reaches into the STXM chamber. This beamline covers the energy range of 100 eV to 2500 eV.

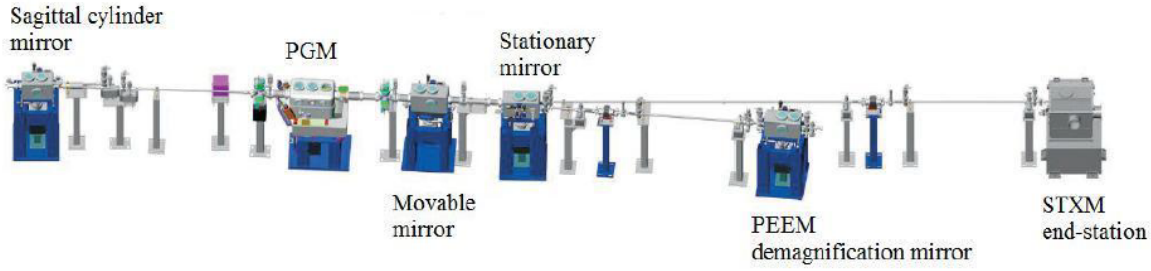

Figure 2.13 Layout of SM beamline 10ID-1 located at the CLS, Saskatoon, Saskatchewan.[2.15] [Reprinted from Nuclear Instruments & Methods in Physics Research Section a-Accelerators Spectrometers Detectors and Associated Equipment, 582 (1), Kaznatcheev, K. V.; Karunakaran, C.; Lanke, U. D.; Urquhart, S. G.; Obst, M.; Hitchcock, A. P., Soft X-ray spectromicroscopy beamline at the CLS: Commissioning results, 96-99, Copyright 2007**,** with permission from Elsevier.]

2.3.1.1 Scanning Transmission X-ray Microscopy (STXM)

X-ray spectromicroscopy combines the chemical sensitivity of NEXAFS spectroscopy with the high spatial resolution of X-ray imaging (<30 nm) in Scanning Transmission X-ray Microscopy (STXM). **Figure 2.14** represents the schematic view of a STXM. In this microscope light produced by an EPU undulator is directed to a monochromator and the monochromatic light is focused to a very small spot by a circular diffracting grating Fresnel Zone Plate (ZP). A silicon nitride window separates the X-ray microscope from the beamline that is kept under ultra high vacuum (UHV). A closer view of the ZP is represented in **Figure 2.15**. Sample is mounted at the focal plane of ZP and can be raster scanned through the focus spot.

A Fresnel zone plate is a circular diffraction focusing element consisting of alternated opaque and transparent concentric rings with a width that varies with radius (smaller at increased radius).[2.17] The ZP has a central stop that blocks the undiffracted light to pass through.

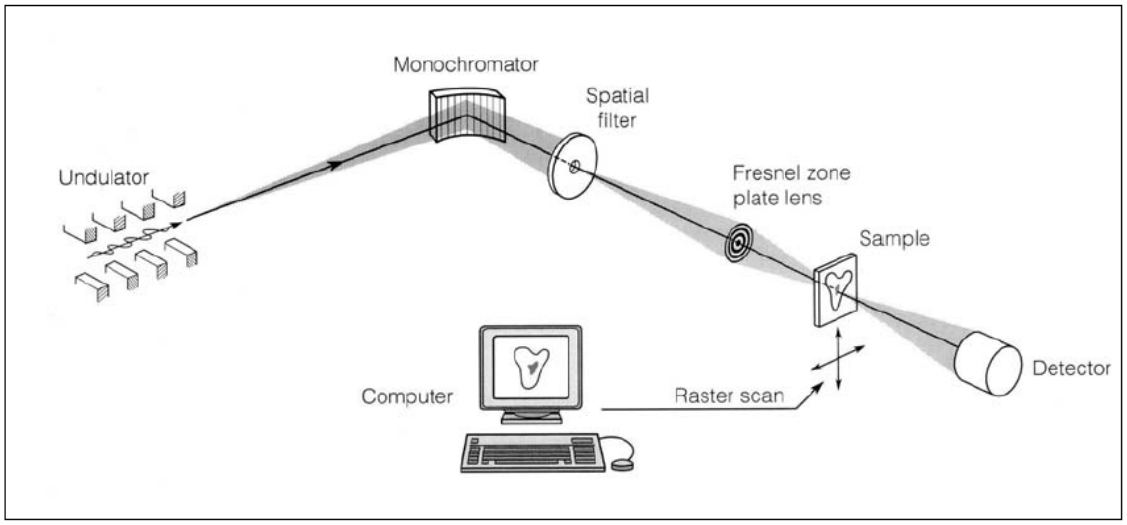

Figure 2.14 Schematic diagram of the layout of a STXM microscope.[2.18] [Reprinted from Journal of Electron Spectroscopy and Related Phenomena, 100, Urquhart, S. G.; Hitchcock, A. P.; Smith, A. P.; Ade, H. W.; Lidy, W.; Rightor, E. G.; Mitchell, G. E., NEXAFS spectromicroscopy of polymers: overview and quantitative analysis of polyurethane polymers, 119-135, Copyright 1999**,** with permission from Elsevier.]

The Order Sorting Aperture (OSA) is located between the ZP and the sample and prevents the higher order diffracted light and undiffracted light to pass.

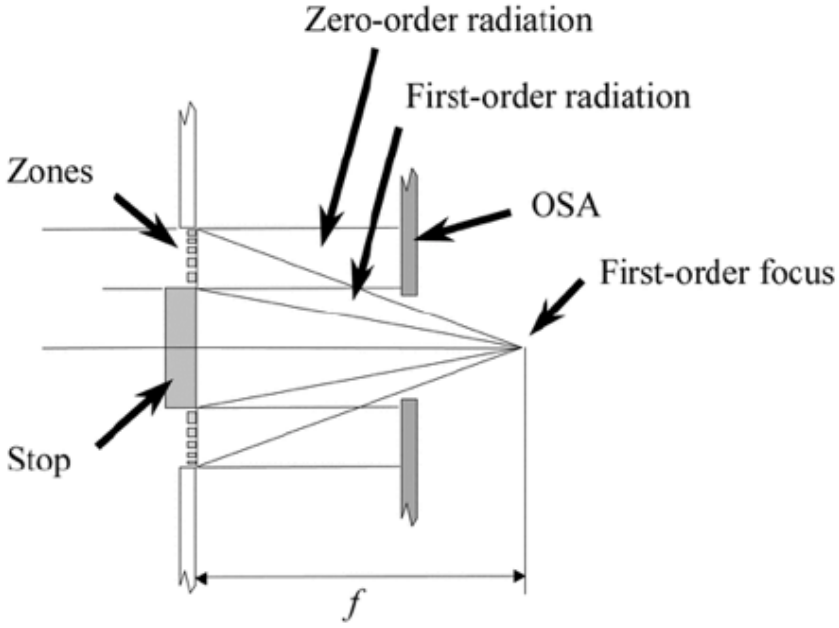

Figure 2.15 Focusing scheme of a STXM.[2.19] [Reprinted with permission from Journal of Synchrotron Radiation, 10, Kilcoyne, A. L. D.; Tylisczack, T.; Steele, W. F.; Fakra, S.; Hitchcock, P.; Frank, K.; Anderson, E.; Harteneck, B.; Rightor, E. G.; Mitchell, G. E.; Hitchcock, A. P.; Yang, L.; Warwick, T.; Ade, H., Interferometer-controlled scanning transmission X-ray microscopes at the Advanced Light Source, 125-136, Copyright 2003, with permission from International Union of Crystallography.]

The focal length (f) of the ZP depends on the energy of X-rays and changing the energy requires the ZP position to be changed with respect to the OSA and sample during a measurement in order to have the focus point fixed on the sample. A laser interferometer is used to monitor the precise displacement of the ZP (x,y) as the focal length changes (z).

A detector including a phosphorus screen and a Photomultiplier Tube (PMT) is placed at the back of the sample. The phosphorous screen converts the transmitted X-rays into visible photons which are counted by the PMT with a count rate of tenths of MHz.[2.19] A schematic diagram of a PMT is presented in **Figure 2.16**.

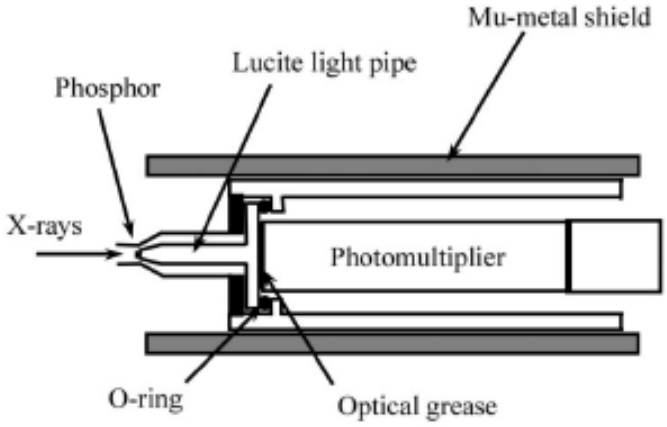

Figure 2.16 Schematic diagram of the Photomultiplier Tube (PMT) used in the STXM.[2.19][Reprinted with permission from Journal of Synchrotron Radiation, 10, Kilcoyne, A. L. D.; Tylisczack, T.; Steele, W. F.; Fakra, S.; Hitchcock, P.; Frank, K.; Anderson, E.; Harteneck, B.; Rightor, E. G.; Mitchell, G. E.; Hitchcock, A. P.; Yang, L.; Warwick, T.; Ade, H., Interferometer-controlled scanning transmission X-ray microscopes at the Advanced Light Source, 125-136, Copyright 2003, with permission from International Union of Crystallography.]

2.3.1.2 Data Acquisition modes used in STXM

There are four types of data acquisition in a STXM microscope in transmission mode. These include imaging, point scan, line scan, and image sequence that are described below:

Imaging: In this method the sample is raster scanned at the focal point of the ZP at specific X-ray energy in (x,y) directions and the transmitted photons are recorded with the detector, I (x,y; E). These images are used for a survey scan of the sample to find an interesting region within the sample, or just for energy specific imaging of the sample.

Point Scan: In this method the beam is focused at a specific location on the sample and the photon energy is scanned and the detector records the transmitted photons. This way the spectrum of that particular point is obtained I(E; x, y).

Line Scan: In this method similar to point scan, the beam is focused to a particular region of interest to acquire the spectra. Line scan involves raster scanning of a straight line across the sample, and the photon energy is varied between lines, I (x, E). Line scans can also be used to obtain the spectrum of an open area within the sample (I_0).

Finally the NEXAFS spectrum can be extracted through the transmitted intensity of the sample (I) and of the open area (I_0), obtained simultaneously.

Image Sequences: Image sequence is the most informative way of acquiring NEXAFS spectra and is called "stacks". This method was first described by Jacobson *et al*. using STXM X-1A beamline at the National Synchrotron Light Source (NSLS) at Brookhaven National Laboratory, in Brookhaven, New York. In this method a series of images of a small region of interest are obtained over a range of energies, I (x, y, E). An example of NEXAFS spectrum obtained with image sequence is presented in **Figure 2.17**. Each image is obtained with the beam completely focused on the sample at that energy to ensure there is no degradation in spatial resolution. For obtaining good NEXAFS spectra it is best to acquire the image sequences of an open area within the sample simultaneously within the region of interest. This provides simultaneous acquisition of I and I_0 within the sample.[2.20]

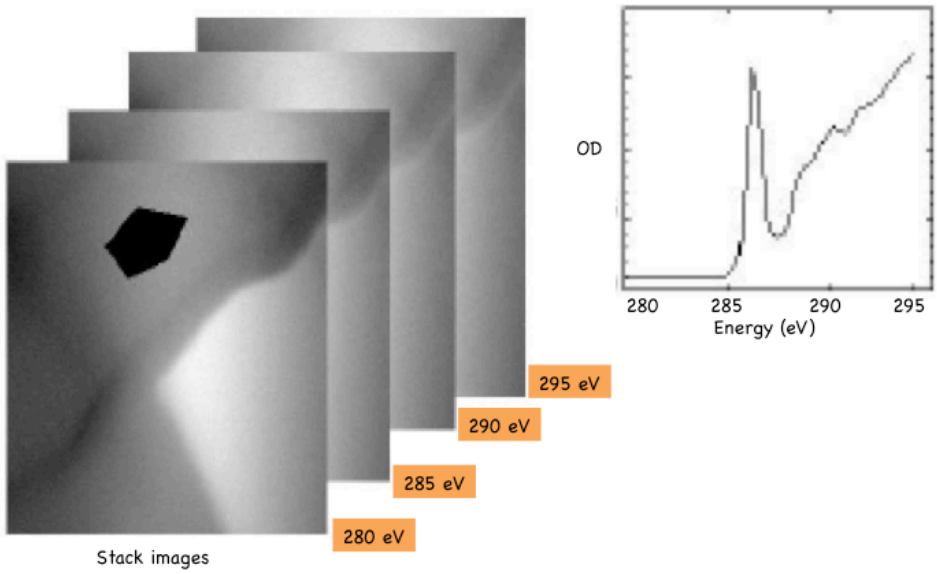

Figure 2.17 Schematic representation of NEXAFS spectrum (OD versus energy) generated from an image stack. The number of counts is averaged per pixel over the area marked off in black for this figure. [This figure is adapted from Figure 2.7 from this reference: Otero, E. Soft X-ray Spectroscopy of Organic and Organometalic Molecules and Polymers, PhD thesis, University of Saskatchewan, 2008.]

For each image at a specific energy a specific region is selected (region of interest in **Figure 2.17**) and the amount of transmitted photons for each pixel over this region is

averaged to obtain the sample signal. The same procedure is performed to obtain I_0 signal and finally the OD is obtained.

2.3.2 Spectroscopy Beamlines

The sulphur 1s NEXAFS spectra acquired for sulphur containing compounds throughout this thesis were obtained at the Soft X-ray Micro-characterization Beamline 06B 1-1 (SXRMB) at the CLS. The energy range covered in this beam line ranges from 1.7-10 *K*eVs. This energy range covers the 1s edge of many important elements such at Si, P, and S, as well as 2p, 3d edges of 4d and 5d transition metals respectively. The optical layout of SXRMB beamline is presented in **Figure 2.18**.

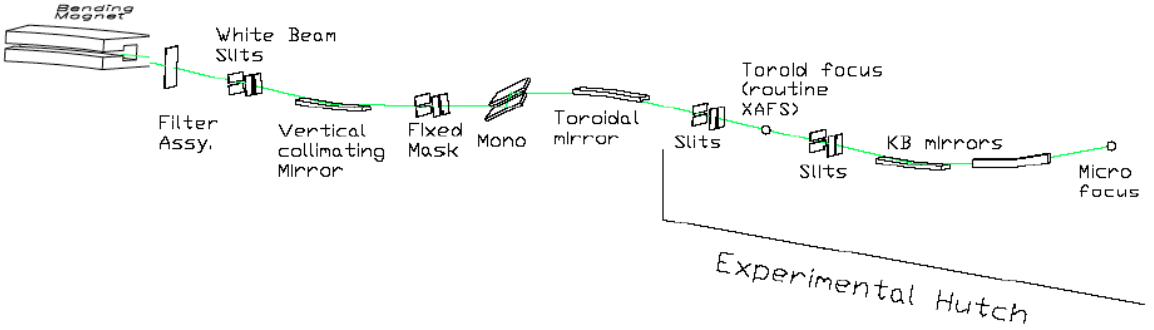

Figure 2.18 Layout of SXRMB beamline 06B 1-1 located at the CLS, Saskatoon, Saskatchewan.[2.21] [Reprinted with permission from AIP Conference Proceedings, Hu, Y. F.; Coulthard, I.; Chevrier, D.; Wright, G.; Igarashi, R.; Sitnikov, A.; Yates, B. W.; Hallin, E. l.; Sham, T. K.; Reininger, R., Preliminary Commissioning and Performance of the Soft X-ray Micro-characterization Beamline at the Canadian Light Source, Copyright 2010, 343-346, American Institute of Physics.]

The light is produced by a bending magnet and is then directed by a bendable cylindrical mirror that deflects and collimates the beam. The beam illuminates a double crystal monochromator and the monochromatic light is directed towards the toroidal mirror that focuses and directs the beam into the experimental hutch. The first component in the hutch is an ion chamber to measure the I_0 signal. The ion chamber is separated from UHV of the beamline by two Be windows. In this thesis research for measuring gas phase spectra, TIY detection was used with two gas cells described in **§2.2.4** and for condensed phase spectra, FLY, and TEY detection modes were used that are described in detail in **§2.2.2** and **§2.2.3** respectively.

In previous work, the energy scale of NEXAFS spectra was calibrated with a relative energy scale, relative to a specific transition energy of a calibrant. However, the problem in this approach is the lack of an absolute energy reference. For example, by using different calibrants, different energies of white line have been reported for methionine with an energy difference of around 2 eV (**Table 2.1**).

Compound	Calibrant	Calibration transition energy (eV)	Location	Main transition energy (eV)
DL-Methionine[2.22]	K_2SO_4 $ZnSO_4$[2.22]	2482.6 2481.44	LUCIA/SLS-Villigen	2471.3
Methionine[2.23]	$Na_2S_2O_3.5H_2O$	2472.02	Beamline 6-2/Stanford Synchrotron radiation lab.	2473.1
Methionine[2.24]	$CaSO_4$	2482.5	ID21/European synchrotron	2473.3
Methionine[2.25]	$Na_2S_2O_3$	2469.2	VI-2/SPEAR	2470.3
Dibenzothiophene [2.22]	K_2SO_4	2482.6	ID 21/ESRF-Grenoble	2472
Dibenzothiophene[2.25]	$Na_2S_2O_3$	2469.2	VI-2/SPEAR	2470.4
Dibenzothiophene[2.24]	$CaSO_4$	2482.5	ID21/European synchrotron	2473.9
Na_2SO_4[2.26] Na_2SO_3 $Na_2S_2O_3$	NiS	2469.8		2479.9 2475.5 2469.2
	$Na_2S_2O_3.5H_2O$[2.27, 2.28]	2469.2		
	Gypsum ($CaSO_4.2H_2O$)[2.29]	2482.90	ID21/ESRF	
	$ZnSO_4$[2.30]	2481.4		
	Native sulphur[2.31]	2472.0		
	SF_6[2.32]	2486.0		

Table 2.1 List of compounds used for calibration of the sulphur 1s NEXAFS spectra, based on a relative energy scale.

Additionally, different transition energies have been used for one calibrant. An example of this kind is the two different energies used for the same transition of

$Na_2S_2O_3.5H_2O$ as a calibrant. This can cause discrepancy in energy scale of the NEXAFS spectra obtained for one sample, especially when the spectra are intended to be used as model standards.

In our studies however, the energy scale for the sulphur 1s NEXAFS spectra (**Chapter 5** through **8**) was calibrated based on an absolute energy scale instead of a relative scale. This was done by setting the energy scale based on the Ar 1s → 4p transition to the value of 3203.54 (10) eV, based on the absolute energy calibration of Breinig *et al*.[2.33] In our experiments, the Ar 1s → 4p transition energy was used to calibrate a weak contaminant signal (presumably from $FeSO_4$ contamination) found on the Be windows of the ion chamber (calibrated value, 2481.62 eV). This signal, recorded at the same time as all other spectra, was used as an internal calibration for all of our experiments. On this scale, the white line of the $ZnSO_4$ appears at 2481.47 eV, which is well within experimental error of the 2481.44 eV value reported in the literature for a relative calibration.[2.22]

2.4 References

2.1. Attwood, D., *Soft X-rays and Extreme Ultraviolet Radiation: Principles and Applications*, Cambridge University Press, Cambridge, UK, **2007**.
2.2. Douglas, A.; Skoog, F.; Holler, J.; Nieman, T. A., *Principles of Instrumental Analysis*, 5th ed.; Saunders College Publishing, **1998**.
2.3. Shenoy, G., *Structural Chemistry,* **2003,** *14* (Synchrotron Radiation in Structural Chemistry), 3-14.
2.4. Hähner, G., *Chemical Society Reviews,* **2006,** *35* (12), 1244-1255.
2.5. Mobilio, S.; Balerna, A., *Introduction to the Main Properties of Synchrotron Radiation*. In *Synchrotron Radiation: Fundamentals, Methodologies and Application*, Conference Proceedings-Italian Physical Society: **2003**; 1-24.
2.6. Henderson, G. S.; Baker, D. R., *Synchrotron Radiation: Earth, Environmental and Material Sciences Applications*, **2002**.
2.7. Als-Niesen, J.; McMorrow, D., *Elements of Modern X-ray Physics*, John Wiley & Sons, Ltd, New York, **2001**.
2.8. García-Gutiérrez, M. C.; Rueda, D. R., *Bases of Synchrotron Radiation, Light Sources, and Features of X-ray Scattering Beamlines*. In *Applications of Synchrotron Light to Scattering and Diffraction in Materials and Life Sciences Lecture Notes in Physics*, Marian Gomez, A. N., Mari Cruz García-Gutiérrez and T.A. Ezquerra, Ed. Springer, **2009**, Vol. 776.
2.9. Otero, E. *Soft X-ray Spectroscopy of Organic and Organometalic Molecules and Polymers*, PhD thesis, University of Saskatchewan, **2008**.

2.10. Watts, B.; Thomsen, L.; Dastoor, P. C., *Journal of Electron Spectroscopy and Related Phenomena,* **2006,** *151* (2), 105-120.
2.11. Jiang, D. T., *X-Ray Absorption Fine Structure Spectroscopy*. In *Synchrotron Radiation: Earth, Environmental and Material Sciences Applications*, Henderson, G. S., Baker, D. R., Ed. Short Courses Series, **2002**, Vol. 30, 65-98.
2.12. Thompson, A.; Attwood, D.; Gullikson, E.; Howells, M.; Kim, K. J.; Kirz, J.; Kortright, J.; Lindau, I.; Pianetta, P.; Robinson, A.; Scofield, J.; Underwood, J.; Vaughan, D.; Williams, G., *X-ray Data Booklet*, 2nd ed.; Center for X-ray Optics, Advanced Light Source, Berkeley, **2001**.
2.13. Stöhr, J., *NEXAFS Spectroscopy*, Springer-Verlag, Berlin, **1992**.
2.14. Hitchcock, A. P.; Tronc, M., *Chemical Physics,* **1988,** *121* (2), 265-277.
2.15. Kaznatcheev, K. V.; Karunakaran, C.; Lanke, U. D.; Urquhart, S. G.; Obst, M.; Hitchcock, A. P., *Nuclear Instruments & Methods in Physics Research Section a-Accelerators Spectrometers Detectors and Associated Equipment,* **2007,** *582* (1), 96-99.
2.16. Bluhm, H.; Andersson, K.; Araki, T.; Benzerara, K.; Brown, G. E.; Dynes, J. J.; Ghosal, S.; Gilles, M. K.; Hansen, H. C.; Hemminger, J. C.; Hitchcock, A. P.; Ketteler, G.; Kilcoyne, A. L. D.; Kneedler, E.; Lawrence, J. R.; Leppard, G. G.; Majzlan, J.; Mun, B. S.; Myneni, S. C. B.; Nilsson, A.; Ogasawara, H.; Ogletree, D. F.; Pecher, K.; Salmeron, M.; Shuh, D. K.; Tonner, B.; Tyliszczak, T.; Warwick, T.; Yoon, T. H., *Journal of Electron Spectroscopy and Related Phenomena,* **2006,** *150* (2-3), 86-104.
2.17. Snigireva, I.; Snigirev, A., *Journal of Environmental Monitoring,* **2006,** *8*, 33.
2.18. Urquhart, S. G.; Hitchcock, A. P.; Smith, A. P.; Ade, H. W.; Lidy, W.; Rightor, E. G.; Mitchell, G. E., *Journal of Electron Spectroscopy and Related Phenomena,* **1999,** *100*, 119-135.
2.19. Kilcoyne, A. L. D.; Tylisczack, T.; Steele, W. F.; Fakra, S.; Hitchcock, P.; Frank, K.; Anderson, E.; Harteneck, B.; Rightor, E. G.; Mitchell, G. E.; Hitchcock, A. P.; Yang, L.; Warwick, T.; Ade, H., *Journal of Synchrotron Radiation,* **2003,** *10*, 125.
2.20. Jacobsen, C.; Wirick, S.; Flynn, G.; Zimba, C., *Journal of Microscopy-Oxford,* **2000,** *197*, 173-184.
2.21. Hu, Y. F.; Coulthard, I.; Chevrier, D.; Wright, G.; Igarashi, R.; Sitnikov, A.; Yates, B. W.; Hallin, E. l.; Sham, T. K.; Reininger, R., *Preliminary Commissioning and Performance of the Soft X-ray Micro-characterization Beamline at the Canadian Light Source*. In *AIP Conference Proceedings*, **2010**; 343-346.
2.22. Mijovilovich, A.; Pettersson, L. G. M.; Mangold, S.; Janousch, M.; Susini, J.; Salome, M.; de Groot, F. M. F.; Weckhuysen, B. M., *Journal of Physical Chemistry A,* **2009,** *113* (12), 2750-2756.
2.23. Rompel, A.; Cinco, R. M.; Latimer, M. J.; McDermott, A. E.; Guiles, R. D.; Quintanilha, A.; Krauss, R. M.; Sauer, K.; Yachandra, V. K.; Klein, M. P., *Proceedings of the National Academy of Sciences of the United States of America,* **1998,** *95* (11), 6122-6127.
2.24. Lemelle, L.; Labrot, P.; Salome, M.; Simionovici, A.; Viso, M.; Westall, F., *Organic Geochemistry,* **2008,** *39* (2), 188-202.
2.25. George, G. N.; Gorbaty, M. L., *Journal of the American Chemical Society,* **1989,** *111* (9), 3182-3186.
2.26. Sekiyama, H.; Kosugi, N.; Kuroda, H.; Ohta, T., *Bulletin of the Chemical Society of Japan,* **1986,** *59* (2), 575-579.

2.27. Damian, E.; Jalilehvand, F.; Abbasi, A.; Pettersson, L. G. M.; Sandstrom, M., *Physica Scripta,* **2005,** *T115*, 1077-1079.
2.28. Risberg, E. D.; Eriksson, L.; Mink, J.; Pettersson, L. G. M.; Skripkin, M. Y.; Sandstrom, M., *Inorganic Chemistry,* **2007,** *46* (20), 8332-8348.
2.29. Mijovilovich, A.; Pettersson, L. G. M.; de Groot, F. M. F.; Weckhuysen, B. M., *Journal of Physical Chemistry A,* **2010,** *114* (35), 9523-9528.
2.30. Prange, A.; Dahl, C.; Truper, H. G.; Behnke, M.; Hahn, J.; Modrow, H.; Hormes, J., *European Physical Journal D,* **2002,** *20* (3), 589-596.
2.31. Mori, R. A.; Paris, E.; Giuli, G.; Eeckhout, S. G.; Kavcic, M.; Zitnik, M.; Bucar, K.; Pettersson, L. G. M.; Glatzel, P., *Analytical Chemistry,* **2009,** *81* (15), 6516-6525.
2.32. Dezarnaud, C.; Tronc, M.; Modelli, A., *Chemical Physics,* **1991,** *156* (1), 129-140.
2.33. Breinig, M.; Chen, M. H.; Ice, G. E.; Parente, F.; Crasemann, B., *Physical Review A,* **1980,** *22* (2), 520-528.

CHAPTER 3 COMPUTATIONAL METHODS

Well-assigned NEXAFS spectra are the basis of different quantitative and qualitative studies as mentioned in **§1.3** and **§1.5**. Therefore, for assigning spectral transitions in NEXAFS spectra, several different approaches have been used including building block approach and the use of computational methods. In the building block method (discussed in **§1.3)** the NEXAFS spectrum is simulated with the spectra of building blocks (diatomic or functional group fragments, etc.).[3.1, 3.2] This method however, cannot account for molecules with high degree of electron delocalization. In computational methods, NEXAFS spectra are simulated theoretically and used to assign spectral transitions. For calculations of core excitation spectra different approaches have been used to treat the core excitation process such as multiple scattering[3.1] and Molecular Orbital (MO) theory.[3.3, 3.4] MO theory has been widely used for calculation of MO energies and wavefunctions with semi-empirical (in which theoretical and experimental parameters are used) and *ab initio* (in which all parameters are calculated theoretically) calculations based on a compromise between speed and quality. Throughout this thesis, computational methods based on *ab initio* calculations have been used to simulate and assign the sulphur 1s NEXAFS spectra of different sulphur functionalities.

The calculations performed for simulation of NEXAFS spectra were based on Improved Virtual Orbital (IVO) Hartree-Fock (HF) *ab initio* calculations in which the effect of the core hole is explicitly considered. §**3.1** provides an overview of the IVO approximation followed by the application of this approximation in *ab initio* calculations for simulation of NEXAFS spectra as well as the programs used for simulations. The spurious Rydberg-valence mixing that can be encountered in the IVO approximation is discussed in §**3.2**. To remove spurious Rydberg-valence mixing, higher quality ΔSelf Consistent Field (ΔSCF) calculations have been used. These calculations are described in §**3.3**. The references for this chapter are provided in §**3.4**.

3.1 Improved Virtual Orbital (IVO) Approximation

In core excitation spectroscopy, the creation of the core hole significantly affects the electronic structure of the excited molecule. Therefore, solving the Schrödinger equation for core electron excitations requires the inclusion of the core hole effect. One of the approximations that considers the core hole effect in MO calculations and has been widely used is the Improved Virtual Orbital (IVO) approximation proposed by Hunt and Goddard.[3.5] This approach includes the effect of the core hole in the Hartree-Fock Hamiltonian for calculation of the molecular potential, but ignores the effect of the excited electron in the outer shell over the other electrons. In this approximation, a specified i^{th} core electron is removed from an inner orbital ϕ_i and the other electrons ((N-1)-electron system, where N indicates the total number of the electrons in the molecule) are allowed to relax in the potential of the core hole. The core hole is prevented from being refilled. The molecular potential is calculated for this core-ionized ion.

Solving the Schrödinger equation for multi-electron systems requires Hartree-Fock and Linear Combination of Atomic Orbitals (LCAO) approximations to be included into the electronic Schrödinger equation, which then leads into a set of matrix equations known as Roothaan-Hall equations as:[3.6]

$$Fc = \varepsilon Sc \tag{3.1}$$

where, F is the Fock matrix, c are the unknown MO coefficients, ε are orbital energies, and S is the overlap matrix. Throughout this chapter, the lower-case Greek letters are used to index the basis functions and lower-case Roman letters used to index the MOs. On this basis the Fock matrix is defined as:[3.6]

$$F_{\mu v} = H_{\mu v}^{core} + J_{\mu v} - K_{\mu v} \tag{3.2}$$

where $H_{\mu v}^{core}$ is core Hamiltonian and is described as:

$$H_{\mu v}^{core} = \int \phi_{\mu}(r)\left[-\frac{\hbar^2}{2m_e}\nabla^2 - \frac{e^2}{4\pi\varepsilon_0}\sum_{A}^{nuclei}\frac{Z_A}{r}\right]\phi_v(r)dr \tag{3.3}$$

where r is the distance of the electron from nucleus and Z_A is the atomic number of nucleus A. m_e is the electron mass, ε_0 is the permittivity of free space, and $J_{\mu v}$ and $K_{\mu v}$ are the coulomb and exchange elements and are defined as:

$$J_{\mu v} = \sum_{\lambda}^{basis\ functions}\sum_{\sigma} P_{\lambda\sigma}(\mu v|\lambda\sigma) \tag{3.4}$$

$$K_{\mu\nu} = \frac{1}{2}\sum_{\lambda}^{basis\ functions}\sum_{\sigma} P_{\lambda\sigma}(\mu\lambda|\nu\sigma) \tag{3.5}$$

$P_{\lambda\sigma}$ is the density matrix and its elements include a product of two MO coefficients summed over all occupied MOs and is defined as:

$$P_{\lambda\sigma} = 2\sum_{i}^{\substack{moleular-orbital\\ occupied}} c_{\lambda i}c_{\sigma i} \tag{3.6}$$

Finally $(\mu\nu|\lambda\sigma)$ are two-electron integrals, and their number increases as the fourth power of the number of basis functions used. This indicates that the cost of the calculations will increase as the number of the basis functions used increases.[3.6]

$$(\mu\nu|\lambda\sigma) = \iint \phi_{\mu}(r_1)\phi_{\nu}(r_1)\left[\frac{1}{r_{12}}\right]\phi_{\lambda}(r_2)\phi_{\sigma}(r_2)dr_1dr_2 \tag{3.7}$$

For solving these equations, the Self-Consistant Field (SCF) method is used.[3.7] In this method, the first step is to guess the one-electron wave functions used for the calculation of the spatial distribution of the field and consequently for building the Hamiltonian operator. Having the Hamiltonian operator and the wave function, now the Schrödinger equation can be solved from which a new set of wave functions is obtained. From this new set that is more accurate than the guessed one, another Hamiltonian is obtained. This process is then repeated until the field after the n^{th} step is identical to that of $(n-1)^{th}$ step. At this point the calculations do not lead to any improvement or a satisfactory convergence is achieved, and the field is said to be "self-consistent". The level of convergence is chosen in a way to satisfy the accuracy as well as computational time. In contrast to semi-empirical calculations, all parameters and integrals are explicitly calculated in *ab initio* calculations. Use of HF-SCF *ab initio* theory was quite successful in improving the calculation of MO energies.[3.8, 3.9]

However, for core excitation calculations and to include the IVO approximation into these calculations, a "static exchange" Fock operator corresponding to the singlet ionization of the i^{th} electron, replaces the usual Fock operator (**Equation 3.2**) as follow:[3.5, 3.10]

$$F_i^{EX} = F - J_i + 2K_i \tag{3.8}$$

where F_i^{EX} is the static exchange Fock operator for removal of the i^{th} electron from the usual Fock operator F, J_i and K_i are the coulomb and exchange operators of the ionized electron. By this approximation, the energies and wave functions of the unoccupied orbitals in the presence of the core hole can be obtained.[3.5, 3.10]

The calculations of core excitation spectra for this research study were performed using Kosugi's GSCF3 package[3.11, 3.12] that is highly optimized in simulating the core-excited spectra[3.12] and uses IVO approximation of Hunt and Goddard for its calculations that explicitly include the core hole in the Hartree Fock Hamiltonian (**Equation 3.8**).[3.5] The basis sets used in these calculations are the high quality Gaussian Type Orbitals (GTO) extended basis sets of Huzinaga *et al*.[3.13] The basis sets used in this study include (41) for hydrogen; second row atoms (carbon, nitrogen, and oxygen) (621 41); sulphur (with the core hole) (311111111 311111), with an additional d polarization function on the sulphur atom (ζ_d = 0.421) for sulphur 1s calculations. For example, a double-zeta contraction scheme applied for hydrogen (41) means a set of 4 s-type and a set of 1 s-type orbitals are used to construct the 1s electron of Hydrogen. The polarization function used on core-excited atom allows more flexibility for the electron density to be distributed away from the nuclear positions. A complete list of all basis sets used and the polarization function for *ab initio* calculations are presented in detail in **Chapters 5**, **6**, **7**, and **8**.

The calculations performed by GSCF3 package include three steps as shown in **Figure 3.1**. This figure is an example for excitation of a 1s electron for an imaginary molecule with 10 electrons. In the first step, the ground state MOs and the total ground state energy of the molecule are calculated. In addition, the outcome of the first step calculations is used to determine which MO will have the core hole, which is used in the second step of calculations.

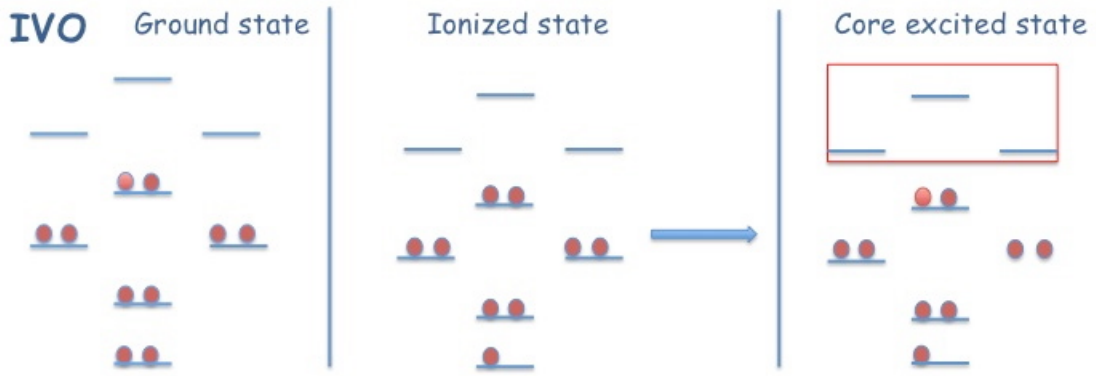

Figure 3.1 Energy level diagram of IVO *ab initio* calculations for calculating the transition intensities and energies.

In the second step (ionized state in **Figure 3.1**), an electron is explicitly removed from the desired core orbital (1s electron in **Figure 3.1**), and the other *(N-1)* electrons (in this example the other 9 electrons) are allowed to relax in the potential of the core-excited cation. In this step the core hole is prevented from being refilled, and the MOs are calculated for the core-excited cation.

The energy difference between the energy of the ground state (first step) and the energy of the core-ionized state (second step) is used for calculation of the ionization potential (IP). There is a good agreement between the experimental IP and the result of IVO approximation, as in this method the relaxation of other electrons in the potential of the core hole has been included in the calculations.[3.3, 3.14] On this basis, the IP obtained by IVO approximation is superior to that of Koopman's method in which the ionization potential is considered as the negative of the calculated orbital energy of the desired electron in atom or molecule. Koopman's method does not account for the electronic relaxation and the change in correlation energy between the neutral molecule and the ion.[3.15]

In the third step, all excited states are calculated for all possible one electron transitions to unoccupied molecular orbitals including valence and Rydberg orbitals. In this step, the excited orbitals (denoted by a red box in **Figure 3.1**) are calculated by minimizing the excitation energy for the excitation of a core level electron ϕ_{1s} to an excited orbital ϕ_k, where ϕ_k is determined for the unoccupied orbitals of the core-ionized molecule in step 2 as follows:[3.10]

$$E(\phi_{1s} \rightarrow \phi_k) = -\varepsilon_{1s} + \left\langle \phi_k \left| F - J_{1s} + 2K_{1s} \right| \phi_k \right\rangle \tag{3.9}$$

Solving this equation provides Term Values (TV) (the difference between the IP energy and the transition energy) and oscillator strength of the core excitation transitions. The oscillator strength f_{os} is used for core excitation intensities as follow:

$$f_{os} = \frac{2}{m\hbar\omega} \left| \left\langle \Psi_{final} \left| \mu \right| \Psi_{initial} \right\rangle \right|^2 \tag{3.10}$$

where ω is the radiation frequency, μ is the transition dipole matrix, m is the mass of electron, and $\hbar = h / 2\pi$ and h is the Planck constant. Recalling **§1.2**, it was mentioned that f_{os} is directly related to the absorption cross-section according to:

$$\sigma_x = C \frac{df}{dE} \tag{3.11}$$

where $C = 2\pi^2 e^2 \hbar / mc = 1.1 \times 10^2$ Mb eV (1Mb = 1 megabarn). The oscillator strength is thus a calculated value to express the probability of transition from an initial orbital to a final orbital.[3.1]

Afterwards the calculated IP is used to transform the calculated TV scale to the experimental scale. Now by having the oscillator strength and the energy of each transition, each peak is broadened by a Gaussian function. The widths of the peaks are chosen to approximately track the experimental line width observed in experimental spectra. For example for sulphur 1s, the line widths used are as follows: 0.6 eV FWHM for bound states, 1.2 eV fwhm for states from the ionization potential (IP) to 4 eV above the IP, and 4.0 eV fwhm for states more than 4.0 eV above the IP. This spectrum simulation process is performed by the program SIMILE2.[3.16]

According to Laporte electric-dipole selection rules, the allowed atomic transitions that correspond to the most intense transitions are those that satisfy a change in orbital angular momentum of $\Delta l = \pm 1$ (i.e. s (l=0) → p (l=1)).[3.17] In core electron excitations of molecules, as the initial core levels remain essentially atomic-like, then the atomic selection rules can be applied in their case and the core excitation transitions are assumed to follow an "atomic propensity rule" in which excitations are considered to obey the atomic selection rule on the core excited atom. On this basis, the final level orbital density can be described as a sum of s, p, d, etc. orbital characters, but with the

maximum contribution from the orbitals with allowed orbital angular momentum (i.e. sulphur 1s (l=0) → a MO with dominant p (l=1) character).

3.2 Rydberg-Valence Mixing

A shortcoming of IVO approximation is in its accuracy of calculations of the energies of Rydberg and valence orbitals. Rydberg orbitals are atomic like orbitals that are far from the nucleus and are observed in the core excitation of atoms and molecules. In these transitions, the excited electron "sees" all other electrons and the nucleus as one entity like the hydrogen nucleus. The energy of Rydberg orbitals can be obtained by Rydberg formula:[3.18]

$$TV = IP - E_n = R / (n - \delta_l)^2$$

(3.12)

where TV is the term value (the difference between the Ionization Potential (IP) energy, and the transition energy (E_n)), R is the Rydberg energy (13.6 eV), δ_l is the quantum defect that is associated with the angular-momentum quantum number (l).[3.18]

In IVO calculations however, in the second step, the calculated potential is for core excited cation and the effect of the core-excited electron is not considered in these calculations, therefore because of the similarity of the cationic electron environment to that of Rydberg core excited state, the core → Rydberg transitions are well described in this electronic environment. On this basis, in IVO approximation the energies of Rydberg core excited states are calculated more accurately than the valence state energies, and therefore spurious Rydberg-valence mixing can occur.[3.19, 3.20]

For a precise interpretation of the NEXAFS spectra, the degree of Rydberg-valence mixing should be considered in spectral transition assignments. The degree of Rydberg-valence mixing can be inferred by considering the orbital size and the energy difference between singlet and triplet core excited states for each transition (ΔE_{S-T}).[3.19, 3.20] Because of the bigger size of Rydberg orbitals compared to that of valence orbitals, when an electron is excited to a pure Rydberg orbital it has a small interaction with other electrons. In contrast if it is excited to a valence orbital, it has much more interaction with other electrons in the molecule. Also based on the Pauli exclusion principle, an electron excited into a triplet excited state has less repulsion from other electrons compared to the

singlet states. Therefore, for second row atoms a $\Delta E_{S-T} > 0.05$ eV and orbital size of less than 3 Å indicate some valence character in that specific transition.[3.19-21] These assumptions for the second row atoms have been extrapolated for the sulphur atom as well. The details of the calculations are provided in **Chapter 8**. For considering the effect of the excited electron on the potential of other electrons, higher quality calculations can be used in ΔSelf-Consistent Field (ΔSCF) method described below.

3.3 ΔSelf-Consistent Field (ΔSCF) Method

In ΔSelf Consistent Field (ΔSCF) method, the shielding effect of the core-excited electron is corrected by recalculating the potential of the other *(N-1)* electrons (see **§3.1**) with the core hole vacancy and the excited orbital occupancy. This process is shown in **Figure 3.2**. Similar to IVO *ab initio* calculations, these calculations are performed for the molecule in ground state and the MO energies and the total energy of the ground state are calculated. In the second step, an electron is introduced in the selected excited orbital (a yellow circle in **Figure 3.2**) and the other occupied orbitals are kept frozen to maintain the orthogonality.[3.20, 3.22, 3.23] The calculations are performed at this step by considering the effect of the core hole and the IP for this specific transition is obtained.

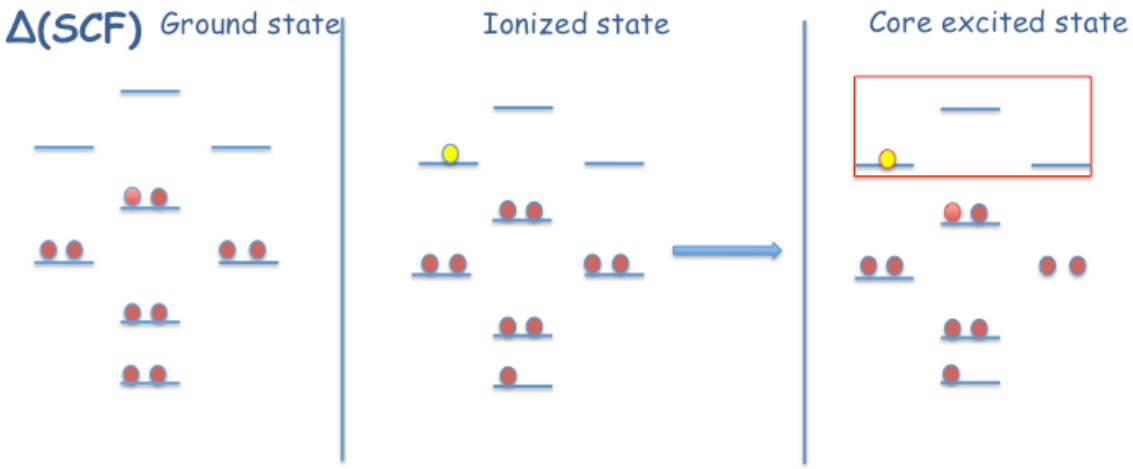

Figure 3.2 Energy level diagram of ΔSCF *ab initio* calculations for calculating the transition intensities and energies of MOs by considering the excited orbital occupancy.

In the core excited state the transition intensity and the TV are calculated for the specific excited MO. This process is repeated for each excited state by considering the shallower orbitals frozen to maintain orthogonality as mentioned above.[3.20, 3.22, 3.23] This

approach is referred as ΔSCF calculations throughout this thesis,[3.22, 3.23] and was first used by Kosugi *et al*. to remove spurious Rydberg-valence mixing in the carbon 1s → σ*(C-F),[3.24] and then was used to determine the degree of Rydberg-valence mixing in the NEXAFS spectra of gaseous alkanes,[3.19] condensed alkanes,[3.20] and amino acids.[3.21]

ΔSCF calculations have been performed to simulate the NEXAFS spectra of thiophenic compounds discussed in more details in **Chapter 8** of this thesis to remove the spurious Rydberg character in thiophenic compounds.

3.4 References

3.1. Stöhr, J., *NEXAFS Spectroscopy*, Springer-Verlag, Berlin, **1992**.
3.2. Ade, H.; Urquhart, S. G., *X-ray Spectromicroscopy of Polymers*. In *Chemical Applications of Synchrotron Radiation*, Sham, T. K., Ed. World Scientific, **2002**.
3.3. Agren, H.; Carravetta, V.; Vahtras, O.; Pettersson, L. G. M., *Chemical Physics Letters,* **1994,** *222* (1-2), 75-81.
3.4. Hitchcock, A. P.; Urquhart, S. G.; Rightor, E. G., *Journal of Physical Chemistry,* **1992,** *96* (22), 8736-8750.
3.5. Hunt, W. J.; Goddard, W. A., *Chemical Physics Letters,* **1969,** *3* (6), 414-418.
3.6. Engel, T., *Quantum Chemistry & Spectroscopy*, 3rd ed.; Jim Smith, San Fransisco , **2005**.
3.7. Hartree, D. R., *Proceedings of the Cambridge Philosophical Society,* **1928,** *24* (89).
3.8. Carmer, C. J., *Essentials of Computational Chemistry*, John Wiley & Sons Ltd., Chichester, **2002**.
3.9. House, J. E., *Fundamentals of Quantum Chemistry*, 2nd ed.; Elsevier Academic Press, **2004**.
3.10. Urquhart, S. G. *Delocalization and Functional Group Fingerprinting in the Core Excitation Spectroscopy of Molecules and Polymers*, PhD thesis, McMaster, **1997**.
3.11. Kosugi, N., *Theoretica Chimica Acta,* **1987,** *72* (2), 149-173.
3.12. Kosugi, N.; Kuroda, H., *Chemical Physics Letters,* **1980,** *74* (3), 490-493.
3.13. Huzinaga, S.; Andzelm, J.; Klobukowski, M.; Radzio-Andzelm, E.; Sakai, Y.; Tatewaki, H., *Gaussian Basis Sets for Molecular Calculations*, Elsevier, **1984**, Vol. 16.
3.14. Kosugi, N.; Shigemasa, E.; Yagishita, A., *Chemical Physics Letters,* **1992,** *190* (5), 481-488.
3.15. Levine, I. N., *Quantum Chemistry*, 4th ed.; Prentice Hall, NJ, **1991**.
3.16. Huo, B.; Hitchcock, A. P. *Simile2; McMaster University, Hamilton, ON*, **1996**.
3.17. Ishii, I.; Hitchcock, A. P., *Journal of Chemical Physics,* **1987,** *87*.
3.18. Robin, M. B., *Higher Excited States of Polyatomic Molecules*, Academic, New York, **1974**, Vol. 1.
3.19. Urquhart, S. G.; Gillies, R., *Journal of Physical Chemistry A,* **2005,** *109* (10), 2151-2159.
3.20. Urquhart, S. G.; Gillies, R., *Journal of Chemical Physics,* **2006,** *124* (23).

3.21. Otero, E.; Urquhart, S. G., *Journal of Physical Chemistry A,* **2006,** *110* (44), 12121-12128.
3.22. Kosugi, N., *Advanced Course in Application of GSCF3 to Inner Shell Excitation*, **2000**.
3.23. Kosugi, N., *Manual of GSCF3*, **1986**.
3.24. Kosugi, N.; Ueda, K.; Shimizu, Y.; Chiba, H.; Okunishi, M.; Ohmori, K.; Sato, Y.; Shigemasa, E., *Chemical Physics Letters,* **1995,** *246* (4-5), 475-480.

CHAPTER 4 SURFACE SENSITIVITY IN SCANNING TRANSMISSION X-RAY MICROSCOPY

Scanning Transmission X-ray Microscopy (STXM) is a powerful technique in imaging and chemical speciation of nanostructured materials. This technique combines the chemical sensitivity of NEXAFS spectroscopy with the high spatial resolution of X-ray microscopy. STXM is sensitive to the bulk chemistry of the sample, however the surface and interface studies are of keen interest as well. Therefore, the goal of this research project was to add surface sensitivity to the current generation of STXMs to have simultaneous bulk and surface measurements within STXM microscopes. **§4.1** provides an overview of the importance of surface sensitive measurements in STXM microscopy. To verify the function of the developed surface sensitive microscopy, different model samples were used within the course of this study. The details of these sample preparations are provided in **§4.2**.

In **§4.3**, the implementation of Total Electron Yield (TEY) detection for achieving high surface sensitive measurements in STXM microscopes is discussed. Implementation of single electron counting in STXM microscopy involved different challenges discussed in detail in **§4.3.1,** including carbon photodeposition in **§4.3.1.1**, and vacuum environment in **§4.3.1.2**. In this research study, TEY measurements were accomplished through two methods including conventional sample current (**§4.3.2)** and single electron counting (**§4.3.3**). Finally the results obtained from this new technique are provided in **§4.4** followed by the conclusion in **§4.5**. The references for this chapter are provided at §**4.6**.

In this study, Dr. Stephen G. Urquhart, Dr. Brian Haines, and Dr. Tolek Tyliszczak performed TEY-STXM experiments at the Advanced Light Source (ALS) and I did the data analysis. At the Canadian Light Source (CLS), Dr. Brian Haines, Dr. Jian Wang, and Dr. Stephen G. Urquhart helped me in mounting the channeltron and performing the experiments and I did the data analysis.

4.1 Introduction

Scanning Transmission X-ray Microscopy (STXM) has found widespread use in the study of polymers,[4.1-4] nanostructured organic compounds,[4.3, 4.5, 4.6] materials and environmental sciences,[4.7, 4.8] and magnetization dynamics.[4.9, 4.10] STXM combines the high spatial resolution imaging of X-ray microscopy, based on a Fresnel zone plate focusing element, with the chemical sensitivity of Near Edge X-ray Absorption Fine Structure (NEXAFS) spectroscopy via spatially resolved spectra, images at specific X-ray energies, or image-sequences across absorption edges in X-ray microscopes.[4.11] Therefore, STXM microscopy allows for both imaging and chemical speciation. NEXAFS spectroscopy can provide detailed information on chemical group functionality, molecular orientation and magnetic structure.[4.12-20] Additionally, orientation information with regard to linear dichroism of specific NEXAFS transitions[4.21, 4.22] can also be obtained.

Current generation of STXM microscopes have a spatial resolution of around 30 nm.[4.23] This is a higher spatial resolution than is currently achievable with other techniques, such as Raman microscopy. STXM microscopy also contribute to less radiation damage in samples than electron based chemical imaging techniques such as Transmission Electron Microscopy-Electron Energy Loss Spectroscopy (TEM-EELS).[4.24]

However, as STXM microscopes operate with transmission detection, this microscopy is essentially sensitive to the bulk chemistry of the sample. Nevertheless, it can be used to study surface and interfacial phenomena. For example, interfaces have been observed at glancing angle imaging of curved surfaces.[4.25] In these examples, the interface signal is enhanced by projection, and the interface width is relatively wide to be seen by STXM microscopy.

Spatially resolved chemical analysis of planar surfaces is of great and general interest. There would be tremendous analytical value in extending the high spatial resolution imaging of STXM microscopy and the chemical sensitivity of NEXAFS spectroscopy to surfaces. For example, such methods would be tremendously useful for studies of the chemical state of mineral surfaces, as well as the surface orientation and dynamics in nanostructured organic thin films.

Other surface sensitive microscopies, such as scanning electron microscopy or scanning probe microscopy, lack the general and flexible chemical sensitivity of

NEXAFS spectroscopy. Photoelectron Emission Microscopy (PEEM) is frequently used for NEXAFS microscopy of surfaces, with ~4 nm sampling depth for organics.[4.26] This technique, however, is limited to conducting samples that are compatible with Ultra High Vacuum (UHV) and the high electric field of the objective lens and cannot be used to study the surfaces of particulates.

Our approach to improve the spatially resolved chemical analysis of surfaces is to add surface sensitive detection to STXM microscopy. Surface sensitivity in NEXAFS spectroscopy is typically obtained with electron yield detection, the simplest variant being Total Electron Yield (TEY). By implementing single electron counting TEY detection in a STXM microscope, we can greatly enhance the surface sensitivity of traditional transmission STXM microscopy. Here TEY-STXM has been implemented to study the surface phenomena and chemical structure of ultrathin films, such as Langmuir-Blodgett self-assembled monolayers, thin patterned metal samples and phase segregated polymers. Our implementation of TEY-STXM allows for simultaneous measurement of both the bulk transmission and the surface sensitive electrons, providing complementary surface and bulk compositional information.

4.2 Sample Preparation

To develop and demonstrate the sensitivity of TEY-STXM, a series of model samples have been examined within the course of this study. The model samples used for TEY-STXM experiments should be conductive to prevent charging effects in TEY measurements and thin enough for simultaneous measurements of transmission. The model samples chosen for this research study are as follows:

- A thin patterned metal sample of Fe with Cr overlayer, used to show the difference in the oxidation state of Fe in the bulk and the surface of the sample.
- A phase separated mixed Langmuir-Blodgett (LB) ultrathin film of arachidic acid (AA) and perfluorotetradecanoic acid (PA) in a 2:1 ratio (2AA:1PA) to show the monolayer sensitivity of TEY-STXM.
- A thin film of a phase segregated copolymer blend of polystyrene (PS) and

poly(methyl methacrylate) (PMMA), or in short notation as PS/PMMA.

As mentioned earlier, for sample current and single-electron counting TEY-STXM measurements, a conductive sample is required, although it is expected that small non-conductive samples can be examined if they are lightly dispersed on a conductive substrate so that there is no significant charging effect. Thickness of the sample is also critical in TEY-STXM measurements, as for simultaneous measurements of transmission in addition to electron yield detection, a thin layer of sample is required to ensure the penetration of the X-ray beam through the sample. For this purpose, all the samples were deposited on a Au coated 75 nm Si_3N_4 membrane/window; the thickness of the Au coating was ~10 nm. The details of the chemicals and substrates used are described in **§4.2.1**. The vapour deposition method used for deposition of thin layers of metals on Si_3N_4 window is described in **§4.2.2**. The Langmuir-Blodgett monolayer film deposition and spin casting of phase segregated PS/PMMA are described in **§4.2.3** and **§4.2.4** respectively.

4.2.1 Chemicals and Substrates

Si_3N_4 membrane/window (Norcada Inc., 75 nm thickness) presented in **Figure 4.1** (right) was used as substrate in all experiments, and thin layers were subsequently deposited on the window. The Transmission Electron Microscope (TEM) copper grid (Structure Probe Inc.) was used for patterning the samples presented in **Figure 4.1** (left).

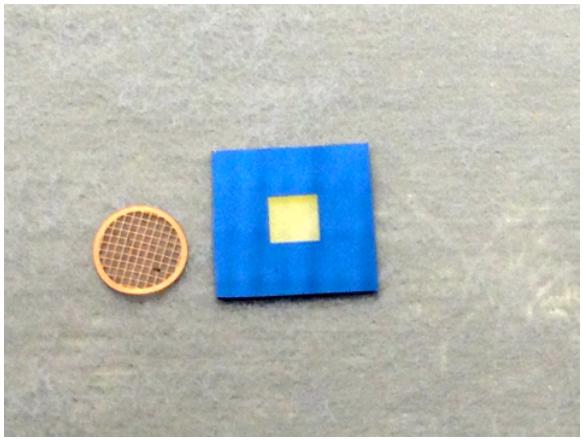

Figure 4.1 An image of typical (left) TEM copper grid and (right) Si_3N_4 membrane window for TEY-STXM measurements.

All the chemicals were purchased commercially and were used without any further purification. Arachidic acid (99%), perfluortetradecanoic acid (97%), iron (Fe) chips (99.98%), and toluene (99.9% Chromasolv®) were purchased from Sigma-Aldrich. Hexane (HPLC grade), and tetrahydrofuran (THF) were purchased from EMD Chemicals Inc., and Merck EM Science respectively. Polystyrene (Molecular weight (Mw): 1065600, weight average molecular weight/number average molecular weight (Mw/Mn): 1.06), and Poly(methyl methacrylate) (Mw: 315000, Mw/Mn: 1.05) were purchased from Polymer Source Inc. PELCO®Mica from Ted Pella, Inc., and chrome plated tungsten rod, and tungsten boat were purchased from R. D. Mathis company.

4.2.2 Vapour Deposition

For patterned metal sample preparation, vapour deposition method was used to create thin layers of metals over the Si_3N_4 window using the thermal deposition instrument (Datacomp Scientific) presented in **Figure 4.2(a)**. All the evapourations were performed inside the bell jar evapouration system equipped with a quartz crystal microbalance to measure thickness, illustrated schematically in **Figure 4.2(b)**.

In vapour deposition method a small amount of the sample was placed in a resistively heated tungsten boat located inside the high vacuum chamber. The temperature of the boat was increased by increasing the current passing through it, until the compound vapourization or sublimation temperature was achieved. At this point the molecules of the sample in the boat traveled to the surface of the substrate (Si_3N_4 window) located 15 cm above the boat. This process was continued until the desired thickness was achieved, as monitored by a quartz crystal microbalance placed in the vicinity of the substrate.

A patterned metal Fe/Cr sample was prepared by the evapouration of 80 Å Fe on the Si_3N_4 window (75 nm thick; Norcada Inc), followed by the adhesion of a TEM grid as a mask on the window and consequent evapouration of 20Å Cr on the top of the Fe layer to obtain a patterned thin film of Cr over Fe.[4.27] After patterning, the TEM grid was removed. This sample was prepared by Dr. Stephen G. Urquhart.

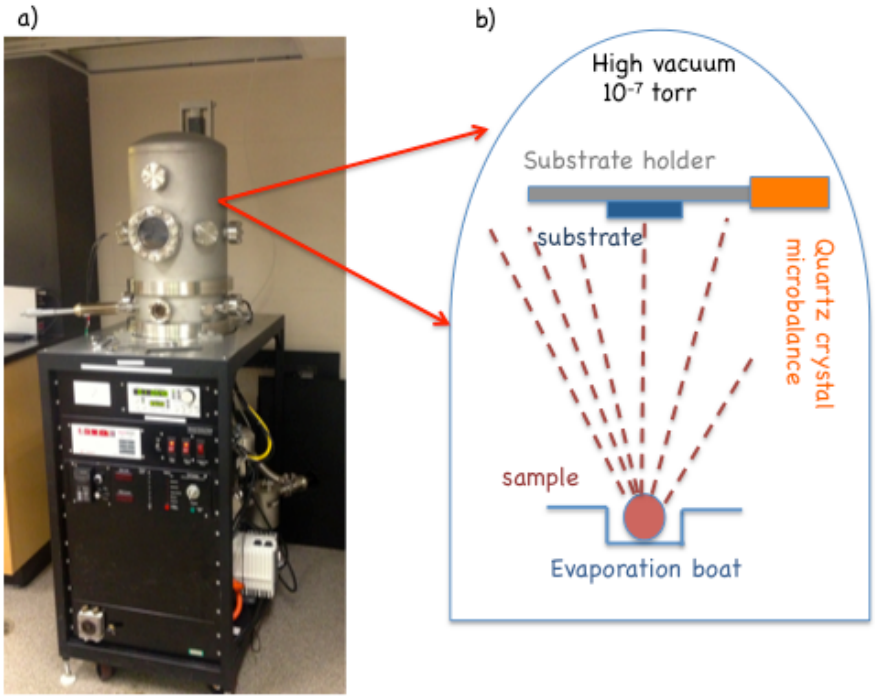

Figure 4.2 The image of thermal deposition instrument (Datacomp Scientific). (a) The evapouration bell jar; (b) schematic diagram of the inside of the evapouration bell jar.

4.2.3 Langmuir-Blodgett Film Preparation

Another model sample used for TEY-STXM measurements was a phase separated mixed Langmuir-Blodgett (LB) ultrathin film of arachidic acid (AA) and perfluorotetradecanoic acid (PA) in a 2:1 ratio (2AA:1PA). Stephen Christensen from Dr. Urquhart's group prepared the LB samples for sample current measurements for the experiments performed at the ALS and I prepared the samples for the experiments performed at the CLS. Stephen Christensen acquired the AFM images of these samples. This system is well understood from past studies including atomic force and photoelectron emission microscopy.[4.28] This system provides a well-defined monolayer system with micron size phases for testing of the monolayer sensitivity of TEY-STXM.

For TEY-STXM measurements, the LB films must have been deposited on a conductive and X-ray transparent substrate. Therefore, Si_3N_4 windows (75 nm thick; Norcada Inc) were used as substrate that were coated with ~3Å Cr for an adhesion layer, and a 15 nm Au thin film for conductivity. As the Au film was insufficiently hydrophilic for LB deposition, this film was subsequently covered with a 3 to 4 nm layer of silicon monoxide. This layer was kept thin to allow electron tunneling to occur and thus maintain

the required conductivity for TEY measurements. The Cr, Au and SiO depositions were performed in a bell jar evapouration system equipped with a quartz crystal microbalance to measure thickness (described in **§4.2.2**). The LB film was then deposited onto the Si monoxide layer.

The preparation and deposition of LB films was performed by a KSV 2000 Langmuir trough system (KSV Instruments, Helsinki, Finland). Ultrapure room temperature water (Millipore with resistivity of 18.2 MΩ cm) was used as the subphase. Individual stock solutions of AA and PA were prepared by dissolving the solid surfactant in a 9:1 volume ratio of hexane:THF, respectively. The final concentrations of the solutions were 8×10^{-3} M for AA and 5×10^{-3} M for PA. These solutions were then mixed to produce a 2AA:1PA mole ratio mixture of the two surfactants. The Si_3N_4 window was attached to a glass slide to constrain deposition to the Au coated side of the Si_3N_4 window and was submerged below the air-water interface. 30 μL aliquot of the 2AA:1PA mixed surfactant solution was spread over the surface of water and was allowed to remain for 10 minutes for solvent evapouration. Then the trough barriers were compressed at a rate of 10 mm/min until a deposition surface pressure of 20 mN/m was achieved. The film was allowed to stabilize at the deposition pressure for 10 minutes, and then the substrate was pulled through the air-water interface at a rate of 4 mm/min. The samples were allowed to dry out at room temperature and then were separated from the glass slide.

4.2.4 Spin casting of polymer blends

Phase segregated copolymer blend of polystyrene (PS) and poly(methyl methacrylate) (PMMA) deposited on Si_3N_4 window was prepared by Adam Leontowich from Adam Hitchcock's research group at McMaster University. The sample preparation is as follows: four drops of a 1%w/w (30 PS:70 PMMA in toluene) were spun cast onto freshly cleaved mica (1.5 cm × 1.5 cm), at 4000 rpm in 40 s. These samples were annealed for 18 hours at 160° C at reduced pressure of 2×10^{-2} torr. After annealing, the film was cut into 2 mm × 2 mm pieces and was slowly dipped into a petri dish filled with HPLC grade water. This way small pieces of the film were released and float on the surface of water. Each piece was caught on 75 nm Si_3N_4 window (Norcada Inc.) that was

Au coated (10 nm), in such way that only partially covered the window to allow for measurements of the spectrum of incident radiation (I_0).

4.2.5 Sample Mounting

The sample mounting for TEY measurements is illustrated in **Figure 4.3**. For sample current measurements, the sample must be electrically isolated from the rest of the microscope, while the sample itself must be conductive. Therefore, a layer of Kapton tape was placed over the sample holder that is made of Al (Al shim) for electrical isolation of the sample from the holder. Then a layer of Al foil was placed on the top of the Kapton tape for electrical connection of the wire (used for sample current measurements) and the samples in case of loading multiple samples on the Al shim sample holder (**Figure 4.3(b)**). The Si_3N_4 windows were then attached to this assembly by carbon tape. Silver paint (from SPI Supplies) was also used to make an electrical connection of the Au coated Si_3N_4 window to the Al foil for sample current measurements.

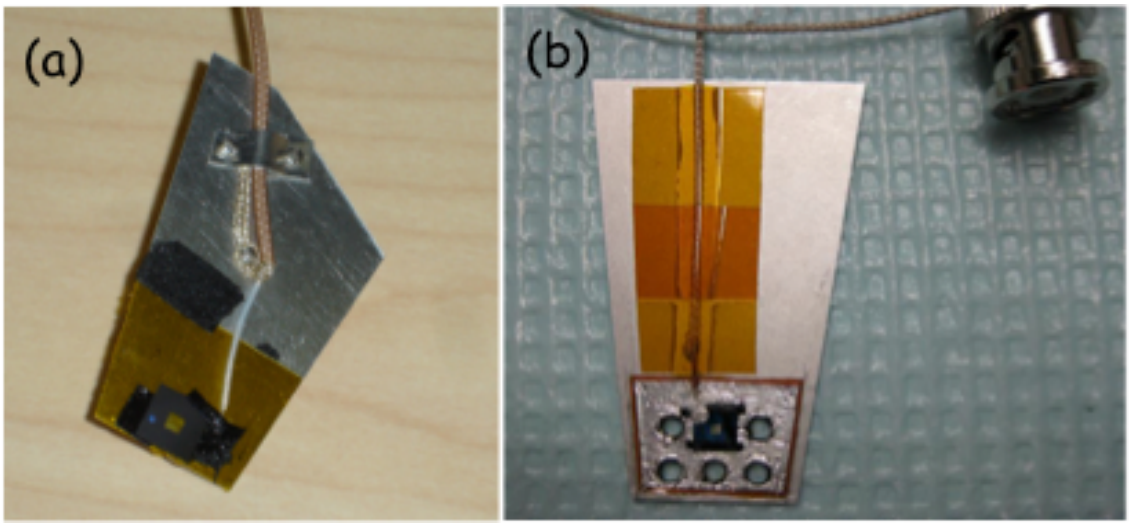

Figure 4.3 (a) Sample mounting for TEY-STXM measurements at beamline 11.0.2 located at the Advanced Light Source (ALS), Lawrence Berkley National Laboratory, University of California, US; (b) sample loading with multiple loading places used at SM beamline 10ID-1 located at the Canadian Light Source (CLS), Saskatoon, Saskatchewan.

The only difference in sample loading at the ALS was the use of Al foil. A layer of Kapton tape covered the holder and the Si_3N_4 window was attached by carbon tape. This assembly then was directly connected to a wire for the sample current

measurements. **Figure 4.3(b)** shows the sample holder used at the CLS capable of multiple sample loading.

4.3 Electron Yield Detection in STXM Microscopy

When a sample absorbs X-ray radiation, primary and secondary photoelectrons are emitted; this photocurrent is the source of the sample current measurements described in **§2.2.3**. Throughout this study, two different methods to measure the total electron yield in a STXM microscope have been explored: sample current and single electron counting. Sample current TEY is a common way of measuring the soft X-ray NEXAFS spectra of materials. This method uses a picoammeter to measure the sample drain current while it is irradiated by X-rays. The second method is direct measurement of the electrons photoemitted by the sample, using a channeltron for single electron counting. The vacuum environment is important for TEY detection, but particularly critical for detection with a channeltron. The environmental requirements for TEY detection will be discussed in detail in **§4.3.1**. The technical details of sample current measurements and single electron counting will be discussed in **§4.3.2** and **§4.3.3**.

4.3.1 Challenges in Implementation of Electron Yield Detection in STXM Microscopy

TEY-STXM Experiments were conducted using STXM microscopes at beamline 11.0.2[4.29] of the Advanced Light Source (ALS) and at the Spectromicroscopy Beamline[4.30] of the Canadian Light Source (CLS). The STXM microscopes at the ALS and CLS are designed to work in 100 mtorr pressure range. However, electron yield detection in the STXM microscope requires a lower vacuum pressure. Another challenge encountered in TEY detection is the partial pressure of hydrocarbons inside the chamber causes photodeposition, as organic buildup on the surface of the sample. Therefore, control of photodeposition and high vacuum are central to the development and efficient utilization of TEY-STXM microscopy.

4.3.1.1 Controlling X-ray Induced Photodeposition

Photodeposition is the rapid deposition of organics from the atmosphere in the chamber onto the sample surface when it is irradiated with highly focused X-ray

radiation. Photodeposition is a particular problem for surface analysis as the high intensity of the X-ray beam leads to rapid cracking of hydrocarbons onto the sample surface. In the current generation of the STXM microscopes, lubricants used in the motors and stages contribute to a high partial pressure of hydrocarbons that contribute in photodeposition in the STXM measurements. While this effect is negligible for transmission, it has a severe effect for surface sensitive measurements, as the photodeposited surface can quickly dominate the electron yield signal. In previous work, to reduce this effect, a liquid nitrogen cold finger[4.31] was employed to decrease the rate of photodeposition. This cold finger has been observed to reduce the photodeposition rate significantly in transmission mode of detection.[4.31] **Figure 4.4** compares the photodeposition rate in transmission and TEY measurements. In this experiment the focused X-ray beam was placed on an unexposed area of the LB film of 2AA:1PA sample. The transmission and channeltron based TEY signals were measured as a function of time (ALS STXM, pressure 3×10^{-5} torr). In this condition, the transmission signal (blue line) dropped much more slowly than the TEY signal (green line). TEY signal decreased by nearly 27% after only 11 seconds of X-ray exposure, indicating how photodeposition has a severe effect on TEY-STXM detection.

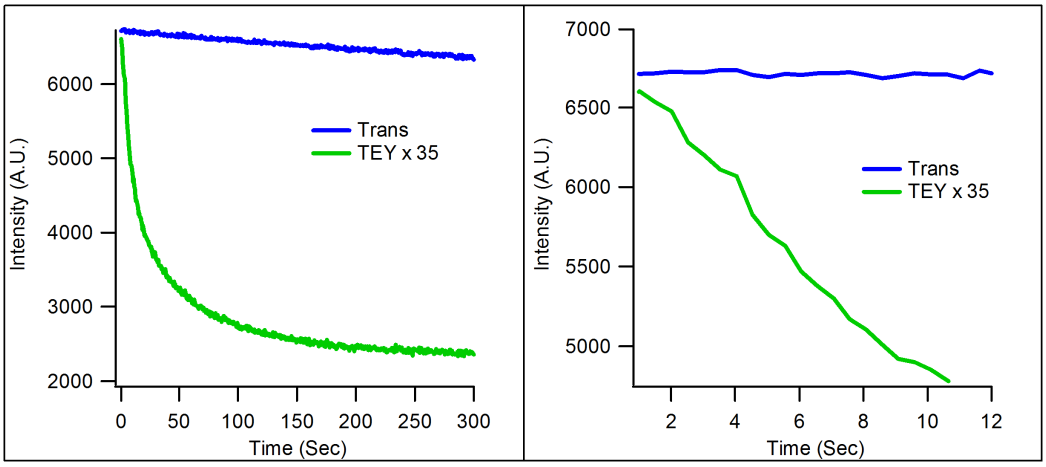

Figure 4.4 (left) Comparison of TEY (green) and transmission (blue) signal obtained by holding the X-ray beam at a fixed position and energy (698.0 eV) on the Langmuir-Blodgett sample surface as a function of time. (Right) The graph at right shows a zoomed in region. [Figure courtesy of Dr. Brian Haines, 2008]

The graph to the left shows that after approximately 2.2 minutes, the TEY signal becomes steady after a sharp drop in signal counts. The transmission plot photodeposition spectrum continues to show only a minor decrease in signal.

4.3.1.2 Vacuum Environment

High vacuum is required for the operation of the channeltron, therefore 270-275 L/s and 300 L/s turbomolecular pumps were directly attached to the STXM microscope chambers at both the ALS and the CLS. These pumps lowered the overall chamber pressure to ~3 x 10^{-5} torr, as measured with an ion-gauge. A liquid nitrogen cooled cold finger[4.32] was also used in addition to the turbo pumps to reduce the partial pressure of hydrocarbons in the chamber.

4.3.2 Conventional Sample Current

Conventional sample current is the simplest variant of measuring the TEY-NEXAFS spectrum. In this method, the drain photocurrent induced by X-ray absorption is measured with a picoammeter. As the material's X-ray absorption cross-section varies, the sample current required to neutralize electrons emitted from primary and secondary photoionization varies accordingly, resulting in the NEXAFS spectrum of the sample.

As mentioned in **§4.2.5** for sample current measurements, the sample must be electrically isolated from the rest of the microscope, but the sample itself must be conductive (see **Figure 4.3(a)**). Kapton tape was used for electrical isolation of the sample from Al shim sample holder (detailed sample preparation is provided in **§4.2**). An electrical schematic for the sample current measurements is illustrated in **Figure 4.5.**

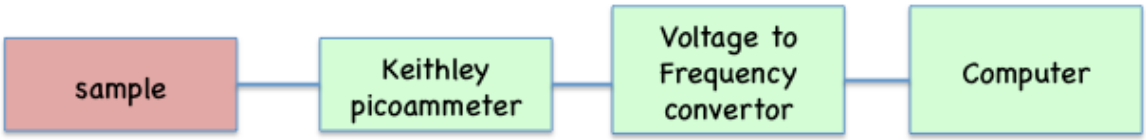

Figure 4.5 Schematic diagram of sample current TEY measurement.

The isolated sample is connected to a Keithley 428 current amplifier. The voltage output is connected to a voltage to frequency converter and is monitored by a computer. The TEY signal is measured along with the transmission signal on a pixel by pixel basis.

However, sample current TEY measurements are not very reliable. The TEY photocurrent from the zone plate focus in the STXM microscope is near the limit of the

sensitivity of the low-current amplifier, and this weak signal is prone to ground loops and current induction from the STXM stage motion.

4.3.3 Single Electron Counting

The photoelectrons ejected from the surface can be measured directly, by using a channeltron, Micro-Channel Plate (MCP), or an electron energy analyzer.[4.17] Since this type of TEY detection is based on direct counting of electrons, it is not prone to leakage currents and the noise associated with extremely weak sample current measurement. **Figure 4.6** presents a schematic diagram of single electron counting, and sample current TEY measurement in the STXM microscope.

In this configuration, imposed by the available space at the STXM chamber, the channeltron/channelplate is mounted behind the sample on top of the photon detector. In this geometry, the sample acts as a "filter" to screen the copious photoelectrons generated by the OSA and other surfaces in the STXM microscope. The channeltron cone is mounted as close to the sample as possible, ~3 mm away in this configuration, to the side of the phosphor / photomultiplier based transmission detector.[4.33] Several channeltrons/channelplate were explored in the course of this work.

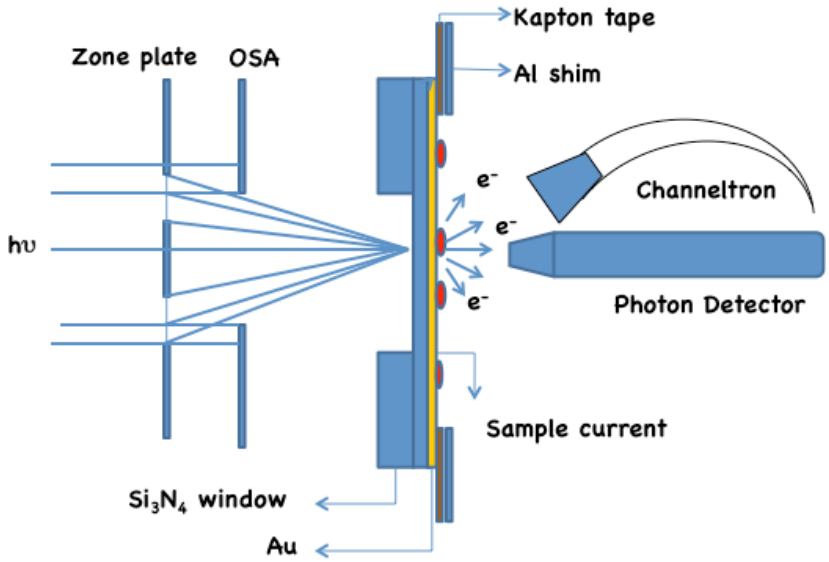

Figure 4.6 Schematic diagram of single electron counting TEY and sample current measurement.

The first experiments of TEY-STXM were performed at beamline 11.0.2 located at the Advanced Light Source (ALS), Berkeley California with a Photonis CEM4504 minichanneltron. Dr. Brian Haines, and Dr. Stephen G. Urquhart performed the experiments at the ALS and I did the data analysis.

These first experiments were performed on a phase separated mixed Langmuir-Blodgett (LB) ultrathin film of arachidic acid (AA) and perfluorotetratradecanoic acid (PA) in a 2:1 ratio (2AA:1PA). The reason for choosing this sample was its sample thickness (20 Å) made it difficult to be studied in transmission mode; therefore it was a good candidate for testing the monolayer sensitivity of TEY-STXM relative to transmission mode. **Figure 4.7** presents the channeltron mount over the Photomultiplier Tube (PMT) in the STXM chamber. The maximum working pressure of this channeltron is about 5×10^{-5} torr, and the pressure inside the chamber was 3×10^{-5} torr.

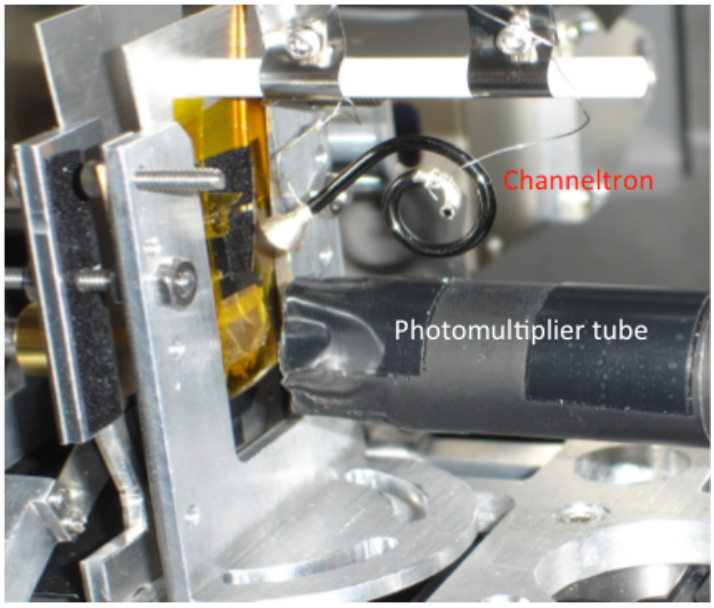

Figure 4.7 Side view of the Photonis CEM4504 minichanneltron mounted over the photon detector at beamline 11.0.2 located at the Advanced Light Source (ALS), Lawrence Berkley National Laboratory, University of California, US.

Figure 4.8 presents the schematic diagram of the channeltron wiring. The channeltron cone was typically biased to + (0-100) V, and the tail to 2.5-3 kV, depending on the channeltron's operating condition. The channeltron pulses were passed through a capacitor box and then to an Ortec VT120C pre-amplifier, further amplified before

passing through an Ortec 9307 discriminator. Finally the signal was monitored by a computer.

After the satisfactory first TEY-STXM results at the ALS, the Photonis 5901 Magnum detector was chosen to be implemented at the SM beamline 10ID-1 located at the CLS, Saskatoon, Saskatchewan. This detector turned out to be the best option with the current experimental conditions at the CLS (vacuum environment) as well as providing higher signal level compared to Photonis CEM4504 minichanneltron.

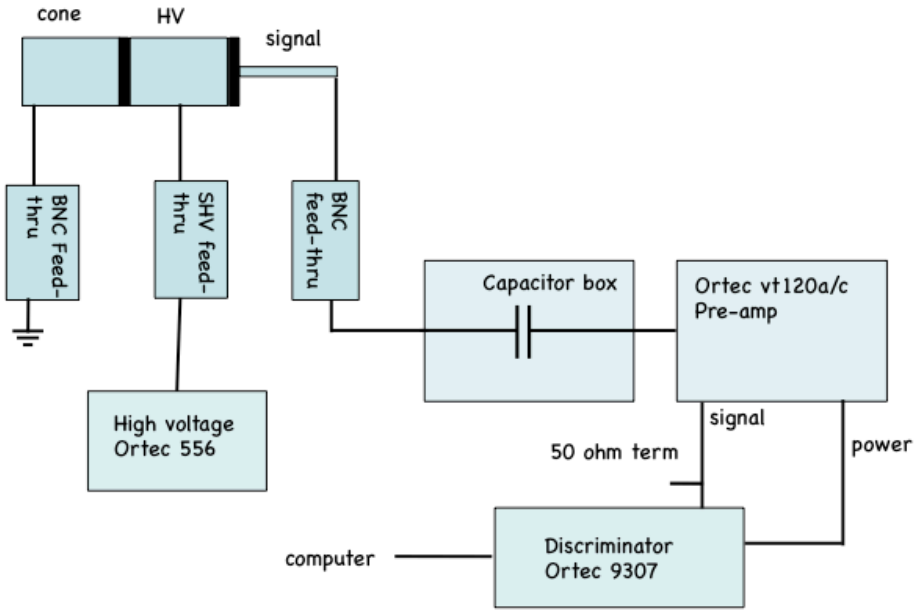

Figure 4.8 Schematic diagram of channeltron wiring at beamline 11.0.2 located at the Advanced Light Source (ALS), Lawrence Berkley National Laboratory, University of California, US.

The Photonis 5901 Magnum detector consists of six individual channeltron tubes that are wrapped in a spiral shape to reduce ion feedback and increase signal levels and lifetime for operations at higher pressures; **Figure 4.9** illustrates the channeltron mount as well as the inside configuration of the channeltron.

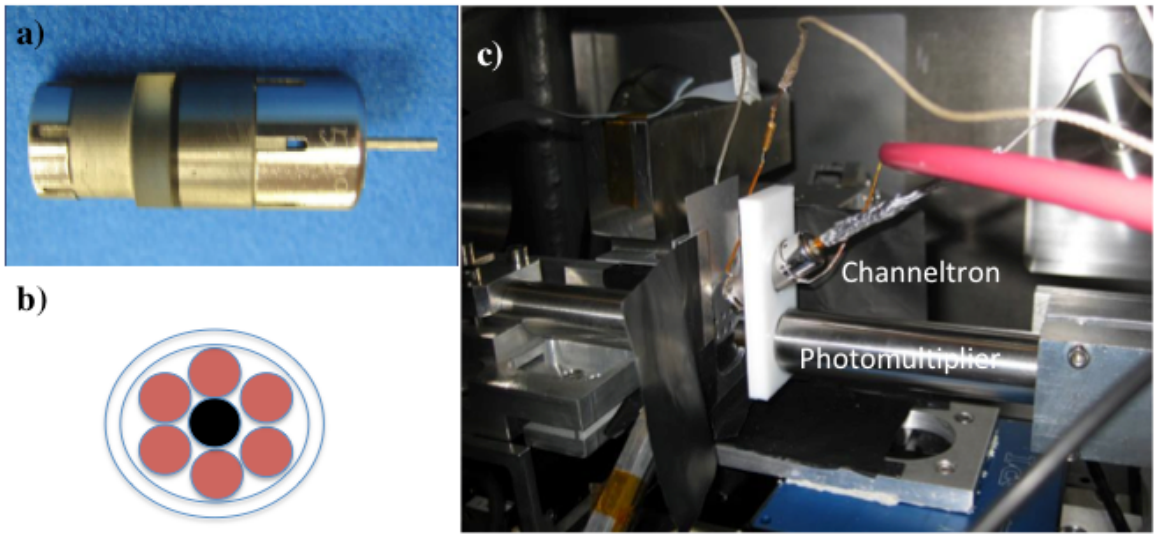

Figure 4.9 (a) Image of a Photonis 5901 Magnum detector; (b) cross section view of the channeltron; (c) channeltron mount over the PMT detector at the STXM chamber at SM beamline 10ID-1 located at the Canadian Light Source (CLS), Saskatoon, Saskatchewan.

The maximum working pressure for this channeltron is about 7×10^{-4} torr. This pressure could be obtained at the current generation of the STXM at the CLS and was the reason to use this detector for the data acquisition as the minimum pressure achieved in this STXM chamber was 5×10^{-5} torr. At the CLS, for verification of the function of TEY-STXM, we chose simpler model samples than LB films including thin patterned metal sample of Cr/Fe (this sample is conductive and produces more electrons) as well as the phase segregated copolymer blends of polystyrene (PS) and polymethylmethacrylate (PMMA). The data for these samples were obtained by this channeltron. For the TEY-STXM experiments performed on Cr/Fe metal sample, Dr. Stephen G. Urquhart and Dr. Jian Wang helped with the setup of the experiments and I did the data analysis.

The electrical wiring of this channeltron is presented in **Figure 4.10**. In the experiments performed with this channeltron, a potential gradient was applied through the channeltron. The cone was typically biased to + (0-100) V, and middle part of the channeltron was biased to 2.4-2.5 kV and the tail to 2.5-2.6 kV, depending on the channeltron's operating conditions. The potential gradient between the tail and the central part was established by a Z-diode. The channeltron pulses were passed to an Ortec VT120C pre-amplifier, further amplified before passing through an Ortec 9307

discriminator. The shape of the pulses was checked by an oscilloscope, and finally the signal was monitored by the computer.

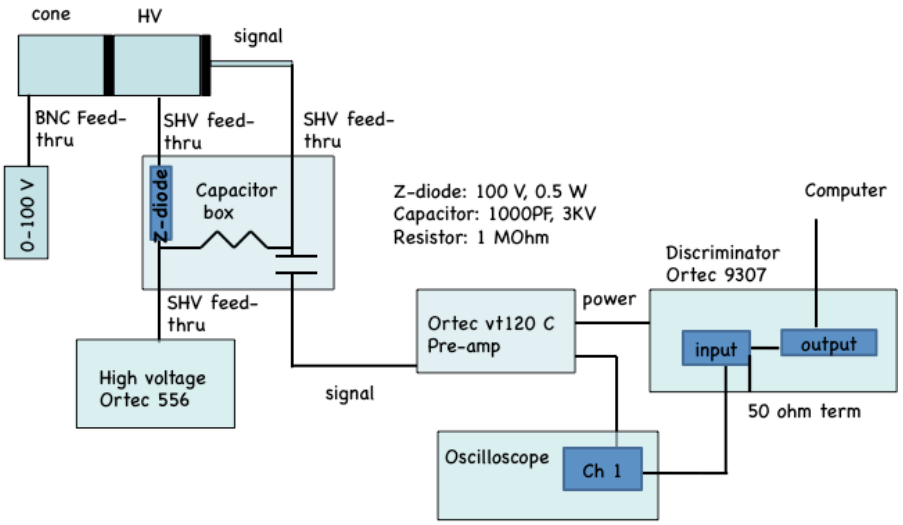

Figure 4.10 Schematic diagram of the channeltron wiring used at SM beamline 10ID-1 located at the Canadian Light Source (CLS), Saskatoon, Saskatchewan.

As it is desired to count as many electrons ejected from the surface of the sample as possible, the channeltron should be very close to the surface of the sample. In both of these channeltrons, the position of the channeltron with respect to the surface of the sample is a challenge. Therefore for decreasing this distance and increasing the signal level, a Micro-Channel Plate (MCP) with a central hole was also explored. This geometry allowed the MCP to be slid onto the PMT detector tube providing a minimal distance with respect to the sample surface. **Figure 4.11(a)** shows the comparison between the distance of the sample and channeltron (~ 3 mm), and of the MCP (< 3 mm) which shows the MCP is closer to the sample. **Figure 4.11(b)** represents the MCP mount over the photon detector.

The MCP itself consists of an array of tiny glass tubes, each acting as a mini channeltron that are fused together to form a thin disk.

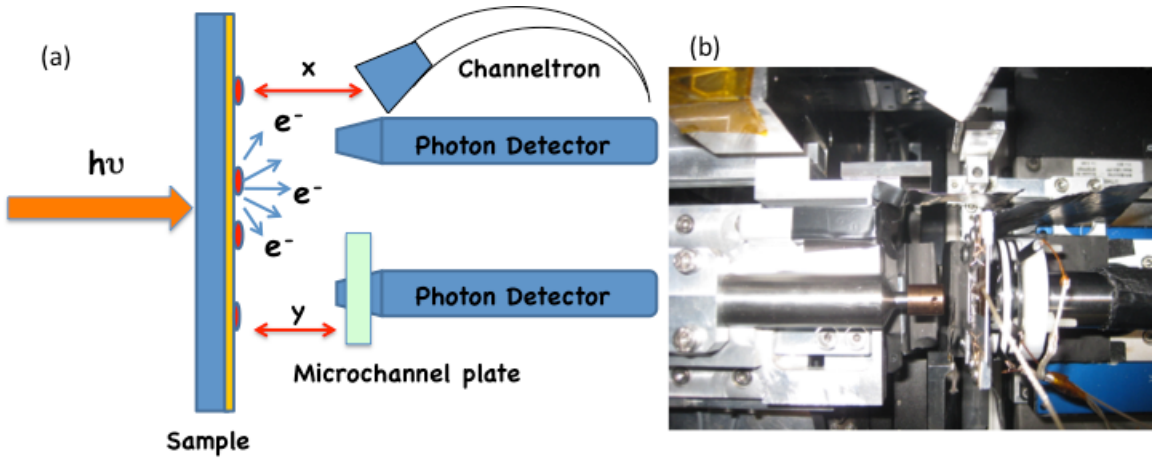

Figure 4.11 (a) Schematic diagram of the comparison between the distance of the channeltron to the sample surface and of the MCP; (b) MCP mount over the PMT detector at the STXM chamber at SM beamline 10ID-1 located at the Canadian Light Source (CLS), Saskatoon, Saskatchewan.

Metal coating used on both faces of disc provides electrical connections. The electrical wiring for this channelplate is the same as the one used for Photonis 5901 Magnum channeltron presented in **Figure 4.10**.

4.4 Results and Discussion

The performance of the developed TEY-STXM was verified by the phase separated LB film of 2AA:1PA deposited over the Si_3N_4 window at beamline 11.0.2 located at the Advanced Light Source, Berkeley California. This sample was chosen to show the monolayer sensitivity of TEY detection mode relative to transmission detection, as the thin layer of the sample (~20 Å) makes it difficult to be studied in transmission mode of detection.

Figure 4.12 presents the sample current TEY and simultaneous transmission images of the LB film of 2AA:1PA sample collected at 288.4 eV corresponding to carbon 1s → σ*(C-H) transition. The sample current image has higher contrast than the transmission image, showing the enhanced surface sensitivity of TEY measurement. In previous studies of this sample, the continuous regions are assigned to be PA-rich, and the discontinuous regions to be AA-rich.[4.28] By considering the structure of AA ($C_{19}H_{39}COOH$) regions compared to the PA ($C_{13}F_{27}COOH$) regions, it is expected that at this imaging energy the discontinuous regions (AA) appear brighter in TEY mode and

consequently darker in transmission mode, as they are more absorbing and consequently more electrons are ejected from these regions.

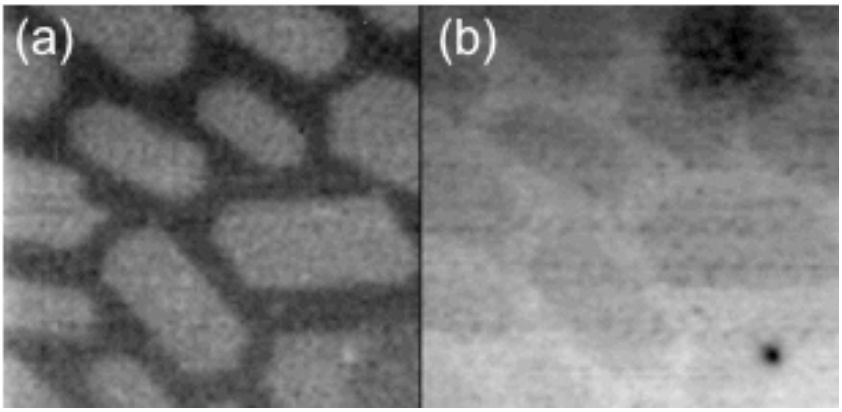

Figure 4.12 STXM images of the phase separated 2AA:1PA LB film (images 10 μm wide) at 288.4 eV corresponding to carbon 1s → σ*(C-H) transition in (a) total sample current detection, and (b) transmission detection mode. [Reprinted with permission from Behyan, S.; Haines, B.; Karanukaran, C.; Wang, J.; Obst, M.; Tyliszczak, T.; Urquhart, S. G., Surface Detection in a STXM Microscope. In 10th International Conference on X-ray Microscopy, Chicago, IL, Aug 15-20; Chicago, IL, 2010; 184-187, Copyright 2011, American Institute of Physics.]

While these results were promising, no meaningful spectrum could be obtained at the carbon edge for this sample, and the spectra collected using sample current were overwhelmed by contamination of electrons from the order sorting aperture and the zone plate. This TEY photocurrent from the zone plate focus in the STXM microscope is near the limit of the sensitivity of the low-current amplifier, and this signal is very prone to ground loops and induction from the STXM stage motion. A further drawback to the sample current method for TEY, is that the weak signal requires a longer dwell time. This longer dwell time in turn leads to increased radiation damage and more importantly, it leads to increased rate of photodeposition. Photodeposition poses a challenge for observing surface phenomena in non-ideal vacuum environments. Overall our experience was that the sample current TEY measurements were unreliable. Two simple methods to minimize photodeposition are to selectively remove the hydrocarbons with a cold finger and to minimize the time that the beam is on the sample by increasing detection efficiency. Electron counting allows for images and spectra to be obtained in a fraction of time to that required for sample current TEY. In addition to minimizing the photodeposition, a short dwell time also leads to less radiation damage.

In contrast to the weak and artifact prone sample current signal, single electron counting method using a channeltron was promising for acquiring surface sensitive NEXAFS spectra. This method is presented in **Figure 4.6**, the sample surface is mounted facing away from the zone plate, and the channeltron is mounted downstream of the sample. In this approach, the sample holder shields the channeltron from stray electrons generated by the OSA and the zone plate. TEY-NEXAFS spectra of LB domains obtained with the channeltron are presented in **Figure 4.13**. Each spectrum was obtained by dividing the TEY signal to the transmission signal for normalization because in TEY measurements the transmitted signal acts as I_0 signal. This normalization method has been used for all TEY-STXM NEXAFS spectra acquired in this chapter.

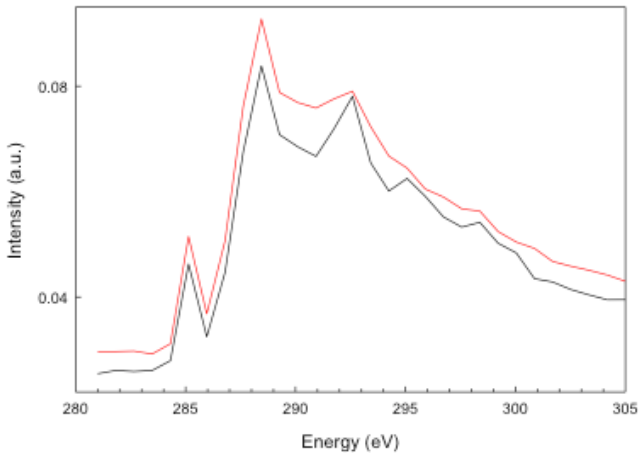

Figure 4.13 NEXAFS spectra obtained from image sequences; black spectrum is from the continuous regions of the 2AA:1PA (PA rich), and the red spectrum is extracted from the discontinuous regions (AA rich). These spectra are dominated by photodeposition. Both spectra are normalized vs. the transmission spectra.

In the LB monolayer film of 2AA:1PA sample, spectra were extracted from both the continuous (PA rich; solid line) and the discontinuous (AA rich; red line) regions**.** Peaks are observed at 285.1 eV, 288.4 eV and 292.6 eV in both spectra. The 285.1 eV peak (carbon 1s → π*(C=C)) is attributed to carbon photodeposition and radiation damage as there are no carbon-carbon double bonds in the LB films, and the peak at 292.6 eV is assigned to the carbon 1s → σ*(C-F) transition characteristic of PA.[4.28] The spectra show that the discontinuous regions have a weaker carbon 1s → σ*(C-F) signal than the continuous regions. This is consistent with the continuous regions being

primarily PA and the discontinuous regions being primarily AA. There is some mixing of the phases and this accounts for the C-F peak at 292.6 eV for discontinuous regions.

While we see some spectroscopic differentiation between the fluorinated PA and the protonated AA domains at 292.6 eV, these spectra are dominated by photodeposition at 285.1 eV and 288.4 eV. Photodeposition can dominate and significantly distort the TEY-NEXAFS spectra.[4.27]

These results showed that TEY-STXM is possible with appropriate modifications to the STXM microscopes, but also has its own challenges. In summary, the spectra collected using sample current TEY were unusable due to the combination of electrons from the OSA and the zone plate, noise, as well as the photodeposition from long dwell times. Spectra collected using single electron counting did not suffer significantly from stray electrons, but had significant artifacts from photodeposition.

After the satisfactory first TEY-STXM results at the Advanced Light Source (ALS), the TEY-STXM was developed at the SM beamline 10ID-1 located at the CLS, Saskatoon, Saskatchewan. To increase the TEY signal level compared to the previous TEY results, the Photonis 5901 Magnum detector was used with the maximum working pressure of 7×10^{-4} torr. In these experiments however we used a simpler model sample rather than LB films for optimizing a challenging TEY experiment. A patterned Cr/Fe metal sample was used to verify the function of this setup (described in **§4.2.2**) at the CLS, illustrated in **Figure 4.14**.

This sample was simpler as it provided higher signal than LB films (it was metallic and conductive and produced more electrons) and it had larger features relative to the micron size domains in 1AA: 2PA sample.

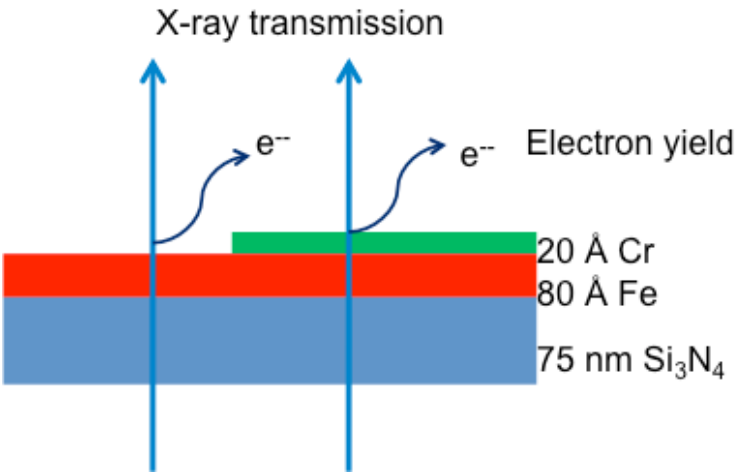

Figure 4.14 Schematic diagram of the patterned metal Fe/Cr sample.[4.27][Reprinted with permission from Behyan, S.; Haines, B.; Karanukaran, C.; Wang, J.; Obst, M.; Tyliszczak, T.; Urquhart, S. G., Surface Detection in a STXM Microscope. In 10th International Conference on X-ray Microscopy, Chicago, IL, Aug 15-20; Chicago, IL, 2010; 184-187, Copyright 2011, American Institute of Physics.]

The transmission and electron counting TEY images of the patterned metal sample at the energy of the Cr $2p_{3/2} \rightarrow$ 3d transition at 577.9 eV are presented in the **Figure 4.15(a)**.

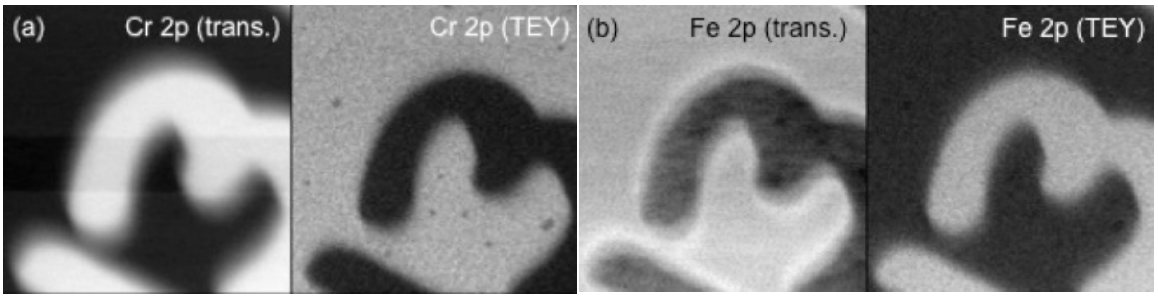

Figure 4.15 (a) Transmission image (left panel) and electron counting TEY-STXM image (right panel) of the patterned metal sample acquired at Cr $2p_{3/2} \rightarrow$ 3d transition at 577.9 eV. The area with the character "3" is the bare Fe film; (b) transmission image (left panel) and electron counting TEY-STXM image (right panel) of the same area acquired at Fe $2p_{3/2} \rightarrow$ 3d transition at 710.0 eV. Images are 50 μm wide. [Reprinted with permission from Behyan, S.; Haines, B.; Karanukaran, C.; Wang, J.; Obst, M.; Tyliszczak, T.; Urquhart, S. G., Surface Detection in a STXM Microscope. In 10th International Conference on X-ray Microscopy, Chicago, IL, Aug 15-20; Chicago, IL, 2010; 184-187, Copyright 2011, American Institute of Physics.]

The Cr overlayer (e.g. outside the character "3") is darker in the transmission image than the bare Fe film. In TEY mode images, the contrast is reversed: the Cr surface area is brighter as this area emits more photoelectrons, exhibiting surface sensitivity.

Figure 4.15(b) represents transmission (left) and TEY (right) images of the same area, but at the Fe $2p_{3/2}$ → 3d energy. The contrast is reversed relative to the images at the Cr $2p_{3/2}$ → 3d energy. Here the Cr/Fe area at the Fe 2p edge is expected to be darker than the bare Fe region in transmission mode (**Figure 4.15(b)** left panel), but it is reversed. We expect that the Cr/Fe area will be darker than the Fe area in all images, as the Cr/Fe film is thicker than the bare Fe film. However, in the transmission image recorded at the 710.0 eV, the Fe film area (e.g. the letter "3") is in fact darker than the thicker Cr/Fe area. This contrast is due to the different oxidation state of the Fe in these two regions and therefore different absorption at this energy (710.0 eV), which is also confirmed by the transmission spectra presented in **Figure 4.16**. In these spectra the transmission data are presented as pseudo optical density, e.g. -ln (transmission data); this was done because of the lack of I_0 signal for normalization of transmission data in this experiment.

The bare-Fe region has a higher absorption compared to the thicker Cr/Fe bilayer at 710.0 eV due to the surface oxidation. Therefore, the oxidized Fe is absorbing more than the covered Fe area; this is the reason for this observed contrast in the image recorded at 710.0 eV.

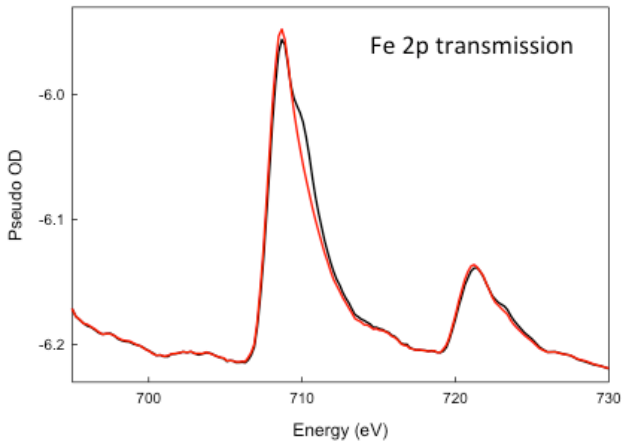

Figure 4.16 Overplot of Fe 2p edge spectra obtained from the image sequences of the patterned metal film: bare Fe (black line), and Fe with Cr overlayer (red line) in transmission mode. The transmission data are pseudo optical density, e.g. -ln (transmission data).

Figure 4.17 shows the overplot of the electron counting TEY spectra obtained from the Cr overlayer and bare Fe regions at Cr 2p and Fe 2p edges.

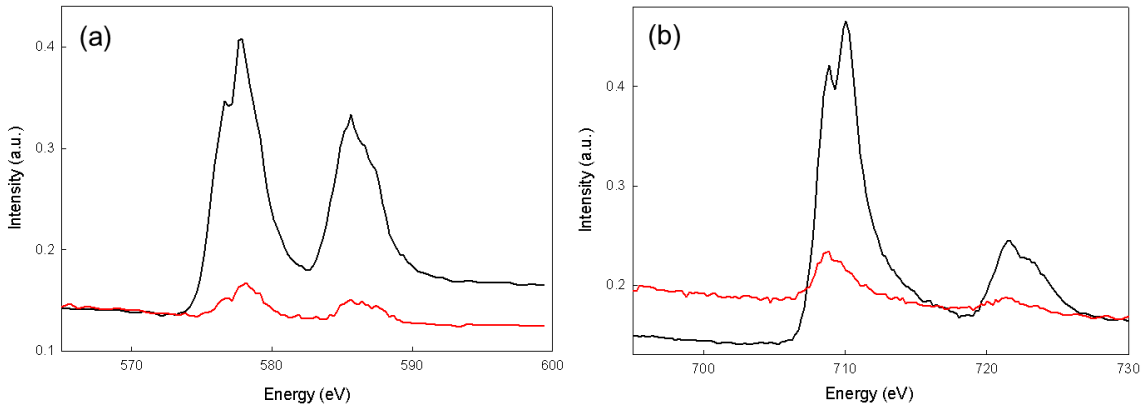

Figure 4.17 (a) Overplot of TEY Cr 2p edge spectra obtained from the image sequences of **Figure 4.15(a)** of Cr overlayer (black line), and Fe regions (red line). Both spectra are normalized vs. the transmission spectra; (b) Overplot of TEY Fe 2p edge spectra obtained from the image sequences of **Figure 4.15(b)** of bare Fe (black line), and Fe with Cr overlayer (red line). Both spectra are normalized vs. the transmission spectra.

The black line in **Figure 4.17(a)** the Cr 2p spectrum is obtained from the Cr overlayer region. The red line represents the Cr spectrum for the bare Fe region at Cr 2p edge. The Cr region spectrum shows splitting of each of the Cr $2p_{3/2}$ and Cr $2p_{1/2}$ peaks which based on the literature is due to the oxidation of the Cr overlayer.[4.34] The existence of a weak Cr 2p spectrum in the bare Fe region is attributed to the Cr impurities in the sample (in sample preparation during the evapouration of Cr, some Cr might have diffused over the Fe area because the TEM grid (acting as a mask) may not be perfectly attached on the sample).

Figure 4.17(b) is the overplot of the electron counting TEY Fe 2p spectra of the bare Fe (black line) and Fe region covered with Cr layer (red line). From the spectra it can be observed that the TEY signal from the bare Fe region has two splitting in each peak ($2p_{3/2}$, and $2p_{1/2}$) compared to the Fe covered with Cr layer. This shows the oxidation of the bare Fe compared to the Cr covered Fe area after 3 months of ages. The difference in the energy of the splitting in $2p_{3/2}$ peak is about 1.11 eV, close to 1.2 eV that is attributed to iron oxide in the form of γ-Fe_2O_3.[4.35] The intensity of the Fe 2p spectrum extracted from the Fe region is stronger than Fe 2p spectrum from Fe area covered by Cr.

This effect shows the surface sensitivity of the TEY-STXM. Photodeposition may be less of an issue in these NEXAFS spectra, as a slightly defocused X-ray spot was used. Overall, these results show the enhanced surface sensitivity of TEY-STXM detection.

Although, surface sensitive measurements were obtained on thin metal samples, satisfactory TEY-STXM results could not be obtained at the carbon 1s edge on organic samples. This was because of the rapid rate of photodeposition of the high level of organics, as well as the distant position of the channeltron compared to the sample surface resulting in a low signal level (see **Figure 4.11(a)**). Therefore, for decreasing the level of carbon photodeposition, the liquid nitrogen cold finger was placed very close to the sample at the front side of the STXM chamber; for increasing the signal level and minimizing the distance of the channeltron compared to the sample surface, a MCP was used that slid over the transmission detector (see **Figure 4.11(a)** and (**b)**). The use of the channelplate placed the TEY detector closer to the sample surface than the previous channeltron geometry (described in **§4.3.3**).

The function of the MCP was then tested on the Fe/Cr patterned metal sample in both transmission and TEY detection modes. **Figure 4.18** presents the transmission and TEY images of the sample at Cr 2p edge. The results obtained are similar to the previous results obtained with the channeltron.

In this experiment, even with a smaller distance between the MCP and the sample surface, there was not any improvement in the signal level. It was also not possible to do spectroscopy at the carbon 1s edge.

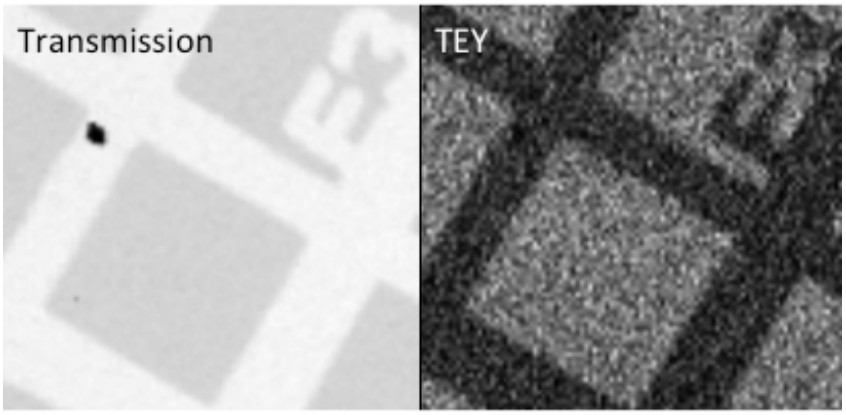

Figure 4.18 Transmission image (left panel) and electron counting TEY-STXM image (right panel) of patterned Fe/Cr metal sample on Si_3N_4 window at Cr 2p edge at 577.4 eV. Images are 100 μm wide.

With the poor vacuum in the current STXM chamber at the CLS, we elected to use the Photonis 5901 Magnum detector over the MCP as the working pressure of the MCP was 2×10^{-6} torr compared to the Photonis 5901 Magnum detector that was 7×10^{-4} torr.

To increase the signal level in TEY mode, a different wiring was used (see **Figure 4.10**). A cold finger was also mounted inside the chamber, close to the sample and OSA, in front side of the STXM chamber for an improvement in decreasing the rate of carbon photodeposition.

This new channeltron bias setup was tested on PS/PMMA samples. **Figure 4.19** shows the STXM images of this sample in transmission and TEY modes. Based on previous studies of this sample, the continuous regions are PS-rich, while the discontinuous regions are PMMA-rich regions.[4.36]

Figure 4.19(a) obtained at the energy of the carbon 1s → π*(C=C) transition at 285.1 eV in transmission and TEY modes, is in agreement with the previous results for this sample.[4.36] In transmission mode, the continuous PS areas are darker than the non-continuous PMMA domains, as more X-rays are absorbed at this excitation energy. In TEY mode in contrast this area is lighter, indicating more electrons are emitted from PS and the PMMA domains are darker. **Figure 4.19(b)** is obtained at the carbon 1s → π*(C=O) transition at 288.3 eV of PMMA. The image contrast is reversed. The PMMA domains are darker in transmission and brighter in TEY mode.

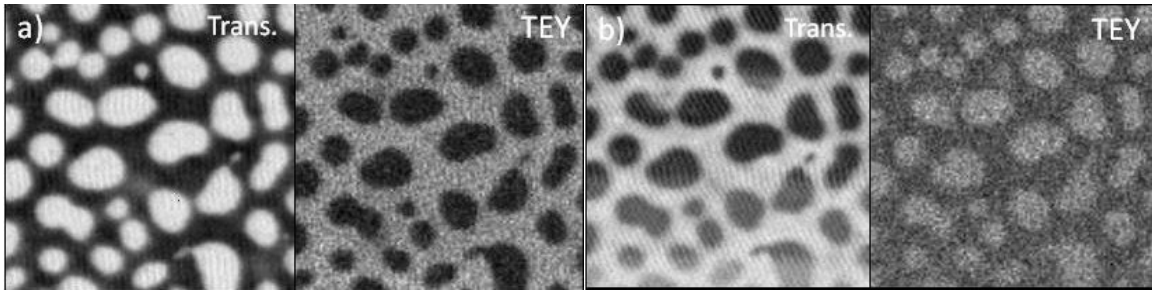

Figure 4.19 (a) Transmission image and electron counting TEY-STXM images of the PS/PMMA sample acquired at carbon 1s → π* (C=C) transition at 285.1 eV of PS; (b) image of the same area at carbon 1s → π*(C=O) transition at 288.3 eV of PMMA. Images are 6 μm wide.

TEY-NEXAFS spectra of PS (black line) and PMMA (red line) are shown in **Figure 4.20**. The PS spectrum is dominated by the transition of the carbon 1s → π*(C=C) at 285.1 eV and the PMMA is dominated by an intense peak at 288.3 eV of carbon 1s → π*(C=O) transition. A small peak at 283.9 eV in both spectra, as well as the peak at 285.1 eV in PMMA spectrum (carbon 1s → π*(C=C)) is attributed to the photodeposition.

The higher surface sensitivity of TEY measurements compared to transmission detection is obvious in **Figure 4.21** on a different area of the PS/PMMA sample imaged at the carbon 1s → π*(C=C) transition energy. There are some dark domains in TEY image that cannot be observed in transmission mode. This is due to surface contamination on some parts of the sample and because of the thin layer could not be detected in transmission mode.

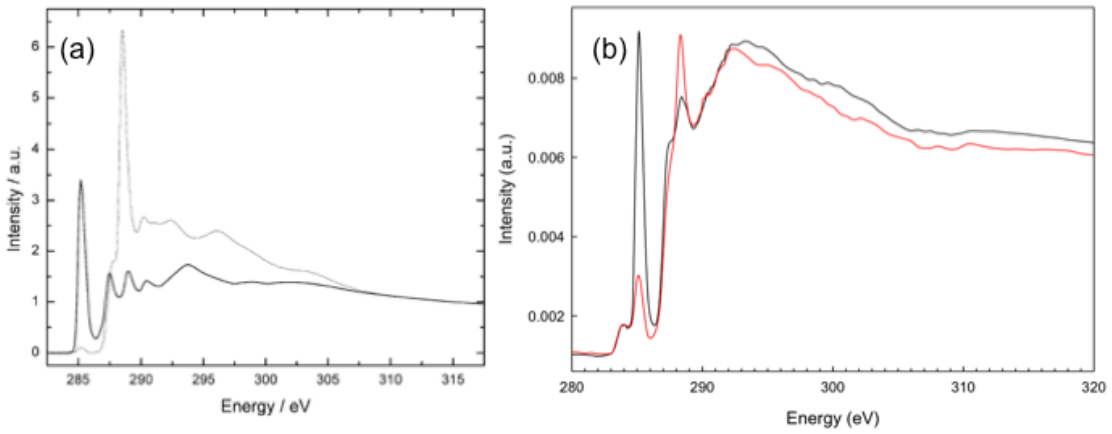

Figure 4.20 (a) TEY-NEXAFS spectra of PS (thick line) and PMMA (thin line) used as reference spectra;[4.37] (b) TEY-NEXAFS spectra extracted from the discontinuous regions of the PMMA/PS (red line; PMMA) and from the continuous regions (black line; PS). Both spectra are normalized vs. the transmission spectra (transmission spectra act as I_0 signal in TEY measurments). These spectra are dominated by photodeposition at 283.9 eV.

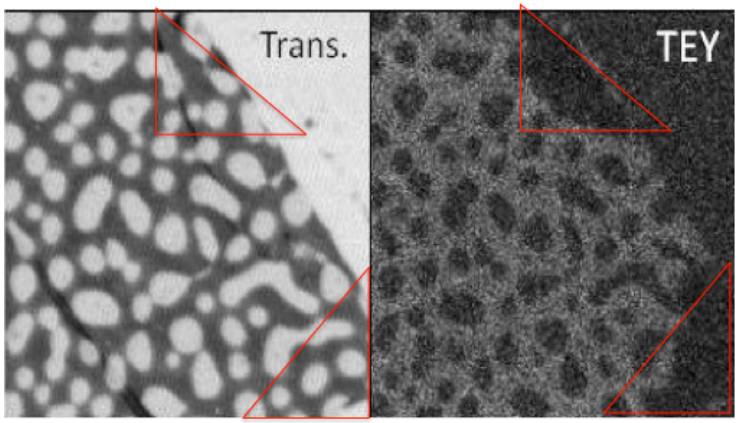

Figure 4.21 Transmission image and electron counting TEY-STXM image of the PS/PMMA sample acquired at carbon 1s → π*(C=C) transition at 285.1 eV of PS, images are 10 μm wide. The red triangles show the areas with surface contamination.

4.5 Conclusion

With simple modifications to the existing STXM microscopes, it is possible to conduct electron counting TEY experiments. This mode of detection allows for surface systems such as LB films, PS/PMMA polymer blends, and thin metal samples to be effectively studied using STXM where they would be poorly suited in transmission mode. Recently this setup has been also implemented at the Swiss Light Source and its performance had been promising in thicker organic films.[4.38]

In our studies, TEY-STXM was shown to be capable of differentiating between the oxidation states of the thin oxide layers in thin Cr/Fe samples, as well as showing higher surface sensitivity in imaging of the organic samples. However, the carbon 1s spectra obtained for organic samples were dominated by carbon photodeposition.

The challenges that remain in single electron counting in the existing generation of STXMs are the low count rate of the electrons by channeltron and the rate of carbon photodeposition. The lifetime of the channeltron is also another important issue that mostly depends upon the vacuum environment. These challenges are expected to be solved by improving the vacuum system in the next generation of UHV STXMs.

4.6 References

4.1. Rightor, E. G.; Urquhart, S. G.; Hitchcock, A. P.; Ade, H.; Smith, A. P.; Mitchell, G. E.; Priester, R. D.; Aneja, A.; Appel, G.; Wilkes, G.; Lidy, W. E., *Macromolecules,* **2002,** *35* (15), 5873-5882.

4.2. Urquhart, S. G.; Smith, A. P.; Ade, H. W.; Hitchcock, A. P.; Rightor, E. G.; Lidy, W., *Journal of Physical Chemistry B,* **1999,** *103* (22), 4603-4610.

4.3. Hitchcock, A. P.; Koprinarov, I.; Tyliszczak, T.; Rightor, E. G.; Mitchell, G. E.; Dineen, M. T.; Hayes, F.; Lidy, W.; Priester, R. D.; Urquhart, S. G.; Smith, A. P.; Ade, H., *Ultramicroscopy,* **2001,** *88*, 33-49.

4.4. Mitchell, G. E.; Wilson, L. R.; Dineen, M. T.; Urquhart, S. G.; Hayes, F.; Rightor, E. G.; Hitchcock, A. P.; Ade, H., *Macromolecules,* **2002,** *35* (4), 1336-1341.

4.5. Fu, J.; Urquhart, S. G., *Langmuir,* **2007,** *23*, 2615-2622.

4.6. Takekoh, R.; Okubo, M.; Araki, T.; Stover, H. D. H.; Hitchcock, A. P., *Macromolecules,* **2005,** *38* (2), 542-551.

4.7. Dynes, J. J.; Tyliszczak, T.; Araki, T.; Lawrence, J. R.; Swerhone, G. D. W.; Leppard, G. G.; Hitchcock, A. P., *Environmental Science and Technology,* **2006,** *40*, 1556-1565.

4.8. Brown, G. E., Jr.; Benzerara, K.; Yoon, T. H.; Ha, J.; Cordova, C. D.; Spormann, A. M.; Tyliszczak, T.; Tanwar, K. S.; Trainor, T. P.; P.J. Eng; Kendelwicz, T.; Yamamoto, S.; Bluhm, H.; Ketteler, G.; Salmeron, M.; Nilsson, A., *Geochimica et Cosmochimica Acta,* **2006,** *70*, A69.

4.9. Van Waeyenberge, B.; Puzic, A.; Stoll, H.; Chou, K. W.; Tyliszczak, T.; Hertel, R.; Fähnle, M.; Brückl, H.; Rott, K.; Reiss, G.; Neudecker, I.; Weiss, D.; Back, C. H.; Schütz, G., *Nature,* **2006,** *444*, 461-464.

4.10. Acremann, Y.; Strachan, J. P.; Chembrolu, V.; Andrews, S. D.; Tyliszczak, T.; Katine, J. A.; Carey, M. J.; Clemens, B. M.; Siegmann, H. C.; Stohr, J., *Physical Review Letters,* **2006,** *96* (21).

4.11. Jacobsen, C.; Wirick, S.; Flynn, G.; Zimba, C., *Journal of Microscopy,* **2000,** *197* (2), 173-184.

4.12. Cooney, R. R.; Urquhart, S. G., *Journal of Physical Chemistry B,* **2004,** *108* (47), 18185-18191.

4.13. Hitchcock, A. P., *Journal of the American Chemical Society,* **1983,** *105* (16), 5525-5526.

4.14. Fu, J.; Urquhart, S. G., *Journal of Physical Chemistry A,* **2005,** *109* (51), 11724-11732.

4.15. Lam, K. P.; Hitchcock, A. P.; Obst, M.; Lawrence, J. R.; Swerhone, G. D. W.; Leppard, G. G.; Tyliszczak, T.; Karunakaran, C.; Wang, J.; Kaznatcheev, K.; Bazylinski, D. A.; Lins, U., *Chemical Geology,* **2010,** *270* (1-4), 110-116.

4.16. Urquhart, S. G.; Lanke, U. D.; Fu, J. X., *International Journal of Nanotechnology,* **2008,** *5* (9-12), 1138-1170.

4.17. Stöhr, J., *NEXAFS Spectroscopy*, Springer-Verlag, Berlin, **1992**.

4.18. Urquhart, S. G.; Ade, H., *Journal of Physical Chemistry B,* **2002,** *106*, 8531-8538.

4.19. Cooney, R.; Urquhart, S., *Journal of Physical Chemistry B,* **2004,** *108*, 18185-18191.

4.20. Hitchcock, A. P.; Mancini, D. C., *Journal of Electron Spectroscopy and Related Phenomena,* **1994,** *67* (1), 1-132.

4.21. Stöhr, J.; Outka, D. A., *Physical Review B,* **1987,** *36* (15), 7891-7905.
4.22. Urquhart, S. G.; Lanke, U. D.; Fu, J., *International Journal of Nanotechnology,* **2008,** *5*, 1138.
4.23. Nilsson, H. J.; Tyliszczak, T.; Wilson, R. E.; Werme, L.; Shuh, D. K., *Analytical and Bioanalytical Chemistry,* **2005,** *383* (1), 41-47.
4.24. Rightor, E. G.; Hitchcock, A. P.; Ade, H.; Leapman, R. D.; Urquhart, S. G.; Smith, A. P.; Mitchell, G.; Fischer, D.; Shin, H. J.; Warwick, T., *Journal of Physical Chemistry B,* **1997,** *101*, 1950-1960.
4.25. Obst, M.; Dynes, J. J.; Lawrence, J. R.; Swerhone, G. D. W.; Benzerara, K.; Karunakaran, C.; Kaznatcheev, K.; Tyliszczak, T.; Hitchcock, A. P., *Geochimica et Cosmochimica Acta,* **2009,** *73* (14), 4180-4198.
4.26. Wang, J.; Morin, C.; Li, L.; Hitchcock, A. P.; Scholl, A.; Doran, A., *Journal of Electron Spectroscopy and Related Phenomena,* **2008,** *in press*.
4.27. Behyan, S.; Haines, B.; Karanukaran, C.; Wang, J.; Obst, M.; Tyliszczak, T.; Urquhart, S. G., *Surface Detection in a STXM Microscope*. In *10th International Conference on X-ray Microscopy*, Chicago, IL, Aug 15-20; Chicago, IL, **2010**; 184-187.
4.28. Christensen, S.; Lanke, U. D.; Haines, B.; Qaqish, S. E.; Paige, M. F.; Urquhart, S. G., *Journal of Electron Spectroscopy and Related Phenomena,* **2008,** *162*, 107-114.
4.29. Bluhm, H.; Andersson, K.; Araki, T.; Benzerara, K.; Brown, G. E.; Dynes, J. J.; Ghosal, S.; Gilles, M. K.; Hansen, H. C.; Hemminger, J. C.; Hitchcock, A. P.; Ketteler, G.; Kilcoyne, A. L. D.; Kneedler, E.; Lawrence, J. R.; Leppard, G. G.; Majzlam, J.; Mun, B. S.; Myneni, S. C. B.; Nilsson, A.; Ogasawara, H.; Ogletree, D. F.; Pecher, K.; Salmeron, M.; Shuh, D. K.; Tonner, B.; Tyliszczak, T.; Warwick, T.; Yoon, T. H., *Journal of Electron Spectroscopy and Related Phenomena,* **2006,** *150* (2-3), 86-104.
4.30. Kaznatcheev, K. V.; Karunakaran, C.; Lanke, U. D.; Urquhart, S. G.; Obst, M.; Hitchcock, A. P., *Nuclear Instruments & Methods in Physics Research Section a-Accelerators Spectrometers Detectors and Associated Equipment,* **2007,** *582* (1), 96-99.
4.31. Covelli, D. *X-ray Microscopy of Hydrocarbon-Clay Interactions*, M.Sc. thesis, University of Saskatchewan, Saskatoon, **2007**.
4.32. Covelli, D.; Hernandez-Cruz, D.; Haines, B. M.; Munoz, V.; Omotoso, O.; Mikula, R.; Urquhart, S., *Journal of Electron Spectroscopy and Related Phenomena,* **2009,** *173* (1), 1-6.
4.33. Haines, B.; Behyan, S.; Christensen, S. L.; Obst, M.; Bertwistle, D.; Karunakaran, C.; Tyliszczak, T.; Urquhart, S. G., *Canadian Light Source, Activity Report No. 2008*, **2008**, p 154.
4.34. Figueiredo, M. O.; Dossantos, A. C.; Carmezim, M. J.; Abbate, M.; Degroot, F. M. F.; Petersen, H.; Braun, W., *Analyst,* **1994,** *119*, 609-611.
4.35. Otero, E.; Shipman, P. O.; Abd-El-Aziz, A. S.; Urquhart, S. G., *Macromolecules,* **2008,** *41* (24), 9532-9541.
4.36. Morin, C., Ikeura-Sekiguchi, H., Tyliszczak, T., Cornelius, R., Brash, J. L., Hitchcock, A. P., Scholl, A., Nolting, F., Appel, G., Winesett, D. A., Kaznacheyev, K., Ade, H., *Journal of Electron Spectroscopy and Related Phenomena,* **2001,** *121*, 203-224.
4.37. Harris, M.; Appel, G.; Ade, H., *Macromolecules,* **2003,** *36* (9), 3307-3314.
4.38. Hub, C.; Wenzel, S.; Raabe, J.; Ade, H.; Fink, R. H., *Review of Scientific Instruments,* **2010,** *81* (3).

CHAPTER 5 SULPHUR 1S NEAR EDGE X-RAY ABSORPTION FINE STRUCTURE (NEXAFS) OF THIOL AND THIOETHER COMPOUNDS

5.1 Description

This chapter is a literal copy of a paper published in the Journal of Chemical Physics. This contribution explores the sulphur 1s NEXAFS of simple thiol and thioether compounds in the gas phase. Sulphur 1s NEXAFS spectroscopy is used as a qualitative and quantitative technique for the speciation of sulphur compounds in different areas such as biology and fossil fuel studies. For this purpose we require a firm understanding of the sulphur 1s NEXAFS spectra. This chapter provides the study of the sulphur 1s NEXAFS spectra of simple thiols and thioethers in gas phase, where the spectra are free from charging effects in total electron yield, saturation effects in florescence yield, and the solid-state broadening problems usually encountered in condensed phases. These highly resolved spectra are further analyzed by the aid of *ab initio* calculations for spectral assignments. The experimental spectra showed the fine features predicated by the calculations. The experimental and theoretical work for this study is provided in the following sections under the form of the manuscript published in the Journal of Chemical Physics. [Reprinted with permission from Behyan, S.; Hu, Y. F.; Urquhart, S. G., Journal of Chemical Physics, 134, 244304, 2011. Copyright 2011, AIP Publishing LLC.]

5.2 Description of the Candidate's Contribution

For this contribution I was the primary investigator in terms of sample preparation, acquisition of experimental data, the simulation of NEXAFS spectra by IVO *ab initio* calculations, the interpretation of the results, and writing of the manuscript. Dr Stephen G. Urquhart greatly helped in writing and editing of this document and provided

extensive guidance throughout the performance of the experiments, data analysis, interpretation of data, and simulations. Dr. Yongfeng Hu installed the gas cells at the CLS and helped in acquiring the experimental spectra. Dr. Stephen Urquhart and Dr. Yongfeng Hu kindly gave me their permission for including this paper in this thesis, and agreed on my contribution in this document.

5.3 Relation of Contribution towards Research Objectives

This contribution was solely performed towards the objective of the thesis research. This study was intended to be a part of the main research objective, which is the study of the sulphur 1s NEXAFS spectroscopy of different sulphur functionalities. Therefore, this contribution is one of the studied sulphur functionalities. We started our study by simple thiol and thioether compounds and examined the reliability of the IVO *ab initio* calculations to simulate the NEXAFS spectra for spectral assignments in this document.

Beside the experimental and computational sections provided in this manuscript, detailed descriptions of these sections are also provided in **Chapter 2** and **3** respectively. A full discussion of the results as part of the whole study of sulphur 1s NEXAFS spectra of different sulphur functionalities is provided in **Chapter 9**.

5.4 Sulphur 1s Near Edge X-ray Absorption Fine Structure (NEXAFS) of Thiol and Thioether Compounds

Shirin Behyan[1], Yongfeng Hu[2], Stephen G. Urquhart[1]*

1. Department of Chemistry, University of Saskatchewan, Saskatoon, SK, Canada S7N 5C9

2. Canadian Light Source, University of Saskatchewan, Saskatoon, SK, Canada S7N 5C6

Abstract

The speciation and quantification of sulphur species based on sulphur K-edge x-ray absorption spectroscopy is of wide interest, particularly for biological and petroleum science. These tasks require a firm understanding of the sulphur 1s near edge x-ray absorption fine structure (NEXAFS) spectra of relevant species. To this end, we have

examined the gas phase sulphur 1s NEXAFS spectra of a group of simple thiol and thioether compounds. These high-resolution gas phase spectra are free of solid-state broadening, charging and saturation effects common in the NEXAFS spectra of solids. These experimental data have been further analyzed with the aid of improved virtual orbital (IVO) Hartree-Fock *ab initio* calculations. The experimental sulphur 1s NEXAFS spectra show fine features predicted by calculation, and the combination of experiment and calculation has been used to improve assignment of spectroscopic features relevant for the speciation and quantification of the sulphur compounds.

Corresponding Author, email: stephen.urquhart@usask.ca

5.4.1 Introduction

The refinement of analytical methods for sulphur speciation, particularly microanalytical methods, is of great interest for the study of energy and fuels, industrial processes and products, biological systems and other complex materials. NEXAFS spectroscopy is ideal for studying the form and quantity of sulphur species. In contrast, nuclear magnetic resonance (NMR) spectroscopy is relatively inefficient, as the NMR active isotope, ^{33}S, has a low natural abundance (0.76%) and its quadruple spin (I=3/2) leads to weak and broad signals.[5.1] Near edge x-ray absorption fine structure (NEXAFS) spectroscopy, at the sulphur 2p (162 eV) and the sulphur 1s (2472 eV) core edges, is frequently used for speciation and quantification of sulphur. For example, sulphur 1s NEXAFS has been used to determine the ratio of thiols to disulphides in biological systems; this difference affects the functionality of many proteins.[5.2] Deconvolution of complex sulphur 1s spectra has been also used for speciation in biological systems.[5.3-6] Sulphur speciation is also important in solid oxide fuel cells, where deactivation occurs as trace sulphur in fuels reacts with the nickel catalyst in the anodes.[5.7] One of the factors determining the fossil fuel quality is the quantity and form of sulphur compounds. As the combustion of these compounds produces sulphur dioxide and decreases the performance of catalytical converters, low sulphur fuel standards have been mandated. Sulphur 1s NEXAFS has been used for speciation and quantification of sulphur compounds in fossil fuel,[5.8-13] studies of the surface adsorption of thiols and thiolates,[5.14-18], and the sulphur chemistry of polymers[5.19, 5.20] and photographic materials.[5.21]

Developments in x-ray microprobe and zone plate microscopies allow for sulphur 1s NEXAFS spectra to be acquired from yet smaller sample volumes,[5.22-26] extending this spectroscopy as a microanalytical method. In sequence with the development of sulphur 1s NEXAFS spectroscopy capabilities at the Scanning Transmission X-ray Microscopy (STXM) at the Canadian Light Source (CLS)[5.27] and the potential for studies of sulphur in asphaltene species from the Canadian oil sands and lignite coal deposits in south-eastern Saskatchewan, we are exploring the basic interpretation of the sulphur 1s NEXAFS spectra.

In this paper, we focus on the simplest organosulphur species, thiols and thioethers, to provide a baseline for studies of complex sulphur species expected in asphaltenes. The sulphur 1s NEXAFS spectra of simple thiols and thioether compounds have been previously assigned by empirical comparisons[5.3, 5.6, 5.14, 5.28-32] and some recent calculations.[5.33-36]

There have been relatively few theoretical studies of sulphur 1s NEXAFS spectra of organosulphur compounds until relatively recently.[5.33-39] Nakamatsu *et al*. examined the sulphur 1s and sulphur 2p NEXAFS spectra of SF_6 and H_2S (relevant for considering S-H / thiol bonding) by discrete variational (DV)-Xα calculations and assigned spectroscopic features in terms of transitions to specific unoccupied molecular orbitals.[5.37] Sarangi *et al*. examined density functional theory (DFT) simulations of the sulphur 1s NEXAFS spectra of species that represent S-CH_3 and S-S bonding as well as the sulfite group, and observed chemical bonding effects in addition to anticipated oxidation state effects.[5.34] Mijovilovich *et al*. simulated the sulphur 1s NEXAFS spectra for sulphides and disulphides by DFT calculations, and showed that significant spectroscopic differences arise from sulphur-sulphur bonding and the nature of ligand groups attached to a sulphur atom (phenyl versus benzyl, etc).[5.33] Mijovilovich *et al*. have compared the experimental sulphur 1s NEXAFS spectra of dibenzothiophene, dibenzothiophene sulfone and DL-methionine to calculations at several different levels of DFT theory.[5.35] From the similar "white line" energy in the spectra of different molecules, the authors suggest that the "fingerprint" resolution of compounds will be difficult.[5.35]

Recently, the effect of solvation and co-ordination on sulphur 1s spectra have also been considered.[5.40] Risberg *et al*. studied the role of external interactions, such as

hydrogen bonding, deprotonation and complexation, on sulphur-containing amino acids and oxidation products by the transition potential DFT method.[5.36] This work demonstrates that spectroscopic models must reflect the chemical surroundings of the materials they seek to model. Damian *et al*. simulated the NEXAFS spectra of dimethyl sulfoxide (DMSO) in the solvated thallium (III), indium (III), gallium (III), and aluminum (III) solutions, and concluded that increased splitting of the sulphur 1s spectra is due to metal / oxygen orbital interactions between the coordinated DMSO ligand and the metal ion.[5.39] Other theoretical studies have addressed mineral, oxyanion and oxide forms of sulphur[5.40-44] and halogenated sulphur species.[5.38, 5.45, 5.46]

A common theme of this recent work is the great sensitivity of sulphur 1s spectroscopy to fine differences in structure, bonding and intermolecular interactions. This spectroscopic sensitivity variation is useful for analytical studies but also creates a substantial risk for chemical mis-assignment when poorly understood spectra are used, particularly when features from different chemical moieties appear in the same energy range.

This work examines simple compounds in the gas phase, and compares these to a wider range of *ab initio* calculations, from simple to complex species. Gas phase spectra are free of solid-state broadening, charging in the total electron yield detection of solids, and self-absorption present in fluorescent yield detection. We have examined the calculated sulphur 1s NEXAFS spectra from *ab initio* IVO calculations of thiols and thioethers of different complexities, such as simple thiols (hydrogen sulphide, methane thiol, and ethane thiol), a simple aromatic thiol (benzene thiol), simple aliphatic thioethers (dimethyl sulphide, methionine), and the aliphatic cyclo-thioether tetrahydrothiophene (see **Scheme 5.1**).

Molecular structure	Name
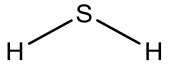	Hydrogen sulphide
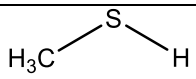	Methanethiol
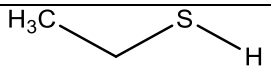	Ethanethiol
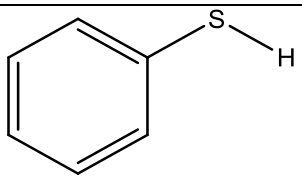	Benzenethiol
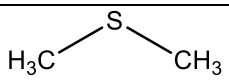	Dimethyl sulphide
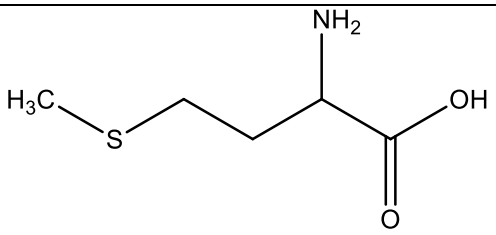	Methionine
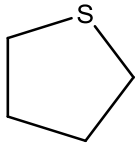	Tetrahydrothiophene

Scheme 5.1 Molecular drawings of thiols and thioethers. [Reprinted with permission from Behyan, S.; Hu, Y. F.; Urquhart, S. G., Journal of Chemical Physics, 134, 244304, 2011. Copyright 2011, American Institute of Physics.]

5.4.2 Computational Methods

Ab initio calculations were carried out by Kosugi's GSCF3 package.[5.47, 5.48] This approach is based on the *ab initio* improved virtual orbital (IVO) approximation, which explicitly includes the core hole in the Hartree-Fock Hamiltonian. The IVO approximation is effective at the simulation of core excitation spectra of organic and organometallic compounds.[5.49-55] The IVO approximation has been widely employed to calculate the NEXAFS spectra of organic compounds at the carbon, nitrogen, oxygen and silicon 1s edges.[5.47-49, 5.53, 5.56, 5.57] On this basis, it is natural to expect a similar success for organosulphur compounds. IVO calculations are particularly effective for transitions

below and near the ionization potential, where the sulphur 1s NEXAFS spectra show the strongest and most distinctive transitions.

The geometries used for these calculations (see **Scheme 5.1**) were provided by *ab initio* geometry optimization at the HF/6-31G* level, by the SPARTAN 06 program.[5.58] Frequency calculations were performed to ensure that the geometries were minimum structures (no imaginary frequencies). For the IVO calculations with GSCF3, we used similar basis sets to that used for organosilicon compounds:[5.54] Hydrogen (41); Second row atoms (carbon, nitrogen, and oxygen) (621 41); sulphur (with the core hole) (311111111 311111), with an additional d polarization function on the sulphur atom (ζ_d = 0.421).

Simulated spectra were obtained from the IVO calculations by broadening each transition as a Gaussian line with the Simile2 package,[5.59] with the following energy dependent widths: 0.6 eV fwhm for bound states, 1.2 eV fwhm for states from the ionization potential (IP) to 4 eV above the IP, and 4.0 eV fwhm for states more than 4.0 eV above the IP. These widths are chosen to approximately track the experimental line width observed in the sulphur 1s NEXAFS spectra, but where the bound states are somewhat narrower than experiment so that fine spectroscopic differences can be more readily observed.[5.53, 5.54, 5.57] MO plots are provided for selected unoccupied orbitals.

5.4.3 Experimental

All compounds (Ethanethiol 97%, Tetrahydrothiophene 99%, DL-Methionine ≥99%, and Benzenethiol ≥99%) were of reagent grade and purchased from Sigma Aldrich with the exception of Dimethyl sulphide (98%), which was purchased from Alfa Aesar.

Experimental spectra of the gas phase molecules as well as the solid phase DL-Methionine were obtained at the Canadian Light Source (CLS) on Soft X-ray Microcharacterization Beamline (SXRMB) beamline, using a Si (111) crystal monochromator which provides an energy resolution of 0.24 eV. The gas samples were introduced into a double gas cell (two gas cells in sequence) from the vapour pressure of the pure samples. The pressure inside the gas cell was in the range of 9.9 - 13.9 mtorr,

below the pressure onset of saturation effects. The absence of saturation was also verified by comparing the spectra from the first and second gas cells.

The experimental spectra of the gas phase molecules were recorded with total ion yield (TIY) detection mode.[5.60] For DL-Methionine, the fine powder was spread homogeneously on the sulphur free carbon tape and its NEXAFS spectrum was measured with total electron yield (TEY) and fluorescence detection. The TIY and TEY NEXAFS spectra were normalized by dividing each spectrum by a simultaneously recorded Io spectrum from an ion chamber upstream from the sample gas cell.

The energy scale was calibrated to an absolute energy scale instead of an agreed energy of a standard. This was done by setting the energy of the Ar 1s → 4p transition to the value of 3203.54 (10) eV, based on the absolute energy calibration of Breinig *et al*.[5.61] In our experiments, the Ar 1s → 4p transition energy was used to calibrate a weak contaminant signal (presumably from $FeSO_4$ contamination) found on the Be windows of the ion chamber (calibrated value, 2481.62 eV). This signal, recorded at the same time as all other spectra, was used as an internal calibration for our experiments. On this scale, the white line of the $ZnSO_4$ appears at 2481.47 eV, which is well within experimental error of the 2481.44 eV value reported in the literature.[5.35] The accuracy of this calibration is estimated to be +/- 0.3 eV, based on the ~0.7 eV life-time broadening of the Ar 1s→ 4p transition. (See **Table 2.1** for a summary of literature calibrations at the sulphur 1s energy).

In comparing the experimental spectra to the calculated (IVO) spectra, the calculated spectra always appear at lower energy than the experimental spectra (4.62 eV lower energy for thiols and 4.47 eV in aliphatic thioethers). IVO spectra for second row species usually appear at higher energy than the corresponding experimental spectra,[5.49-52, 5.54] but strong relativistic effects for higher Z (third row) species, lead to a shift in the opposite direction.[5.39-42] For example, in DFT calculations by Risberg *et al*., the sulphur 1s ionization potential increased by 7.4 eV when relativistic terms are included.[5.40] In this paper, we present experimental data on the calibrated energy scale, and the theoretical data on their calculated energy scales.

5.4.4 Results and Discussion

In this section, experimental sulphur 1s NEXAFS spectra are compared to the simulated sulphur 1s NEXAFS spectra of a series of thiols and thioethers. The sensitivity of the NEXAFS spectra is explored in more detail below.

5.4.4.1 Thiols

Figure 5.1(a) examines the simulated sulphur 1s NEXAFS spectra of hydrogen sulphide (H_2S), methanethiol (CH_3SH), ethanethiol (C_2H_5SH), and benzenethiol (C_6H_5SH), and compares these spectra with the experimental sulphur 1s spectra of ethanethiol and benzene thiol. **Figure 5.1(b)** presents MO plots of the unoccupied orbitals of the most intense pre-edge features in these spectra. **Table 5.1** presents the calculated energies, term values (term value = ionization potential – transition energy), ionization potentials and transition character for the features appearing below the ionization potential. **Table 5.2** presents the experimental energies and assignments for these transitions.

The experimental sulphur 1s NEXAFS spectrum of ethanethiol and benzenethiol show higher resolution than the previous results, now clearly showing the splitting in the white line.[5.28] We observe that the white line and the higher energy shoulder (peaks 1 and 2) in benzenethiol move to higher energy than of the ethanethiol. This can be ascribed to the inductive effect of the phenyl ring, which depletes the electron density on the sulphur atom and increases the sulphur 1s binding energy.

The simulated spectra and molecular orbitals show that the most intense feature in the sulphur 1s NEXAFS spectrum of hydrogen sulphide is formed from two nearly degenerate transitions. MO diagrams show that these transitions are to σ^*(S-H) unoccupied orbitals corresponding to the b_1 (LUMO) and a_1 (LUMO+1) symmetry representations within the C_{2v} point group for H_2S.

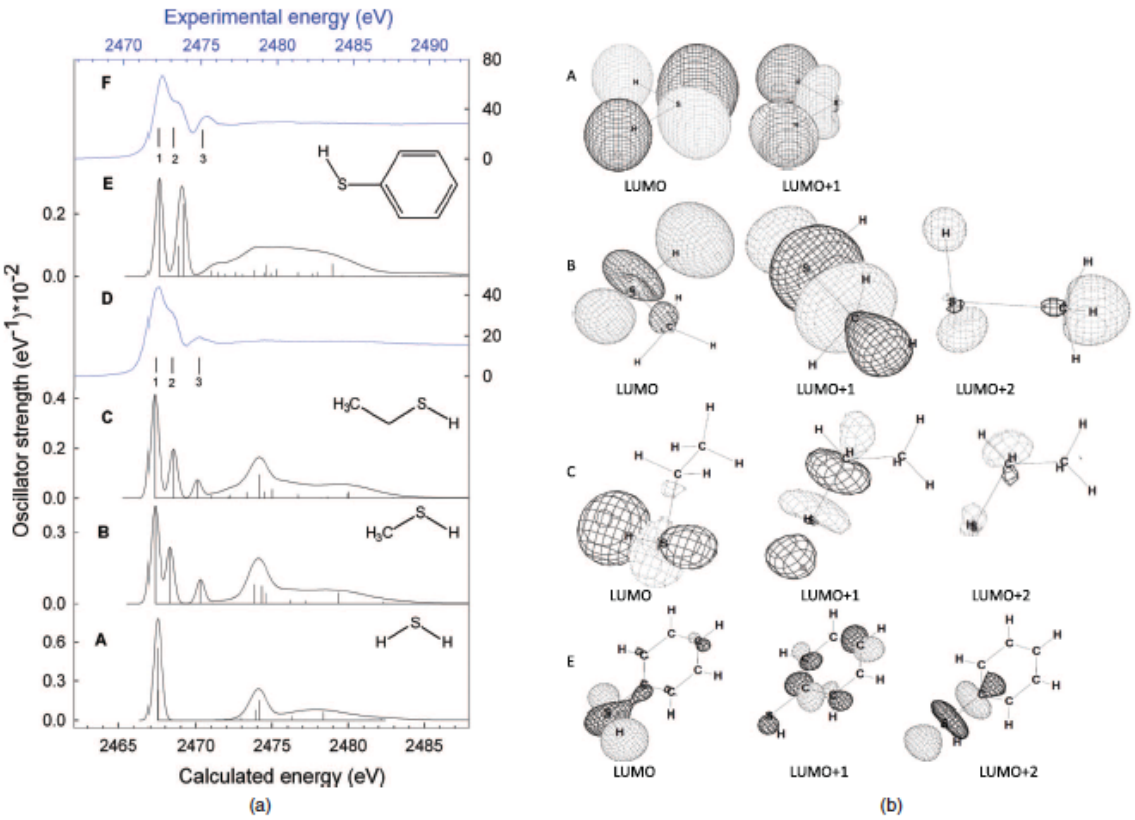

Figure 5.1 (a) Comparison of experimental gas phase sulphur 1s NEXAFS spectra, recorded by total ion yield, to the predicted sulphur 1s spectra from *ab initio* IVO calculations. (A) Calculated spectrum of hydrogen sulphide; (B) calculated spectrum of methanethiol; (C) calculated spectrum of ethanethiol; (D) experimental spectrum of ethanethiol; (E) calculated spectrum of benzenethiol; (F) experimental spectrum of Benzenethiol. **(b)** Unoccupied molecular orbital diagrams for the strong features contributing to the simulated spectra. (A) Hydrogen sulphide; (B) methanethiol; (C) ethanethiol; (E) benzenethiol**.** [Reprinted with permission from Behyan, S.; Hu, Y. F.; Urquhart, S. G., Journal of Chemical Physics, 134, 244304, 2011. Copyright 2011, American Institute of Physics.]

#	Energy (eV)	Term value (eV)	Oscillator strength	Assignment
Hydrogen sulfide ionization potential: 2471.37 eV				
LUMO	2467.47	3.898	0. 003524	S $1s \rightarrow \sigma^*$(S–H)
LUMO + 1	2467.51	3.860	0.001473	S $1s \rightarrow \sigma^*$(S–H)
Methanethiol ionization potential: 2470.54 eV				
LUMO	2467.32	3.221	0.002621	S $1s \rightarrow \sigma^*$(S–H)
				Weak S $1s \rightarrow \sigma$(S–C)
LUMO + 1	2468.29	2.250	0.001510	S $1s \rightarrow \sigma^*$(S–C)
LUMO + 2	2470.29	0.252	0.0006318	Poorly defined
Ethanethiol ionization potential: 2470.28 eV				
LUMO	2467.30	2.987	0.002665	S $1s \rightarrow \sigma^*$(S–H)
				Weak S $1s \rightarrow \sigma$ (S–C)
LUMO + 1	2468.52	1.766	0.001267	S $1s \rightarrow \sigma^*$(S–C)
LUMO + 2	2470.09	0.193	0.0004423	Poorly defined
Benzenethiol ionization potential: 2470.42 eV				
LUMO	2467.57	2.842	0.002008	S $1s \rightarrow \sigma^*$(S–H)
				Weak S $1s \rightarrow \sigma$ (S–C)
LUMO + 1	2468.83	1.583	0.0006201	S $1s \rightarrow \pi^*$(C=C) weak
LUMO + 2	2469.13	1.289	0.001485	S $1s \rightarrow \sigma^*$(S–C)

Table 5.1 Calculated energies, term values, ionization potentials, and assignments for sulphur 1s transitions appearing below the ionization potential for hydrogen sulphide, methanethiol, ethanethiol, and benzenethiol from *ab initio* IVO calculations. [Reprinted with permission from Behyan, S.; Hu, Y. F.; Urquhart, S. G., Journal of Chemical Physics, 134, 244304, 2011. Copyright 2011, American Institute of Physics.]

Relative to hydrogen sulphide, we expect additional σ*(S-C) unoccupied orbital character in the sulphur 1s spectrum of methane thiol. The simulations predict that the LUMO is predominantly sulphur 1s → σ*(S-H) character, with a small, poorly defined sulphur 1s → σ*(S-C) contribution. In contrast, the LUMO+1 is entirely sulphur 1s → σ*(S-C) character. Surprisingly, the two transitions have almost completely separated sulphur 1s → σ*(S-H) and sulphur 1s → σ*(S-C) character. A similar observation is made for ethanethiol. However, the second transition is not fully resolved in the experimental sulphur 1s spectrum of ethanethiol and appears as a higher energy shoulder on the main peak at 2473.11 eV (peak 2).

A third peak (LUMO+2) in methane thiol and ethane thiol appears at slightly higher energy in the calculated spectra; this is associated with the feature (peak 3) at a similar position in the experimental sulphur 1s NEXAFS spectrum of ethanethiol at 2474.87 eV. This feature cannot easily be assigned to a specific antibonding orbital, and the LUMO has σ*(S-H) and σ (S-C) character.

These assignments differ somewhat from those in the literature, where the first peak (1) in the experimental ethane thiol was assigned as a sulphur 1s → σ*(S-C) transition, the higher energy shoulder (2) was not resolved, and the third energy peak (3) was assigned as a sulphur 1s → σ*(S-H)/4p transition.[5.28] Our new calculations clearly show that separate and resolvable sulphur 1s → σ*(S-C) and the sulphur 1s → σ*(S-H) transitions contribute to the main peak.

In benzenethiol, the first transition is predominantly sulphur 1s → σ*(S-H) character with some small but poorly defined sulphur 1s → σ(S-C) character, similar to the other thiols. The second transition (corresponding to the LUMO+1) is relatively weak, and this transition samples the π* density in the phenyl ring. Similar π* interactions were observed by Mijovilovich *et al*. in the sulphur 1s spectra of phenyl benzyl sulphide.[5.33] The transition to the LUMO+2 is stronger with sulphur 1s → σ*(S-C) character, similar to the LUMO+1 in methane thiol and ethane thiol. In the previous assignments for the sulphur 1s spectrum of benzenethiol, the main peak (1), and its high energy shoulder (2), were assigned as sulphur 1s → σ*(S-C), and sulphur 1s → 4s respectively.[5.28] Our results show that the main peak has sulphur 1s → σ*(S-H) and σ(S-C) character. The sulphur 1s → σ*(S-H) contribution occurs in the first strong peak, and not at higher energy as previously assigned.[5.28] The higher energy shoulders in benzenethiol contains a transition with clear sulphur 1s → σ*(S-C) character (LUMO+2), while the LUMO+1 transition cannot be assigned to a simple orbital symmetry.

Compound name	Feature #	Energy (eV)
Ethanethiol	1	2472.17
	2	2473.11
	3	2474.87
Benzenethiol	1	2472.42
	2	2473.47
	3	2475.33
Dimethyl sulfide	1	2472.60
	2	2473.23
	3	2474.70
DL-methionine	1	2472.62
	2	2473.41
	3	2475.14
Tetrahydrothiophene	1	2472.23
	2	2473.31
	3	2474.24

Table 5.2 Transition energies for the experimental sulphur 1s NEXAFS spectra of ethanethiol, benzene thiol, dimethyl sulphide, DL-methionine and tetrahydrothiophene, recorded using total ion yield detection.[a] a. Spectra calibrated by setting the white line of the sulfate contamination in the I_0 signal to 2481.62 eV. See text for a discussion of the calibration procedure. [Reprinted with permission from Behyan, S.; Hu, Y. F.; Urquhart, S. G., Journal of Chemical Physics, 134, 244304, 2011. Copyright 2011, American Institute of Physics.]

Overall, these results show differentiated sulphur 1s → σ*(S-H) and sulphur 1s → σ*(S-C) transitions, closely spaced in energy and resolvable. The first transition in the aliphatic thiols is not a pure σ*(S-H), but includes some σ(S-C) character.

In the calculated NEXAFS spectra, the first transition energies of the aliphatic thiols behave as follows: benzenethiol > hydrogen sulphide > methanethiol ≈ ethanethiol. The difference in the first transition energy from methanethiol to ethanethiol is only 0.02 eV, but the difference is 0.26 eV between benzenethiol to methanethiol. The same trend is observed in the experimental sulphur 1s spectra of benzene thiol and ethane thiol. This result shows that the benzene group has a larger effect than the aliphatic groups in the first energy transition.

5.4.4.2 Thioethers

Figure 5.2(a) presents the simulated sulphur 1s NEXAFS spectra of three aliphatic thioethers, dimethyl sulphide, methionine, and tetrahydrothiophene, and compares these spectra with their experimental sulphur 1s spectra. **Figure 5.2(b)** presents MO plots of the unoccupied orbitals corresponding to the most intense pre-edge features in these spectra. **Table 5.2** presents the energies and assignments from the experimental sulphur 1s spectra.

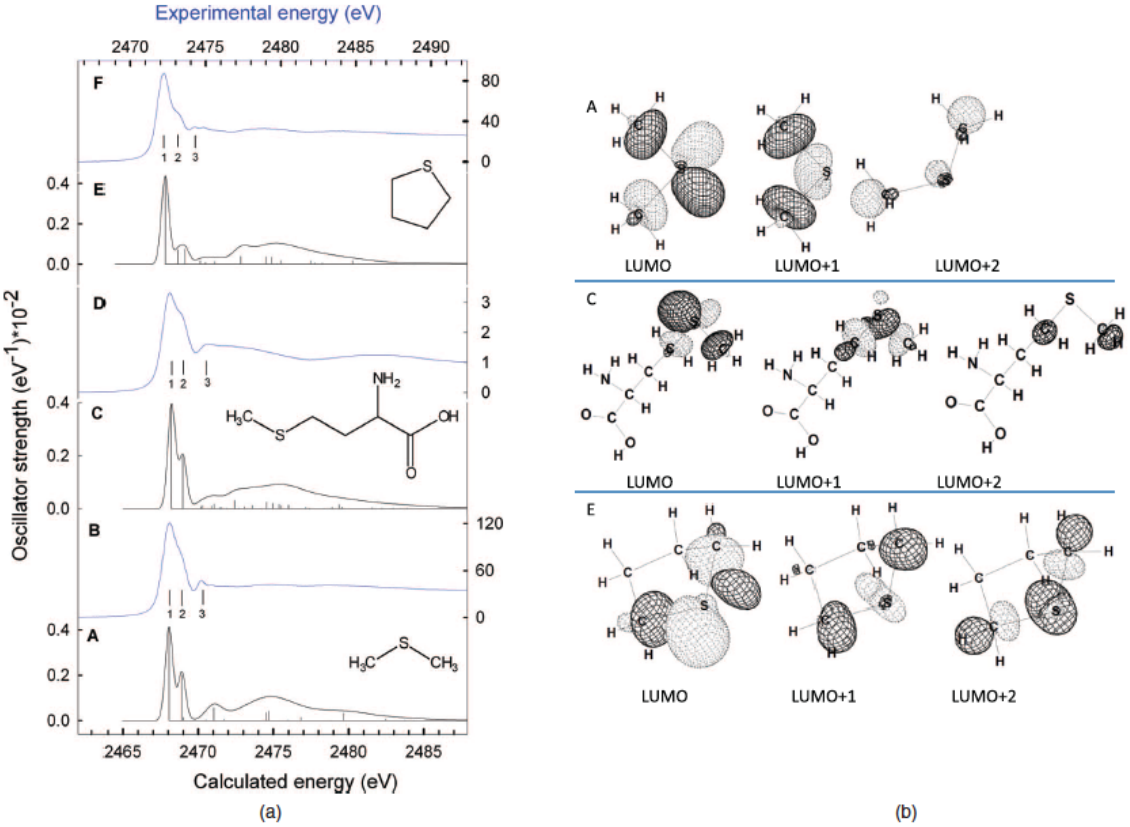

Figure 5.2 (a) Comparison of experimental gas phase sulphur 1s NEXAFS spectra, recorded by total ion yield, to the predicted sulphur 1s spectra from *ab initio* IVO calculations. (A) Calculated spectrum of dimethyl sulphide; (B) experimental spectrum of dimethyl sulphide; (C) calculated spectrum of methionine; (D) experimental spectrum of DL-methionine in solid phase; (E) calculated spectrum of tetrahydrothiophene; (F) experimental spectrum of tetrahydrothiophene. The experimental energy scale (shown on the top of graph) is shifted relative to the calculated energy scale (shown at the bottom); **(b)** unoccupied molecular orbital diagrams for the strong features contributing to the simulated spectra. (A) dimethyl sulphide; (C) methionine; (E) tetrahydrothiophene. [Reprinted with permission from Behyan, S.; Hu, Y. F.; Urquhart, S. G., Journal of Chemical Physics, 134, 244304, 2011. Copyright 2011, American Institute of Physics.]

Table 5.3 presents the calculated energies, term values, ionization potentials and transition character for the features that appear below the ionization potential. The sulphur 1s NEXAFS spectrum of methionine is similar to that previously published,[5.35] while the new gas phase spectrum of dimethyl sulphide is improved relative to the literature,[5.28] showing a clearer definition of the higher energy shoulder in the main peak. The experimental sulphur 1s spectra of dimethyl sulphide and DL-methionine have an intense transition with a higher energy shoulder, and weak features at higher energy. Two, slightly separated sulphur 1s → σ*(S-C) transitions (see discussion of assignments, below) contribute to the intense feature. However, a greater splitting is observed in the DL-methionine for the sulphur 1s → σ*(S-C) transitions, perhaps due to the inductive effect of amino acid group on the molecular orbital with strong σ*(S-C) character, relative to the two other thioethers. In tetrahydrothiophene, the single intense feature makes the experimental white line appear narrower, with a weaker higher energy shoulder at 2473.31 eV (peak 2).

#	Energy (eV)	Term value (eV)	Oscillator strength	Assignment
Dimethyl sulfide ionization potential: 2469.94 eV				
LUMO	2468.07	1.876	0.002644	S $1s \rightarrow \sigma^*$(S–C)
LUMO + 1	2468.91	1.039	0.001285	S $1s \rightarrow \sigma^*$(S–C)
LUMO + 2	2469.01	0.937	0.0000945	S $1s \rightarrow \sigma^*$(S–C)
Methionine ionization potential: 2470.01 eV				
LUMO	2468.24	1.769	0.002514	S $1s \rightarrow \sigma^*$(S–C)
LUMO + 1	2468.99	1.025	0.001279	S $1s \rightarrow \sigma^*$(S–C)
LUMO + 2	2469.25	0.765	0.0000078	S $1s \rightarrow \sigma^*$(S–C)
Tetrahydrothiophene ionization potential: 2469.47 eV				
LUMO	2467.82	1.659	0.002791	S $1s \rightarrow \sigma^*$(S–C)
LUMO + 1	2468.67	0.806	0.0004623	S $1s \rightarrow \sigma^*$(S–C)
LUMO + 2	2469.15	0.323	0.0004886	S $1s \rightarrow \sigma^*$(S–C)

Table 5.3 Calculated energies, term values, ionization potentials, and assignments for sulphur 1s transitions appearing below the ionization potential for dimethyl sulphide, methionine, and tetrahydrothiophene from *ab initio* calculations. [Reprinted with permission from Behyan, S.; Hu, Y. F.; Urquhart, S. G., Journal of Chemical Physics, 134, 244304, 2011. Copyright 2011, American Institute of Physics.]

In the simulated NEXAFS spectrum of dimethyl sulphide, the main transition is formed from two adjacent transitions, each with sulphur 1s → σ*(S-C) character. These features correspond to the b_1 (LUMO) and a_1 (LUMO+1) features observed in H_2S, consistent with the C_{2v} symmetry in these species. A comparison to **Figure 5.1(a)** illustrates a clear trend from hydrogen sulphide (H_2S), methyl thiol (CH_3SH) to dimethyl sulphide, $(CH_3)_2S$, as the orbital character changes from nearly degenerate σ*(S-H), mixed σ*(S-C) and σ*(S-H), to adjacent transitions of σ*(S-C) character.

Methionine is very similar to dimethyl sulphide, which is not surprising as the sulphur has a similar thioether environment in both cases. The MO plots are similar, with a decrease in symmetry relative to dimethyl sulphide. On this basis, one expects the sulphur 1s spectrum of methionine to be similar to $CH_3SCH_2CH_3$ or $CH_3SCH_2CH_2CH_3$, e.g. as an asymmetric dialkyl thioether. Tetrahydrothiophene has a cyclic thioether environment, and a different pattern of sulphur 1s → σ*(S-C) transitions; one intense transition, and two weaker transitions at slightly higher energy.

The energy order of the first transition in the simulated spectra is as follows:, tetrahydrothiophene < dimethylsulphide < methionine. As seen in Table 5.3, the position of these features correlate with the sulphur 1s ionization potential, reflecting slight differences in the inductive environment of the thioether substituent. The lower energy transition of the white line in tetrahydrothiophene can be ascribed to the heterocyclic ring tension. The experimental spectra are well reproduced by the calculations, and the order of the white line energies are also in agreement with the calculations.

5.4.5 Conclusion

In this study, the sulphur 1s NEXAFS spectra of a group of simple thiol and thioether molecules were studied by experiment and computational methods. The spectra of thiols are dominated by sulphur 1s → σ*(S-H) and sulphur 1s → σ*(S-C) transitions. These features are closely spaced in energy, and the higher energy sulphur 1s → σ*(S-H) transition can be resolved as a shoulder in our high-energy resolution gas phase spectra of the thiols. In benzenethiol, a π*(C=C) transition also contributes to the higher energy shoulder. The white line energy in the thiol spectra is partly determined by the ligand

groups attached to the sulphur atom, with a stronger effect from the phenyl group than from the aliphatic groups. Therefore the speciation of the aliphatic thiols can be problematic due to feature overlap.

In aliphatic thioethers, the main peak in experimental spectra is composed of several closely spaced σ*(S-C) character transitions, and the white line transition energy is affected by the ligand groups attached to the sulphur atom. The shapes of the spectra of the non-cyclic thioethers are similar, while the cyclic thioether (tetrahydrothiophene) differ. The inductive effect of the amino acid group may be responsible for the small differences in the non-cyclic thioether compounds, and the cyclic strain in tetrahydrothiophene determines the relative intensity of the σ*(S-C) transitions.

The comparison between theory and experiment is excellent. The best selected DFT methods, such as the half-core hole approximation calculations,[5.35] are comparable to our standard *ab initio* IVO calculation results. Our high resolution gas phase data shows improved energy resolution relative to that previously published. These data are also free from solid-state broadening and common detection artefacts, providing an excellent comparison to theory. This allows us to identify the character of analytically useful transitions in the NEXAFS spectra of organosulphur molecules.

For speciation, care must be taken to avoid simplistic σ*(S-H) and σ*(S-C) assignments and spectroscopic interpretation as both σ*(S-H) and σ*(S-C) orbital character contributes to the white line in thiol and thioether molecules. Shifts in the energy of these features are apparent: thioethers appear at slightly higher energy than thiols; however, strained systems such as tetrahydrothiophene show the white line closer to thiol energies. As in all analytical studies, evidence from NEXAFS spectroscopy must be weighed together with other information about a complex sample, to either narrow the range of possible chemical composition, or to make specific composition assignments, where warranted.

5.4.6 References

5.1. Jalilehvand, F., *Chemical Society Reviews,* **2006,** *35* (12), 1256-1268.
5.2. Rompel, A.; Cinco, R. M.; Latimer, M. J.; McDermott, A. E.; Guiles, R. D.; Quintanilha, A.; Krauss, R. M.; Sauer, K.; Yachandra, V. K.; Klein, M. P., *Proceedings*

of the National Academy of Sciences of the United States of America, **1998,** *95* (11), 6122-6127.
5.3. Prange, A.; Dahl, C.; Truper, H. G.; Behnke, M.; Hahn, J.; Modrow, H.; Hormes, J., *European Physical Journal D,* **2002,** *20* (3), 589-596.
5.4. Pickering, I. J.; George, G. N.; Yu, E. Y.; Brune, D. C.; Tuschak, C.; Overmann, J.; Beatty, J. T.; Prince, R. C., *Biochemistry,* **2001,** *40* (27), 8138-8145.
5.5. Frank, P.; Hedman, B.; Hodgson, K. O., *Inorganic Chemistry,* **1999,** *38* (2), 260-270.
5.6. Pickering, I. J.; Prince, R. C.; Divers, T.; George, G. N., *FEBS Letters,* **1998,** *441* (1), 11-14.
5.7. Braun, A.; Janousch, M.; Sfeir, J.; Kiviaho, J.; Noponen, M.; Huggins, F. E.; Smith, M. J.; Steinberger-Wilckens, R.; Holtappels, P.; Graule, T., *Journal of Power Sources,* **2008,** *183* (2), 564-570.
5.8. Matsumoto, S.; Tanaka, Y.; Ishii, H.; Tanabe, T.; Kitajima, Y.; Kawai, J., *Spectrochimica Acta Part B: Atomic Spectroscopy,* **2006,** *61* (8), 991-994.
5.9. Wiltfong, R.; Mitra-Kirtley, S.; Mullins, O. C.; Andrews, B.; Fujisawa, G.; Larsen, J. W., *Energy & Fuels,* **2005,** *19* (5), 1971-1976.
5.10. Sarret, G.; Connan, J.; Kasrai, M.; Bancroft, G. M.; Charrié-Duhaut, A.; Lemoine, S.; Adam, P.; Albrecht, P.; Eybert-Bérard, L., *Geochimica et Cosmochimica Acta,* **1999,** *63* (22), 3767-3779.
5.11. George, G. N.; Gorbaty, M. L.; Kelemen, S. R.; Sansone, M., *Energy & Fuels,* **1991,** *5* (1), 93-97.
5.12. George, G. N.; Gorbaty, M. L., *Journal of the American Chemical Society,* **1989,** *111* (9), 3182-3186.
5.13. Almkvist, G.; Boye, K.; Persson, I., *Journal of Synchrotron Radiation, 17*, 683-688.
5.14. Allegretti, F.; Bussolotti, F.; Woodruff, D. P.; Dhanak, V. R.; Beccari, M.; Di Castro, V.; Betti, M. G.; Mariani, C., *Surface Science,* **2008,** *602* (14), 2453-2462.
5.15. Sardar, S. A.; Syed, J. A.; Yagi, S.; Tanaka, K., *Thin Solid Films,* **2004,** *450* (2), 265-271.
5.16. Syed, J. A.; Sardar, S. A.; Yagi, S.; Tanaka, K., *Surface Science,* **2004,** *566*, 597-602.
5.17. Syed, J. A.; Sardar, S. A.; Yagi, S.; Tanaka, K., *Journal of Vacuum Science & Technology A,* **2004,** *22* (3), 683-688.
5.18. Syed, J. A.; Sardar, S. A.; Yagi, S.; Tanaka, K., *Thin Solid Films,* **2006,** *515* (4), 2130-2136.
5.19. Modrow, H.; Calderon, G.; Daly, W. H.; de Souza, G. G. B.; Tittsworth, R. C.; Moelders, N.; Schilling, P. J., *Journal of Synchrotron Radiation,* **1999,** *6*, 588-590.
5.20. Winter, I.; Hormes, J.; Hiller, M., *Nuclear Instruments & Methods in Physics Research Section B-Beam Interactions with Materials and Atoms,* **1995,** *97* (1-4), 287-291.
5.21. Smith, T. A.; Dewitt, J. G.; Hedman, B.; Hodgson, K. O., *Journal of the American Chemical Society,* **1994,** *116* (9), 3836-3847.
5.22. Howells, M.; Jacobsen, C.; Warwick, T.; Bos, A., *Principles and Applications of Zone Plate X-Ray Microscopes*. In *Science of Microscopy*, **2007**, 835-926.

5.23. Van der Snickt, G.; Dik, J.; Cotte, M.; Janssens, K.; Jaroszewicz, J.; De Nolf, W.; Groenewegen, J.; Van der Loeff, L., *Analytical Chemistry,* **2009,** *81* (7), 2600-2610.
5.24. Cotte, M.; Welcomme, E.; Sole, V. A.; Salome, M.; Menu, M.; Walter, P.; Susini, J., *Analytical Chemistry,* **2007,** *79* (18), 6988-6994.
5.25. Prietzel, J.; Thieme, J.; Neuhausler, U.; Susini, J.; Kogel-Knabner, I., *European Journal of Soil Science,* **2003,** *54* (2), 423-433.
5.26. Norlund, K. L. I.; Southam, G.; Tyliszczak, T.; Hu, Y. F.; Karunakaran, C.; Obst, M.; Hitchcock, A. P.; Warren, L. A., *Environmental Science & Technology,* **2009,** *43* (23), 8781-8786.
5.27. Kaznatcheev, K. V.; Karunakaran, C.; Lanke, U. D.; Urquhart, S. G.; Obst, M.; Hitchcock, A. P., *Nuclear Instruments & Methods in Physics Research Section A - Accelerators Spectrometers Detectors and Associated Equipment,* **2007,** *582* (1), 96-99.
5.28. Dezarnaud, C.; Tronc, M.; Hitchcock, A. P., *Chemical Physics,* **1990,** *142*, 455-462.
5.29. Dezarnaud, C.; Tronc, M.; Modelli, A., *Chemical Physics,* **1991,** *156* (1), 129-140.
5.30. Hitchcock, A. P.; Bodeur, S.; Tronc, M., *Physica B,* **1989,** *158* (1-3), 257-258.
5.31. Chauvistre, R.; Hormes, J.; Hartmann, E.; Etzenbach, N.; Hosch, R.; Hahn, J., *Chemical Physics,* **1997,** *223* (2-3), 293-302.
5.32. Hitchcock, A. P., *Journal de Physique IV (Proceedings),* **1986,** *T.47 C8 vol.2*, C8-575-C8578.
5.33. Mijovilovich, A.; Pettersson, L. G. M.; de Groot, F. M. F.; Weckhuysen, B. M., *Journal of Physical Chemistry A,* **2010,** *114* (35), 9523-9528.
5.34. Sarangi, R.; Frank, P.; Hodgson, K. O.; Hedman, B., *Inorganica Chimica Acta,* **2008,** *361* (4), 956-964.
5.35. Mijovilovich, A.; Pettersson, L. G. M.; Mangold, S.; Janousch, M.; Susini, J.; Salome, M.; de Groot, F. M. F.; Weckhuysen, B. M., *Journal of Physical Chemistry A,* **2009,** *113* (12), 2750-2756.
5.36. Risberg, E. D.; Jalilehvand, F.; Leung, B. O.; Pettersson, L. G. M.; Sandstrom, M., *Dalton Transactions,* **2009,** (18), 3542-3558.
5.37. Nakamatsu, H.; Mukoyama, T.; Adachi, H., *Journal of Chemical Physics,* **1991,** *95* (5), 3167-3174.
5.38. Bodeur, S.; Hitchcock, A. P.; Kosugi, N., *Chemical Physics,* **1992,** *162* (2-3), 293-302.
5.39. Damian, E.; Jalilehvand, F.; Abbasi, A.; Pettersson, L. G. M.; Sandstrom, M., *Physica Scripta,* **2005,** *T115*, 1077-1079.
5.40. Risberg, E. D.; Eriksson, L.; Mink, J.; Pettersson, L. G. M.; Skripkin, M. Y.; Sandstrom, M., *Inorganic Chemistry,* **2007,** *46* (20), 8332-8348.
5.41. Mori, R. A.; Paris, E.; Giuli, G.; Eeckhout, S. G.; Kavcic, M.; Zitnik, M.; Bucar, K.; Pettersson, L. G. M.; Glatzel, P., *Analytical Chemistry,* **2009,** *81* (15), 6516-6525.
5.42. Mori, R. A.; Paris, E.; Giuli, G.; Eeckhout, S. G.; Kavcic, M.; Zitnik, M.; Bucar, K.; Pettersson, L. G. M.; Glatzel, P., *Inorganic Chemistry,* **2010,** *49* (14), 6468-6473.
5.43. Tossell, J. A.; Vaughan, D. J., *Journal of Colloid and Interface Science,* **1993,** *155* (1), 98-107.
5.44. Adachi, J.-i.; Takata, Y.; Kosugi, N.; Shigemasa, E.; Yagishita, A.; Kitajima, Y., *Chemical Physics Letters,* **1998,** *294* (6), 559-564.

5.45. Gianturco, F. A.; Lamanna, U.; Guidotti, C., *Journal of Chemical Physics,* **1972,** *57* (2), 840-&.
5.46. Reynaud, C.; Bodeur, S.; Marechal, J. L.; Bazin, D.; Millie, P.; Nenner, I.; Rockland, U.; Baumgartel, H., *Chemical Physics,* **1992,** *166* (3), 411-424.
5.47. Kosugi, N., *Theoretica Chimica Acta,* **1987,** *72* (2), 149-173.
5.48. Kosugi, N.; Kuroda, H., *Chemical Physics Letters,* **1980,** *74* (3), 490-493.
5.49. Cooney, R. R.; Urquhart, S. G., *Journal of Physical Chemistry B,* **2004,** *108* (47), 18185-18191.
5.50. Otero, E.; Urquhart, S. G., *Journal of Physical Chemistry A,* **2006,** *110* (44), 12121-12128.
5.51. Ueda, K.; Okunishi, M.; Chiba, H.; Shimizu, Y.; Ohmori, K.; Sato, Y.; Shigemasa, E.; Kosugi, N., *Chemical Physics Letters,* **1995,** *236* (3), 311-317.
5.52. Urquhart, S. G.; Ade, H., *The Journal of Physical Chemistry B,* **2002,** *106* (34), 8531-8538.
5.53. Urquhart, S. G.; Turci, C. C.; Tyliszczak, T.; Brook, M. A.; Hitchcock, A. P., *Organometallics,* **1997,** *16* (10), 2080-2088.
5.54. Urquhart, S. G.; Hitchcock, A. P.; Lehmann, J. F.; Denk, M., *Organometallics,* **1998,** *17* (11), 2352-2360.
5.55. Urquhart, S. G.; Smith, A. P.; Ade, H. W.; Hitchcock, A. P.; Rightor, E. G.; Lidy, W., *Journal of Physical Chemistry B,* **1999,** *103* (22), 4603-4610.
5.56. Otero, E.; Kosugi, N.; Urquhart, S. G., *Journal of Chemical Physics,* **2009,** *131* (11).
5.57. Lehmann, J. F.; Urquhart, S. G.; Ennis, L. E.; Hitchcock, A. P.; Hatano, K.; Gupta, S.; Denk, M. K., *Organometallics,* **1999,** *18* (10), 1862-1872.
5.58. Spartan 6.0; Wavefunction Inc.: Irvine, CA, **1994**.
5.59. Huo, B.; Hitchcock, A. P. *Simile2; McMaster University, Hamilton, ON*, **1996**.
5.60. Hitchcock, A. P.; Tronc, M., *Chemical Physics,* **1988,** *121* (2), 265-277.
5.61. Breinig, M.; Chen, M. H.; Ice, G. E.; Parente, F.; Crasemann, B., *Physical Review A,* **1980,** *22* (2), 520-528.

CHAPTER 6 CHEMICAL SENSITIVITY OF SULPHUR 1S NEXAFS SPECTROSCOPY TOWARDS THE SPECIATION OF DISULPHIDES

6.1 Description

This chapter is a copy of the manuscript under preparation, and explores the sulphur 1s NEXAFS spectra of disulphides and their comparison to sulphides (thiols and thioethers). This contribution discusses the chemical sensitivity of sulphur 1s NEXAFS in probing the changes in the number of carbon atoms in aliphatic ligands attached to sulphur atom in disulphides, as well as the changes in the symmetry of groups attached to sulphur atom (for example dibutyl compared to methyl-ethyl). It also examines the effect of changing the nature of the ligand (aliphatic versus unsaturated ligands) on the shape of the NEXAFS spectra, and finally compares the sulphur 1s NEXAFS of this functionality with the spectra of sulphides. These spectra are further analyzed with the aid of *ab initio* calculations for assigning the spectral transitions. The experimental part and computational methods for this study are provided in the following sections under the form of the manuscript.

6.2 Description of the Candidate's Contribution

For this contribution I was the primary investigator in terms of sample preparation, acquisition of experimental data, the simulation of NEXAFS spectra by *ab initio* calculations, the interpretation of the results, and writing of the manuscript. Dr Stephen G. Urquhart provided extensive guidance throughout the performance of the experiments, data analysis, interpretation of data, and simulations. He also assisted in writing and editing this document, however I played a greater role in writing this manuscript than in the first one. Dr. Yongfeng Hu assisted and helped in acquiring the experimental spectra.

Dr. S. G. Urquhart, and Dr. Yongfeng Hu kindly gave me their permission for including this paper in this thesis, and agreed on my contribution in this document.

6.3 Relation of Contribution towards Research Objectives

This contribution was solely performed towards the objectives of the thesis research. This contribution is part of our main research goals, which explores the sulphur 1s NEXAFS spectra of disulphides and the chemical sensitivity of NEXAFS spectroscopy in tracking the small changes in the ligand groups attached to the sulphur atom and the shape and energy position of the white line of NEXAFS spectra of relevant compounds. This study also examines the similarities and differences between sulphides and disulphides spectra, which are crucial in speciation and quantification of sulphur compounds.

Beside the experimental and computational sections provided in this manuscript, detailed descriptions of these sections are also provided in **Chapters 2** and **3** respectively. A full discussion of the results as part of the whole study of sulphur 1s NEXAFS spectra of different sulphur functionalities is provided in **Chapter 9**.

6.4 Chemical Sensitivity of Sulphur 1s NEXAFS Spectroscopy towards the Speciation of Disulphides

Shirin Behyan[1], Yongfeng Hu[2], Stephen G. Urquhart[1]*

1. Department of Chemistry, University of Saskatchewan, Saskatoon, SK, Canada S7N 5C9

2. Canadian Light Source, University of Saskatchewan, Saskatoon, SK, Canada S7N 0X4

Abstract

Speciation of disulphides as well as determination of the ratio of thiols to disulphides is of great interest in fossil fuel studies, rubber industries and biological systems. Sulphur 1s NEXAFS spectroscopy is proved to be a powerful technique for these studies; however overlapping the energy position of the white line in thiols and disulphides can be problematic in speciation of these compounds. Speciation is also greatly dependent on a well-defined database of sulphur model spectra. Therefore, in this study, we acquired highly resolved sulphur 1s NEXAFS spectra of a group of disulphides with aliphatic and unsaturated ligand groups. The spectral transitions in these spectra then were assigned by

the aid of Improved Virtual Orbital (IVO) *ab initio* calculations. Finally the combination of experiment and calculations was used to study the effect of molecular symmetry and the nature of the ligand groups on the shape of the NEXAFS spectra. The calculations also proved to be useful in differentiation of different transitions in thiols and disulphides that can be targeted for use in speciation.

Corresponding Author, email: stephen.urquhart@usask.ca

6.4.1 Introduction

Disulphides are constituents of fossil fuels[6.1] as well as many biological systems. These compounds play an important role in folding, functionality, and stability of many proteins[6.2-5] and act as crosslinking groups in vulcanization of rubber.[6.6-9] The vast applications of these compounds in diverse fields such as polysulphide polymers, vulcanized rubber, sulphur cement, oil producing industries, and medicine[6.10] makes the speciation and quantification of this compounds to be of great and general interest.

Sulphur 1s NEXAFS spectroscopy has been successfully implemented in speciation and quantification of sulphur compounds in diverse areas such as: fossil fuel studies,[6.11-21] biological systems,[6.4, 6.5, 6.22-25] rubber industries[6.6-9], and waterlogged woods.[6.26] The merits of NEXAFS spectroscopy such as being non-destructive, element specific, sensitive to the symmetry, oxidation state, and electronic structure of the absorbing site, makes this technique preferable to other techniques.[6.11, 6.27]

It has been shown that in speciation studies by NEXAFS spectroscopy, choosing only one representative from each functional group irrespective of the nature of the ligand groups attached to the sulphur atom can be problematic.[6.28-30] This can be even worse in speciation of sulphur compounds with overlapping energy position of the white lines (e.g., thiols versus disulphides), in which different ligand groups can also alter the shape and energy position of the white line.

Therefore, in this work the sulphur 1s NEXAFS spectra of a series of disulphide species relevant petroleum with different ligand groups were studied. The spectral transitions were further analyzed with the aid of IVO *ab initio* Hartree-Fock calculations. These calculations enabled us to have better assignments of the spectral transitions and

provided useful insights in tracking different transitions for differentiation of thiols from disulphides.

In previous studies of organosulphur compounds, the transitions in each spectrum have been assigned on an empirical basis.[6.6, 6.22, 6.25, 6.31-36] However, there have been few theoretical studies on sulphur 1s NEXAFS spectra of organosulphur compounds until recently.[6.29, 6.37-45] Sulphur 1s NEXAFS calculations of organosulphur species have been reviewed in our recent study of aliphatic thioethers and thiols,[6.44] and thiophenic compounds[6.46]; only studies relevant to this work are mentioned here.

Chauvistré *et al*. studied the NEXAFS spectra of different polysulphides with varying number of sulphur atoms by experimental and computational methods. In this study it was shown that changing the ligand groups, as well as changing the number of sulphur atoms from two to four, could alter the intensities and energy position of the white line in NEXAFS spectra. In this work transitions were assigned with the aid of MS-Xα calculations.[6.6]

Mijovilovich *et al*. studied the chemical sensitivity of NEXAFS spectra of two disulphide species: dibenzyldisulphide, and diphenyldisulphide.[6.29] The spectral transitions were assigned by DFT calculations. These studies showed that the sulphur-sulphur bonding in disulphides causes a change in shape and intensity of the white line compared to sulphides as a result of enhanced splitting of the first two LUMOs and for the speciation of disulphides from sulphides, the differences in edge position of the white line can be used.[6.29]

Sarangi *et al*. studied the NEXAFS spectra of cystine and (±)6-thioctic amide and used TD-DFT calculations to simulate the spectra. In this study, it was concluded that the symmetry, as well as the ligand groups could alter the edge position of the NEXAFS spectra even in the same functional group.[6.37]

In the present work, we have studied the high-resolution experimental NEXAFS spectra of different disulphides (see **Scheme 6.1**) and used IVO *ab initio* calculations to assign the transitions.

Molecular structure	IUPAC name
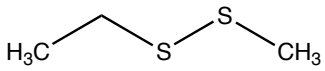	(Methyldisulfanyl)ethane
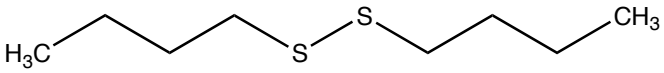	1-(Butyldisulfanyl)butane
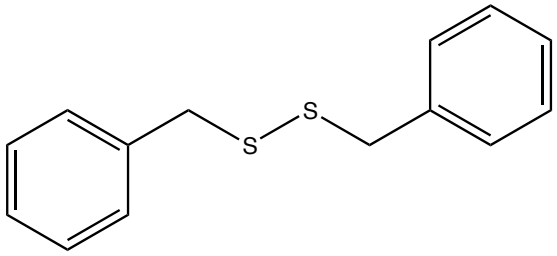	1,1'-[Disulfanediylbis(methylene)]dibenzene

Scheme 6.1 Molecular drawings of disulphides.

The goal of this work was to probe the changes involved in the NEXAFS spectra as a result of changing the number of carbon atoms in aliphatic ligands attached to sulphur atom, the symmetry of groups attached to sulphur atom (for example dibutyl compared to ethyl-methyl), and the nature of the ligand (aliphatic versus unsaturated ligands). Finally the complications imposed by changing the ligand groups on speciation of disulphides from thiols are explored, as these two functional groups have very close white line energy. This study was performed in order to see how the calculations and experiment could be used in speciation of disulphides as well as differentiating of thiols from disulphides.

6.4.2 Computational Methods

Ab initio calculations were carried out with Kosugi's GSCF3 package.[6.47, 6.48] This approach is based on the *ab initio* Improved Virtual Orbital (IVO) approximation, which explicitly includes the core hole in the Hartree-Fock Hamiltonian. The IVO approximation has been proved to be effective at the simulation of core excitation spectra of organic and organometallic compounds.[6.49-55] The IVO approximation has been widely used to calculate the NEXAFS spectra of organic compounds at the carbon, nitrogen, oxygen, silicon, and sulphur 1s edges.[6.46-49, 6.53, 6.56, 6.57] IVO calculations are particularly effective for transitions below and near the ionization potential, where the sulphur 1s NEXAFS spectra show the strongest and most distinctive transitions. The geometries used for these calculations (see **Scheme 6.1**) were provided by *ab initio* geometry

optimization at the HF/6-31G* level, by the SPARTAN 06 program.[6.58] Frequency calculations were performed to ensure that the geometries were minimum structures (no imaginary frequencies). For the IVO calculations with GSCF3, the following basis sets were used: hydrogen (41); second row atoms (carbon, nitrogen, and oxygen) (621 41); sulphur (4321 421) and sulphur with the core hole (311111111 311111), with an additional d polarization function on the sulphur atom with core hole ($\zeta_d = 0.421$).

Simulated spectra were obtained from the IVO calculations by broadening each transition as a Gaussian line with the Simile2 package,[6.59] with the following energy dependent widths: 0.6 eV fwhm for bound states, 1.2 eV fwhm for states from the ionization potential (IP) to 4 eV above the IP, and 4.0 eV fwhm for states more than 4.0 eV above the IP. MO plots are provided for selected optical orbitals.

6.4.3 Experimental

All compounds**,** 1-(butyldisulfanyl)butane (dibutyl disulphide) **(**> 97%), and benzenthiol (≥ 99%), were of reagent grade and purchased from Sigma Aldrich with the exception of 1,1'-[disulfanediylbis(methylene)]dibenzene (benzyl disulphide) (98%) which was purchased from Alfa Aesar.

Experimental spectra of the gas and condensed phases were obtained at the Canadian Light Source (CLS) on Soft X-ray Microcharacterization Beamline (SXRMB), using a Si(111) crystal monochromator which provides an energy resolution of 0.24 eV. Liquid and gas phase spectra were acquired when permitted by the physical properties of the species studied (vapour pressure, etc.). The experimental procedure for acquiring the gas phase spectra is described in detail in our previous study of thiols and thioethers.[6.44] The experimental spectra of the gas phase molecules were recorded with total ion yield (TIY) detection mode.[6.60]

For solid sample of 1,1'-[disulfanediylbis(methylene)]dibenzene, a fine powder of the sample was spread homogeneously on a kapton tape (previously verified to be sulphur-free) and the NEXAFS spectra were measured with Total Electron Yield (TEY) in a He filled chamber. For liquid sample of 1-(butyldisulfanyl)butane, the sample was placed in a Teflon plate holder, which was then sandwiched by two layers of kapton tape.

NEXAFS spectra were measured by fluorescence yield (FLY) with a Vortex 4-element Si drift detector.

The TIY, TEY and FLY NEXAFS spectra were normalized by dividing each spectrum by an I_o spectrum, recorded simultaneously from an ion chamber upstream from the sample cell. In our experiments, the Ar 1s → 4p transition energy was used to calibrate a weak contaminant signal (presumed to be $FeSO_4$) found on the Be windows of the ion chamber (calibrated value, 2481.62 eV based on absolute energy scale calibration). This signal, recorded at the same time as all other spectra, was used as an internal calibration for our experiments.[6.44]

The calculated IVO sulphur 1s simulations always appear at lower energy than the experimental NEXAFS spectra because of strong relativistic effects for third row species.[6.42, 6.44, 6.61-63] In this paper, the experimental and theoretical data are presented on their own energy scales.

6.4.4 Results and discussion

Figure 6.1 examines the simulated sulphur 1s NEXAFS spectra of (methyldisulfanyl)ethane ($CH_3S_2C_2H_5$), 1-(butyldisulfanyl)butane ($C_4H_9S_2C_4H_9$), 1,1'-[disulfanediylbis(methylene)]dibenzene ($C_6H_5CH_2S_2CH_2C_6H_5$) and compares these spectra with the high resolution experimental spectra of 1-(butyldisulfanyl)butane, and 1,1′-[disulfanediylbis(methylene)]dibenzene. **Figure 6.2** shows the molecular orbital plots corresponding to the most intense pre-edge features of the simulated spectra. **Table 6.1** presents the experimental energies and assignments for the most intense transitions below the ionization potential. **Table 6.2** presents the calculated energies, term values (term value = ionization potential – transition energy), ionization potentials, and transition character for the features appearing below the ionization potential.

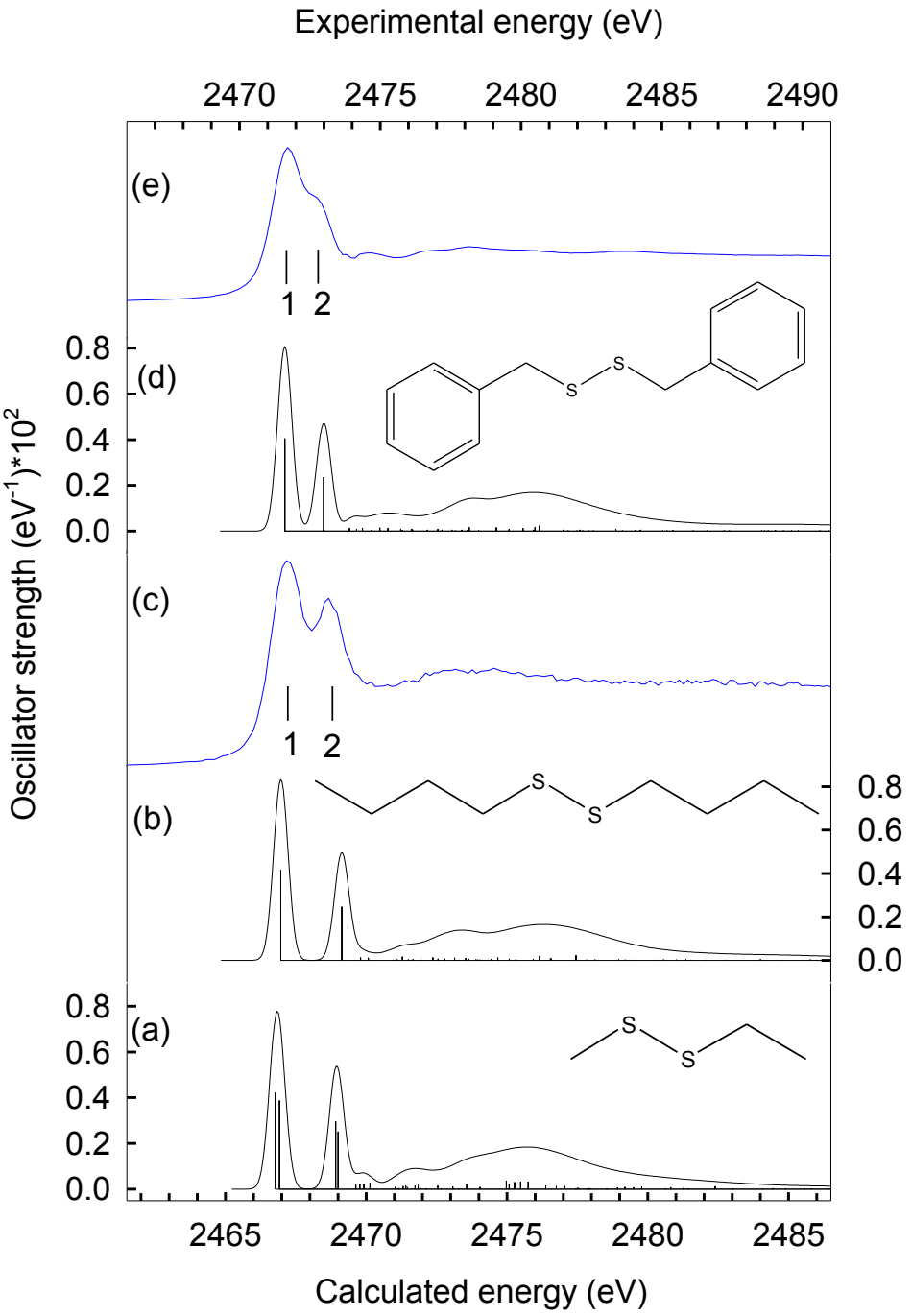

Figure 6.1 Comparison of experimental sulphur 1s NEXAFS spectra to the simulated sulphur 1s spectra from *ab initio* IVO calculations. (a) Calculated spectrum of (methyldisulfanyl)ethane; (b) calculated spectrum of 1-(butyldisulfanyl)butane; (c) experimental spectrum of 1-(butyldisulfanyl)butane obtained in florescence yield detection; (d) calculated spectrum of 1,1'-[disulfanediylbis(methylene)]dibenzene; (e) experimental spectrum of 1,1'-[disulfanediylbis(methylene)]dibenzene obtained in total electron yield detection. The experimental energy scale (shown on the top of graph) is shifted relative to the calculated energy scale (shown at the bottom).

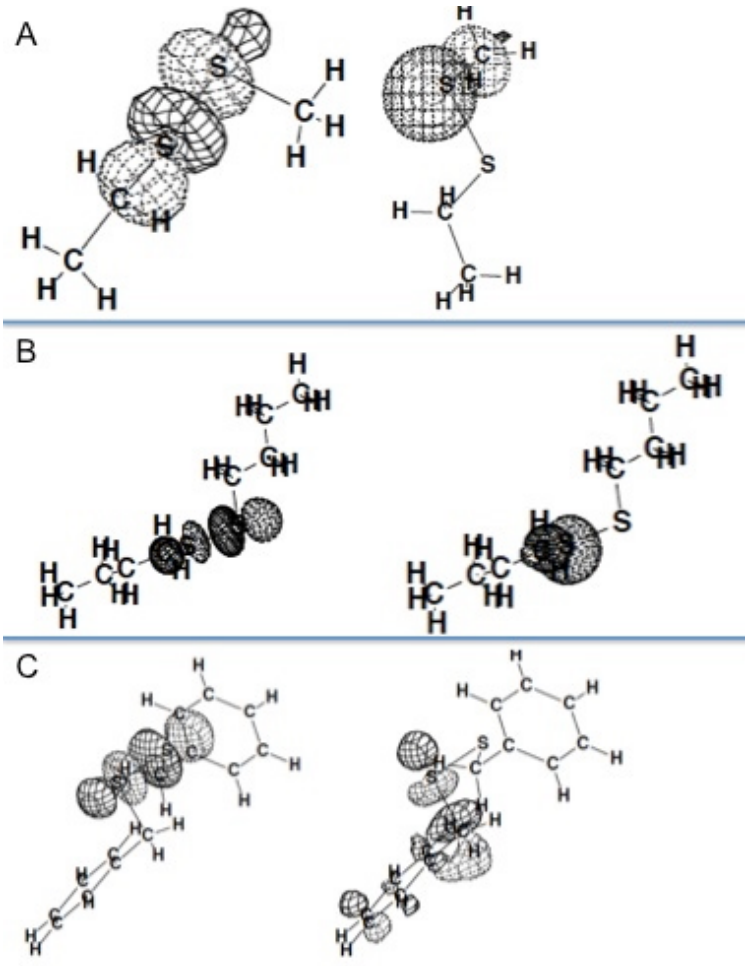

Figure 6.2 Unoccupied molecular orbital diagrams for the strong features contributing to the simulated spectra. (A) (Methyldisulfanyl)ethane; (B) 1-(butyldisulfanyl)butane; (C) 1,1′-[disulfanediylbis(methylene)]dibenzene.

In **Figure 6.1**, the higher energy shoulder in the white line of the experimental spectra of 1-(butyldisulfanyl)butane and 1,1′-[disulfanediylbis(methylene)]dibenzene are now more clearly resolved.[6.6] It is also shown that the ligand group attached to the sulphur atom plays an important role on the shape, relative splitting and intensity of the NEXAFS spectra of disulphides (e.g., benzyl versus butyl). The edge positions of the white line in both 1,1'-[disulfanediylbis(methylene)]dibenzene and 1-(butyldisulfanyl)butane appear at the same energy. This is not surprising as both disulphides have a similar environment and the phenyl ring is not directly attached to the sulphur atom. However, in another study by Mijovilovich *et al*. similar white line energies have been reported for dibenzyl disulphide (1,1'-[disulfanediylbis(methylene)]dibenzene) and diphenyl disulphide,[6.29]

where the sulphur atom is directly attached to the phenyl ring.[6.29] Although in their study the energy calibration is different than this study, in a uniform energy calibration scheme, it is expected that the white line energies of all the above-mentioned species (aliphatic and aromatic disulphides) appear at the same energy. This comparison is in contrast to our previous results for benzenethiol (see §**5.4.4.1**) in which the inductive effect of the phenyl ring had a direct influence on the sulphur atom, resulting in change of the energy position of the white line compared to aliphatic thiols.[6.44]

Compound name	Feature #	Energy (eV)	Assignments
1-(butyldisulfanyl)butane	1	2471.7	S 1s → σ*(S-S)
	2	2473.2	S 1s → σ*(S-C)
1,1'-[disulfanediylbis(methylene)]dibenzene	1	2471.7	S 1s → σ*(S-S)
	2	2472.8	S 1s → σ*(S-C)/π*(C=C)
benzenthiol	1	2472.4	S 1s → σ*(S-H)/weak σ(S-C)
	2	2473.5	S 1s → σ*(S-C)/ π*(C=C)

Table 6.1 Transition energies for the experimental sulphur 1s NEXAFS Spectra of (Methyldisulfanyl)ethane, 1-(butyldisulfanyl)butane**,** 1,1′-[disulfanediylbis(methylene)] dibenzene, and benzenthiol.[6.44]

The simulated NEXAFS spectrum of (methyldisulfanyl)ethane shows two peaks in the white line, each consisting of two nearly degenerate transitions. The molecular orbital plots (the MOs are just shown for the sulphur atom attached to the methyl group) show that the first intense peak has sulphur 1s → σ*(S-S) character, while, the second peak has sulphur 1s → σ*(S-C) character. The nearly degenerate transitions in each peak are the result of asymmetric ligand groups around the sulphur atoms (methyl versus ethyl) and depend on the location of the sulphur 1s core hole. The same simulated NEXAFS spectra are obtained for 1-(butyldisulfanyl)butane, and 1,1'-[disulfanediylbis(methylene)] dibenzene molecules, however the contributions from the two sulphur atoms are symmetrically equivalent. This makes each peak to be narrower and more intense than the less symmetric molecule. Although this splitting effect might be minimal for similar aliphatic moieties (ethyl and methyl), it should be greater for functional groups of a different nature (e.g., phenyl compared to ethyl). This will affect the amount of splitting and consequently the shape and broadening of the white line.

The calculations show that in 1-(butyldisulfanyl)butane the first transition associated (peak (1)) is from a sulphur 1s → σ*(S-S) transition and the second transition associated (peak (2)) is from sulphur 1s → σ*(S-C) transition.

The simulated spectrum in 1,1'-[disulfanediylbis(methylene)]dibenzene shows two intense peaks, but the energy difference between these two peaks is smaller than for the aliphatic disulphides. This is also reflected in the experimental spectrum of this species where the second peak has appeared as a higher energy shoulder. The simulated spectrum and molecular orbital plots of this molecule show that the most intense feature (peak (1)) in the simulated spectrum associated is a sulphur 1s → σ*(S-S) transition, while the second peak (peak (2)) has sulphur 1s → σ*(S-C) character, which also samples from the π*(C=C) of the phenyl ring. The relatively lower intensity of the second peak in this molecule compared to the aliphatic disulphides is the result of delocalized σ*(S-C) on this molecule and therefore less overlap of sulphur 1s with the excited state. Our results for 1,1'-[disulfanediylbis(methylene)]dibenzene are in agreement with previously reported results by Mijovilovich *et al*. for this species.[6.29] In their study, they also have compared the NEXAFS spectrum of diphenyl disulphide, in which the sulphur atom is directly attached to the phenyl ring, to 1,1'-[disulfanediylbis(methylene)]dibenzene.[6.29] However, the NEXAFS spectrum of diphenyl disulphide is similar to the aliphatic disulphides, which are reported in this manuscript. The shape difference of the white line in this molecule relative to 1,1'-[disulfanediylbis(methylene)]dibenzene was attributed to the presence of additional molecular orbitals at higher energies in which the sulphur atom has higher contribution in the molecular orbitals corresponding to these transitions.[6.29]

The effect of the ligand group on the shape and energy position of the white line is very important in the speciation of sulphur compounds specially in determining the ratio of thiols to disulphides, as the energy positions of the white lines in these functional groups are very close. This is illustrated in **Figure 6.3,** where the spectra of benzenethiol is compared to that of 1,1'-[disulfanediylbis(methylene)]dibenzene. The NEXAFS spectra of these molecules have a similar shape, with a small but characteristic difference in the energy of the white line.

(Methyldisulfanyl)ethane, sulphur attached to methyl group Ionization Potential: 2470.232 eV				
#	Energy (eV)	Term Value (eV)	Oscillator Strength	Assignment
LUMO	2466.918	3.314	0.0024737	S 1s→σ*(S-S)
LUMO+1	2468.922	1.310	0.0018841	S 1s→σ*(S-C)

(Methyldisulfanyl)ethane, sulphur attached to ethyl group Ionization Potential: 2470.093 eV				
#	Energy (eV)	Term Value (eV)	Oscillator Strength	Assignment
LUMO	2466.780	3.313	0.0026950	S 1s→σ*(S-S)
LUMO+1	2469.000	1.093	0.0015986	S 1s→σ*(S-C)

1-(Butyldisulfanyl)butane Ionization Potential: 2469.854eV				
#	Energy (eV)	Term Value (eV)	Oscillator Strength	Assignment
LUMO	2466.969	2.885	0.0026604	S 1s→σ*(S-S)
LUMO+1	2469.135	0.719	0.0015713	S 1s→σ*(S-C)

1,1'-[Disulfanediylbis(methylene)]dibenzene Ionization Potential: 2469.808 eV				
#	Energy (eV)	Term Value (eV)	Oscillator Strength	Assignment
LUMO	2467.111	2.697	0. 0025802	S 1s→σ*(S-S)
LUMO+1	2468.495	1.313	0.0015047	S 1s→σ*(S-C)/ π*(C=C)

Table 6.2 Calculated energies, term values, ionization potentials, and assignments for sulphur 1s transitions appearing below the ionization potential for (methyldisulfanyl)ethane**,** 1-(butyldisulfanyl)butane**,** and 1,1'-[disulfanediylbis(methylene)]dibenzene from *ab initio* IVO calculations.

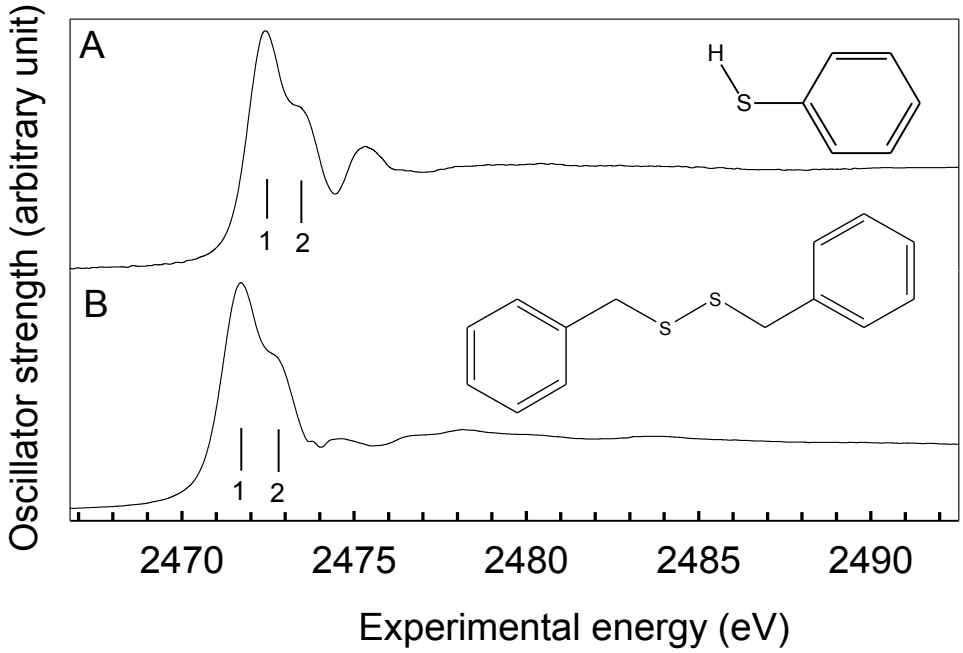

Figure 6.3 Comparison of experimental sulphur 1s NEXAFS spectra of (A) benzenethiol in gas phase acquired in total ion yield[6.44] to (B) 1,1'-[disulfanediylbis(methylene)] dibenzene in solid phase acquired in total electron yield.

The calculations however have shown that these peaks have a different transition character. The first peak in disulphide is from sulphur 1s → σ*(S-S) transition, while in benzenethiol is to σ*(S-H) transition with a weak σ(S-C) character.[6.44] The second peak in both species have σ*(S-C) character overlapped with π*(C=C) of phenyl ring in both the disulphide and thiol. These transition differences showed by *ab initio* calculations can provide insights in targeting specific transitions that are absent in the other species for a better speciation in cases with very close energy position of the white line (thiols and disulphides).

6.4.5 Conclusion

In this study, highly resolved NEXAFS spectra of a group of disulphides with different ligand groups were studied by experimental and computational methods. These studies showed that the white lines of disulphides are dominated by two peaks that are not base line resolved with sulphur 1s → σ*(S-S) and σ*(S-C) transitions respectively.

However, in unsaturated disulphides the second peak also samples from the π*(C=C) of the phenyl ring in addition to σ*(S-C) transitions.

In asymmetric disulphides, the simulated NEXAFS spectrum is similar to the other disulphides but each peak is consisting of two nearly degenerate transitions as a result of asymmetric ligand groups around the sulphur atoms (methyl versus ethyl) in contrast to the symmetrically equivalent ligand groups. Although in this example of the asymmetric ligands (ethyl and methyl) the splitting effect is minimal on the shape and broadening of the white line, it is anticipated to be greater for functional groups of a different nature (e.g., phenyl compared to methyl).

In summary, the ligand groups attached to the sulphur atoms affect the shape, intensity and the relative splitting of the white line.[6.29] These changes are due to different transitions involved in the corresponding NEXAFS spectra as a result of bonding to different ligands (phenyl, benzyl),[6.29] symmetry (phenyl versus methyl) and different MO calculations.[6.29] However, in disulphides bonding to phenyl rings does not make any significant change in the energy position of the edge in contrast to thiols where the edge position has a blue shift in benzenethiol relative to aliphatic thiols.[6.44] Therefore, the speciation of aliphatic and unsaturated disulphides can be problematic due to feature overlap.

Comparison of the NEXAFS spectra of disulphides to thiols and thioethers, shows that the presence of (S-S) bond in disulphides causes a change in the shape and energy position of the white line due to the enhanced splitting of the first and second LUMOs.[6.29, 6.44] The energy of the edge position of the white line in disulphides, thiols, and thioethers has a trend as follow: thioethers > thiols > disulphides.

It is shown that the energy difference of the edge position can be used for speciation of disulphides from sulphides, and the enhanced width of the white line for an unknown sample in the energy regime of the disulphides can suggest the simultaneous presence of disulphides and sulphides.[6.29] However for speciation of thiols and disulphides, the edge positions are very close and specially the ligand groups attached to the sulphur atom can cause features overlap between these functional groups. However, IVO *ab initio* calculations showed that the first transition in disulphides is sulphur 1s → σ*(S-S) transition while in thiols is sulphur 1s → σ*(S-H) transition, indicating that the

overlapping features in the spectra of thiols and disulphides have different natures. Therefore, by targeting these transitions a good speciation can be obtained in speciation of disulphides from thiols.

6.4.6 References

6.1. Hua, R.; Wang, J.; Kong, H.; Liu, J.; Lu, X.; Xu, G., *Journal of Separation Science,* **2004,** *27* (9), 691-698.

6.2. Sevier, C. S.; Kaiser, C. A., *Nature Review Molecular Cell Biology,* **2002,** *3* (11), 836-847.

6.3. Inoue, T.; Takehara, K.; Shimizu, N.; Kitajima, Y.; Shinohara, K.; Ito, A., *Journal of X-ray Science and Technology,* **2011,** *19* (3), 313-320.

6.4. Rompel, A.; Cinco, R. M.; Latimer, M. J.; McDermott, A. E.; Guiles, R. D.; Quintanilha, A.; Krauss, R. M.; Sauer, K.; Yachandra, V. K.; Klein, M. P., *Proceedings of the National Academy of Sciences of the United States of America,* **1998,** *95* (11), 6122-6127.

6.5. Ito, A.; Inoue, T.; Takehara, K.; Shimizu, N.; Kitajima, Y.; Shinohara, K., *Journal of X-ray Science and Technology,* **2011,** *19* (2), 249-260.

6.6. Chauvistre, R.; Hormes, J.; Hartmann, E.; Etzenbach, N.; Hosch, R.; Hahn, J., *Chemical Physics,* **1997,** *223* (2-3), 293-302.

6.7. Vairavamurthy, A.; Manowitz, B.; Zhou, W. Q.; Jeon, Y. S., *Determination of HydrogenSulfide Oxidation-Products by Sulfur K-edge X-ray-Absorption Near-Edge Structure Spectroscopy*. In *Environmental Geochemistry of Sulfide Oxidation*, Alpers, C. N.; Blowes, D. W., Eds. **1994**, Vol. 550.

6.8. Brendebach, B.; Modrow, H., *Kautschuk Gummi Kunststoffe,* **2002,** *55* (4), 157-163.

6.9. Modrow, H., Hormes, J., Visel, F., Zimmer, R., *Rubber Chemistry and Technology,* **2001,** *74:2*, 281-294.

6.10. Steudel, R., *Chemical Reviews,* **2002,** *102* (11), 3905-3946.

6.11. Sarret, G.; Connan, J.; Kasrai, M.; Bancroft, G. M.; Charrié-Duhaut, A.; Lemoine, S.; Adam, P.; Albrecht, P.; Eybert-Bérard, L., *Geochimica et Cosmochimica Acta,* **1999,** *63* (22), 3767-3779.

6.12. Waldo, G. S.; Mullins, O. C.; Penner-Hahn, J. E.; Cramer, S. P., *Fuel,* **1992,** *71* (1), 53-57.

6.13. George, G. N.; Gorbaty, M. L., *Journal of the American Chemical Society,* **1989,** *111* (9), 3182-3186.

6.14. George, G. N.; Gorbaty, M. L.; Kelemen, S. R.; Sansone, M., *Energy & Fuels,* **1991,** *5* (1), 93-97.

6.15. Huffman, G. P.; Mitra, S.; Huggins, F. E.; Shah, N.; Vaidya, S.; Lu, F. L., *Energy & Fuels,* **1991,** *5* (4).

6.16. Huffman, G. P.; Shah, N.; Huggins, F. E.; Stock, L. M.; Chatterjee, K.; Kilbane, J. J.; Chou, M. I. M.; Buchanan, D. H., *Fuel,* **1995,** *74* (4).

6.17. Matsumoto, S.; Tanaka, Y.; Ishii, H.; Tanabe, T.; Kitajima, Y.; Kawai, J., *Spectrochimica Acta Part B: Atomic Spectroscopy,* **2006,** *61* (8), 991-994.

6.18. Wiltfong, R.; Mitra-Kirtley, S.; Mullins, O. C.; Andrews, B.; Fujisawa, G.; Larsen, J. W., *Energy & Fuels,* **2005,** *19* (5), 1971-1976.
6.19. Almkvist, G.; Boye, K.; Persson, I., *Journal of Synchrotron Radiation, 17*, 683-688.
6.20. Braun, A.; Janousch, M.; Sfeir, J.; Kiviaho, J.; Noponen, M.; Huggins, F. E.; Smith, M. J.; Steinberger-Wilckens, R.; Holtappels, P.; Graule, T., *Journal of Power Sources,* **2008,** *183* (2), 564-570.
6.21. Bolin, T. B., *Energy & Fuels,* **2010,** *24*, 5479-5482.
6.22. Prange, A.; Dahl, C.; Truper, H. G.; Behnke, M.; Hahn, J.; Modrow, H.; Hormes, J., *European Physical Journal D,* **2002,** *20* (3), 589-596.
6.23. Pickering, I. J.; George, G. N.; Yu, E. Y.; Brune, D. C.; Tuschak, C.; Overmann, J.; Beatty, J. T.; Prince, R. C., *Biochemistry,* **2001,** *40* (27), 8138-8145.
6.24. Frank, P.; Hedman, B.; Hodgson, K. O., *Inorganic Chemistry,* **1999,** *38* (2), 260-270.
6.25. Pickering, I. J.; Prince, R. C.; Divers, T.; George, G. N., *FEBS Letters,* **1998,** *441* (1), 11-14.
6.26. Fors, Y.; Jalilehvand, F.; Sandstrom, M., *Analytical Sciences,* **2011,** *27* (8), 785-792.
6.27. Jalilehvand, F., *Chemical Society Reviews,* **2006,** *35* (12), 1256-1268.
6.28. Prange, A.; Birzele, B.; Kramer, J.; Modrow, H.; Chauvistre, R.; Hormes, J.; Kohler, P., *Journal of Agricultural and Food Chemistry,* **2003,** *51* (25), 7431-7438.
6.29. Mijovilovich, A.; Pettersson, L. G. M.; de Groot, F. M. F.; Weckhuysen, B. M., *Journal of Physical Chemistry A,* **2010,** *114* (35), 9523-9528.
6.30. Pickering, T. J.; Prince, R. C.; Divers, T.; George, G. N., *FEBS Letters,* **1998,** *441* (1), 11-14.
6.31. Dezarnaud, C.; Tronc, M.; Hitchcock, A. P., *Chemical Physics,* **1990,** *142*, 455-462.
6.32. Dezarnaud, C.; Tronc, M.; Modelli, A., *Chemical Physics,* **1991,** *156* (1), 129-140.
6.33. Hitchcock, A. P.; Bodeur, S.; Tronc, M., *Physica B,* **1989,** *158* (1-3), 257-258.
6.34. Allegretti, F.; Bussolotti, F.; Woodruff, D. P.; Dhanak, V. R.; Beccari, M.; Di Castro, V.; Betti, M. G.; Mariani, C., *Surface Science,* **2008,** *602* (14), 2453-2462.
6.35. Hitchcock, A. P., *Journal de Physique IV (Proceedings),* **1986,** *T.47 C8 vol.2*, C8-575-C8578.
6.36. Perera, R. C. C.; Lavilla, R. E., *Journal of Chemical Physics,* **1986,** *84* (8), 4228-4234.
6.37. Sarangi, R.; Frank, P.; Hodgson, K. O.; Hedman, B., *Inorganica Chimica Acta,* **2008,** *361* (4), 956-964.
6.38. Mijovilovich, A.; Pettersson, L. G. M.; Mangold, S.; Janousch, M.; Susini, J.; Salome, M.; de Groot, F. M. F.; Weckhuysen, B. M., *Journal of Physical Chemistry A,* **2009,** *113* (12), 2750-2756.
6.39. Risberg, E. D.; Jalilehvand, F.; Leung, B. O.; Pettersson, L. G. M.; Sandstrom, M., *Dalton Transactions,* **2009,** (18), 3542-3558.
6.40. Nakamatsu, H.; Mukoyama, T.; Adachi, H., *Journal of Chemical Physics,* **1991,** *95* (5), 3167-3174.

6.41. Bodeur, S.; Hitchcock, A. P.; Kosugi, N., *Chemical Physics,* **1992,** *162* (2-3), 293-302.
6.42. Damian, E.; Jalilehvand, F.; Abbasi, A.; Pettersson, L. G. M.; Sandstrom, M., *Physica Scripta,* **2005,** *T115*, 1077-1079.
6.43. Kwiatek, W. M.; Czapla, J.; Podgorczyk, M.; Kisiel, A.; Konior, J.; Balerna, A., *Radiation Physics and Chemistry,* **2011,** *80* (10), 1104-1108.
6.44. Behyan, S.; Hu, Y. F.; Urquhart, S. G., *Journal of Chemical Physics,* **2011,** *134* (24), 244304-244307.
6.45. Hitchcock, A. P.; Horsley, J. A.; Stohr, J., *The Journal of Chemical Physics,* **1986,** *85* (9), 4835-4848.
6.46. Behyan, S.; Hu, Y.; Urquhart, S. G., *Sulfur 1s Near Edge X-ray Absorption Fine Structure Spectroscopy of Thiophenic and Aromatic Compounds*, Accepted by Journal of Chemical Physics, **2013**.
6.47. Kosugi, N., *Theoretica Chimica Acta,* **1987,** *72* (2), 149-173.
6.48. Kosugi, N.; Kuroda, H., *Chemical Physics Letters,* **1980,** *74* (3), 490-493.
6.49. Cooney, R. R.; Urquhart, S. G., *Journal of Physical Chemistry B,* **2004,** *108* (47), 18185-18191.
6.50. Otero, E.; Urquhart, S. G., *Journal of Physical Chemistry A,* **2006,** *110* (44), 12121-12128.
6.51. Ueda, K.; Okunishi, M.; Chiba, H.; Shimizu, Y.; Ohmori, K.; Sato, Y.; Shigemasa, E.; Kosugi, N., *Chemical Physics Letters,* **1995,** *236* (3), 311-317.
6.52. Urquhart, S. G.; Ade, H., *Journal of Physical Chemistry B,* **2002,** *106* (34), 8531-8538.
6.53. Urquhart, S. G.; Turci, C. C.; Tyliszczak, T.; Brook, M. A.; Hitchcock, A. P., *Organometallics,* **1997,** *16* (10), 2080-2088.
6.54. Urquhart, S. G.; Hitchcock, A. P.; Lehmann, J. F.; Denk, M., *Organometallics,* **1998,** *17* (11), 2352-2360.
6.55. Urquhart, S. G.; Smith, A. P.; Ade, H. W.; Hitchcock, A. P.; Rightor, E. G.; Lidy, W., *Journal of Physical Chemistry B,* **1999,** *103* (22), 4603-4610.
6.56. Otero, E.; Kosugi, N.; Urquhart, S. G., *Journal of Chemical Physics,* **2009,** *131* (11).
6.57. Lehmann, J. F.; Urquhart, S. G.; Ennis, L. E.; Hitchcock, A. P.; Hatano, K.; Gupta, S.; Denk, M. K., *Organometallics,* **1999,** *18* (10), 1862-1872.
6.58. Spartan 6.0; Wavefunction Inc.: Irvine, CA, **1994**.
6.59. Huo, B.; Hitchcock, A. P. *Simile2; McMaster University, Hamilton, ON*, **1996**.
6.60. Hitchcock, A. P.; Tronc, M., *Chemical Physics,* **1988,** *121* (2), 265-277.
6.61. Risberg, E. D.; Eriksson, L.; Mink, J.; Pettersson, L. G. M.; Skripkin, M. Y.; Sandstrom, M., *Inorganic Chemistry,* **2007,** *46* (20), 8332-8348.
6.62. Mori, R. A.; Paris, E.; Giuli, G.; Eeckhout, S. G.; Kavcic, M.; Zitnik, M.; Bucar, K.; Pettersson, L. G. M.; Glatzel, P., *Inorganic Chemistry,* **2010,** *49* (14), 6468-6473.
6.63. Mori, R. A.; Paris, E.; Giuli, G.; Eeckhout, S. G.; Kavcic, M.; Zitnik, M.; Bucar, K.; Pettersson, L. G. M.; Glatzel, P., *Analytical Chemistry,* **2009,** *81* (15), 6516-6525.

CHAPTER 7 SULPHUR 1S NEXAFS SPECTROSCOPY OF SULFOXIDES AND SULFONES

7.1 Description

This chapter is a copy of the manuscript under preparation, and explores the sulphur 1s NEXAFS spectra of sulfoxide and sulfones. This contribution includes a detailed study of the sulphur 1s NEXAFS spectra of these compounds and shows the chemical sensitivity of NEXAFS spectroscopy towards changing the ligand groups in these functionalities. It is shown that ligand group changes the position of the white line even for the same sulphur group. The experimental spectra have been analyzed by the aid of IVO *ab initio* calculations for assigning the spectral transitions. Both experiments and calculations contribute to improve the assignments of spectroscopic features relevant to speciation and quantification of sulphur compounds. The experimental and theoretical work for this study is provided in the following sections under the form of the manuscript.

7.2 Description of the Candidate's Contribution

For this contribution I was the primary researcher in terms of sample preparation, acquisition of experimental data, the simulation of NEXAFS spectra by IVO *ab initio* calculations, interpretation of the results, and writing of the manuscript. Dr Stephen G. Urquhart provided extensive guidance throughout the performance of the experiments, data analysis, interpretation of data, and simulations. He also assisted in writing and editing this document, however I played a greater role in writing this manuscript than in the previous paper. Dr. Yongfeng Hu assisted in acquiring the experimental spectra.

Dr. S. G. Urquhart, and Dr. Yongfeng Hu kindly gave me their permission for including this paper in this thesis, and agreed on my contribution in this document.

7.3 Relation of Contribution towards Research Objectives

This contribution was solely performed towards the objectives of the thesis research. This study is part of the study intended for the study of sulphur 1s NEXAFS spectroscopy of different sulphur functionalities. This contribution also explores the

effect of ligand groups on the shape and position of the white line for the same sulphur group.

Beside the experimental and computational sections provided in this manuscript, detailed descriptions of these sections are also provided in **Chapter 2** and **3** respectively. A full discussion of the results as part of the whole study of sulphur 1s NEXAFS spectra of different sulphur functionalities is provided in **Chapter 9**.

7.4 Sulphur 1s NEXAFS Spectroscopy of Sulfoxides and Sulfones

Shirin Behyan[1], Yongfeng Hu[2], Stephen G. Urquhart[1]*

1. Department of Chemistry, University of Saskatchewan, Saskatoon, SK, Canada S7N 5C9

2. Canadian Light Source, University of Saskatchewan, Saskatoon, SK, Canada S7N 0X4

Abstract

Speciation and quantification of sulphur functionalities using sulphur 1s Near Edge X-ray Absorption Fine Structure (NEXAFS) spectroscopy requires a well-defined and interpreted database of sulphur 1s NEXAFS spectra. In this study the high-resolution experimental sulphur 1s NEXAFS spectra of a series of sulfoxides and sulfones were obtained and the spectral transitions were assigned by the aid of *ab initio* calculations based on the Improved Virtual Orbital (IVO) approximation. Analysis of these spectra showed that the shape, broadening, and energy position of the white line in sulfones are highly dependent on the ligand groups attached to the sulphur atom. This can be ascribed to the higher oxidation state of the sulphur atom in this functional group with the consequent higher energy spacing among the molecular orbitals. The aromatic ligands in sulfones cause a red shift as well as broadening of the white line. This effect can pose speciation problems in cases where the white line in sulfones overlaps with the sulfoxide functional group.

Corresponding Author, email: stephen.urquhart@usask.ca

7.4.1 Introduction

The utilization of desulphurization and hydrogenation processes in the petroleum industries requires a good knowledge of the molecular composition of crude oil.[7.1] Similarly, the application of coal beneficiation technologies is dependent on knowledge of the chemistry of sulphur in the coal. Sulphur 1s NEXAFS spectroscopy has found wide spread use in the speciation and quantification of sulphur compounds in diverse areas such as archaeology,[7.2] fossil fuel studies,[7.3-13] geology,[7.14] and life science studies.[7.15-18] Development of X-ray microprobe and zone plate microscopy[7.19-23] has further extended sulphur 1s NEXAFS spectroscopy as a microanalytical method. Speciation studies based on NEXAFS spectroscopy however rely on the fact that each functional group has a NEXAFS fingerprint, mostly irrespective of the nature of the ligand groups attached to the sulphur atom. This simple assumption has been shown to be problematic in speciation studies where different functional groups have very similar NEXAFS spectra.[7.24-28]A good speciation, therefore, requires a complete database of well-defined sulphur 1s NEXAFS spectra obtained by experimental or computational methods.

Recently, we have studied the sulphur 1s NEXAFS spectra of different sulphur functionalities relevant to petroleum including thiols and thioethers,[7.25] disulphides,[7.27] and thiophenic compounds[7.28] by experimental and computational methods. In this study, we have expanded our studies to sulfoxide and sulfone functional groups and examined the effect of the ligand groups on the shape and energy position of the white line in the associated NEXAFS spectra.

Computational studies of sulphur 1s NEXAFS spectra of different functionalities have been provided in our previous work.[7.25, 7.27, 7.28] Theoretical studies of relevant sulfoxides and sulfones will be discussed here.

Francesco *et al*. have used time-dependent density functional (TDDFT) to study the sulphur 1s NEXAFS spectra of SO_2 to understand the interaction of SO_2 adsorbed on the TiO_2 (110) surface by comparing the spectrum of free SO_2 to the spectrum of the adsorbed species.[7.29] Similarly Cao *et al*., studied the surface interaction of SO_2 with Pd(111) with multiple scattering and self-consistent field DV-Xα method.[7.30] Mijovilovich *et al*. simulated the sulphur 1s NEXAFS spectra of dibenzothiophene,

dibenzothiophene sulfone and DL-methionine at several different levels of DFT theory and compared these to the experimental spectra. They concluded that the edge position for dibenzothiophene sulfone moves to higher energy relative to the other species because of its higher oxidation state.[7.1]

In this work, the effect of ligand groups as well as cyclic ring tension on the shape and energy position of the white line of sulphur 1s NEXAFS spectra of a series of sulfoxides and sulfones was studied (see **Scheme 7.1**). High quality experimental NEXAFS spectra were obtained for these molecules and were further analyzed by the aid of IVO *ab initio* calculations. Spectral transitions were assigned accordingly. The effect of the ligand group on the speciation of sulfoxides and sulfones is discussed.

7.4.2 Computational Methods

Ab initio calculations were performed with Kosugi's GSCF3 package program[7.31, 7.32] that is highly optimized for the calculations of the core excited states. This approach is based on the Improved Virtual Orbital (IVO) approximation, which explicitly includes the core hole in the Hartree-Fock Hamiltonian. The IVO approximation has been used for the simulation of core excitation spectra of organic and organometallic compounds at the carbon, nitrogen, oxygen, silicon, and sulphur 1s edges.[7.25, 7.31-41] IVO calculations are particularly effective for transitions below and near the ionization potential, where the sulphur 1s NEXAFS spectra show the strongest and most distinctive transitions.

The geometries used for these calculations (see **Scheme 7.1**) were provided by *ab initio* geometry optimization at the HF/6-31G* level, using the SPARTAN 06 program.[7.42] Frequency calculations were performed to ensure that the geometries were minimum structures (no imaginary frequencies). For the IVO calculations with GSCF3, the basis sets were similar to those used previously:[7.25, 7.28] hydrogen (41); second row atoms (carbon, nitrogen, and oxygen) (621 41); sulphur (with the core hole) (311111111 311111), with an additional d polarization function on the sulphur atom ($\zeta_d = 0.421$).

Simulated spectra were obtained from the IVO calculations by broadening each transition as a Gaussian line with the Simile2 package,[7.43] with the following energy dependent widths: 0.6 eV fwhm for bound states, 1.2 eV fwhm for states from the ionization potential (IP) to 4 eV above the IP, and 4.0 eV fwhm for states more than 4.0

eV above the IP. These widths are chosen to approximately track the experimental line width observed in the sulphur 1s NEXAFS spectra, although bound states are modeled narrower than experiment so that fine spectroscopic differences can be more readily observed.[7.37, 7.38, 7.41] MO plots are provided for selected unoccupied orbitals.

Molecular structure	IUPAC name
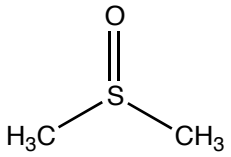	(Methylsulphinyl)methane
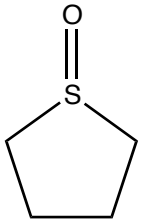	Tetrahydrothiophene 1-oxide
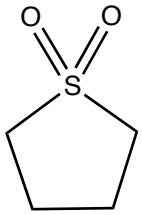	Tetrahydrothiophene 1,1-dioxide
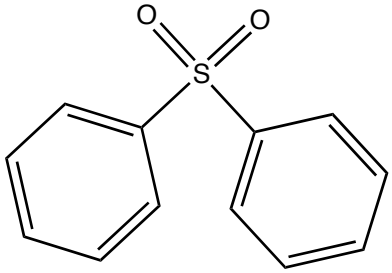	1,1'-Sulfonyldibenzene
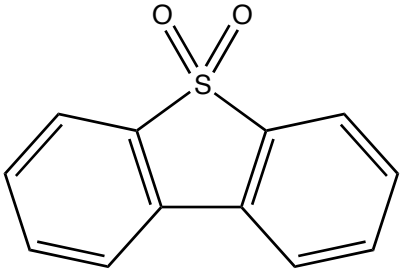	Dibenzo[b,d]thiophene 5,5-dioxide

Scheme 7.1 Molecular drawings of sulfoxides and sulfones.

7.4.3 Experimental

All compounds (methylsulfinyl)methane (dimethylsulfoxide) > 99.7%, tetrahydrothiophene 1-oxide 96%, tetrahydrothiophene 1,1-dioxide (sulfolane) 99%, 1,1'-sulfonyldibenzene (diphenylsulfone) 97%, dibenzo[b,d]thiophene 5,5-dioxide (dibenzothiophene sulfone) 97%) were of reagent grade and purchased from Sigma Aldrich and used without further purification.

Experimental spectra were obtained at the Canadian Light Source (CLS) on the Soft X-ray Microcharacterization Beamline (SXRMB), using a Si(111) crystal monochromator which provides an energy resolution of 0.24 eV. For solid samples (1,1'-sulfonyldibenzene, and dibenzo[b,d]thiophene 5,5-dioxide), a fine powder of the sample was spread homogeneously on a kapton tape (previously verified to be sulphur-free). For liquid samples ((methylsulphinyl)methane, tetrahydrothiophene 1-oxide, tetrahydrothiophene 1,1-dioxide) the sample was placed in a Teflon plate holder, which was then sandwiched by two layers of kapton tape. NEXAFS spectra were measured by fluorescence yield (FLY) detection with a Vortex 4-element Si drift detector in a He filled chamber. The FLY NEXAFS spectra were normalized by dividing each spectrum by an I_o spectrum, recorded simultaneously from an ion chamber upstream from the sample cell. The energy scale was calibrated to an absolute energy scale by setting the energy of a weak contaminant signal (presumed to be $FeSO_4$) found on the Be windows of the ion chamber to the calibrated value of 2481.62 eV.[7.25] This signal, recorded at the same time as all other spectra, was used as an internal calibration for our experiments.[7.25]

In this paper, the experimental and theoretical data are presented on their own energy scales, as the calculated IVO sulphur 1s simulations always appear at lower energy than the experimental NEXAFS spectra. This is due to the strong relativistic effects for the third row species.[7.25, 7.44-47]

7.4.4 Results and Discussion

In this section the experimental sulphur 1s NEXAFS spectra of a series of sulfoxides and sulfones are compared to the simulated spectra. The effect of ligand groups and the sulphur oxidation state on the shape and edge position of the NEXAFS spectra are discussed in more detail below.

7.4.4.1 Sulfoxides. Figure 7.1 compares the experimental sulphur 1s NEXAFS spectra of (methylsulfinyl)methane and tetrahydrothiophene 1-oxide to their simulated spectra. **Figure 7.2** presents molecular orbital (MO) plots of the unoccupied orbitals of the most intense pre-edge features in these spectra. **Table 7.1** presents the experimental energies and assignments for the most intense transitions below the ionization potential. **Table 7.2** presents the calculated energies, term values (term value = ionization potential – transition energy), ionization potentials, and transition character for the features appearing below the ionization potential.

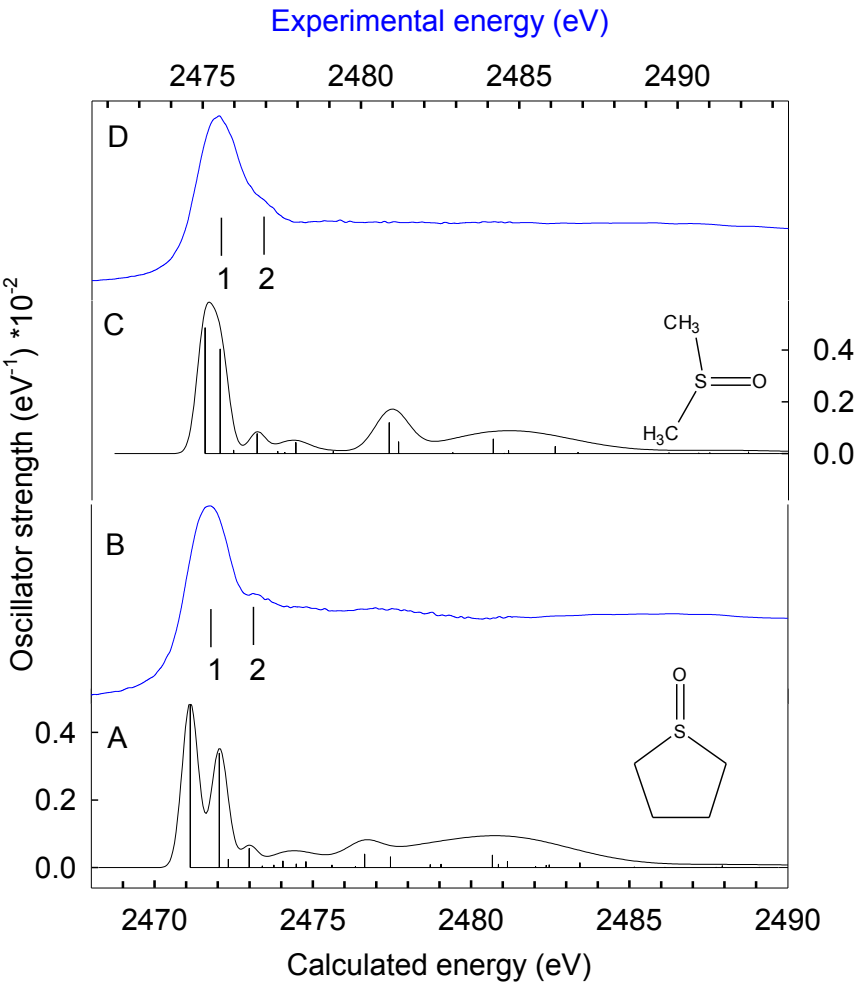

Figure 7.1 Comparison of experimental sulphur 1s NEXAFS spectra obtained in florescence yield detection to the simulated sulphur 1s spectra from *ab initio* IVO calculations. (A) Calculated spectrum of tetrahydrothiophene 1-oxide; (B) experimental spectrum of tetrahydrothiophene 1-oxide; (C) Calculated spectrum of (methylsulphinyl)methane; (D) Experimental spectrum of (methylsulphinyl)methane**.** The experimental energy scale (shown on the top of graph) is shifted relative to the calculated energy scale (shown at the bottom).

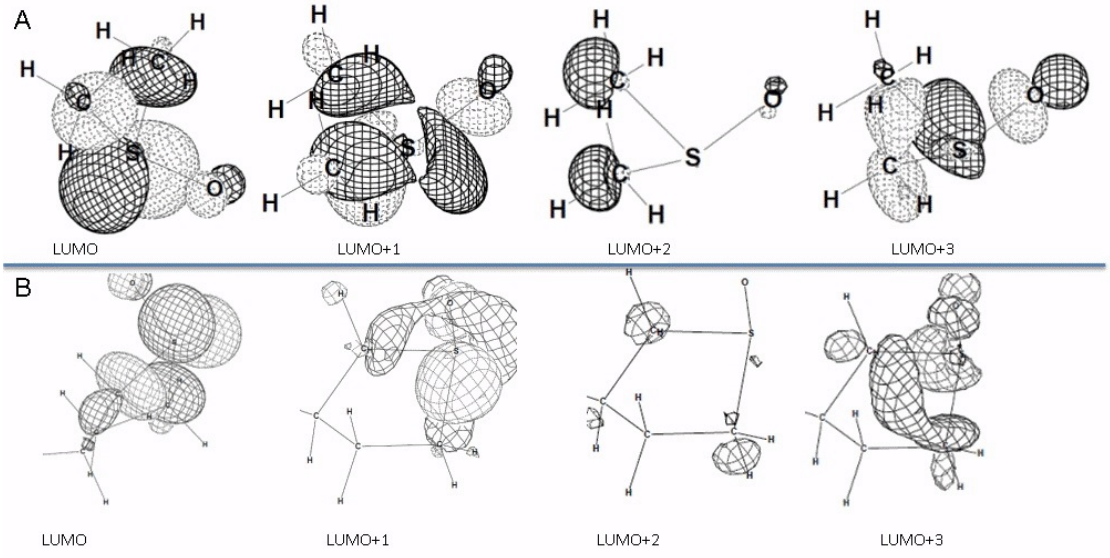

Figure 7.2 Unoccupied molecular orbital diagrams for the strong features contributing to the simulated spectra. (A) (methylsulphinyl)methane; (B) tetrahydrothiophene 1-oxide.

Compound name	Feature #	Energy (eV)	Assignments
(Methylsulphinyl)methane	1	2475.5	S 1s → π*(S=O)/σ*(S-C)/σ*(S-O)
	2	2476.9	S 1s → σ*(S-O), σ*(S-C)
Tetrahydrothiophene 1-oxide	1	2475.2	S 1s → π*(S=O)/σ*(S-C)/σ*(S-O)
	2	2476.6	S 1s → σ*(S-O)/ σ*(S-C)
Tetrahydrothiophene 1,1-dioxide	1	2478.8	S 1s → σ*(S-O)/σ*(S-C)/π*(S=O)
1,1'-Sulfonyldibenzene	1	2477.3	S 1s → σ*(S-O)/σ*(S-C)/π*(C=C)
	2	2478.5	S 1s → σ*(S-C)/π*(C=C)/ weak π*(S=O)
	3	2480.1	S 1s → σ*(S-O)/σ*(S-C)/ π*(S=O)
Dibenzo[b,d]thiophene 5,5-dioxide	1	2477.1	S 1s → σ*(S-O)/π*(C=C)/π*(S=C)
	2	2479.1	S 1s → σ*(S-O)/σ*(S-C) /π*(S=O)
	3	2480.5	S 1s → σ*(S-C)

Table 7.1 Transition energies and assignments for the experimental sulphur 1s NEXAFS spectra of (methylsulphinyl)methane, tetrahydrothiophene 1-oxide, tetrahydrothiophene 1,1-dioxide, 1,1′-sulfonyldibenzene, and dibenzo[b,d]thiophene 5,5-dioxide.

The experimental spectrum of tetrahydrothiophene 1-oxide consists of an intense white line at 2475.2 eV followed by a weak higher energy transition at 2476.6 eV, and broad features in the continuum. The white line of (methylsulfinyl)methane is at higher energy relative to tetrahydrothiophene 1-oxide, with the most intense transition at 2475.5 eV and a low intensity shoulder at 2476.9 eV, and broad features in the continuum. The lower energy of the white line transition in tetrahydrothiophene 1-oxide compared to (methylsulphinyl)methane can be attributed to the heterocyclic ring tension, similar to

cyclic thioethers studied previously.[7.25] This is confirmed by the lower calculated ionization potential of tetrahydrothiophene 1-oxide (see **Table 7.2**) as well.

The simulated spectra and MO plots for these molecules show that the first transition is from sulphur 1s → π*(S=O)/σ*(S-C) transition. The second transition has σ*(S-O)/σ*(S-C) character, while the third transition is poorly defined on the simple σ* and π* basis. The fourth transition is similar to the second transition.

(methylsulphinyl)methane Ionization Potential: 2473.716 eV				
#	Energy (eV)	Term Value (eV)	Oscillator Strength	Assignment
LUMO	2471.575	2.141	0.0031013	S 1s → π*(S=O)/σ*(S-C)
LUMO+1	2472.053	1.663	0.0025746	S 1s → σ*(S-O) /σ*(S-C)
LUMO+2	2472.481	1.235	0.0000814	Poorly defined
LUMO+3	2473.218	0.498	0.0004906	S 1s → σ*(S-O)/ σ*(S-C)

tetrahydrothiophene 1-oxide Ionization Potential: 2473.225 eV				
#	Energy (eV)	Term Value (eV)	Oscillator Strength	Assignment
LUMO	2471.126	2.099	0.0031171	S 1s → π*(S=O)/σ*(S-C)
LUMO+1	2472.044	1.181	0.0021615	S 1s → σ*(S-O) /σ*(S-C)
LUMO+2	2472.33	0.895	0.0001585	Poorly defined
LUMO+3	2472.986	0.239	0.0003592	S 1s → σ*(S-O)/ σ*(S-C)

tetrahydrothiophene 1,1-dioxide Ionization Potential: 2477.123 eV				
#	Energy (eV)	Term Value (eV)	Oscillator Strength	Assignment
LUMO	2475.778	1.345	0.0016458	S 1s → σ*(S-O) /σ*(S-C)
LUMO+1	2475.821	1.302	0.0036804	S 1s → π*(S=O)/σ*(S-C)
LUMO+2	2476.219	0.904	0.0009634	S 1s → σ*(S-O)
LUMO+3	2476.392	0.731	0.0005177	S 1s → σ*(S-C)/ weak σ*(S-O)
LUMO+4	2476.89	0.233	0.0000032	S 1s → σ*(S-O) /σ*(S-C)

1,1'-sulfonyldibenzene Ionization Potential: 2477.171 eV				
#	Energy (eV)	Term Value (eV)	Oscillator Strength	Assignment
LUMO	2474.382	2.789	0.0005050	S 1s → σ*(S-O) /σ*(S-C)/ π*(C=C)
LUMO+1	2475.687	1.484	0.0003181	S 1s → σ*(S-C)/π*(C=C)/ weak π*(S=O)
LUMO+2	2475.801	1.370	0.0000464	S 1s → π*(C=C)
LUMO+4	2477.172	-0.001	0.0001263	S 1s → σ*(S-O) /σ*(S-C)
LUMO+5	2477.814	-0.643	0.0021028	S 1s → π*(S=O)/ σ*(S-C)

dibenzo[b,d]thiophene 5,5-dioxide Ionization Potential:2477.271 eV				
#	Energy (eV)	Term Value (eV)	Oscillator Strength	Assignment
LUMO	2473.988	3.283	0.0002346	S 1s → σ*(S-O) /π*(S=C)/ π*(C=C)
LUMO+1	2475.169	2.102	0.0000574	S 1s → π*(C=C)
LUMO+2	2475.94	1.331	0.00000	S 1s → π*(C=C)
LUMO+3	2476.729	0.542	0.0037042	S 1s → π*(S=O)/σ*(S-C)
LUMO+4	2476.982	0.289	0.0019231	S 1s → σ*(S-O)
LUMO+5	2477.628	-0.357	0.0003576	S 1s → σ*(S-C)
LUMO+6	2478.158	-0.887	0.0001011	S 1s → σ*(S-C)

Table 7.2 Calculated energies, term values, ionization potentials, and assignments for sulphur 1s transitions appearing below the ionization potential for (methylsulphinyl)methane, tetrahydrothiophene 1-oxide, tetrahydrothiophene 1,1-dioxide, 1,1'-sulfonyldibenzene, and dibenzo[b,d]thiophene 5,5-dioxide from *ab initio* IVO calculations.

On this basis the white line in the sulphur 1s NEXAFS spectra of both sulfoxide species is assigned as an overlap of the low energy sulphur 1s → π*(S=O)/σ*(S-C) transition and a higher energy sulphur 1s → σ*(S-O)/σ*(S-C) transition. The second peak (peak 2) in both spectra is assigned to σ*(S-O)/σ*(S-C) character.

In summary, the NEXAFS spectra of sulfoxides consist of an intense white line followed by a weak higher energy transition and broad features in the continuum. The

white line in sulfoxide has moved to higher energies compared to thiols and thioethers,[7.25] disulphides[7.28] and thiophenic compounds.[7.27] This is expected because of the higher oxidation state of sulphur in this functional group. The white line is assigned as an overlap of the low energy sulphur 1s → π*(S=O)/σ*(S-C) transition and a higher energy sulphur 1s → σ*(S-O)/σ*(S-C) transition. In contrast to thiophenic compounds with a low intensity sulphur 1s → π*(S=C) transition[7.27], the sulphur 1s → π*(S=O) transition in sulfoxides has a higher intensity, with additional σ*(S-C) character. This higher intensity originates from the higher sulphur oxidation state, which gives a higher contraction of the 1s and 3p orbitals that results in stronger overlap of orbitals.[7.48] The heterocyclic ring tension also affects the position and shape of the white line slightly shifting to lower energy position compared to noncyclic ligands.

7.4.4.2 Sulfones. Figure 7.3 presents the experimental sulphur 1s NEXAFS spectra of tetrahydrothiophene 1,1-dioxide, 1,1'-sulfonyldibenzene, and dibenzo[b,d]thiophene 5,5-dioxide and compares these spectra with the corresponding simulated spectra. **Figure 7.4** presents MO plots of the unoccupied orbitals of the most intense pre-edge features in these spectra. **Table 7.1** presents the experimental energies and assignments for the most intense transitions below the ionization potential. **Table 7.2** presents the calculated energies, term values, ionization potentials, and transition character for the features appearing below the ionization potential. These results are reviewed on a molecule-by-molecule basis below.

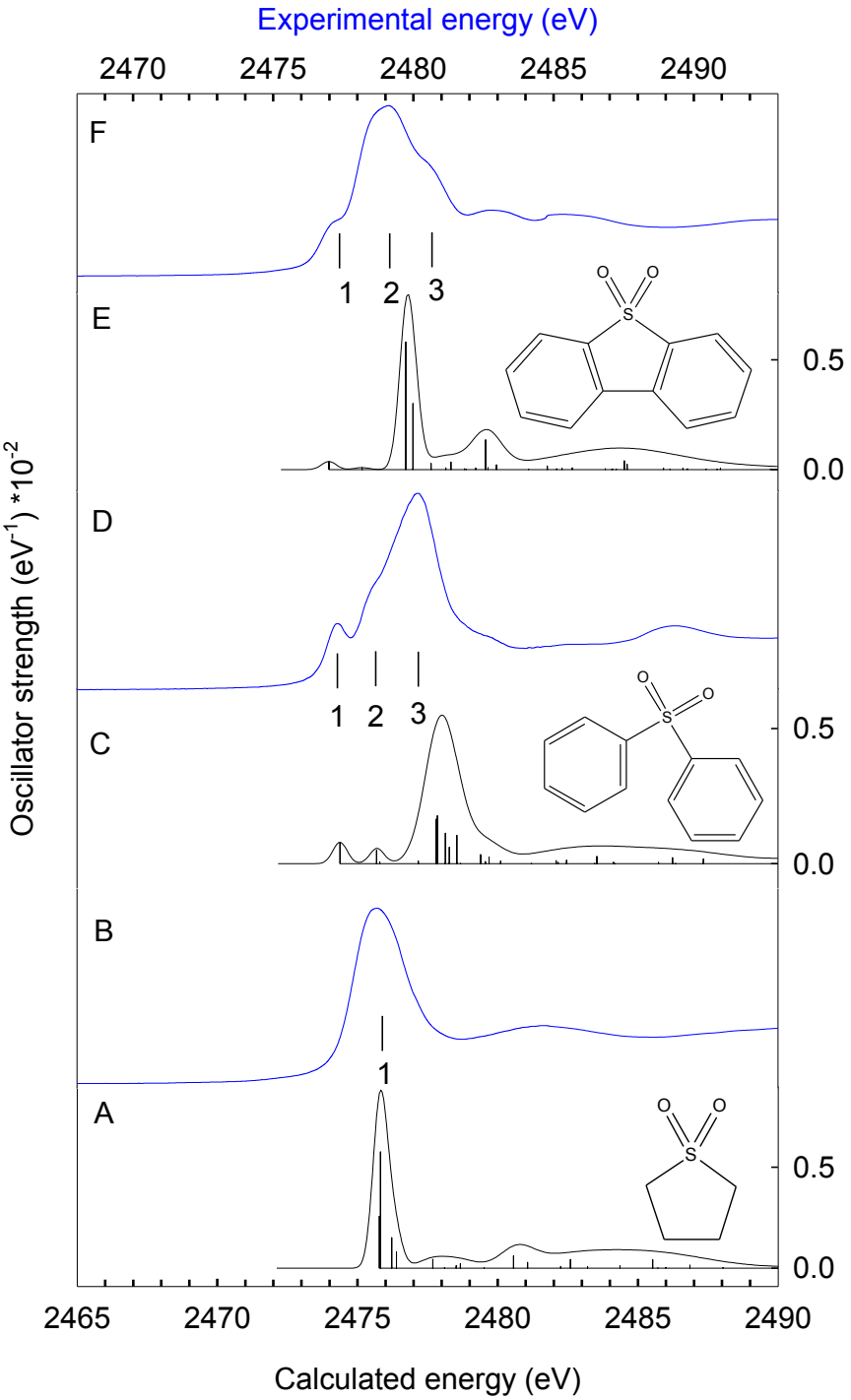

Figure 7.3 Comparison of experimental sulphur 1s NEXAFS spectra obtained in florescence yield detection to the simulated sulphur 1s spectra from *ab initio* IVO calculations. (A) Calculated spectrum of tetrahydrothiophene 1,1-dioxide; (B) experimental spectrum of tetrahydrothiophene 1,1-dioxide**;** (C) calculated spectrum of 1,1'-sulfonyldibenzene; (D) Experimental spectrum of 1,1'-sulfonyldibenzene**;** (E) calculated spectrum of dibenzo[b,d]thiophene 5,5-dioxide; (F) Experimental spectrum of dibenzo[b,d]thiophene 5,5-dioxide.

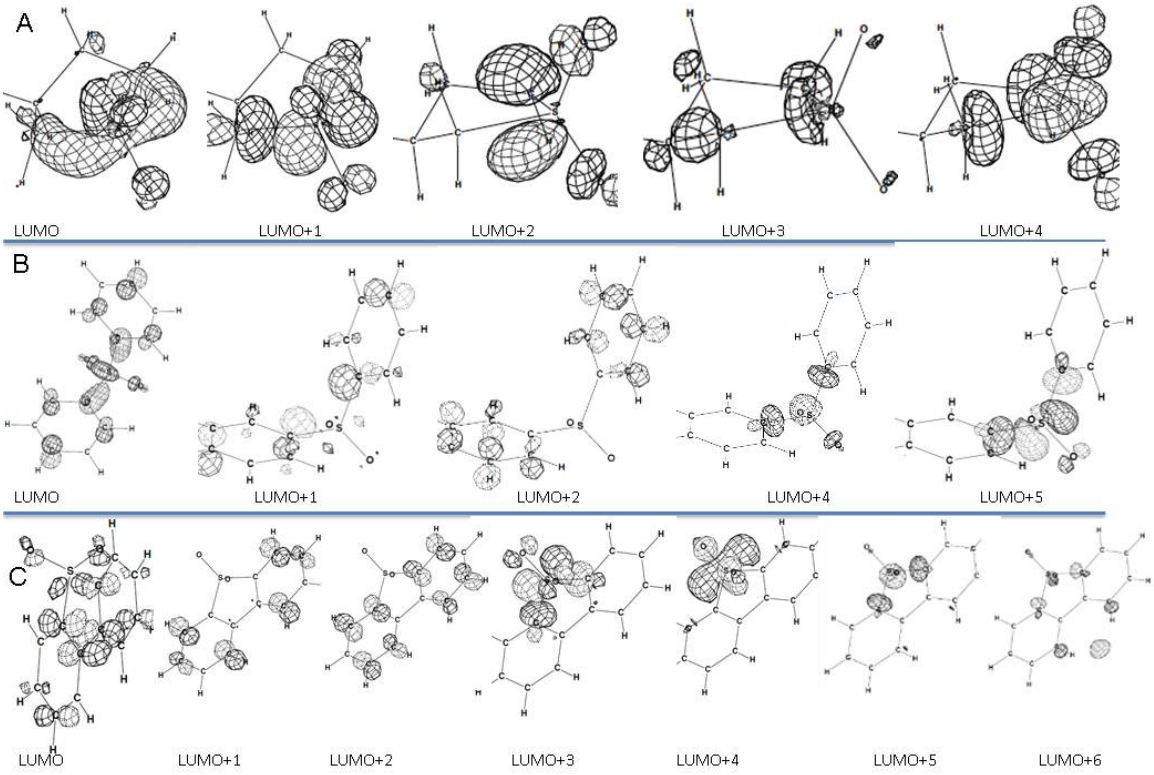

Figure 7.4 Unoccupied molecular orbital diagrams for the strong features contributing to the simulated spectra. (A) tetrahydrothiophene 1,1-dioxide; (B) 1,1'-sulfonyldibenzene; (C) dibenzo[b,d]thiophene 5,5-dioxide.

Tetrahydrothiophene 1,1-dioxide. The experimental spectrum of tetrahydrothiophene 1,1-dioxide consists of an intense white line at 2477.3 eV followed by broad features in the continuum.

The simulated spectrum of this molecule consists of four closely spaced transitions that overlap to create the white line of the simulated NEXAFS spectrum. The LUMO and LUMO+1 are closely spaced in energy with σ*(S-O)/σ*(S-C), and π*(S=O)/σ*(S-C) character respectively. The third transition however has a pure σ*(S-O) character, while the other transitions have σ*(S-O)/σ*(S-C) character.

On this basis, the white line of the experimental spectrum is assigned as the overlap of the mixture of sulphur 1s → σ*(S-O)/σ*(S-C), π*(S=O)/σ*(S-C) transition, and σ*(S-O)/σ*(S-C) character.

1,1′-sulfonyldibenzene. The experimental spectrum of this molecule consists of a low energy transition at 2477.3 eV, followed by a low energy shoulder at 2478.5 eV

superimposed on an intense white line transition at 2480.1 eV, and broad features in the continuum.

The simulated spectrum is similar to the experiment in the presence of two low energy transitions followed by a higher intensity transition of the white line; however the first two transitions are not baseline resolved in the experimental spectrum because of lifetime broadening.

The first transition in the simulated spectrum is from sulphur 1s → σ*(S-O)/σ*(S-C) transition that also samples the π*(C=C) of the phenyl ring. The LUMO+1 however, has sulphur 1s → σ*(S-C) character that again samples from the π*(C=C) of phenyl ring as well as a weak π*(S=O) character. LUMO+4 is sulphur 1s → σ*(S-O)/σ*(S-C) transition, and the last transition is sulphur 1s → π*(S=O)/σ*(S-C) transition.

The low energy shoulder in the experimental white line therefore is assigned as sulphur 1s → σ*(S-O)/σ*(S-C) transition that samples from the π*(C=C) of the phenyl ring. Peak 2 however is sulphur 1s → σ*(S-C) transition that samples from the π*(C=C) of phenyl ring as well as weak π*(S=O) character, and the intense transition (peak 3) consist of the overlap of π*(S=O) and the σ*(S-O)/σ*(S-C) transitions.

In this molecule, the presence of the phenyl ring causes a red shift, as well as broadening of the white line relative to tetrahydrothiophene 1,1'-dioxide. The electron withdrawing character of the phenyl ring causes the LUMOs to be far spaced in energy and shifts the π*(S=O) transition to higher energies compared to tetrahydrothiophene 1,1'-dioxide. This electron withdrawing effect is confirmed by the higher calculated Ionization Potential (I.P) of this molecule. The phenyl rings also impose the π*(C=C) character in LUMOs and cause the first two LUMOs to shift to lower energies. This red energy shift of the LUMO and LUMO+1 can be attributed to the stability of the excited state as a result of electron delocalization over phenyl rings.

Dibenzo[b,d]thiophene 5,5-dioxide. The white line of the experimental spectrum for this molecule consists of a low intensity low energy shoulder at 2477.1 eV followed by an intense transition at 2479.1 eV and a higher energy shoulder at 2480.5 eV followed by broad features in the continuum. The simulated NEXAFS spectrum is similar to the experimental spectrum except than the intensity of the experimental high-energy shoulder (peak 3).

The first transition in the simulated NEXAFS spectrum has sulphur 1s → σ*(S-O) character that also samples from the π*(C=C) of the aromatic rings. The second and third transitions have π*(C=C) character, while the forth transition has sulphur 1s → π*(S=O)/σ*(S-C) character. The sulphur 1s → LUMO+4 transition has pure σ*(S-O) character, while the subsequent transitions have pure σ*(S-C) character.

On this basis, the first peak in the experimental NEXAFS spectrum is assigned as sulphur 1s → σ*(S-O) transition that also samples from the π*(C=C) of the aromatic rings. The second peak consists of the overlap of sulphur 1s → π*(C=C) and π*(S=O) transitions as well as to σ*(S-O)/σ*(S-C) transition. Peak (3) at 2480.5 eV is a pure sulphur 1s → σ*(S-C) transition.

In summary, the higher oxidation state of the sulphur atom in sulfones compared to sulfoxides causes a shift to blue energy of the white line as well as the enhanced splitting of the LUMOs which in turn causes the broadening of the white line compared to other sulphur functional groups.[7.1, 7.24, 7.25, 7.27, 7.28]The higher oxidation state causes a stronger overlap between the contracted 1s and 3p orbitals and results in high energy differences between LUMOs. The aromaticity of the central ring results in a higher calculated sulphur I.P for this molecule.

7.4.5 Conclusion

In this study, sulphur 1s NEXAFS spectra of a group of sulfoxides and sulfones have been studied by experimental and computational methods using IVO *ab initio* calculations. Because of the higher oxidation state of the sulphur atom in these molecules the edge position of the white line has shifted to higher energies compared to other studied functionalities.[7.25, 7.27, 7.28] In sulfoxides, the NEXAFS spectra consist of an intense white line followed by a weak higher energy transition and broad features in the continuum. Similar to cyclic thioethers the cyclic ring tension causes a red shift in the edge position of the white line. Based on the IVO *ab initio* calculations the first peak is assigned as an overlap of the low energy sulphur 1s → π*(S=O)/σ*(S-C) transition and a higher energy sulphur 1s → σ*(S-O)/σ*(S-C) transition. The second peak in both spectra is assigned to σ*(S-O)/σ*(S-C) transition. In sulfones however, the white line of the NEXAFS spectra shift to higher energies relative to sulfoxides because of the higher

oxidation state of the sulphur atom. The ligand groups have high impact on the shape and broadening of the white line as a result of enhanced splitting of the LUMOs. The most intense transition of the white line in these species is assigned as sulphur 1s → σ*(S-C)/σ*(S-O) transition, which also have π*(S=O) transition as well. Additionally the π*(S=O) transitions move to higher energies in sulfones with phenyl rings compared to tetrahydrothiophene 1,1-dioxide. This transition energy shift can be attributed to the electron withdrawing character of the phenyl rings. This is also confirmed by the higher calculated I.P for species with phenyl rings; the I.P is even higher for the molecule with aromatic character (dibenzo[b,d]thiophene 5,5-dioxide). For speciation of sulfones and sulfoxide the energy difference in edge position can be used for differentiation of these functional groups. In sulfoxides the edge position is sensitive to the cyclic ring tension and shifts the white line to lower energies compared to noncyclic ones. In sulfones however, the ligand groups can cause broadening of the white line, which can cause feature overlap and poses speciation problems in these compounds. Also a NEXAFS spectrum of an unknown sample with enhanced white line width in sulfones energy regime shows the presence of species with phenyl rings. The comparison of our simulated spectra with experiment is excellent and the spectroscopic differences in transitions provided by the calculations as well as other information on a complex sample can be used for revealing the chemical composition of the sample or composition assignments where possible.

7.4.6 References

7.1. Mijovilovich, A.; Pettersson, L. G. M.; Mangold, S.; Janousch, M.; Susini, J.; Salome, M.; de Groot, F. M. F.; Weckhuysen, B. M., *Journal of Physical Chemistry A,* **2009,** *113* (12), 2750-2756.

7.2. Sandstrom, M.; Jalilehvand, F.; Persson, I.; Gelius, U.; Frank, P.; Hall-Roth, I., *Nature,* **2002,** *415* (6874), 893-897.

7.3. Sarret, G.; Connan, J.; Kasrai, M.; Bancroft, G. M.; Charrié-Duhaut, A.; Lemoine, S.; Adam, P.; Albrecht, P.; Eybert-Bérard, L., *Geochimica et Cosmochimica Acta,* **1999,** *63* (22), 3767-3779.

7.4. Waldo, G. S.; Mullins, O. C.; Penner-Hahn, J. E.; Cramer, S. P., *Fuel,* **1992,** *71* (1), 53-57.

7.5. George, G. N.; Gorbaty, M. L., *Journal of the American Chemical Society,* **1989,** *111* (9), 3182-3186.

7.6. George, G. N.; Gorbaty, M. L.; Kelemen, S. R.; Sansone, M., *Energy & Fuels,* **1991,** *5* (1), 93-97.
7.7. Huffman, G. P.; Mitra, S.; Huggins, F. E.; Shah, N.; Vaidya, S.; Lu, F. L., *Energy & Fuels,* **1991,** *5* (4).
7.8. Huffman, G. P.; Shah, N.; Huggins, F. E.; Stock, L. M.; Chatterjee, K.; Kilbane, J. J.; Chou, M. I. M.; Buchanan, D. H., *Fuel,* **1995,** *74* (4).
7.9. Matsumoto, S.; Tanaka, Y.; Ishii, H.; Tanabe, T.; Kitajima, Y.; Kawai, J., *Spectrochimica Acta Part B: Atomic Spectroscopy,* **2006,** *61* (8), 991-994.
7.10. Wiltfong, R.; Mitra-Kirtley, S.; Mullins, O. C.; Andrews, B.; Fujisawa, G.; Larsen, J. W., *Energy & Fuels,* **2005,** *19* (5), 1971-1976.
7.11. Almkvist, G.; Boye, K.; Persson, I., *Journal of Synchrotron Radiation, 17*, 683-688.
7.12. Braun, A.; Janousch, M.; Sfeir, J.; Kiviaho, J.; Noponen, M.; Huggins, F. E.; Smith, M. J.; Steinberger-Wilckens, R.; Holtappels, P.; Graule, T., *Journal of Power Sources,* **2008,** *183* (2), 564-570.
7.13. Bolin, T. B., *Energy & Fuels,* **2010,** *24*, 5479-5482.
7.14. Majzlan, J.; Myneni, S. C. B., *Environmental Science & Technology,* **2005,** *39* (1), 188-194.
7.15. Sevier, C. S.; Kaiser, C. A., *Nature Review Molecular Cell Biology,* **2002,** *3* (11), 836-847.
7.16. Inoue, T.; Takehara, K.; Shimizu, N.; Kitajima, Y.; Shinohara, K.; Ito, A., *Journal of X-ray Science and Technology,* **2011,** *19* (3), 313-320.
7.17. Rompel, A.; Cinco, R. M.; Latimer, M. J.; McDermott, A. E.; Guiles, R. D.; Quintanilha, A.; Krauss, R. M.; Sauer, K.; Yachandra, V. K.; Klein, M. P., *Proceedings of the National Academy of Sciences of the United States of America,* **1998,** *95* (11), 6122-6127.
7.18. Ito, A.; Inoue, T.; Takehara, K.; Shimizu, N.; Kitajima, Y.; Shinohara, K., *Journal of X-ray Science and Technology,* **2011,** *19* (2), 249-260.
7.19. Howells, M.; Jacobsen, C.; Warwick, T.; Bos, A., *Principles and Applications of Zone Plate X-Ray Microscopes*. In *Science of Microscopy*, **2007**, 835-926.
7.20. Van der Snickt, G.; Dik, J.; Cotte, M.; Janssens, K.; Jaroszewicz, J.; De Nolf, W.; Groenewegen, J.; Van der Loeff, L., *Analytical Chemistry,* **2009,** *81* (7), 2600-2610.
7.21. Cotte, M.; Welcomme, E.; Sole, V. A.; Salome, M.; Menu, M.; Walter, P.; Susini, J., *Analytical Chemistry,* **2007,** *79* (18), 6988-6994.
7.22. Prietzel, J.; Thieme, J.; Neuhausler, U.; Susini, J.; Kogel-Knabner, I., *European Journal of Soil Science,* **2003,** *54* (2), 423-433.
7.23. Norlund, K. L. I.; Southam, G.; Tyliszczak, T.; Hu, Y. F.; Karunakaran, C.; Obst, M.; Hitchcock, A. P.; Warren, L. A., *Environmental Science & Technology,* **2009,** *43* (23), 8781-8786.
7.24. Mijovilovich, A.; Pettersson, L. G. M.; de Groot, F. M. F.; Weckhuysen, B. M., *Journal of Physical Chemistry A,* **2010,** *114* (35), 9523-9528.
7.25. Behyan, S.; Hu, Y. F.; Urquhart, S. G., *Journal of Chemical Physics,* **2011,** *134* (24), 244304-244307.
7.26. Sarangi, R.; Frank, P.; Hodgson, K. O.; Hedman, B., *Inorganica Chimica Acta,* **2008,** *361* (4), 956-964.

7.27. Behyan, S.; Hu, Y.; Urquhart, S. G., *Sulfur 1s Near Edge X-ray Absorption Fine Structure Spectroscopy of Thiophenic and Aromatic Compounds*, Accepted by *Journal of Chemical Physics*, **2013**.
7.28. Behyan, S.; Hu, Y.; Urquhart, S. G., *Chemical Sensitivity of Sulfur 1s NEXAFS Spectroscopy towards the Speciation of Disulfides*. In *Preparation*.
7.29. De Francesco, R.; Stener, M.; Fronzoni, G., *Physical Chemistry Chemical Physics,* **2009,** *11* (8), 1146-1151.
7.30. Cao, S.; Tang, J. C.; Wang, L.; Zhu, P.; Shen, S. L., *Journal of Physics-Condensed Matter,* **2002,** *14* (12), 3099-3113.
7.31. Kosugi, N., *Theoretica Chimica Acta,* **1987,** *72* (2), 149-173.
7.32. Kosugi, N.; Kuroda, H., *Chemical Physics Letters,* **1980,** *74* (3), 490-493.
7.33. Cooney, R. R.; Urquhart, S. G., *Journal of Physical Chemistry B,* **2004,** *108* (47), 18185-18191.
7.34. Otero, E.; Urquhart, S. G., *Journal of Physical Chemistry A,* **2006,** *110* (44), 12121-12128.
7.35. Ueda, K.; Okunishi, M.; Chiba, H.; Shimizu, Y.; Ohmori, K.; Sato, Y.; Shigemasa, E.; Kosugi, N., *Chemical Physics Letters,* **1995,** *236* (3), 311-317.
7.36. Urquhart, S. G.; Ade, H., *Journal of Physical Chemistry B,* **2002,** *106* (34), 8531-8538.
7.37. Urquhart, S. G.; Turci, C. C.; Tyliszczak, T.; Brook, M. A.; Hitchcock, A. P., *Organometallics,* **1997,** *16* (10), 2080-2088.
7.38. Urquhart, S. G.; Hitchcock, A. P.; Lehmann, J. F.; Denk, M., *Organometallics,* **1998,** *17* (11), 2352-2360.
7.39. Urquhart, S. G.; Smith, A. P.; Ade, H. W.; Hitchcock, A. P.; Rightor, E. G.; Lidy, W., *Journal of Physical Chemistry B,* **1999,** *103* (22), 4603-4610.
7.40. Otero, E.; Kosugi, N.; Urquhart, S. G., *Journal of Chemical Physics,* **2009,** *131* (11).
7.41. Lehmann, J. F.; Urquhart, S. G.; Ennis, L. E.; Hitchcock, A. P.; Hatano, K.; Gupta, S.; Denk, M. K., *Organometallics,* **1999,** *18* (10), 1862-1872.
7.42. Spartan 6.0; Wavefunction Inc.: Irvine, CA, **1994**.
7.43. Huo, B.; Hitchcock, A. P. *Simile2; McMaster University, Hamilton, ON*, **1996**.
7.44. Damian, E.; Jalilehvand, F.; Abbasi, A.; Pettersson, L. G. M.; Sandstrom, M., *Physica Scripta,* **2005,** *T115*, 1077-1079.
7.45. Risberg, E. D.; Eriksson, L.; Mink, J.; Pettersson, L. G. M.; Skripkin, M. Y.; Sandstrom, M., *Inorganic Chemistry,* **2007,** *46* (20), 8332-8348.
7.46. Mori, R. A.; Paris, E.; Giuli, G.; Eeckhout, S. G.; Kavcic, M.; Zitnik, M.; Bucar, K.; Pettersson, L. G. M.; Glatzel, P., *Inorganic Chemistry,* **2010,** *49* (14), 6468-6473.
7.47. Mori, R. A.; Paris, E.; Giuli, G.; Eeckhout, S. G.; Kavcic, M.; Zitnik, M.; Bucar, K.; Pettersson, L. G. M.; Glatzel, P., *Analytical Chemistry,* **2009,** *81* (15), 6516-6525.
7.48. Jalilehvand, F., *Chemical Society Reviews,* **2006,** *35* (12), 1256-1268.

CHAPTER 8 SULPHUR 1S NEAR EDGE X-RAY ABSORPTION FINE STRUCTURE OF THIOPHENIC AND AROMATIC THIOETHER COMPOUNDS

8.1 Description

This chapter is a copy of the manuscript under preparation to be submitted to the Journal of Chemical Physics. In this contribution we have expanded our study to thiophenic compounds. The sulphur 1s NEXAFS spectra of these compounds have been acquired in gas and condensed phases. These high-resolution spectra have been further analyzed with the aid of *ab initio* calculations. Systematic differences with phase are also explored. The experimental and theoretical work for this study is provided in the following sections under the form of the manuscript accepted by the Journal of Chemical Physics.

The following article has been accepted by the Journal of Chemical Physics. After it is published, it will be found at (http://link.aip.org/link/jcp)

8.2 Description of the Candidate's Contribution

For this contribution I was the primary researcher in terms of sample preparation, acquisition of experimental data, the simulation of NEXAFS spectra by *ab initio* calculations, the interpretation of the results, and writing of the manuscript. Dr Stephen G. Urquhart was greatly involved in writing, and editing of this document and provided extensive guidance throughout the performance of the experiments, data analysis, interpretation of data, and simulations. Dr. Yongfeng Hu assisted and helped in acquiring the experimental spectra.

Dr. S. G. Urquhart, and Dr. Yongfeng Hu kindly gave me their permission for including this paper in this thesis, and agreed on my contribution in this document.

8.3 Relation of Contribution towards research objectives

This contribution was solely performed towards the objectives of the thesis research. This study is part of the research intended for the study of sulphur 1s NEXAFS spectroscopy of different sulphur functionalities, and explores the sulphur 1s NEXAFS spectra of thiophenic compounds in gas and condensed phases.

Beside the experimental and computational sections provided in this manuscript, detailed descriptions of these sections are also provided in **Chapter 2** and **3** respectively. A full

discussion of the results as part of the whole study of sulphur 1s NEXAFS spectra of different sulphur functionalities is provided in **Chapter 9**.

8.4 Sulphur 1s Near Edge X-ray Absorption Fine Structure Spectroscopy of Thiophenic and Aromatic Thioether Compounds

Shirin Behyan[1], Yongfeng Hu[2], Stephen G. Urquhart[1]*

1. Department of Chemistry, University of Saskatchewan, Saskatoon, SK, Canada S7N 5C9

2. Canadian Light Source, University of Saskatchewan, Saskatoon, SK, Canada S7N 0X4

Abstract

Thiophenic compounds are major constituents of fossil fuels and pose problems for fuel refinement. The quantification and speciation of these compounds is of great interest in different areas such as biology, fossil fuels studies, geology, and archaeology. Sulphur 1s Near-Edge X-ray Absorption Fine Structure (NEXAFS) spectroscopy has emerged as a qualitative and quantitative method for sulphur speciation. A firm understanding of the sulphur 1s NEXAFS spectra of organosulphur species is required for these analytical studies. To support this development, the sulphur 1s NEXAFS spectra of simple thiols and thioethers was previously examined, and is now extended to studies to thiophenic and aromatic thioether compounds, in the gas and condensed phases. High-resolution spectra have been further analyzed with the aid of improved virtual orbital (IVO) and Δ(SCF) *ab initio* calculations. Experimental sulphur 1s NEXAFS spectra show fine features predicted by calculation, and the combination of experiment and calculation has been used to improve the assignment of spectroscopic features important for the speciation and quantification of sulphur compounds. Systematic differences between gas and condensed phases are also explored; these differences suggest a significant role for conformational effects in the NEXAFS spectra of condensed species.

Corresponding Author, email: stephen.urquhart@usask.ca

8.4.1 Introduction

Sulphur compounds are an environmentally significant constituent of fossil fuels.[8.1] The quality and utilization of fossil fuels depends on their sulphur content as sulphur combustion products can impede the performance of catalytic converters. The anthropogenic emission and combustion of sulphur compounds produces poisonous compounds such as H_2S, SO_2, and SO_3, with the consequent acidification of water.[8.2, 8.3] Knowledge of the molecular composition of crude oil is needed to improve desulphurization and hydrogenation processes in the petroleum industries.[8.3]

Similarly, the application of coal beneficiation technologies is dependent on knowledge of the chemistry of sulphur in the coal. As thiophenic and thioether compounds are an important family of sulphur compounds in crude oil,[8.4-9] the study of this class of sulphur compounds is of keen analytical interest.

Near Edge X-ray Absorption Fine Structure (NEXAFS) spectroscopy is a powerful technique for studying the chemical form and quantity of sulphur species.[8.10] Sulphur 1s NEXAFS has been used for speciation and quantification of sulphur compounds in fossil fuels,[8.11-17] magmatic systems,[8.18] waterlogged wood from historical shipwrecks,[8.19] soils,[8.20] coal samples,[8.1] studies of the surface adsorption by thiol and thiolate species,[8.21-25] the sulphur chemistry of polymers,[8.26, 8.27] photographic materials,[8.28] and in biological systems[8.29-32] such as study of biological transformation in cancerous cells.[8.33] The ratio of thiols to disulphides, which affects the functionality of many proteins, has been determined by sulphur 1s NEXAFS spectroscopy.[8.34] NEXAFS spectroscopy has been further extended to a microanalytical method with the development of X-ray microprobe and zone plate microscopy.[8.35-39]

In this work, the sulphur 1s NEXAFS spectra of the most relevant thiophenic and aromatic thioether species found in petroleum are studied in the gas, liquid and condensed phases. These NEXAFS spectra have been further analyzed with the aid of *ab initio* Hartree-Fock calculations. The effect of phase on the NEXAFS spectra and the nature of Rydberg-valence mixing of transitions have also been studied.

In previous studies, spectral transitions of organosulphur compounds with different functionalities have been assigned on an empirical basis,[8.21, 8.29, 8.32, 8.40-45] with some recent computational studies.[8.3, 8.46-49] There have been few theoretical studies on

sulphur 1s NEXAFS spectra of organosulphur compounds until recently.[8.3, 8.46-54] Sulphur 1s NEXAFS calculations of organosulphur species have been reviewed in a recent study of aliphatic thioethers and thiols;[8.54] only studies relevant to this work are briefly mentioned here. Hitchcock *et al*. used MS-Xα calculations to interpret spectral transitions in thiophene and thiolane species at sulphur 1s, and 2p edges.[8.49] Mijovilovich *et al*. used DFT calculations to show that ligand groups attached to a sulphur atom (phenyl versus benzyl, etc.) and sulphur-sulphur bonding have a significant effect on the shape of the sulphur 1s NEXAFS spectra of sulphides and disulphides.[8.46] Mijovilovich *et al*. also simulated the sulphur 1s NEXAFS spectra of dibenzothiophene, dibenzothiophene sulfone and DL-methionine at several different levels of DFT theory and compared these data to experimental data.[8.3] The authors concluded that resolution of these compounds is difficult due to the similar energy of the main feature in the spectra of the different molecules.[8.3] Recently, the NEXAFS spectra of some organic and inorganic sulphur compounds have been also simulated theoretically by FEFF8 and WIEN97, showing that the combination of experiment and calculations can give useful information in mechanism of carcinogenesis.[8.53]

This work examines the sulphur 1s NEXAFS spectra of thiophenic and aromatic thioether compounds relevant to petroleum (see **Scheme 8.1**) in the gas, liquid and solid phases and compares these data to a wider range of *ab initio* simulations. To select molecules, molecular symmetry, the identity of ligand groups attached to the sulphur atom, and the overall size of the molecules were considered. The results of *ab initio* Improved Virtual Orbital (IVO) and Δ(SCF) calculations have been used to examine the degree of Rydberg-valence mixing, and to establish the assignments of features observed in the experimental spectra.

Gas phase spectra are free of solid-state broadening, and solid phase spectra can suffer from charging effects in the case of total electron yield detection or self-absorption in the case of fluorescent yield detection. However, the condensed phase spectra (liquid and solid phases) are more likely to represent a realistic picture of the spectroscopy of sulphur in analytical targets such as coal and petroleum. Gas phase compounds are examined for the simplicity of their assignments and their direct relationship to *ab initio* simulations. Condensed and liquid phases are examined for the practical application of

these spectra for sulphur speciation and quantification in fossil fuel studies, and as shown in this work, the important role of conformation effects.

Molecular structure	IUPAC name
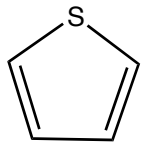	Thiophene
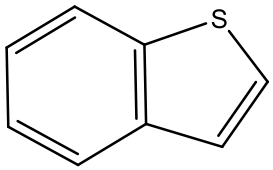	1-Benzothiophene
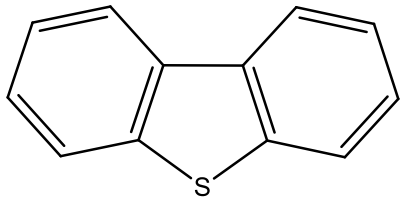	dibenzo[b,d]thiophene
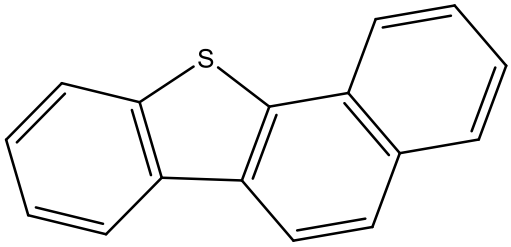	Benzo[b]naphtho[2,1-d]thiophene
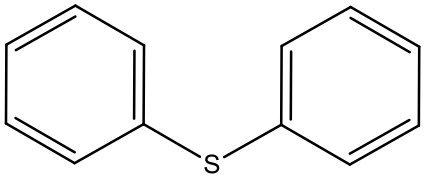	1,1'-Sulfanediyldibenzene
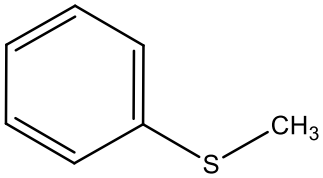	(Methylsulfanyl)benzene

Scheme 8.1 Molecular drawings of thiophenic and unsaturated thioether compounds.

8.4.2 Computational Methods

Ab initio calculations were performed by Kosugi's GSCF3 package.[8.55, 8.56] This approach is based on the Improved Virtual Orbital (IVO) approximation, which explicitly includes the core hole in the Hartree-Fock Hamiltonian. The IVO approximation has been proved to be effective at the simulation of core excitation spectra of organic and organometallic compounds at the carbon, nitrogen, oxygen, silicon, and sulphur 1s edges.[8.54-65] IVO calculations are particularly effective for transitions below and near the ionization potential, where the sulphur 1s NEXAFS spectra show the strongest and most distinctive transitions.

The geometries used for these calculations (see **Scheme 8.1**) were provided by *ab initio* geometry optimization at the HF/6-31G* level, using the SPARTAN 06 program.[8.66] Frequency calculations were performed to ensure that the geometries were minimum structures (no imaginary frequencies) except for the additional conformational isomers of 1,1'-sulfanediyldibenzene, where a particular geometry was fixed and the remaining structural variables optimized. For the IVO calculations with GSCF3, the basis sets were similar to those used previously including:[8.54] Hydrogen (41); Second row atoms (carbon, nitrogen, and oxygen) (621 41); sulphur (with the core hole) (311111111 311111). Additional d polarization functions were placed on the sulphur atom (ζ_d = 0.183, and ζ_d = 0.659).

Simulated spectra were obtained from the IVO calculations by broadening each transition as a Gaussian line with the Simile2 package,[8.67] with the following energy dependent widths: 0.6 eV fwhm for bound states, 1.2 eV fwhm for states from the ionization potential (IP) to 4 eV above the IP, and 4.0 eV fwhm for states more than 4.0 eV above the IP. These widths are chosen to track the experimental line width observed in the sulphur 1s NEXAFS spectra. The natural width of the sulphur 1s core shell is 0.59 eV,[8.68] although observed transitions are wider due to vibrational broadening and other excited state lifetime effects. MO plots are provided for selected unoccupied orbitals.

The presence of Rydberg transitions, as well as Rydberg-valence mixing, should be considered in the interpretation of gas phase NEXAFS spectra. In the IVO approximation, the energies of Rydberg states are calculated more accurately than the valence state energies; therefore spurious Rydberg-valence mixing can occur. This effect

can be minimized in Δ(Self Consistent Field) or"Δ(SCF)" calculations where the screening effect of the excited electron is explicitly included. This process is performed for each excited state; for higher excited states, the shallower unoccupied orbitals are frozen to maintain orthogonality.[8.69-71] These Δ(SCF) calculations have been described in more detail elsewhere.[8.70, 8.71] This approach was used by Kosugi *et al*. to remove spurious Rydberg-valence mixing in the C 1s → σ*(C-F) transitions of CH_3F,[8.72] and was also used to examine Rydberg-valence mixing in the NEXAFS spectra of gaseous[8.73] and condensed alkanes,[8.69] as well as amino acids.[8.58]

The degree of Rydberg character can be inferred by considering the orbital size and the energy difference between singlet and triplet core excited states for each transition (ΔE_{S-T}), as described previously.[8.69, 8.73] For second row atoms, an ΔE_{S-T} energy difference of less than 0.05 eV and orbital size greater than 3 Å usually indicates some Rydberg character for the transition.[8.58, 8.69, 8.73] This trend was extrapolated for sulphur atom in determining the degree of Rydberg-valence mixing as well as the term values, and quantum defects of the Rydberg transitions.[8.74]

8.4.3 Experimental

All compounds (thiophene >99%, 1-benzothiophene (thianaphthene) 98%, dibenzo[b,d]thiophene (dibenzothiophene) 99%, benzo[b]naphtho[2,1-d]thiophene (1,2-benzodiphenylene sulphide) 99%, (methylsulfanyl)benzene >99%, and 1,1'-sulfanediyldibenzene (diphenyl sulphide) 98%) were of reagent grade and purchased from Sigma Aldrich and used without further purification.

Experimental spectra of gas and condensed phases were obtained at the Canadian Light Source (CLS) on Soft X-ray Microcharacterization Beamline (SXRMB), using a Si(111) crystal monochromator which provides an energy resolution of 0.24 eV. Liquid and gas phase spectra were acquired when permitted by the physical properties of the species studied (vapour pressure, etc). Gas samples (thiophene, (methylsulfanyl)benzene, and 1,1'-sulfanediyldibenzene) were introduced into a double gas cell (two gas cells in sequence) from the vapour pressure of the pure sample. The pressure inside the gas cell was in the range of 9.9 - 13.9 mtorr, below the pressure onset for saturation effects. A comparison of the spectra from the first and second gas cells was used to verify the

absence of saturation. The experimental spectra of the gas phase molecules were recorded with total ion yield (TIY) detection mode.[8.75]

For solid samples (dibenzo[b,d]thiophene, and benzo[b]naphtho[2,1-d]thiophene), a fine powder of the sample was spread homogeneously on a kapton tape (previously verified to be sulphur-free). For liquid and solid samples with a low melting point (1,1'-sulfanediyldibenzene, thiophene, 1-benzothiophene, and (methylsulfanyl)benzene), the sample was placed in a Teflon plate holder, which was then sandwiched by two layers of kapton tape. NEXAFS spectra were measured by fluorescence yield (FLY) detection with a Vortex 4-element Si(Li) drift detector, in a He filled chamber.

The TIY and FLY NEXAFS spectra were normalized by dividing each spectrum by an I_o spectrum, recorded simultaneously from an ion chamber upstream from the sample cell. The energy scale was calibrated to an absolute energy scale by setting the energy of the Ar 1s → 4p transition to the value of 3203.54(10) eV, based on the absolute energy calibration of Breinig *et al*.[8.76] In previous work, the Ar 1s → 4p transition energy was used to calibrate a weak contaminant signal (presumed to be $FeSO_4$) found on the Be windows of the ion chamber (calibrated value, 2481.62 eV). This signal, recorded at the same time as all other spectra, was used as an internal calibration for these experiments.[8.54] The accuracy of this calibration is estimated to be +/- 0.3 eV, based on the ~0.7 eV lifetime broadening of the Ar 1s→ 4p transition used for the source calibration.

The calculated IVO sulphur 1s simulations always appear at lower energy than the experimental NEXAFS spectra because of strong relativistic effects for higher Z (third row) species.[8.2, 8.52, 8.54, 8.77, 8.78] In this paper, the experimental and theoretical data are presented on their own energy scales.

8.4.4 Results and Discussion

8.4.4.1 Thiophenic Compounds

Figures 8.1 to **8.4** present the experimental and simulated NEXAFS spectra of thiophenic compounds (thiophene, 1-benzothiophene, dibenzo[b,d]thiophene, and benzo[b]naphtho[2,1-d]thiophene), at two different levels of theory (IVO, and Δ(SCF)). **Figure 8.5** presents MO plots of the unoccupied molecular orbitals corresponding to the

most intense pre-edge transitions in the Δ(SCF) spectra. **Table 8.1** lists the energies and assignments for transitions observed in the experimental spectra. **Table 8.2** presents the calculated energies, term values (term value = ionization potential – transition energy), ionization potentials, and the transition character for the features appearing below the ionization potential for both IVO and Δ(SCF) calculations. These results are reviewed on a molecule-by-molecule basis.

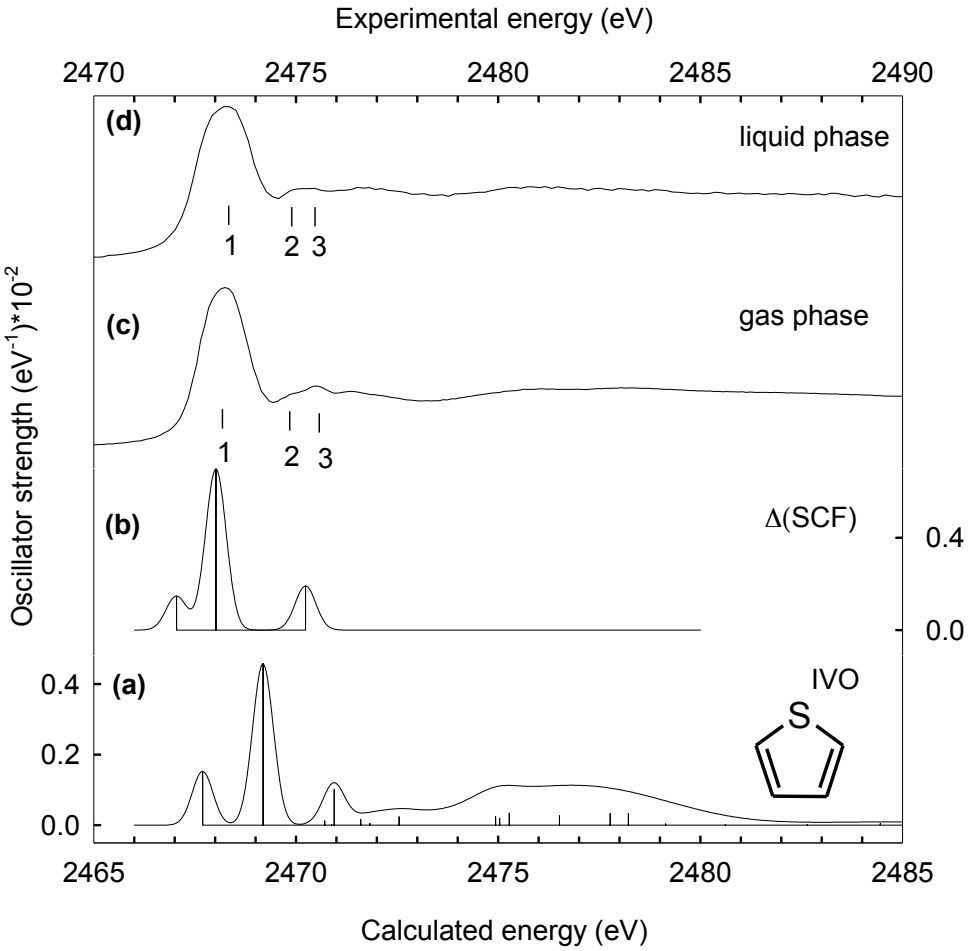

Figure 8.1 Comparison of experimental gas phase sulphur 1s NEXAFS spectrum of thiophene, recorded by total ion yield, and liquid phase spectrum, recorded in fluorescence yield, to the simulated sulphur 1s spectra from *ab initio* IVO and Δ(SCF) calculations. (a) Simulated spectrum from IVO calculation; (b) simulated spectrum from Δ(SCF) calculations; (c) experimental spectrum in gas phase; (d) experimental spectrum in liquid phase.

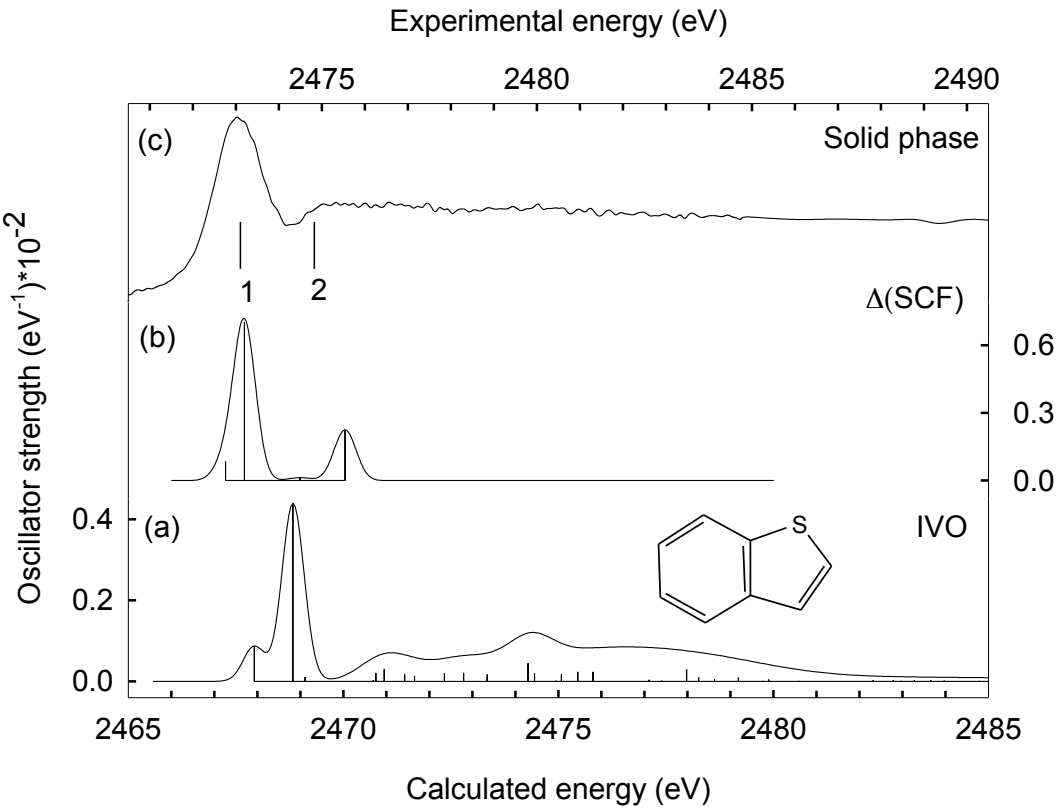

Figure 8.2 Comparison of experimental solid phase sulphur 1s NEXAFS spectrum of 1-benzothiophene, recorded in fluorescence yield, to the predicted sulphur 1s spectra from *ab initio* IVO and Δ(SCF) calculations. (a) Simulated spectrum in IVO; (b) simulated spectrum in Δ(SCF); (c) experimental spectrum in solid phase.

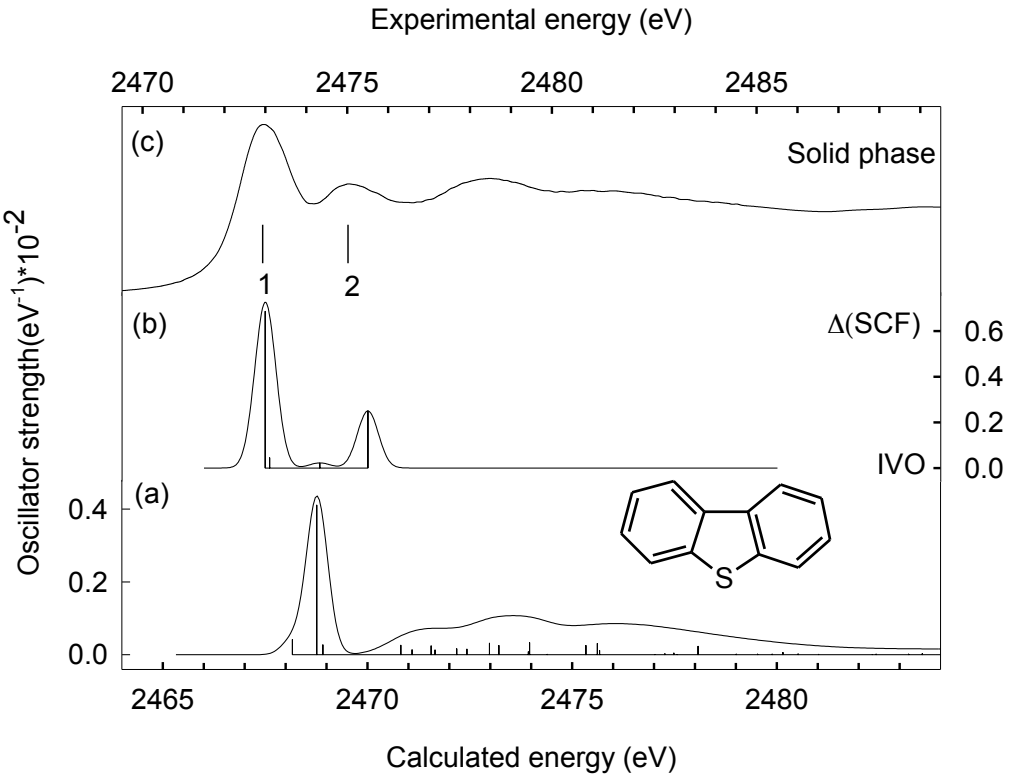

Figure 8.3 Comparison of experimental solid phase sulphur 1s NEXAFS spectrum of dibenzo[b,d]thiophene, recorded in fluorescence yield, to the predicted sulphur 1s spectra from *ab initio* IVO and Δ(SCF) calculations. (a) Simulated spectrum in IVO; (b) simulated spectrum in Δ(SCF); (c) experimental spectrum in solid phase.

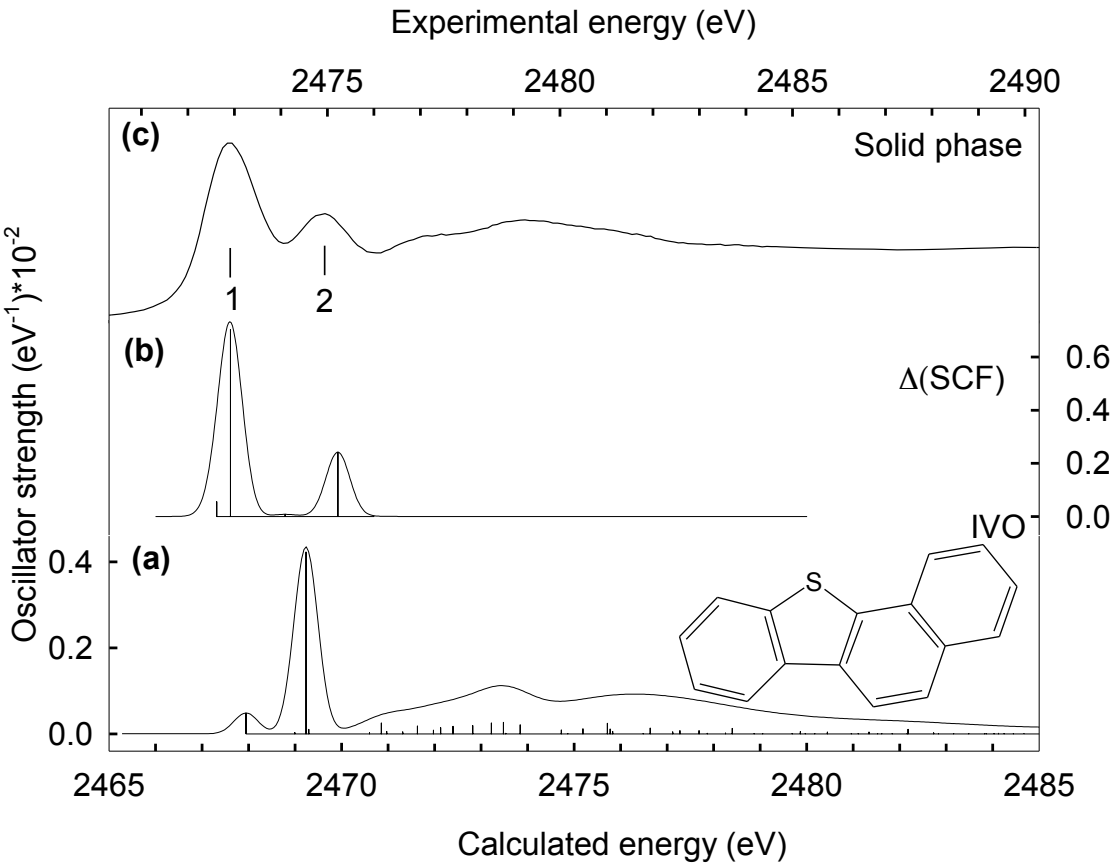

Figure 8.4 Comparison of experimental solid phase sulphur 1s NEXAFS spectrum of benzo[b]naphtho[2,1-d]thiophene, recorded in fluorescence yield, to the predicted sulphur 1s spectra from *ab initio* IVO and Δ(SCF) calculations. (a) Simulated spectrum in IVO; (b) simulated spectrum in Δ(SCF); (c) experimental spectrum in solid phase.

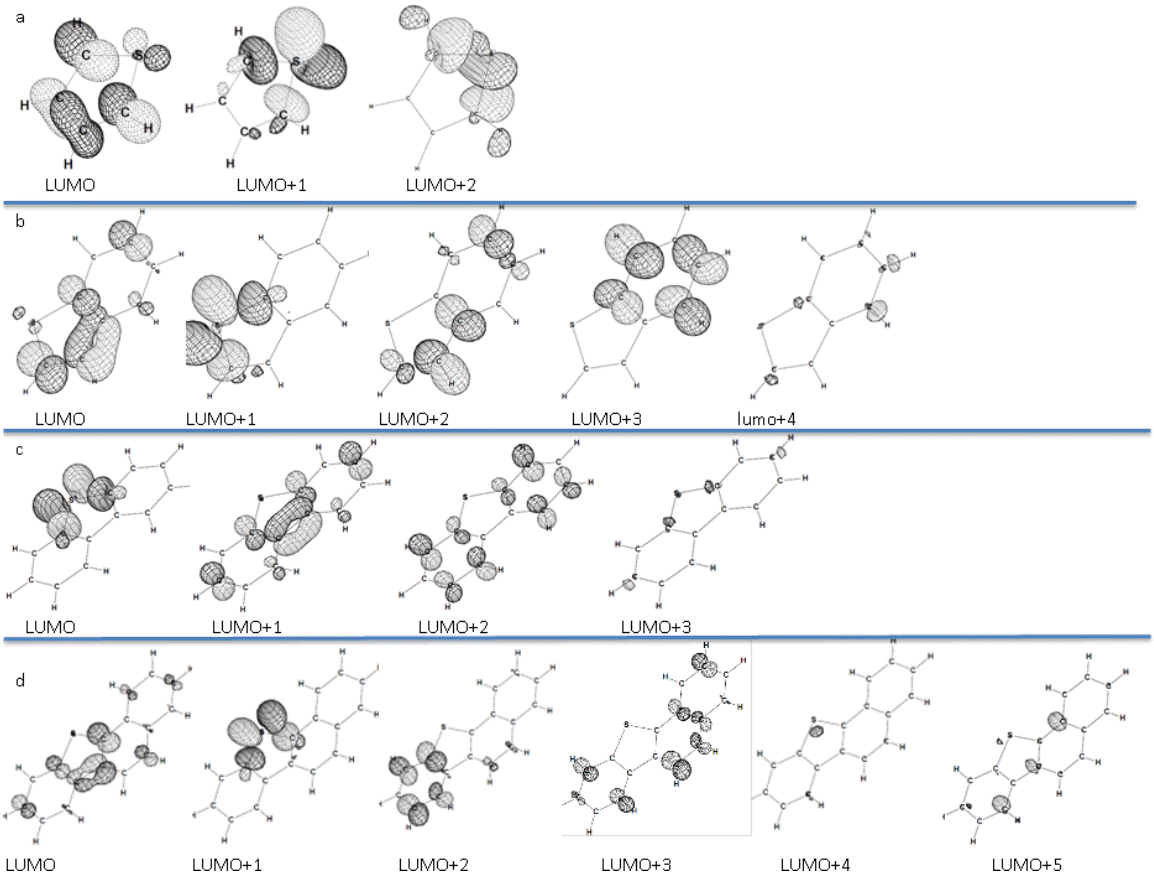

Figure 8.5 Unoccupied molecular orbital diagrams obtained with Δ(SCF) calculations for the pre-edge features contributing to the simulated spectra (a) thiophene; (b) 1-benzothiophene; (c) dibenzo[b,d]thiophene; and (d) benzo[b]naphto[2,1-d]thiophene.

Compound name	# Gas phase	Energy (eV) Gas phase	# Liquid/solid phase	Energy (eV) Liquid phase	Assignments
Thiophene	1	2473.1	1	2473.2	S 1s → π*(S=C) S 1s → σ*(S-C)
	2	2474.6	2	2474.9	4s
	3	2475.2	3	2475.3	S 1s → σ*(S-C)/4p
1-benzothiophene			1	2472.9	S 1s → π*(S=C)/(C=C) S 1s → σ*(S-C)
			2	2474.5	S 1s → π*(C=C)
Dibenzo[b,d]thiophene			1	2472.8	S 1s → π*(S=C)/(C=C)/σ*(S-C)
			2	2474.9	S 1s → σ*(S-C)
benzo[b]naphtho[2,1-d]thiophene			1	2472.8	S 1s → π*(S=C) / (C=C) and S 1s → σ*(S-C)
			2	2474.8	Poorly defined
(Methylsulfanyl)benzene	1	2472.5			S 1s → σ*(S-C) / π*(C=C)
	2	2473.4			S 1s → σ*(S-C) / π*(C=C)
	3	2474.5			S 1s → σ*(S-C)
1,1'-sulfanediyldibenzene	1	2472.1	1	2472.5	S 1s → σ*(S-C) / π*(C=C)
	2	2473.1	2	2473.9	S 1s → π*(C=C)
	3	2474.1			S 1s → π*(C=C)

Table 8.1 Transition energies for the experimental sulphur 1s NEXAFS Spectra of thiophene, 1-benzothiophene, dibenzo[b,d]thiophene, benzo[b]naphtho[2,1-d]thiophene , (methylsulfanyl)benzene, and 1,1'-sulfanediyldibenzene.

(a) Thiophene Δ(SCF)						Thiophene (IVO) I.P.=2470.974 eV		
#	Ionization potential	Energy (eV)	Term Value (eV)	Oscillator Strength	Assignment	Energy (eV)	Term value (eV)	Oscillator Strength
LUMO	2471.642	2467.045	4.597	0.0009396	S1s→π*(S=C)	2467.663	3.311	0.0009739
LUMO+1	2472.210	2468.021	4.189	0.0044561	S1s→σ*(S-C)	2468.971	2.003	0.0029614
LUMO+2	2471.971	2470.238	1.733	0.0012207	S1s→σ*(S-C)/ 4p	2470.644	0.330	0.0000804

(b) 1-Benzothiophene Δ(SCF)						1-Benzothiophene IVO, I.P.= 2470.575 eV		
#	Ionization potential	Energy (eV)	Term Value (eV)	Oscillator Strength	Assignment	Energy (eV)	Term value (eV)	Oscillator Strength
LUMO	2471.532	2467.261	4.271	0.0005360	S1s→π*(S=C)/ π*(C=C)	2467.933	2.642	0.0005540
LUMO+1	2472.132	2467.702	4.430	0.0044707	S1s→σ*(S-C)	2468.827	1.748	0.0027757
LUMO+2	2471.593	2468.992	2.601	0.0000422	S 1s→π*(C=C)	2469.114	1.461	0.0000606
LUMO+3	2471.593	2468.992	2.601	0.0000422	S 1s→π*(C=C)	2470.700	-0.125	0.0000272
LUMO+4	2472.004	2470.042	1.962	0.0014345	Poorly defined	2470.759	-0.184	0.0002590

(c) Dibenzo[b,d]thiophene Δ(SCF)						Dibnzo[b,d]thiophene IVO, I.P.=2470.322 eV		
#	Ionization potential	Energy (eV)	Term Value (eV)	Oscillator Strength	Assignment	Energy (eV)	Term value (eV)	Oscillator Strength
LUMO	2471.996	2467.496	4.5	0.0043827	S1s→σ*(S-C)	2468.168	2.154	0.0002677
LUMO+1	2470.989	2467.606	3.383	0.0002820	S1s→π*(S=C)/ π*(C=C)	2468.764	1.558	0.0026241
LUMO+2	2470.840	2468.833	2.045	0.0001428	S1s→π*(C=C)	2468.915	1.407	0.0001726
LUMO+3	2471.877	2470.008	1.869	0.0015955	Poorly defined	2469.336	0.986	0.0000000

(d) Benzo[b]naphtho[2,1-d]thiophene Δ(SCF)						Benzo[b]naphtho[2,1-d]thiophene IVO, I.P.=2470.275		
#	Ionization potential	Energy (eV)	Term Value (eV)	Oscillator Strength	Assignment	Energy (eV)	Term value (eV)	Oscillator Strength
LUMO	2471.069	2467.319	3.750	0.0003540	S1s→π*(S=C)/ π*(C=C)	2467.933	2.342	0.0003127
LUMO+1	2472.087	2467.614	4.473	0.0045006	S1s→σ*(S-C)	2468.976	1.299	0.0000220
LUMO+2	2471.353	2468.787	2.566	0.0000511	S1s→π*(C=C)	2469.038	1.237	0.0027307
LUMO+3	2471.268	2468.962	2.306	0.0000002	S1s→π*(C=C)	2469.279	0.996	0.0000640
LUMO+4	2471.988	2469.922	2.066	0.0015463	Poorly defined	2470.591	-0.316	0.0000256
LUMO+5	2471.077	2470.695	0.382	0.0000027	Poorly defined	2470.779	-0.504	0.0003162

(e) (Methylsulfanyl)benzene Δ(SCF)						(Methylsulfanyl)benzene IVO, I.P.=2469.843 eV		
#	Ionization potential	Energy (eV)	Term Value (eV)	Oscillator Strength	Assignment	Energy (eV)	Term value (eV)	Oscillator Strength
LUMO	2471.047	2467.169	3.878	0.0026386	S 1s→σ*(S-C)/ π*(C=C)	2467.766	2.077	0.0009825
LUMO+1	2471.741	2468.035	3.706	0.0018383	S1s→σ*(S-C)	2468.833	1.010	0.0000028
LUMO+2	2470.896	2468.674	2.222	0.0000023	S1s→π*(C=C)	2468.993	0.850	0.0015440
LUMO+3	2470.789	2468.75	2.039	0.0009145	S1s→σ*(S-C)	2469.365	0.478	0.0012687
LUMO+4	2470.430	2469.845	0.585	0.0000551	S1s→σ*(S-C)	2469.643	0.200	0.0002515

(f) 1,1'-sulfanediyldibenzene Δ(SCF)						1,1'-sulfanediyldibenzene IVO, I.P.= 2469.856		
#	Ionization potential	Energy (eV)	Term Value (eV)	Oscillator Strength	Assignment	Energy (eV)	Term value (eV)	Oscillator Strength
LUMO	2471.303	2467.35	3.953	0.0034235	S1s→σ*(S-C)/ π*(C=C)	2468.181	1.675	0.0012648
LUMO+1	2471.049	2467.906	3.143	0.0003734	S1s→π*(C=C)	2468.245	1.611	0.0000040
LUMO+2	2470.570	2468.716	1.854	0.0004787	S1s→σ*(S-C)	2468.833	1.023	0.0001509
LUMO+3	2470.484	2469.267	1.217	0.0000137	S1s→π*(C=C)	2469.298	0.558	0.0000237
LUMO+4	2470.588	2469.474	1.114	0.0006801	S1s→π*(C=C)	2469.900	-0.044	0.0014770
LUMO+5	2470.687	2469.753	0.934	0.0009975	Poorly defined	2470.167	-0.311	0.0006728

Table 8.2 Calculated energies, term values, ionization potentials, and assignments for sulphur 1s transitions appearing below the ionization potential for (a) thiophene, (b) 1-benzothiophene, (c) dibenzo[b,d]thiophene, (d) benzo[b]naphtho[2,1-d]thiophene, (e) (methylsulfanyl)benzene, and (f) 1,1'-sulfanediyldibenzene from *ab initio* IVO and Δ(SCF) calculations.

Thiophene. **Figure 8.1** presents the NEXAFS spectra of thiophene, acquired in gas and liquid phases, along with the simulated spectra from IVO and Δ(SCF) calculations. Energies and assignments of the most intense transitions are presented in **Table 8.1**. The gas phase experimental spectrum consists of an intense white line at 2473.1 eV, followed by weak features at 2474.6, and 2475.2 eV. The white line of liquid phase spectrum is somewhat broader (2.0 eV fwhm compared to 1.5 eV fwhm for the gas phase spectrum), with broader features above the white line.

The simulated NEXAFS spectra differ from experiment in the character of the low energy transitions. The simulated spectra consist of weak, low energy feature, followed by a strong transition. However, the experimental spectra do not show a low energy shoulder. The low energy feature is 1.50 eV below the second transition in the IVO calculations; this energy difference should be resolvable in the experimental sulphur 1s NEXAFS spectra. This 1.50 eV energy difference between the first and second transitions in IVO calculations could arise from differences in the quality of calculated core-excited valence, Rydberg states and mixed Rydberg-valence states. The intense low energy states were recalculated with the Δ(SCF) method, where screening effects in the core excited states are better accounted (see calculation section). In the Δ(SCF) calculations, the energy difference between the first and the second excited states decreased to 0.98 eV. This smaller difference could be obscured by lifetime broadening in the experimental spectra, suggesting that both transitions overlap in the white line peak. The presence of the lower energy feature in the calculated spectra has been

confirmed by the high quality calculations including Configuration Interaction (CI)[8.79] and Δ(SCF) calculations performed by Kosugi as well as the angle dependent NEXAFS spectroscopy of thiophene.[8.70]

MO diagrams of the major transitions observed in the simulated NEXAFS spectrum obtained in Δ(SCF) are presented in **Figure 8.5(a)**. Based on the character of the LUMO orbital, the first transition in Δ(SCF) simulation is assigned as sulphur 1s → π*(S=C) character. The second transition in the simulation is to σ*(S-C) core excited state. The third transition, associated with the higher energy peak (3) in the experimental spectra, also has sulphur 1s → σ*(S-C) character that could be mixed with 4p Rydberg character based on the symmetry and the value of its quantum defect (see supplementary document in **§8.4.7**). The white line observed in the experimental sulphur 1s NEXAFS spectrum of thiophene is assigned as an overlap of the lower energy sulphur 1s → π*(S=C) transition, and a slightly higher energy sulphur 1s → σ*(S-C) transition that is also confirmed by angle resolved NEXAFS spectroscopy and the CI calculations.[8.70, 8.79] In previous assignments of the thiophene spectrum by Hitchcock *et al.*,[8.49] the second and the third peaks were assigned to sulphur 1s → 4s and 4p Rydberg transitions respectively. These calculations indicate that peak (3) has also σ*(S-C) character in addition to 4p Rydberg character.

The liquid phase NEXAFS spectrum is broader than the gas phase spectrum, and edge position is shifted slightly to the higher energy relative to the gas phase spectrum. This energy shift is consistent with previous results obtained for the carbon 1s NEXAFS spectra of condensed neopentane relative to its gas phase spectra.[8.69] The broadening of the spectra in the condensed phase can arise from a decrease in core excited state lifetime because of quenching of the Rydberg character or increased dissociative σ*(S-C) character.[8.69]

1-Benzothiophene. A comparison of the experimental sulphur 1s NEXAFS spectrum of 1-benzothiophene in solid phase to simulated spectra from IVO and Δ(SCF) calculations is shown in **Figure 8.2**. Energies and assignments of the most intense transitions are presented in **Table 8.1**.

The solid phase experimental sulphur 1s spectrum of 1-benzeothiophene consists of an intense white line at 2472.9 eV, followed by a weak feature at 2474.5 eV, and very broad features in the continuum. Similar to thiophene, the simulated IVO NEXAFS spectrum differs from experiment in the presence of two lines at low energy: a weaker line, followed by a strong transition. The experimental spectrum does not show a low energy shoulder. In the IVO calculations, the low energy feature is 0.89 eV below the second transition, which should be resolvable in the experimental spectrum. This energy difference decreases to 0.44 eV in high quality Δ(SCF) calculations. This small difference could be obscured by lifetime broadening, suggesting that both transitions overlap in the white line peak in the experimental spectra.

The first transition in the Δ(SCF) simulation (**Figure 8.5(b)**) has π*(S=C)/(C=C) character. The second transition is to a state with pure σ*(S-C) character. Subsequent weak transitions, associated with the higher energy peak (2) in the experimental spectrum at 2474.5 eV, do not have clearly defined orbital character. The white line in the sulphur 1s NEXAFS spectrum of 1-benzothiophene is assigned as an overlap of the lower energy sulphur 1s → π*character from the 1-benzothiophene ring, and a slightly higher energy sulphur 1s → σ*(S-C) transition. The second peak is assigned to sulphur 1s → π*(C=C) transition.

Dibenzo[b,d]thiophene. **Figure 8.3** presents the solid phase NEXAFS spectrum of dibenzo[b,d]thiophene, compared to the simulated spectra from IVO and Δ(SCF) calculations. Energies and assignments for spectral transitions are presented in **Table 8.1**.

The solid phase experimental spectrum consists of an intense white line at 2472.8 eV, and a weak peak at 2474.9 eV followed by broad features in continuum. The experimental spectrum is the most similar to the Δ(SCF) simulated spectrum.

MO diagrams of the major transitions for simulated Δ(SCF) spectrum are presented in **Figure 8.5(c)**. Based on the character of the LUMO orbital, the first transition in the Δ(SCF) simulation has sulphur 1s → σ*(S-C) character, while the weak second transition has sulphur 1s → π*(S=C)/π*(C=C) character. The third transition in the simulation has sulphur 1s → π*(C=C) character. The fourth transition is to σ*(S-C) core excited state, which corresponds to peak (2) in the experimental spectrum.

The white line in the sulphur 1s NEXAFS spectrum of dibenzo[b,d]thiophene can be assigned as an overlap of the low energy sulphur 1s → σ*(S-C) core excited state and a slightly higher energy sulphur 1s → π* molecular orbital of the two aromatic rings and the second peak is assigned to σ*(S-C) state. In this molecule, the Δ(SCF) calculations reproduce the experiment better than the IVO calculations, in terms of the shape and energy splitting of the transitions.

Benzo[b]naphtho[2,1-d]thiophene. Figure 8.4 presents the comparison of experimental NEXAFS spectrum of benzo[b]naphtho[2,1-d]thiophene in solid phase to the simulated NEXAFS spectra from IVO and Δ(SCF) calculations. The major transitions and assignments of the experimental spectrum are presented in **Table 8.1**.

The experimental solid phase spectrum of benzo[b]naphtho[2,1-d]thiophene consists of an intense white line transition at 2472.8 eV, followed by a low intensity high-energy transition at 2474.8 eV and broad features in the continuum. This spectrum is similar to the experimental spectrum of dibenzo[b,d]thiophene. **Figure 8.4(b)** shows that the simulated NEXAFS spectrum obtained in Δ(SCF) calculations is the most similar to the experimental spectrum.

In IVO calculations, the energy difference between the first and second transitions is about 1.04 eV, which should be resolved by experiment. In high quality Δ(SCF) calculations, this energy difference has been decreased to 0.30 eV, so it is reasonable that the low energy feature is not resolved.

Based on the shape of the unoccupied molecular orbitals corresponding to the dominant transitions from Δ(SCF) calculations (**Figure 8.5(d)**), the first transition in the simulation has sulphur 1s → π*(S=C)/π*(C=C) character. The second transition has pure σ*(S-C) character, and subsequent transitions have π*(C=C) character except the last two transitions which are difficult to classify within a simple π* or σ* picture.

The white line of the experimental spectrum is assigned as an overlap of the sulphur 1s → π* transition, (where the π* MO is delocalized over the aromatic rings) with the higher energy σ*(S-C) excited states. Peak (2) is poorly understood on a simple π* or σ* basis.

In the study of the sulphur 1s NEXAFS spectra of a group of thiophenic compounds relevant to petroleum, it has observed that the liquid phase spectrum of thiophene is slightly different from the gas phase spectrum and is shifted to higher energy. The white lines of all of the experimental spectra are assigned as an overlap of sulphur 1s → σ*(S-C) and π* transitions. The Rydberg character is more pronounced in small molecules such as thiophene, and this Rydberg character likely decreases as the molecule size increases. The relative intensity of the π* transition decreases as the molecule size increases, and this transition shifts to higher energy relative to the dominant sulphur 1s → σ*(S-C) transition.

The second distinctive peak (2) observed in all of the thiophene experimental spectra becomes more distinct in the larger thiophene hetrocycles. This transition does not have a clearly defined orbital character. The higher energy above the white line could indicate some 2-electron transition character.

8.4.4.2 Aromatic Thioethers:

The sulphur 1s NEXAFS spectra of simple aliphatic thioethers has been previously reported.[8.54] This work extends these studies to unsaturated thioethers: (methylsulfanyl)benzene, and 1,1′-sulfanediyldibenzene, because of their relationship to the aromatic thiophenes. The experimental spectra are compared to IVO simulations.

(Methylsulfanyl)benzene. Figure 8.6(A) represents the gas phase spectrum of (methylsulfanyl)benzene, along with the simulated spectra from IVO and Δ(SCF) calculations. Energies and assignments of the most intense transitions are presented in **Table 8.1**.

The experimental gas phase spectrum consists of an intense white line at 2472.5 eV, a higher energy shoulder at 2473.4 eV, followed by a weak high-energy peak at 2474.5 eV (peak 3), and broad features in the continuum. The white line of the experimental spectrum differs from the IVO simulation as two bands are observed in IVO simulation and three closely spaced transitions in the Δ(SCF) simulation. The low energy transition in the IVO simulation is stronger than in the thiophene simulations. The gas phase experimental spectrum is the most similar to the Δ(SCF) spectrum.

(A)

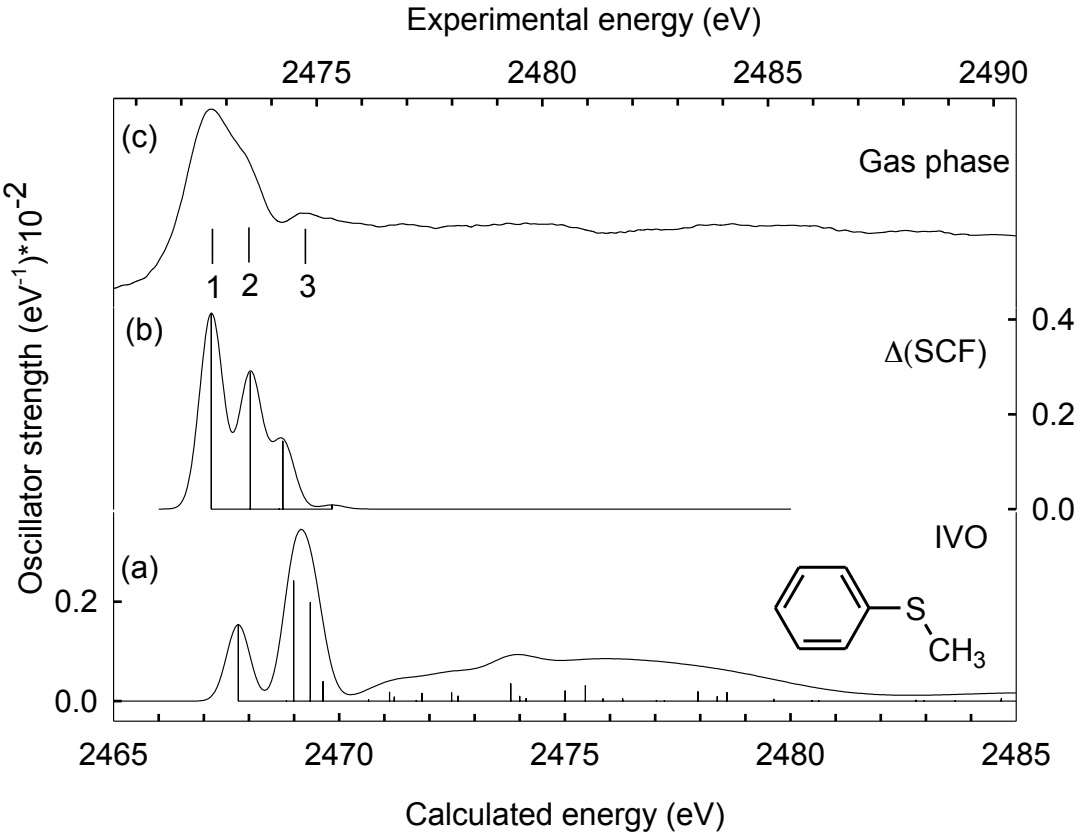

(B)

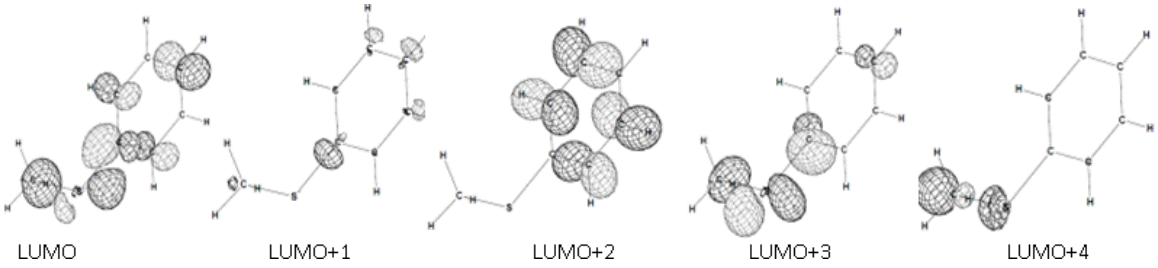

Figure 8.6 (A) Comparison of the experimental gas phase sulphur 1s NEXAFS spectrum of (methylsulfanyl)benzene, recorded by total ion yield, to the predicted sulphur 1s spectra from *ab initio* IVO and Δ(SCF) calculations. (a) Simulated spectrum from IVO calculations; (b) Simulated spectrum from Δ(SCF) calculations; (c) Experimental spectrum recorded in the gas phase. (B) Unoccupied molecular orbital diagrams for the strong features contributing to the simulated spectra obtained from Δ(SCF) calculations.

Based on the character of the unoccupied MOs (**Figure 8.6(B)**), the first transition in the experimental spectrum is assigned as sulphur 1s → σ*(S-C) / π*(C=C) excited state. The higher energy shoulder (peak 2) consists of the overlap of sulphur 1s to σ*(S-C) and π*(C=C) character, and the third transition has a pure σ*(S-C) character. The shape of NEXAFS spectrum is similar to the previously studied aliphatic thioethers.[8.54] The spectral transitions in this molecule have an additional π* character as a result of phenyl substituent, compared to methyl group in dimethyl sulphide.[8.54]

1,1′-sulfanediyldibenzene. Figure 8.7 represents the gas and liquid phase spectra of 1,1′-sulfanediyldibenzene and compares these spectra to IVO simulations obtained for different conformational isomers.

The experimental gas phase spectrum of 1,1′-sulfanediyldibenzene consists of an intense white line at 2472.1 eV, and a higher energy shoulder at 2473.1 eV, followed by a weak feature at 2474.1 eV and broad features in continuum. The liquid phase spectrum consists of an intense peak at 2472.5 eV, followed by a second peak at 2474.1 eV, and broad features in continuum. The liquid phase spectrum is different from the gas phase spectrum with having two intense peaks instead of one peak with higher energy shoulders in the gas phase spectrum.

The gas phase spectrum is the most similar to the Δ(SCF) simulation for the equilibrium geometry (conformer 1 in **Figure 8.7**). The difference between the gas and liquid phase spectrum could suggest the presence of a range of conformers in the liquid phase. Several different conformers were investigated, in addition to the equilibrium geometry. One potential conformer (conformer 2 in **Figure 8.7**) has the two phenyl rings with the same tilt while another conformer (conformer 3 in **Figure 8.7**) has the two phenyl rings in the same plane. The Δ(SCF) simulation of conformer 2 is the most similar to the liquid phase spectrum, but the liquid phase spectrum is probably a combination on conformers.

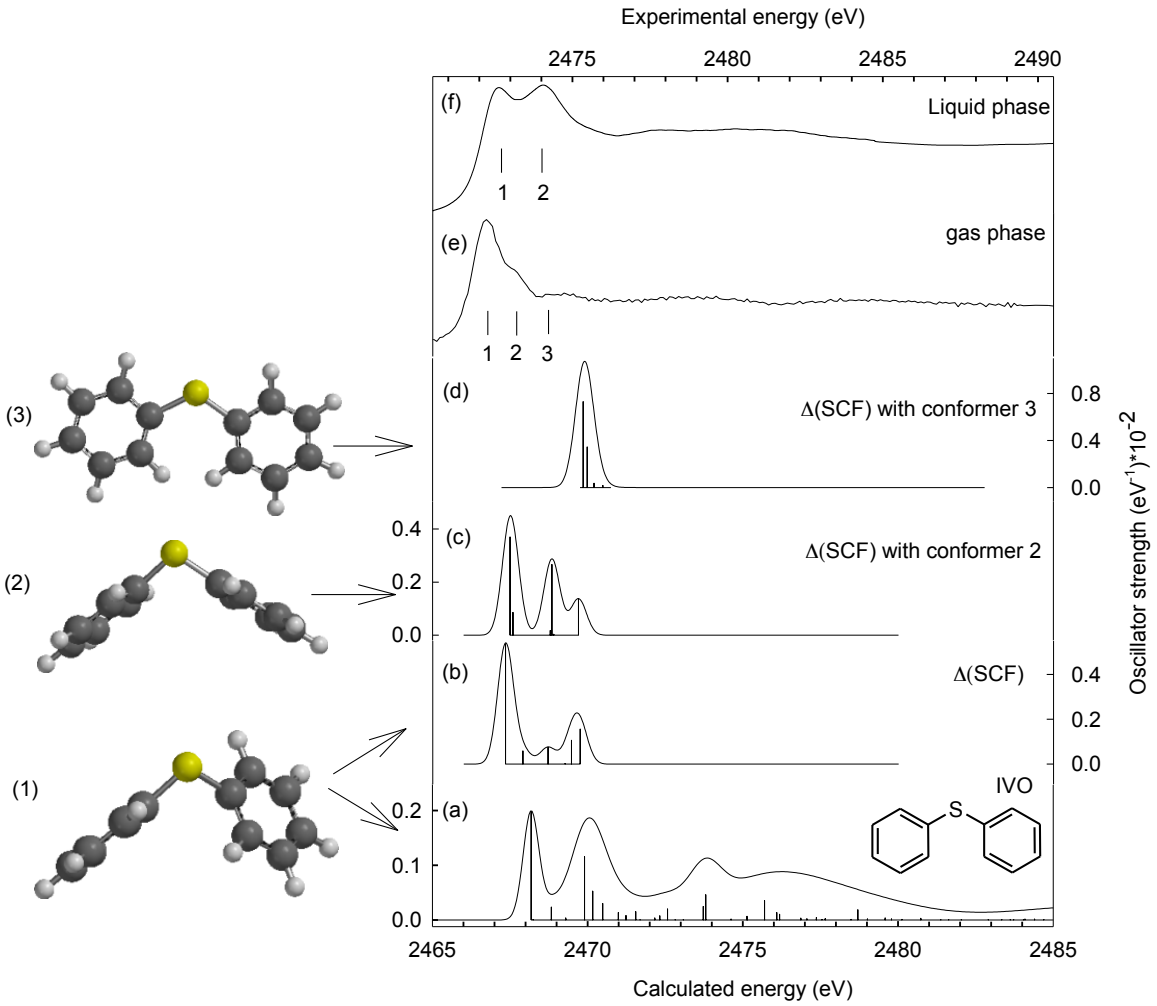

Figure 8.7 Comparison of experimental gas phase sulphur 1s NEXAFS spectrum of 1,1'sulfanediyldibenzene, recorded by total ion yield, and in liquid phase, recorded in fluorescence yield, to the predicted sulphur 1s spectra from *ab initio* IVO and Δ(SCF) calculations. (a) Simulated spectrum from IVO calculation with the equilibrium geometry (conformer 1); (b) Simulated spectrum from Δ(SCF) calculations of the equilibrium geometry (conformer 1); (c) Simulated spectrum from Δ(SCF) calculations of conformer 2; (d) Simulated spectrum from Δ(SCF) calculations from conformer 3; (e) Experimental spectrum recorded in the gas phase; (f) experimental spectrum recorded in the liquid phase.

Comparison of the Δ(SCF) simulations for the two conformers (see **Figure 8.7(c)** and **(d)**) to the liquid phase spectrum shows distinct changes. The intensity of a band at ~2469 eV on the calculated energy scale (corresponding to the peak (2) in the liquid phase spectrum) increases and reaches a maximum in flat geometry while the intensity of the first peak decreases. The different shape of peak 2 in the liquid phase spectra could be

due to the presence of different conformers in the liquid phase while the gas phase spectrum should be most similar to the equilibrium geometry.

The MO diagrams of the major transitions for Δ(SCF) spectrum at equilibrium geometry are presented in **Figure 8.8(a)**.

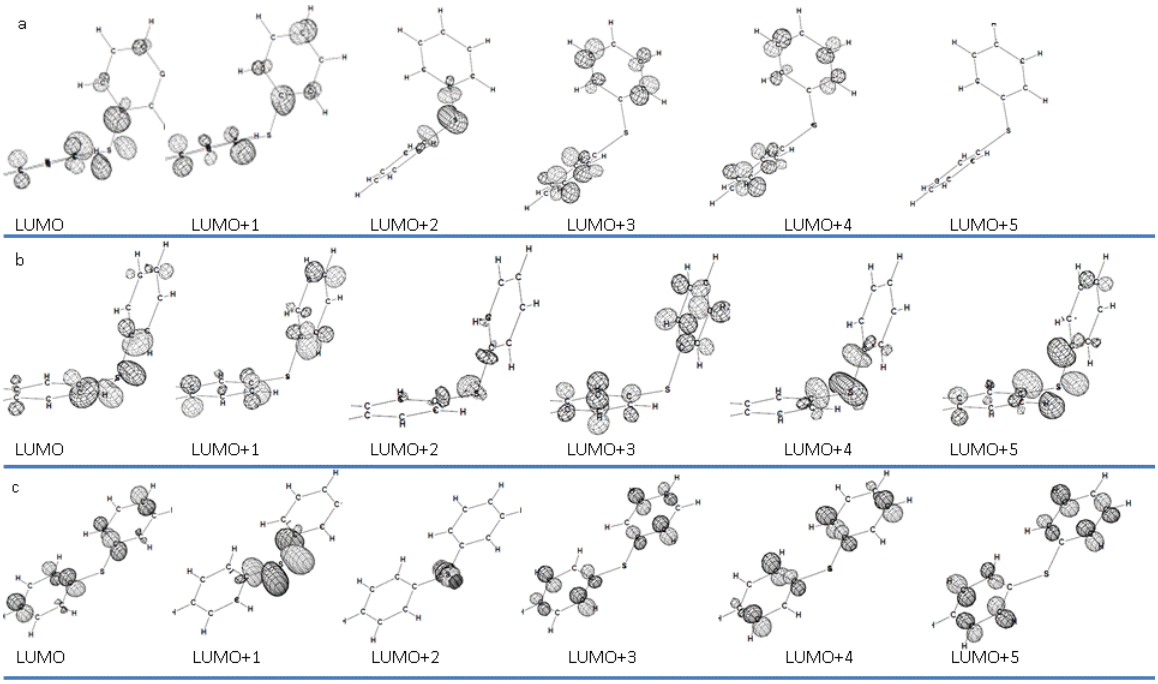

Figure 8.8 Unoccupied molecular orbital diagrams for the strong features contributing to the simulated spectra obtained from Δ(SCF) calculations (a) 1,1' sulfanediyldibenzene at equilibrium geometry; (b) 1,1' sulfanediyldibenzene of conformer (2) from conformer 2; (c) 1,1' sulfanediyldibenzene of conformer 3.

Based on the shape of the unoccupied molecular orbitals, the first transition of the spectrum (**Figure 8.7(b)**) has sulphur 1s→σ*(S-C)/π*(C=C) character. The third transition is to σ*(S-C) excited state and the subsequent transitions have sulphur 1s → π*(C=C) character. The third transition is not understood on a simple σ* or π* basis.

The first peak of the experimental spectra is assigned as an overlap of sulphur 1s→σ*(S-C), and π*(C=C) character and the second transition in the liquid phase and peak (4) in the gas phase as sulphur 1s→π*(C=C) excited state. The shape of the gas phase spectrum is similar to the aliphatic thioethers, but with a difference in the shape of liquid phase spectrum.

The sulphur 1s NEXAFS spectra of aromatic thioethers were examined by experimental and IVO simulations. The shape of the NEXAFS spectra of aromatic thioethers are very similar to those of aliphatic thioethers.[8.54] The edge position of aromatic thioethers are at lower energy than the alphatic thioethers (~0.1 eV for (methylsulfanyl)benzene, and ~0.5 eV for 1,1′-sulfanediyldibenzene relative to dimethyl sulphide and DL-methionine). This difference can be ascribed to the delocalization of electron density in aromatic compounds and the higher stability of excited states.

In the aromatic thioethers, the first transition has sulphur 1s → σ*(S-C) character, overlapped with sulphur 1s → π*(C=C). In (methylsulfanyl)benzene, the third transition has been replaced by pure σ*(S-C) excited state instead of π*(C=C) character in 1,1'-sulfanediyldibenzene. In 1,1′-sulfanediyldibenzene, the gas phase spectrum is the most similar to the spectrum in equilibrium geometry, and in contrast the liquid phase spectrum likely contains a mixture of different conformers, representing different interactions between the sulphur and phenyl π* orbitals. These results show that conformation effects can be significant in analytical studies: experimental molecular models and computational studies must reflect the environment of the condensed (liquid or solid phase) to provide a correct spectroscopic interpretation.

8.4.5 Conclusion

The NEXAFS spectra of a group of thiophenic compounds and aromatic thioethers have been obtained in gas and condensed phases and have been compared to the simulated spectra in two different levels of calculations; IVO and Δ(SCF). It was shown that Δ(SCF) calculations reproduce the experimental spectra better than IVO calculations as the spurious Rydberg – valence mixing is minimized. Calculations show that the most intense feature in the NEXAFS spectra of thiophenic compounds is from a sulphur 1s → σ*(S-C) transition that has some π* character from the phenyl ring. The Rydberg character decreases as the number of phenyl rings in the molecule increases. The phase of the molecules has an important role on the shape of the NEXAFS spectra. The edge position of the NEXAFS spectra moves to the higher energies in the condensed phase compared to the gas phase spectra and the white line feature becomes broader. The

broadening in the condensed phase NEXAFS spectra can arise from a decrease in core excited state lifetime from quenching of the Rydberg character or increased dissociative σ*(S-C) character.[8.69]

In aromatic thioethers and thiophenic compounds, the first transition is a sulphur 1s → σ*(S-C) transition that overlaps with a sulphur 1s → π*(C=C) character transition. In (methylsulfanyl)benzene, the last transition has been replaced by pure σ*(S-C) excited state instead of π*(C=C) character in 1,1'-sulfanediyldibenzene. In a previous study of aliphatic thioethers[8.54] all transitions showed to have σ*(S-C) character while in aromatic thioethers these transitions also samples the π* density of the phenyl ring.

In summary, the modest changes in the sulphur compounds environment including the symmetry, phase of the sample, and its functionality can modify or shift its spectral features as it affects the mixing of atomic orbitals in the LUMOs. Conformation effects can have a significant effect in the sulphur 1s NEXAFS spectra of aromatic organosulphur species, providing a caution to how experimental and computational models are used to interpret analytical NEXAFS spectra.

Acknowledgements

We thank Dr. N. Kosugi for his comments and advice on IVO and Δ(SCF) calculations in this paper. SGU is funded by NSERC (Canada). Research described in this paper was performed at the Canadian Light Source, which is supported by the Natural Sciences and Engineering Research Council of Canada, the National Research Council Canada, the Canadian Institutes of Health Research, the Province of Saskatchewan, Western Economic Diversification Canada, and the University of Saskatchewan.

8.4.6 References

8.1. Bolin, T. B., *Energy & Fuels,* **2010,** *24*, 5479-5482.
8.2. Mori, R. A.; Paris, E.; Giuli, G.; Eeckhout, S. G.; Kavcic, M.; Zitnik, M.; Bucar, K.; Pettersson, L. G. M.; Glatzel, P., *Inorganic Chemistry,* **2010,** *49* (14), 6468-6473.
8.3. Mijovilovich, A.; Pettersson, L. G. M.; Mangold, S.; Janousch, M.; Susini, J.; Salome, M.; de Groot, F. M. F.; Weckhuysen, B. M., *The Journal of Physical Chemistry A,* **2009,** *113* (12), 2750-2756.

8.4. Miki, Y.; Toba, M.; Yoshimura, Y., *Journal of the Japan Petroleum Institute,* **2008,** *51* (4), 225-233.
8.5. Kropp, K. G.; Fedorak, P. M., *Canadian Journal of Microbiology,* **1998,** *44* (7), 605-622.
8.6. Lyapina, N. K.; Marchenko, G. N.; Parfenova, M. A.; Galkin, E. G.; Nugumanov, R. M.; Grishina, R. E., *Petroleum Chemistry,* **2010,** *50* (1), 31-41.
8.7. Mossner, S. G.; Wise, S. A., *Analytical Chemistry,* **1999,** *71* (1), 58-69.
8.8. Hua, R. X.; Li, Y. Y.; Liu, W.; Zheng, J. C.; Wei, H. B.; Wang, J. H.; Lu, X.; Kong, H. W.; Xu, G. W., *Journal of Chromatography A,* **2003,** *1019* (1-2), 101-109.
8.9. Hegazi, A. A. H.; Andersson, J. T., *Energy & Fuels,* **2007,** *21* (6), 3375-3384.
8.10. Jalilehvand, F., *Chemical Society Reviews,* **2006,** *35* (12), 1256-1268.
8.11. Matsumoto, S.; Tanaka, Y.; Ishii, H.; Tanabe, T.; Kitajima, Y.; Kawai, J., *Spectrochimica Acta Part B: Atomic Spectroscopy,* **2006,** *61* (8), 991-994.
8.12. Wiltfong, R.; Mitra-Kirtley, S.; Mullins, O. C.; Andrews, B.; Fujisawa, G.; Larsen, J. W., *Energy & Fuels,* **2005,** *19* (5), 1971-1976.
8.13. Sarret, G.; Connan, J.; Kasrai, M.; Bancroft, G. M.; Charrié-Duhaut, A.; Lemoine, S.; Adam, P.; Albrecht, P.; Eybert-Bérard, L., *Geochimica et Cosmochimica Acta,* **1999,** *63* (22), 3767-3779.
8.14. George, G. N.; Gorbaty, M. L.; Kelemen, S. R.; Sansone, M., *Energy & Fuels,* **1991,** *5* (1), 93-97.
8.15. George, G. N.; Gorbaty, M. L., *Journal of the American Chemical Society,* **1989,** *111* (9), 3182-3186.
8.16. Almkvist, G.; Boye, K.; Persson, I., *Journal of Synchrotron Radiation,* **2010,** *17*, 683-688.
8.17. Braun, A.; Janousch, M.; Sfeir, J.; Kiviaho, J.; Noponen, M.; Huggins, F. E.; Smith, M. J.; Steinberger-Wilckens, R.; Holtappels, P.; Graule, T., *Journal of Power Sources,* **2008,** *183* (2), 564-570.
8.18. Jugo, P. J.; Wilke, M.; Botcharnikov, R. E., *Geochimica et Cosmochimica Acta,* **2010,** *74* (20), 5926-5938.
8.19. Fors, Y.; Jalilehvand, F.; Sandstrom, M., *Analytical Sciences,* **2011,** *27* (8), 785-792.
8.20. Prietzel, J.; Botzaki, A.; Tyufekchieva, N.; Brettholle, M.; Thieme, J.; Klysubun, W., *Environmental Science & Technology,* **2011,** *45* (7), 2878-2886.
8.21. Allegretti, F.; Bussolotti, F.; Woodruff, D. P.; Dhanak, V. R.; Beccari, M.; Di Castro, V.; Betti, M. G.; Mariani, C., *Surface Science,* **2008,** *602* (14), 2453-2462.
8.22. Sardar, S. A.; Syed, J. A.; Yagi, S.; Tanaka, K., *Thin Solid Films,* **2004,** *450* (2), 265-271.
8.23. Syed, J. A.; Sardar, S. A.; Yagi, S.; Tanaka, K., *Surface Science,* **2004,** *566*, 597-602.
8.24. Syed, J. A.; Sardar, S. A.; Yagi, S.; Tanaka, K., *Journal of Vacuum Science & Technology A,* **2004,** *22* (3), 683-688.
8.25. Syed, J. A.; Sardar, S. A.; Yagi, S.; Tanaka, K., *Thin Solid Films,* **2006,** *515* (4), 2130-2136.
8.26. Modrow, H.; Calderon, G.; Daly, W. H.; de Souza, G. G. B.; Tittsworth, R. C.; Moelders, N.; Schilling, P. J., *Journal of Synchrotron Radiation,* **1999,** *6*, 588-590.

8.27. Winter, I.; Hormes, J.; Hiller, M., *Nuclear Instruments & Methods in Physics Research Section B-Beam Interactions with Materials and Atoms,* **1995,** *97* (1-4), 287-291.
8.28. Smith, T. A.; Dewitt, J. G.; Hedman, B.; Hodgson, K. O., *Journal of the American Chemical Society,* **1994,** *116* (9), 3836-3847.
8.29. Prange, A.; Dahl, C.; Truper, H. G.; Behnke, M.; Hahn, J.; Modrow, H.; Hormes, J., *European Physical Journal D,* **2002,** *20* (3), 589-596.
8.30. Pickering, I. J.; George, G. N.; Yu, E. Y.; Brune, D. C.; Tuschak, C.; Overmann, J.; Beatty, J. T.; Prince, R. C., *Biochemistry,* **2001,** *40* (27), 8138-8145.
8.31. Frank, P.; Hedman, B.; Hodgson, K. O., *Inorganic Chemistry,* **1999,** *38* (2), 260-270.
8.32. Pickering, I. J.; Prince, R. C.; Divers, T.; George, G. N., *FEBS Letters,* **1998,** *441* (1), 11-14.
8.33. Ito, A.; Inoue, T.; Takehara, K.; Shimizu, N.; Kitajima, Y.; Shinohara, K., *Journal of X-Ray Science and Technology,* **2011,** *19* (2), 249-260.
8.34. Rompel, A.; Cinco, R. M.; Latimer, M. J.; McDermott, A. E.; Guiles, R. D.; Quintanilha, A.; Krauss, R. M.; Sauer, K.; Yachandra, V. K.; Klein, M. P., *Proceedings of the National Academy of Sciences of the United States of America,* **1998,** *95* (11), 6122-6127.
8.35. Howells, M.; Jacobsen, C.; Warwick, T.; Bos, A., *Principles and Applications of Zone Plate X-Ray Microscopes*. In *Science of Microscopy*, Hawkes, P. W.; Spence, J. C. H., Eds. Springer, New York, **2007**, 835-926.
8.36. Van der Snickt, G.; Dik, J.; Cotte, M.; Janssens, K.; Jaroszewicz, J.; De Nolf, W.; Groenewegen, J.; Van der Loeff, L., *Analytical Chemistry,* **2009,** *81* (7), 2600-2610.
8.37. Cotte, M.; Welcomme, E.; Sole, V. A.; Salome, M.; Menu, M.; Walter, P.; Susini, J., *Analytical Chemistry,* **2007,** *79* (18), 6988-6994.
8.38. Prietzel, J.; Thieme, J.; Neuhausler, U.; Susini, J.; Kogel-Knabner, I., *European Journal of Soil Science,* **2003,** *54* (2), 423-433.
8.39. Norlund, K. L. I.; Southam, G.; Tyliszczak, T.; Hu, Y. F.; Karunakaran, C.; Obst, M.; Hitchcock, A. P.; Warren, L. A., *Environmental Science & Technology,* **2009,** *43* (23), 8781-8786.
8.40. Dezarnaud, C.; Tronc, M.; Hitchcock, A. P., *Chemical Physics,* **1990,** *142*, 455-462.
8.41. Dezarnaud, C.; Tronc, M.; Modelli, A., *Chemical Physics,* **1991,** *156* (1), 129-140.
8.42. Hitchcock, A. P.; Bodeur, S.; Tronc, M., *Physica B,* **1989,** *158* (1-3), 257-258.
8.43. Chauvistre, R.; Hormes, J.; Hartmann, E.; Etzenbach, N.; Hosch, R.; Hahn, J., *Chemical Physics,* **1997,** *223* (2-3), 293-302.
8.44. Hitchcock, A. P., *Journal de Physique IV (Proceedings),* **1986,** *T.47 C8 vol.2*, C8575-C8578.
8.45. Perera, R. C. C.; Lavilla, R. E., *Journal of Chemical Physics,* **1986,** *84* (8), 4228-4234.
8.46. Mijovilovich, A.; Pettersson, L. G. M.; de Groot, F. M. F.; Weckhuysen, B. M., *Journal of Physical Chemistry A,* **2010,** *114* (35), 9523-9528.
8.47. Sarangi, R.; Frank, P.; Hodgson, K. O.; Hedman, B., *Inorganica Chimica Acta,* **2008,** *361* (4), 956-964.

8.48. Risberg, E. D.; Jalilehvand, F.; Leung, B. O.; Pettersson, L. G. M.; Sandstrom, M., *Dalton Transactions,* **2009,** *14* (18), 3542-3558.
8.49. Hitchcock, A. P.; Horsley, J. A.; Stohr, J., *The Journal of Chemical Physics,* **1986,** *85* (9), 4835-4848.
8.50. Nakamatsu, H.; Mukoyama, T.; Adachi, H., *Journal of Chemical Physics,* **1991,** *95* (5), 3167-3174.
8.51. Bodeur, S.; Hitchcock, A. P.; Kosugi, N., *Chemical Physics,* **1992,** *162* (2-3), 293-302.
8.52. Damian, E.; Jalilehvand, F.; Abbasi, A.; Pettersson, L. G. M.; Sandstrom, M., *Physica Scripta,* **2005,** *T115*, 1077-1079.
8.53. Kwiatek, W. M.; Czapla, J.; Podgorczyk, M.; Kisiel, A.; Konior, J.; Balerna, A., *Radiation Physics and Chemistry,* **2011,** *80* (10), 1104-1108.
8.54. Behyan, S.; Hu, Y. F.; Urquhart, S. G., *Journal of Chemical Physics,* **2011,** *134* (24), 244304.
8.55. Kosugi, N., *Theoretica Chimica Acta,* **1987,** *72* (2), 149-173.
8.56. Kosugi, N.; Kuroda, H., *Chemical Physics Letters,* **1980,** *74* (3), 490-493.
8.57. Cooney, R. R.; Urquhart, S. G., *Journal of Physical Chemistry B,* **2004,** *108* (47), 18185-18191.
8.58. Otero, E.; Urquhart, S. G., *Journal of Physical Chemistry A,* **2006,** *110* (44), 12121-12128.
8.59. Ueda, K.; Okunishi, M.; Chiba, H.; Shimizu, Y.; Ohmori, K.; Sato, Y.; Shigemasa, E.; Kosugi, N., *Chemical Physics Letters,* **1995,** *236* (3), 311-317.
8.60. Urquhart, S. G.; Ade, H., *The Journal of Physical Chemistry B,* **2002,** *106* (34), 8531-8538.
8.61. Urquhart, S. G.; Turci, C. C.; Tyliszczak, T.; Brook, M. A.; Hitchcock, A. P., *Organometallics,* **1997,** *16* (10), 2080-2088.
8.62. Urquhart, S. G.; Hitchcock, A. P.; Lehmann, J. F.; Denk, M., *Organometallics,* **1998,** *17* (11), 2352-2360.
8.63. Urquhart, S. G.; Smith, A. P.; Ade, H. W.; Hitchcock, A. P.; Rightor, E. G.; Lidy, W., *Journal of Physical Chemistry B,* **1999,** *103* (22), 4603-4610.
8.64. Otero, E.; Kosugi, N.; Urquhart, S. G., *Journal of Chemical Physics,* **2009,** *131* (11).
8.65. Lehmann, J. F.; Urquhart, S. G.; Ennis, L. E.; Hitchcock, A. P.; Hatano, K.; Gupta, S.; Denk, M. K., *Organometallics,* **1999,** *18* (10), 1862-1872.
8.66. Spartan 4.0; Wavefunction Inc.: Irvine, CA, **1994**.
8.67. Huo, B.; Hitchcock, A. P. *Simile2*, McMaster University: **1996**.
8.68. Krause, M. O.; Oliver, J. H., *J. Phys. Chem. Ref. Data,* **1979,** *8* (2), 329-338.
8.69. Urquhart, S. G.; Gillies, R., *Journal of Chemical Physics,* **2006,** *124* (23), 2151.
8.70. Kosugi, N., *Molecular Inner-Shell Spectroscopy: Polarization Dependence and Characterization of Unoccupied States*. In *Chemical Applications of Synchrotron Radiation*, Sham, T. K., Ed. World Scientific, **2002**.
8.71. Imanishi, A., Yokoyama, T., Kitajima, Y., Ohta, T., *Bulletin of the Chemical Society of Japan,* **1998,** *71*, 831-835.
8.72. Kosugi, N.; Ueda, K.; Shimizu, Y.; Chiba, H.; Okunishi, M.; Ohmori, K.; Sato, Y.; Shigemasa, E., *Chemical Physics Letters,* **1995,** *246* (4-5), 475-480.

8.73. Urquhart, S. G.; Gillies, R., *Journal of Physical Chemistry A,* **2005,** *109* (10), 2151-2159.
8.74. See Supplementary Material Document No._____ for information on Rydberg character. For information on Supplementary Material, see http://www.aip.org/pubservs/epaps.html.
8.75. Hitchcock, A. P.; Tronc, M., *Chemical Physics,* **1988,** *121* (2), 265-277.
8.76. Breinig, M.; Chen, M. H.; Ice, G. E.; Parente, F.; Crasemann, B., *Physical Review A,* **1980,** *22* (2), 520-528.
8.77. Risberg, E. D.; Eriksson, L.; Mink, J.; Pettersson, L. G. M.; Skripkin, M. Y.; Sandstrom, M., *Inorganic Chemistry,* **2007,** *46* (20), 8332-8348.
8.78. Mori, R. A.; Paris, E.; Giuli, G.; Eeckhout, S. G.; Kavcic, M.; Zitnik, M.; Bucar, K.; Pettersson, L. G. M.; Glatzel, P., *Analytical Chemistry,* **2009,** *81* (15), 6516-6525.
8.79. Kosugi, N., private communication. **2012**.

8.4.7 Supplementary document

Rydberg Transition[8.80]	Term value ± 0.5 (eV)[8.80]	Calculated Quantum defect (δ_l) in this study
4s	3.3	2.0±0.15
4p	2.8	1.8±0.2

Table 8.3 Term values associated with Rydberg transitions used by Hitchcock *et al*.,[8.80] to assign the Rydberg transitions in thiophene.

The quantum defects provided in this table are calculated from these term values by the equation: $TV(eV) = \frac{13.6}{(n-\delta_l)^2}$ [8.81] where TV (eV) is the term value of the Rydberg transition, n is the principal quantum number, and δ_l is the quantum defect.[8.81]

Based on an analysis of ΔE(S-T) in **Table 8.4**, a small value of ΔE(S-T) is often associated with a high Rydberg character in IVO calculations. However this value might also be small if the core-excited state is not highly localized on the core excited atom. The Rydberg character tends to be quenched in larger molecules as the big size of the Rydberg orbital can extend to the periphery of the molecule. In this case, the small difference in energy of singlet and triplet states does not imply Rydberg character (Kosugi, N., in *Chemical Applications of Synchrotron Radiation*, edited by Sham T. K. (World Scientific, 2002).

(a) Thiophene Δ(SCF)				Thiophene (IVO) I.P.=2470.974 eV	
#	Size (Å)	Calculated quantum defect	ΔE(S-T) (eV)	Size (Å)	ΔE(S-T) (eV)
LUMO	1.853	2.270	0.040	1.895	0.045
LUMO+1	1.926	2.190	0.192	2.078	0.142
LUMO+2	2.113	1.198	0.265	3.180	0.126

(b) 1-Benzothiophene Δ(SCF)				1-Benzothiophene IVO, I.P.= 2470.575 eV	
#	Calculated quantum defect	Size (Å)	ΔE(S-T) (eV)	Size (Å)	ΔE(S-T) (eV)
LUMO	2.215	2.384	0.024	2.392	0.024
LUMO+1	2.248	2.490	0.194	2.652	0.120
LUMO+2	1.713	2.390	0.002	2.422	0.003
LUMO+3	1.713	2.390	0.002	2.498	0.001
LUMO+4	1.367	2.574	0.287	3.467	0.130

(c) Dibenzo[b,d]thiophene Δ(SCF)				Dibenzo[b,d]thiophene IVO, I.P.=2470.322 eV	
#	Calculated quantum defect	Size (Å)	ΔE(S-T) (eV)	Size (Å)	ΔE(S-T) (eV)
LUMO	2.262	2.464	0.191	2.802	0.013
LUMO+1	1.994	2.628	0.013	2.721	0.091
LUMO+2	1.422	3.000	0.044	3.015	0.007
LUMO+3	1.302	2.480	0.300	2.979	0.000

(d) Benzo[b]naphtho[2,1-d]thiophene Δ(SCF)				Benzo[b]naphtho[2,1-d]thiophene IVO, I.P.=2470.275	
#	Calculated quantum defect	Size (Å)	ΔE(S-T) (eV)	Size (Å)	ΔE(S-T) (eV)
LUMO	2.096	2.727	0.016	3.100	0.015
LUMO+1	2.256	2.426	0.197	3.471	0.070
LUMO+2	1.698	3.829	0.002	2.741	0.062
LUMO+3	1.571	3.117	0.000	3.642	0.003
LUMO+4	1.434	2.522	0.299	3.719	0.002
LUMO+5	-1.966	3.552	0.000	3.470	0.146

(e) (Methylsulfanyl)benzene Δ(SCF)				(Methylsulfanyl)benzene IVO, I.P.=2469.843 eV	
#	Calculated quantum defect	Size (Å)	ΔE(S-T) (eV)	Size (Å)	ΔE(S-T) (eV)
LUMO	2.127	2.682	0.150	2.601	0.052
LUMO+1	2.084	2.092	0.208	2.421	0.000
LUMO+2	1.526	2.426	0.000	2.748	0.078
LUMO+3	1.417	2.433	0.082	2.875	0.134
LUMO+4	-0.821	3.463	0.033	3.349	0.091

(f) 1,1'-sulfanediyldibenzene Δ(SCF)				1,1'-sulfanediyldibenzene IVO, I.P.= 2469.856	
#	Calculated quantum defect	Size (Å)	ΔE(S-T) (eV)	Size (Å)	ΔE(S-T) (eV)
LUMO	2.145	2.346	0.152	2.836	0.051
LUMO+1	1.920	2.602	0.089	3.089	0.011
LUMO+2	1.291	3.017	0.047	3.163	0.017
LUMO+3	0.657	3.264	0.001	3.274	0.001
LUMO+4	0.505	2.984	0.038	3.035	0.014
LUMO+5	0.184	2.845	0.136	3.452	0.053

Table 8.4 Orbital size, calculated quantum defects, and energy difference between singlet and triplet states for IVO and Δ(SCF) calculations.

1,1'-sulfanediyldibenzene Δ(SCF) for conformational isomer (2)						
#	Ionization potential	Energy (eV)	Term Value (eV)	Size (Å)	Oscillator Strength	Assignment
LUMO	2471.157	2467.496	3.661	2.385	0.0023600	S1s → σ*(S-C)/π*(C=C)
LUMO+1	2470.562	2467.592	2.970	2.723	0.0005501	S1s → π*(C=C)
LUMO+2	2470.681	2468.794	1.887	3.237	0.0001141	S1s → σ*(S-C)
LUMO+3	2470.968	2468.849	2.119	2.508	0.0017013	S1s → π*(C=C)
LUMO+4	2470.703	2468.910	1.793	3.278	0.0000225	S1s → σ*(S-C)
LUMO+5	2470.574	2469.704	0.870	3.008	0.0008761	S1s → σ*(S-C)/π*(C=C)

1,1'-sulfanediyldibenzene Δ(SCF) for conformational isomer (3)						
#	Ionization potential	Energy (eV)	Term Value (eV)	Size (Å)	Oscillator Strength	Assignment
LUMO	2470.437	2467.840	2.160	3.250	0.0000000	S1s → π*(C=C)
LUMO+1	2471.458	2468.369	3.089	2.079	0.0046646	S1s → σ*(S-C)
LUMO+2	2471.748	2468.485	3.263	1.865	0.0022039	S1s → 4P
LUMO+3	2470.394	2468.681	1.713	3.239	0.0002310	S1s → π*(C=C)
LUMO+4	2470.397	2468.939	1.458	3.385	0.0001157	S1s → π*(C=C)
LUMO+5	2470.379	2469.173	1.206	3.512	0.0000000	S1s → π*(C=C)

Table 8.5 Calculated energies, term values, ionization potentials, and assignments for sulphur 1s transitions appearing below the ionization potential for 1,1'-sulfanediyldibenzene from Δ(SCF) calculations.

References

8.80. Hitchcock, A. P.; Horsley, J. A.; Stohr, J., *The Journal of Chemical Physics,* **1986,** *85* (9), 4835-4848.

8.81. Robin, M. B., *Higher Excited States of Polyatomic Molecules*, Academic, New York, **1974**, Vol. 1.

CHAPTER 9 DISCUSSION AND CONCLUSION

In this research thesis, two objectives were followed. The first objective was development of a surface sensitive detection mode in Scanning Transmission X-ray Microscopy (STXM) at the Canadian Light Source (CLS) and Advanced Light Source (ALS). The second objective was the study of sulphur 1s NEXAFS spectra of different sulphur functional groups relevant to petroleum through computational and experimental methods. The purpose of this study was to obtain a fully defined and interpreted database of sulphur 1s NEXAFS spectra used in speciation and quantification of sulphur compounds in fossil fuels.

Towards the first objective Total Electron Yield (TEY) detection of the NEXAFS signal in STXM microscope was implemented by two methods; sample current and single electron counting detection modes (see **Chapter 4** for detailed study of TEY-STXM). A detailed discussion of the modifications performed for developing TEY-STXM as well as the summary of the results and challenges encountered for implementation of TEY detection mode for improving surface sensitive analysis is provided in §**9.1**.

Towards the second objective, different sulphur compounds relevant to petroleum where chosen and the high quality sulphur 1s NEXAFS spectra of these compounds were acquired at the CLS (see **Chapter 2** for experimental procedure). The studied functionalities include: thiols and thioethers, disulphides, thiophenic compounds, sulfoxides and sulfones. These high resolution experimental NEXAFS spectra were further analyzed by the aid of IVO *ab initio* calculations that are highly optimized for simulating the core excited spectra (see **Chapter 3** for calculation detail). **Chapters 5** through **8** of this thesis were dedicated to the detailed study of the NEXAFS spectra for each functional group as well as the results and challenges encountered for speciation in each group. Below in §**9.2,** a detailed discussion of the results obtained by computational and experimental studies for all sulphur compounds is provided, along with the challenges, problems, and insights provided by these studies for improving speciation of different sulphur compounds in complex samples. §**9.3** provides a summary of the results and achievements throughout this PhD research study on TEY-STXM and sulphur 1s

NEXAFS spectroscopy of organosulphur compounds followed by future work plans provided in §**9.4**. Finally the references for this chapter are provided in §**9.5**.

9.1 Developing Surface Sensitivity in Scanning Transmission X-ray Microscopy (STXM)

In **Chapter 4** of this thesis, it was mentioned that spatially resolved chemical analysis of planar surfaces with a resolution of better than 30 nm is of general interest. Among different available microscopes, Scanning Transmission X-ray Microscopy (STXM) proved to be a good candidate for chemical imaging and spectroscopic studies of nanostructured surfaces, as it has the chemical sensitivity of the NEXAFS spectroscopy as well as the high special resolution of the X-ray microscopy (~30 nm). STXM is also less destructive than electron based microscopes such as Transmission Electron Microscopy-Electron Energy Loss Spectroscopy (TEM-EELS).[9.1] STXM can also be used for study of particulate samples, in contrast to Photoelectron Emission Microscopy (PEEM) where such samples are limited by the high electric field of the objective lens. However STXM microscope is a bulk sensitive technique and has a very limited surface sensitivity.

Therefore, for improving surface sensitive analysis in STXM microscopes, Total Electron Yield (TEY) detection of the NEXAFS signal has been implemented at the Canadian Light Source (CLS), Saskatoon, Saskatchewan, and the Advanced Light Source (ALS), Berkeley, California. Two approaches were used for implementation of total electron yield detection in these microscopes including conventional sample current measurements and single electron counting method.

Conventional sample current is the simplest method for measuring TEY spectra. In this method, a picoammeter is used to measure the drain photocurrent induced by X-ray absorption; this current is proportional to X-ray absorption cross section. Sample current TEY-STXM was used for simultaneous transmission and TEY imaging of the phase separated LB film of 2AA:1PA deposited over the Au coated Si_3N_4 window at beamline 11.0.2 at the ALS (see **Figure 4.5**). In spite of the difficulty in transmission measurements of this sample because of its thinness (~ 20Å), higher contrast TEY images of this sample were obtained at the carbon 1s edge (see **Figure 4.12**). While these results

were promising for obtaining higher surface sensitive images in TEY mode relative to transmission mode of detection, no meaningful spectrum could be obtained at the carbon edge for this sample, and the spectra collected using sample current were overwhelmed by contamination of electrons from the order sorting aperture and the zone plate. The sample current TEY signal was also near the limit of the sensitivity of the low-current amplifier, and this signal was very prone to ground loops and induction from the STXM stage motion. Increasing the signal level also required longer dwell time that in turn resulted in increased radiation damage and an increased rate of photodeposition (rapid build up of organic contamination on the surface of the sample while it is irradiated by X-ray radiation).

In contrast to the weak and artifact prone sample current signal, single electron counting method using a channeltron was promising in acquiring the spectra of this sample. Two simple methods to minimize photodeposition were also used including: use of a liquid nitrogen cold finger as well as turbo pumps to improve the vacuum (§**4.3.1**). Electron counting allows for images and spectra to be obtained in a fraction of time to that required for sample current TEY. In this method a channeltron was used on the top of the photon detector, with the sample surface was facing towards the channeltron (see **Figure 4.6**). In this geometry, the sample also worked as a physical filter to prevent the stray electrons from OSA and zone plate to be collected by the channeltron. By these modifications, TEY-NEXAFS spectra were acquired for LB films by single electron counting method. However the spectra were dominated by the carbon photodeposition (see **Figure 4.13**).

After the satisfactory first TEY-STXM results at the ALS, the TEY-STXM was developed at the SM beamline 10ID-1 located at the CLS. For verification of the function of the newly developed TEY-STXM at the CLS, we decided to use a simpler sample (a patterned Cr/Fe metal sample that was conductive and therefore provided more electrons relative to LB monolayer film of 2AA: 1PA sample). TEY images and spectra of this sample were successfully obtained and we could differentiate between the oxidation states of the thin oxide layers in thin patterned metal sample of Fe with Cr overlayer by TEY mode of detection (see **Figures 4.15** through **4.17**). After satisfactory first results of TEY-STXM on metal sample, an organic model sample of a phase segregated polymer

blend of PS-PMMA was used, and simultaneous TEY and transmission measurements were obtained for this sample. Although TEY and transmission images and spectra were obtained for this sample, the spectra obtained on PS-PMMA were still dominated by the carbon photodeposition (see **Figure 4.19** and **4.20**). However, in TEY images of this sample, some dark regions were observed that could not be seen in transmission mode (see **Figure 4.21**). These regions were attributed to the surface contamination that were not visible in transmission mode. This observation however showed the higher surface sensitivity of the TEY mode relative to transmission mode for surface analysis.

In summary, beside the satisfactory results obtained by the newly developed TEY-STXM for improved surface analysis, the challenges in single electron counting in the existing generation of STXMs are the rate of carbon photodeposition as well as the lifetime of the channeltron. These challenges mostly depend to the vacuum environment and are expected to be solved by improving the vacuum system in the next generation of UHV-STXMs.

9.2 Sulphur 1s NEXAFS Spectroscopy of Organosulphur Compounds

As mentioned in §**1.5,** improving desulphurization and hydrogenation processes in petroleum industries requires a knowledge of crude oil composition at molecular level.[9.2] Also for speciation of sulphur compounds in fossil fuels studies, a fully defined and interpreted database of sulphur 1s NEXAFS spectra is required. Therefore, the sulphur 1s NEXAFS spectra of different sulphur functionalities relevant to petroleum were studied within the framework of this project by experimental and computational methods. The studied functionalities included: thiols and thioethers (**Chapter 5**), disulphides (**Chapter 6**), thiophenic compounds (**Chapter 8**), and sulfoxides and sulfones (**Chapter 7**). In these studies, the combination of the experimental and computational studies was used to explore the effect of different ligands, phase of the sample, and symmetry of the ligands on chemical sensitivity of NEXAFS spectra and how these studies can be used for improving sulphur speciation.

The high-resolution experimental spectra were acquired at the SXRMB beamline at the CLS in gas, liquid and condensed phases based on the physical properties of the sample (e.g. boiling point, vapour pressure, etc.). Gas phase spectra were preferred

relative to condensed phase spectra, as these spectra were free from solid-state broadening, charging effects in total electron yield detection, and self-absorption in florescence yield detection. Gas phase spectra provide the best model for comparison to simulated spectra. However condensed phase spectra provide a more realistic model for speciation studies. Spectral transitions were assigned with the aid of IVO *ab initio* calculations. Studies were started by simple thiol and thioether molecules to examine the efficiency of the IVO *ab initio* calculations for simulation of the NEXAFS spectra for sulphur compounds. The comparison between simulated spectra and the experimental ones proved to be excellent and allowed an expansion of these studies to other sulphur functionalities.

These studies showed that the ligand groups, the symmetry of the ligands, phase of the sample, as well as the oxidation state of the sulphur atom determine the shape and energy position of the white line in the NEXAFS spectra. For example, Vairavamurthy observed that the white line energies of different functional groups are affected by both the local bonding environment as well as the oxidation sate in different functional groups.[9.3] Therefore, he defined an oxidation index instead of formal oxidation state to reflect both the effect of the local bonding environment and of the oxidation state on the shape and energy position of the white line.[9.3] The assigned oxidation indexes relevant to this study are provided in **Table 9.1**.

Sulphur functional group	Oxidation index
Disulphides	+0.2
Thiols and thioethers	+0.6
Thiophenes	+1
Sulfoxides	+2.2
sulfones	+4.3

Table 9.1 Oxidation indexes for different function groups.[9.3]

Based on **Table 9.1**, very similar white line energies are expected for thiols and thioethers (similar oxidation index), but this research study showed that the shape and energy of the white line is determined by a combination of different effects that will be discussed in detail below.

Figure 9.1 presents a selection example of the experimental NEXAFS spectra obtained for different sulphur functional groups in this research study.

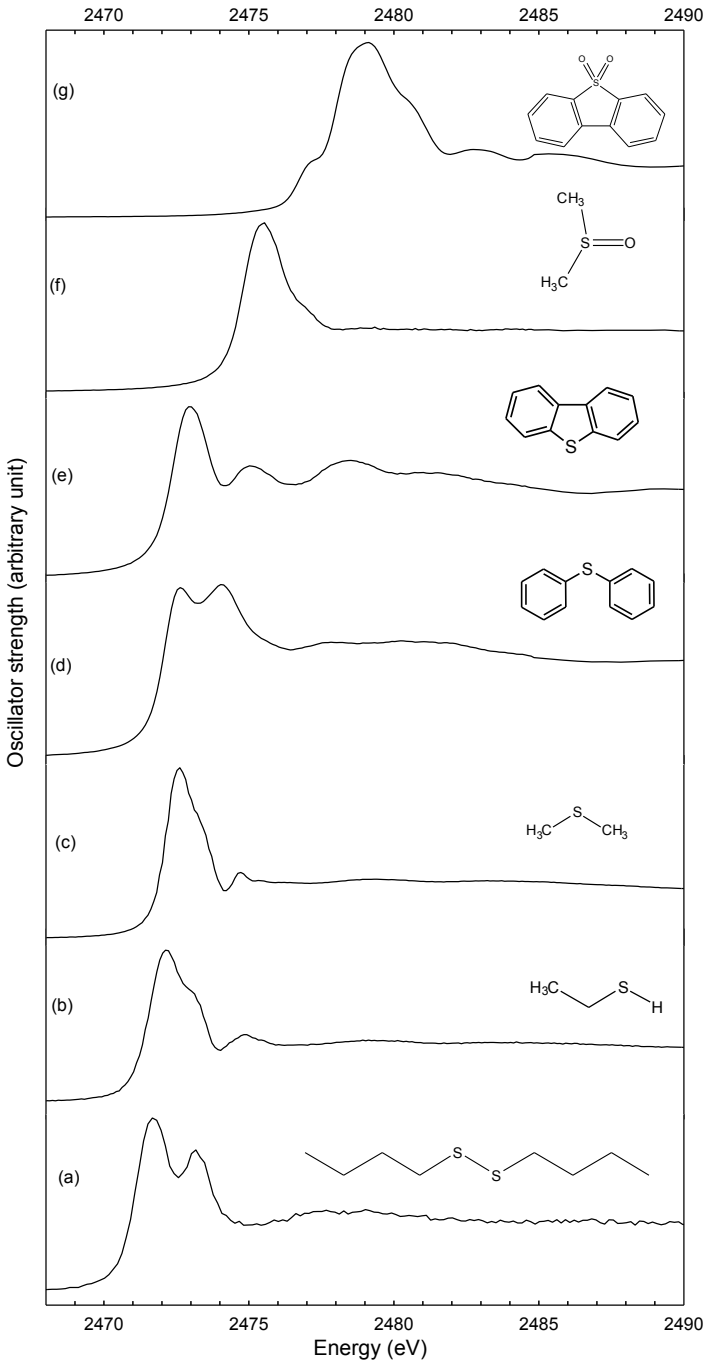

Figure 9.1 Experimental sulphur 1s NEXAFS spectra of (a) 1-(butyldisulfanyl)butane obtained with FLY; (b) ethanethiol obtained with TIY; (c) dimethyl sulphide obtained with TIY; (d) 1,1'-sulfanediyldibenzene obtained in FLY; (e) dibenzo[b,d]thiophene obtained in FLY; (f) (methylsulfinyl)methane; (g) dibenzo[b,d]thiophene 5,5-dioxide obtained in FLY.

The first intense transition (white line) in these spectra ranges from 2471.7 eV to 2477.1 eV with disulphides having the minimum energy transition and sulfones having the maximum energy transition. Except for sulfoxides and sulfones, the energy difference of the edge position for other sulphur functionalities including disulphides, thiols, thioethers, and thiophenic compounds are very close in energy (~ 0.4 eV) in accordance with the trends of the oxidation indexes in **Table 9.1**, but these NEXAFS spectra have different shapes. The detailed study of the NEXAFS spectra of each functional group has been provided in specific chapters as outlined above. In this summary, the characteristics and differences such as the shape, energy of the white line, and the spectroscopic transitions involved in the sulphur 1s NEXAFS spectra of different functional groups will be discussed. Then the useful transitions and differences in the NEXAFS spectra that can be targeted for speciation of sulphur compounds are provided.

9.2.1 Disulphides

Among all studied functional groups within this thesis disulphides have the lowest white line energy (2471.7 eV for first transition, **Figure 9.1(a)**. Their white line is dominated by two closely spaced peaks that are assigned as sulphur 1s → σ*(S-S) and σ*(S-C) transitions respectively. However, in molecules with phenyl rings bonded to sulphur atom, the second peak also samples the π*(C=C) MO of the phenyl ring in addition to σ*(S-C) transition. The effect of the asymmetric ligand groups showed no change in the shape of the NEXAFS spectra relevant to aliphatic ligands. IVO calculations show that each peak consists of two nearly degenerate transitions as a result of asymmetric ligand groups (see **Figure 6.1**). Based on these calculations it is anticipated that the NEXAFS spectra can be broadened for ligand groups of a different nature (e.g., phenyl compared to methyl) in asymmetric disulphides. It was also shown that the nature of the ligand group could change the shape of the NEXAFS spectrum. For example, in 1,1'-[disulfanediylbis(methylene)]dibenzene, the benzyl groups changed the shape of the NEXAFS spectrum to be similar to that of benzenethiol (see **Figure 6.3**), but with different energy of the white line. However, studies performed by Mijovilovich *et al*. showed that diphenyldisulphide and aliphatic disulphides have a similar shape and energy of the white line.[9.4] Therefore, based on these studies the speciation of the

aliphatic and unsaturated disulphides can be problematic as a result of similar spectra. Calculations also showed that the white line peaks in disulphides consist of different transitions originating from bonding to different ligands groups (phenyl or benzyl),[9.4] symmetry (phenyl versus methyl), and different MOs in the excited states.[9.4]

9.2.2 Thiols and Thioethers

Thiols and thioethers were also studied. The energy of the most intense transition of the white line in disulphides, thiols, and thioethers had a trend as follow: thioethers > thiols > disulphides (**Figure 9.1**). The sulphur 1s NEXAFS spectra of thiols consist of an intense peak followed by a higher energy shoulder and broad features in the continuum. The spectra of thiols were dominated by sulphur 1s → σ*(S-H) and sulphur 1s → σ*(S-C) transitions which also sampled from the π*(C=C) transition in thiols with phenyl ligand group. In both thiols and thioethers the white line energy was changed with ligand groups, however the phenyl ligands had greater effect in shifting the white line energy relative to aliphatic ligands. Therefore, the speciation of the aliphatic thiols can be problematic due to feature overlap.

In thioethers, the white line was narrower than that of the thiols and was composed of several closely spaced σ*(S-C) character transitions. Similar to thiols the ligand groups changed the shape and energy of the white line. For example the inductive effect of the amino acid group shifted the white line energy to higher energies and the cyclic strain in tetrahydrothiophene determined the relative intensity of the σ*(S-C) transitions (see **Figure 5.2**).

9.2.3 Aromatic Thioethers and Thiophenic Compounds

In aromatic thioethers, the white line of the sulphur 1s NEXAFS spectra appeared at lower energies than the alphatic thioethers (~0.1 eV for (methylsulfanyl)benzene, and ~0.5 eV for 1,1'-sulfanediyldibenzene relative to dimethyl sulphide and DL-methionine).[9.5, 9.6] This difference in energy position of the white line was attributed to the delocalization of electron density in aromatic compounds. **Figure 9.1** shows the condensed phase spectra of 1,1'-sulfanediyldibenzene. However, two different NEXAFS spectra were obtained for this molecule in gas and condensed phase (see **Figure 8.7**). The

difference between the gas phase and condensed phase NEXAFS spectra of 1,1'-sulfanediyldibenzene was attributed to different interactions between the sulphur and phenyl π* orbitals in a mixture of conformers.[9.5, 9.6] In §**9.2.2** it was mentioned that in aliphatic thioethers[9.6] all transitions have σ*(S-C) character however, in aromatic thioethers these transitions also sample from π* of the phenyl ring. This study also showed that the phase of the molecules play an important role in shape and energy of the white line. It has been also observed that the edge position of the NEXAFS spectra moves to the higher energies in condensed phase compared to the gas phase spectra, and it became broader. This broadening effect in condensed phase can arise from a decrease in core excited state lifetime because of quenching of the Rydberg character or increased dissociative σ*(S-C) character.[9.7] In speciation of sulphur compounds therefore, the phase of the model standards should be similar to the unknown sample, as this study proved that different phases could result in different NEXAFS spectra for one sample. Also the difference in white line energy and the shape of the NEXAFS spectra can be used for differentiation of aliphatic from aromatic thioethers (see **Figure 9.2**).

Thiophenic compounds were another studied functional group. **Figure 9.1(e)** shows the NEXAFS spectrum of dibenzo[b,d]thiophene which includes an intense peak followed by a low intensity second peak at higher energies and broad features in the continuum. In all thiophenic compounds the white line of the NEXAFS spectra was assigned as an overlap of sulphur 1s → σ*(S-C) that overlaps with π* transitions. In these compounds, the Rydberg character decreased (as the number of the phenyl rings increased). The second distinctive peak (2) observed in all of the thiophene experimental spectra became more distinct in the larger thiophene hetrocycles. This transition did not have a clearly defined orbital character.

For assigning the NEXAFS spectra, the simulated spectra were obtained at two different levels of calculations; IVO and Δ(SCF). It was shown that Δ(SCF) calculations reproduced the experimental spectra better than IVO calculations, as the spurious Rydberg-valence mixing in the unoccupied molecular orbitals was minimized (see **Chapter 3** for details of the calculations). The white line energy in these compounds moved to higher energies relative to aliphatic and aromatic thioethers. This energy shift of the white line can be used for speciation of these compounds from other functional

groups. Also for speciation of the thiophenic compounds the presence of an intense second peak in the NEXAFS spectrum of the mixture can be an indication for the presence of the large thiophenic heterocycles.

9.2.4 Sulfoxides and Sulfones

The NEXAFS spectra of these two functional groups appeared at higher energies compared to other functional groups studied. This is expected because of the higher oxidation state of sulphur in these species. The NEXAFS spectra of sulfoxides consisted of an intense white line followed by a weak higher energy transition and broad features in the continuum. **Figure 9.1(f)** presents the NEXAFS spectrum for (methylsulfinyl)methane as an example. The white line in these compounds was assigned as an overlap of the low energy sulphur 1s → π*(S=O)/σ*(S-C) transition and a higher energy sulphur 1s → σ*(S-O)/σ*(S-C) transition. Calculations also showed that in contrast to thiophenic compounds with a low intensity sulphur 1s → π*(S=C) transition,[9.5] the sulphur 1s → π*(S=O) transition in sulfoxides has a higher intensity and with an additional σ*(S-C) character. This higher intensity is due to higher oxidation state of sulphur atom and consequently higher contraction of the 1s and 3p orbitals for a stronger overlap relative to other functional groups.[9.8] In these compounds similar to thioethers the heterocyclic ring tension affected the shape and energy of the white line compared to noncyclic ligands.

In aliphatic sulfones, the NEXAFS spectra had the highest energy of the white line relative to other compounds. The white line also consisted of an intense transition followed by broad features in the continuum, but introducing the phenyl ring as a ligand to the molecules greatly changed the shape and energy of the white line. In sulfones with phenyl rings the white line energy moved to lower energies and became very broadened. This broadening of the white line was due to the enhanced splitting of the LUMOs. The most intense transition of the white line in these species was assigned as sulphur 1s → σ*(S-C)/σ*(S-O) transition, which also sampled form π*(S=O) transition as well. Additionally the π*(S=O) transitions moved to higher energies in aromatic sulfones compared to aliphatic ones. This energy shift could be attributed to the electron

withdrawing character of the phenyl rings, which was confirmed by the higher calculated Ionization Potential (IP) for species with phenyl rings.

For speciation of sulfones and sulfoxide the energy difference in white line can be used. In sulfoxides the edge position was sensitive to the cyclic ring tension and shifted the white line to lower energies compared to noncyclic ones. In sulfones however, the ligand groups could cause broadening of the white line, which cause feature overlap with aliphatic sulfones and poses speciation problems in these compounds. Also a NEXAFS spectrum of an unknown sample with enhanced white line width in sulfones energy regime can indicate the presence of the species with phenyl rings.

In summary, although the small differences in the white line energy can be used for speciation of different functional groups as presented in **Figure 9.1**, the modest changes in the sulphur compound's environment including the symmetry, phase of the sample, and the ligand groups can modify or shift the spectral features in the NEXAFS spectra and can cause feature overlap with the spectra of other functional groups. This can pose speciation problems especially with functional groups with very close white line energies such as disulphides, thiols, and thioethers. It has been shown that the gas phase spectra are different than the condensed phase spectra, and their edge positions move to higher energies and become broader in condensed phase relative to gas phase. The ligand groups also can change the shape and energy position of the white line. However, in disulphides bonding to phenyl ring does not make any significant change in the energy and shape of the white line,[9.4] while the benzyl groups change both the shape and energy of the white line. Therefore, the speciation of aliphatic and aromatic disulphides can be problematic due to feature overlap. The comparison of the NEXAFS spectra of disulphides to thiols and thioethers, shows that the presence of (S-S) bond in disulphides causes a change in the shape and energy position of the white line due to the enhanced splitting of the first and second LUMOs.[9.4, 9.6]

For speciation of disulphides from sulphides the energy difference of the edge position can be used, and the enhanced width of the white line for an unknown sample in the energy regime of the disulphides can suggest the simultaneous presence of disulphides and sulphides.[9.4] For speciation of thiols and disulphides, the edge positions are very close and the ligand groups attached to the sulphur atom can easily cause

features overlap between these functional groups. However, IVO *ab initio* calculations showed that the first transition in disulphides is sulphur 1s → σ*(S-S) transition while in thiols is sulphur 1s → σ*(S-H) transition, indicating that the overlapping features in the spectra of thiols and disulphides have different natures. Therefore, by targeting these transitions a good speciation can be obtained for speciation of disulphides from thiols. **Figure 9.2** presents the energy region of specific transitions that are absent or less intense in other functional groups and can be targeted for speciation of different functional groups. Also the spectral assignments of the NEXAFS spectra provided by the calculations can be used for interpretation of the NEXAFS spectra as well as the type of reactions occurred. For example in hydrogenation or desulphurization procedures by obtaining different spectra at different stages of the reactions, and tracking specific transitions, one can anticipate the efficiency of the reactions as well as the type of the resultant products.

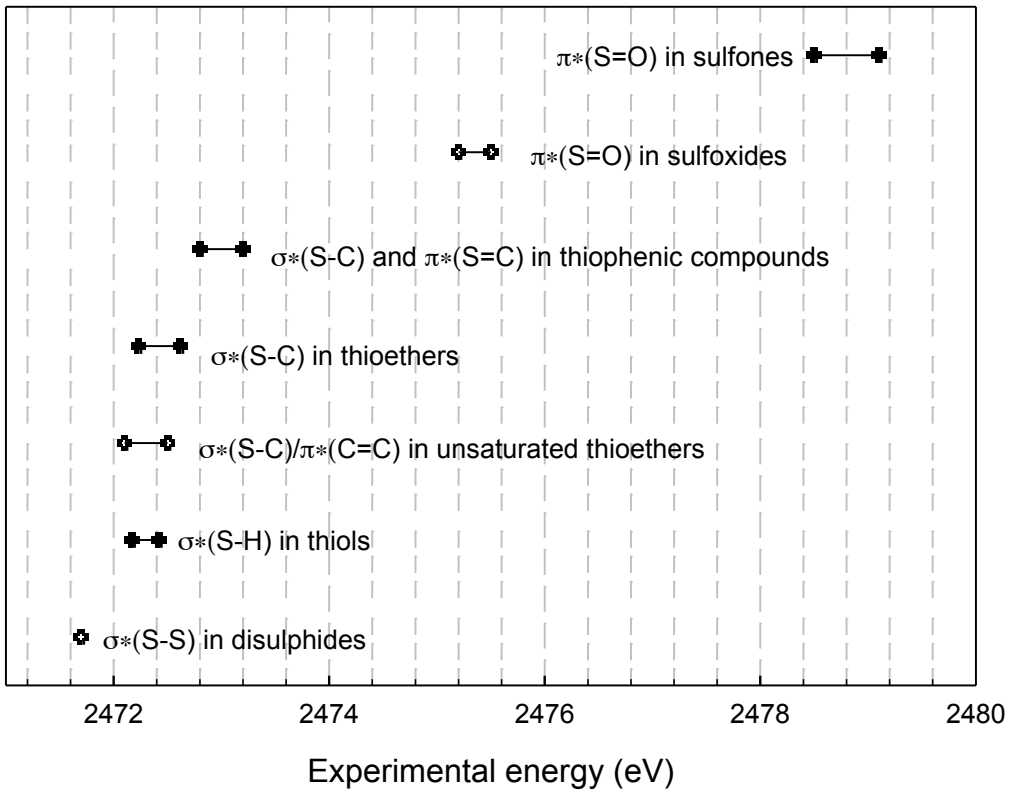

Figure 9.2 Schematic diagram of the energy region of specific transitions that can be used for targeting different functional groups.

9.3 Conclusion

In this research study, the STXM microscopes at the CLS and the ALS were modified to improve surface sensitive analysis by implementation of TEY detection mode. These methods were used for implementation of the TEY detection mode including sample current measurements and single electron counting using a channeltron. The function of the newly developed TEY-STXM microscope was verified by different model samples of LB monolayer film of 2AA: 1PA, phase segregated polymer blend of PS/PMMA, and thin metal sample of Cr/Fe, where they would be poorly studied in transmission mode. These studies however, showed that single electron counting measurements were more reliable than sample current measurements and were free from noise and stray electrons collected from OSA and zone plate in other method. Although it was possible to obtain images and spectra in TEY mode, the spectra at the carbon 1s edge were dominated by the carbon photodeposition.

Currently, one of the big challenges for implementation of single electron counting on organic samples at carbon edge is the poor vacuum in the current generation of the STXM microscope at the CLS, which operates at the pressure around 100 mtorr. This poor vacuum affects the rate of carbon photodeposition and the lifetime of the channeltron. These challenges are expected to be solved by improving the vacuum system in the next generation of UHV STXMs.

In the second part of this research, the sulphur 1s NEXAFS spectra of a series of sulphur compounds with different functionalities were studied through experimental and computational methods. In these studies, the effect of the ligands, symmetry, and the phase of the sample on the shape and energy of the white line were examined by NEXAFS spectroscopy. The experimental spectra were obtained in gas and condensed phases based on the physical properties of the sample. The gas phase experimental spectra showed improved energy resolution compared to those previously published and provided a good model for comparison to the simulated spectra. However, the condensed phase spectra provided a more realistic model for speciation problems.

The experimental NEXAFS spectra were further analyzed by the aid of IVO *ab initio* calculations that are highly optimized for the simulation of the core-excited spectra. Our results showed excellent agreement between experiment and calculations. The best

selected DFT methods, such as the half-core hole approximation calculations,[9.2] are also comparable to our standard IVO *ab initio* calculation results. In thiophenic compounds and aromatic thioethers however, we used Δ(SCF) calculations for simulating the spectra, as in these calculations the effect of the core excited electron is considered on the calculations of the potential of other electrons and spurious Rydberg-valence mixing was minimized.

Finally, the combination of the experimental and computational studies allowed us to identify the character of analytically useful transitions in the NEXAFS spectra of organosulphur molecules for a better speciation. These studies also showed that the modest changes such as the ligand groups, symmetry, and phase of the sample can affect the shape and energy of the white line, and for speciation studies the spectra of the model compounds and unknown sample should have similar phase.

9.4 Future Work

This part discusses the future possible studies following the research studies performed in this thesis.

9.4.1 Future Work for TEY-STXM Measurements

It was mentioned in §**9.1** that the biggest challenge in TEY-STXM experiments at the carbon 1s edge in the current generation of STXM microscopes is the high rate of carbon photodeposition. This problem can be overcome by the next generation of the UHV-STXM microscope, which is planned to be developed at the CLS. However, the high vacuum environment will limit the samples to those compatible with the UHV environment. For example it cannot be used for liquid samples or the samples with high vapour pressure.

9.4.2 Future Work for Sulphur 1s NEXAFS Spectroscopy

In this research study, sulphur 1s NEXAFS spectra were studied by computational and experimental methods. However, the transition energies obtained by *ab initio* calculations cannot be directly used for chemical analysis, as there is a difference between the calculated energies and the experimental energies. This difference has been

proved to be systematic for a series of carbonyl containing compounds and a semiempirical method has been explored to predict the absolute experimental transition energies from *ab initio* calculations.[9.9] In this method a specific transition of a functional group (for example the carbon 1s → π*(C=O) of carbonyl functional group) is chosen. Then a large number of experimental and calculated core → (π*/σ*) transition energies are obtained. Usually the narrower core → unoccupied MO transitions are chosen, as these transitions are easier to be tracked in samples with low concentration and signal level. Also all the computational energies should be obtained with the same level of theory and the experimental spectra should be carefully calibrated.[9.9] Finally the calculated energies are plotted versus the experimental energies. An example of this correlation diagram is shown in **Figure 9.3** for a series of carbonyl containing compounds that have different ligand groups attached to the carbonyl group.

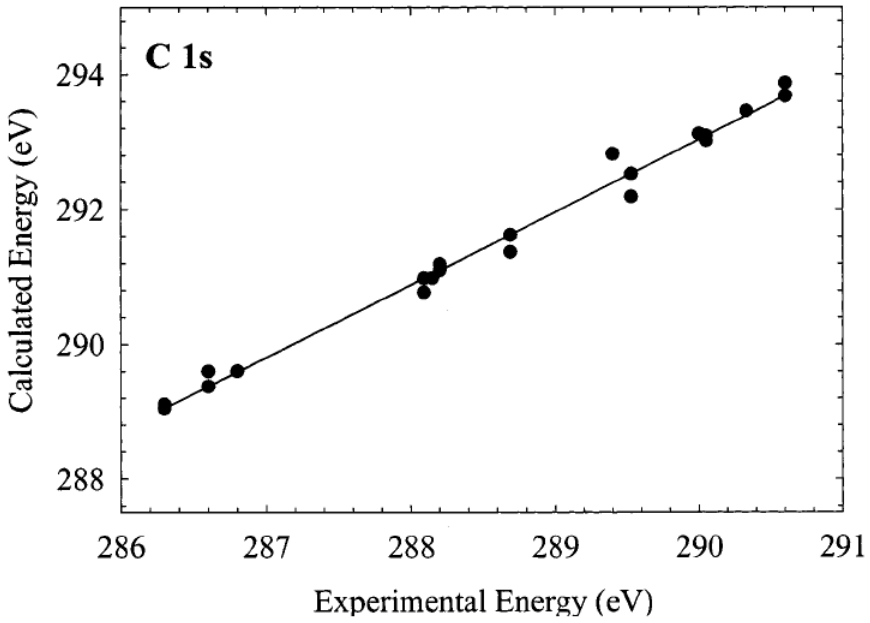

Figure 9.3 Plot of the relationship between the calculated and experimentally measured energy for the carbon 1s (C=O) → π*(C=O) transition for a series of molecules containing the carbonyl group (points) and a fit to these data (solid line). These data are fit to the equation $y = mx + b$. [Reprinted with permission from Urquhart, S. G.; Ade, H., Journal of Physical Chemistry B, 2002, *106* (34), 8531-8538. Copyright (2002) American Chemical Society.]

This figure shows a linear correlation between the experimental and calculated carbon 1s (C=O) → π*(C=O) transition energies for a series of molecules.[9.9] A high value

of slope shows that the difference between experimental and calculated energies increases for features at higher energies. Based on this correlation diagram, by calculating a specific transition energy, the experimental transition energy can be predicted.

This semiempirical method can also be used for sulphur 1s NEXAFS spectra of different sulphur functionalities by choosing a specific transition such as σ*(S-C) or π*(S=O) transitions and obtaining a correlation diagram to predict the experimental values. This method is of great values for predicting the experimental energy transitions of the reactive intermediates with short lifetime, and those samples that good model experimental spectra are not available.[9.3]

9.5 References

9.1. Rightor, E. G.; Hitchcock, A. P.; Ade, H.; Leapman, R. D.; Urquhart, S. G.; Smith, A. P.; Mitchell, G.; Fischer, D.; Shin, H. J.; Warwick, T., *Journal of Physical Chemistry B,* **1997,** *101* (11), 1950-1960.

9.2. Mijovilovich, A.; Pettersson, L. G. M.; Mangold, S.; Janousch, M.; Susini, J.; Salome, M.; de Groot, F. M. F.; Weckhuysen, B. M., *Journal of Physical Chemistry A,* **2009,** *113* (12), 2750-2756.

9.3. Vairavamurthy, A., *Spectrochimica Acta Part A: Molecular and Biomolecular Spectroscopy,* **1998,** *54* (12), 2009-2017.

9.4. Mijovilovich, A.; Pettersson, L. G. M.; de Groot, F. M. F.; Weckhuysen, B. M., *Journal of Physical Chemistry A,* **2010,** *114* (35), 9523-9528.

9.5. Behyan, S.; Hu, Y.; Urquhart, S. G., *Sulfur 1s Near Edge X-ray Absorption Fine Structure Spectroscopy of Thiophenic and Aromatic Compounds*, Accepted by *Journal of Chemical Physics*, **2013**.

9.6. Behyan, S.; Hu, Y. F.; Urquhart, S. G., *Journal of Chemical Physics,* **2011,** *134* (24), 244304-244307.

9.7. Urquhart, S. G.; Gillies, R., *Journal of Chemical Physics,* **2006,** *124* (23).

9.8. Jalilehvand, F., *Chemical Society Reviews,* **2006,** *35* (12), 1256-1268.

9.9. Urquhart, S. G.; Ade, H., *Journal of Physical Chemistry B,* **2002,** *106* (34), 8531-8538.